Spring 2019

Interfacial Ligand Dynamics and Chemistry on Highly Curved Nanoparticle Surfaces: A Plasmon-Enhanced Spectroscopic Study

Esteban Villarreal

Interfacial Ligand Dynamics and Chemistry on Highly Curved Nanoparticle Surfaces: A Plasmon-Enhanced Spectroscopic Study

by

Esteban Villarreal

Bachelor of Science
University of Pittsburgh, 2014

Submitted in Partial Fulfillment of the Requirements

For the Degree of Doctor of Philospohy in

Chemistry

College of Arts and Sciences

University of South Carolina

2019

Accepted by:

Hui Wang, Major Professor

Mark Berg, Committee Member

Timothy Shaw, Committee Member

Kevin Huang, Committee Member

Cheryl L. Addy, Vice Provost and Dean of the Graduate School

Dedication

I would like to dedicate this dissertation to God, my parents and my grandparents, as well as my brother and sister for all the love and support over the years.

Acknowledgements

I would like to give special thanks to Dr. Hui Wang, my advisor who I admire and respect, for his continued support and constructive criticism. Under his guidance, I have gained a better understanding of research and the importance of fundamental science. Secondly, I would like to thank my current lab mates, Mengqi (Will) Sun, Zixin Wang, Yang Zhang, Kexun Chen and Jing Wang for all their help and support, I enjoyed learning and getting to know these great people. I am grateful for the hard work and help from Qingfeng Zhang, Lichao Sun and Guangfang (Grace) li, I will always be thankful to these people for making me feel welcome when I first started. Finally, I would like to thank my committee members for pushing me in right direction and for their strong criticism and honesty.

Abstract

The dynamic interactions between capping ligands and nanoparticle surfaces play a critical role in guiding shape-controlled nanocrystalline growth, imparting unique physical and chemical properties to the nanoparticles. It has been well established that nanoparticles within the size regime of sub 5 nm possess unique heterogeneous catalytic properties, while sub wavelength metallic nanoparticles exhibit tunable plasmonic activity, when these properties are integrated into a single nanoparticle, it presents a significant opportunity to monitor, in real time, the molecular transformations associated with interfacial interactions at the nanoparticle surface. Using plasmon-enhanced Raman scattering as an ultrasensitive spectroscopic tool combining molecular fingerprinting with time resolving capabilities, I quantitatively demonstrated the correlation between local surface structures of Au nanoparticles with the interfacial adsorption, desorption, and exchange behaviors of thiol ligands by in situ measurements of these kinetic processes. These results provide mechanistic understanding of key thermodynamic, kinetic and geometric factors underpinning the surface curvature dependence of interfacial ligand dynamics and chemistry.

I next focused on understanding aryl grafting and polymerization on highly curved Au nanoparticle surfaces. This allowed for further real-time examination of unconventional coupling reactions between grafted aryl and thiophenol derivatives chemisorbed on Au nanoparticle surfaces that otherwise will not occur in the absence of the Au nanoparticles,

revealing two distinct mechanistic pathways for dimerization and azo formation at the surface. Understanding that surface morphology of nanoparticles plays a crucial role for both interfacial dynamics, as well as, plasmonic enhancement associated with distinctive molecular fingerprinting capability is key to developing fundamental knowledge of interfacial chemical process between nanocrystals and ligands. To further, understand the structure property relationship of plasmonic nanocrystals, I presented experimental evidence detailing structural evolution dictated by the interdependence of oxidative etching and nanocrystalline growth. Deliberately controlling the nanocrystal surface topography allows fundamental insight towards better integration and optimization of desired plasmonic and catalytic properties.

Finally, I concluded my research with investigation into understanding the impact of surface coordination of isocyanide molecules to both Au and Au-Pd core shell nanocrystalline structures evaluating the associated kinetic binding events and thermodynamic stability onto those surfaces, precisely monitoring the different mechanistic pathways associated with interfacial ligand nanoparticle interactions. The insights gained from this investigation will improve understanding for optimizing plasmonic-enhanced catalysis.

The goal of this dissertation is to couple laser spectroscopic techniques with plasmonic nanocrystalline structures to understand molecular transformation kinetics and mechanistic pathways at the nanocrystal interface towards optimization of rational design principles for both plasmonic-enhanced catalysis and plasmon-driven photocatalysis. The fundamental insight gained from these studies will improve our ability to tailor and fine tune properties of metallic nanocrystals for use in environmental and energy applications.

Table of Contents

List of Tables

List of Figures

Chapter 1
Effects of Nanoscale Surface Curvature on Ligand-Nanoparticle Interactions: A Plasmon-Enhanced Spectroscopic Study of Thiolated Ligand Adsorption, Desorption, and Exchange on Gold Nanoparticles

1.1 Introduction

The interfacial adsorption, desorption, and exchange behaviors of thiolated ligands on nanotextured Au nanoparticle surfaces exhibit phenomenal site-to-site variations essentially dictated by the local surface curvatures, resulting in heterogeneous thermodynamic and kinetic profiles remarkably more sophisticated than those associated with the self-assembly of organothiol ligand monolayers on the atomically flat surfaces of planar Au substrates. Here we use plasmon-enhanced Raman scattering as a spectroscopic tool combining time-resolving and molecular fingerprinting capabilities to quantitatively correlate the ligand dynamics with detailed molecular structures in real time under a diverse set of ligand adsorption, desorption, and exchange conditions at both equilibrium and non-equilibrium states, which enables us to delineate the effects of nanoscale surface curvature on the binding affinity, cooperativity, structural ordering, and the adsorption/desorption/exchange kinetics of organothiol ligands on colloidal Au nanoparticles. The time-resolved SERS results shown in this work provide quantitative insights on the key thermodynamic, kinetic, and geometric factors underpinning the surface curvature-dependent interfacial ligand behaviors, which may serve as a central knowledge framework guiding the site-selective incorporation of desired surface functionalities on individual metallic nanoparticles with fine-tailored surface architectures for specific applications.

1.2. Experimental Details

Chemicals and Materials:

Gold(III) chloride trihydrate ($HAuCl_4 \cdot 3H_2O$, ACS grade) was purchased from J.T. Baker. Sodium borohydride ($NaBH_4$, 99%), hydrochloric acid (HCl, 37%), and L-ascorbic

acid (AA, 99.5%) were obtained from Sigma-Aldrich. Cetyltrimethylammonium chloride (CTAC, 96%), 4-aminothiophenol (C_6H_7NS, 4-ATP, 97%), and 4-mercaptobenzonitrile (C_7H_5NS, 4-MBN, 99%) were obtained from Alfa Aesar. All reagents were used as received without further purification. Ultrapure water (18.2 MΩ resistivity, Barnstead EasyPure II 7138) was used for all experiments.

Nanoparticle Synthesis:

Au surface roughened nanoparticles (SRNPs) and quasi-spherical nanoparticles (QSNPs) were synthesized using a kinetically controlled, seed-mediated nanocrystal growth method previously developed by our group.[1, 2] Colloidal Au seeds (~3 nm in diameter) were first prepared by reducing $HAuCl_4$ with $NaBH_4$ in the presence of CTAC. Briefly, 0.25 mL of $HAuCl_4$ (10 mM) was introduced into an aqueous solution of CTAC (10 mL, 100 mM) under magnetic stir. Then 0.30 mL of ice cold, freshly prepared $NaBH_4$ (10 mM) was quickly added to the solution containing both CTAC and $HAuCl_4$. The mixture solution was stirred for 1 min, then left undisturbed for 2 h, and finally diluted 1000-fold with 100 mM CTAC. The diluted seed colloids were used for the subsequent seed-mediated growth of Au SRNPs and QSNPs.

The growth solution for SRNPs was prepared by sequentially adding 0.50 mL of $HAuCl_4$ (10 mM) and 0.10 mL of AA (100 mM) into 10.0 mL of CTAC (100 mM) solution. To prepare Au SRNPs with average diameter of ~ 128 nm, 40 μL of the diluted Au seed solution was added into the growth solution. The reactants were gently mixed for 30 s and then left undisturbed at room temperature for 4 h. The as-obtained Au SRNPs were washed with water 3 times through centrifugation/redispersion cycles, and finally redispersed in

water. The Au QSNPs were fabricated following a similar protocol for the Au SRNPs except for the addition of HCl. The growth solution was prepared by sequentially adding 0.50 mL of $HAuCl_4$ (10 mM), 0.20 mL of HCl (1.0 M), and 0.10 mL of AA (100 mM) into 10.00 mL of CTAC (100 mM) solution. After gently mixing the reactants for 30 s, the growth of Au QSNPs was initiated by adding 35 μL of the diluted Au seed solution, and then left undisturbed at room temperature for 4 h. The obtained Au QSNPs were washed with water 3 times and finally redispersed in water.

Structural Characterizations of Nanoparticles:

The structures of the nanoparticles were characterized by scanning electron microscopy (SEM) using a Zeiss Ultraplus thermal field emission scanning electron microscope. The samples for SEM measurements were dispersed in water and drop-dried on silicon wafers. The optical extinction spectra of the NPs were measured on aqueous colloidal samples at room temperature using a Beckman Coulter Du 640 spectrophotometer. The hydrodynamic sizes and ζ–potentials of the colloidal NPs were measured at room temperature using ZETASIZER nanoseries (Nano-ZS, Malvern). The samples for ζ–potential measurements were all freshly prepared, centrifuged, and dispersed in water. The concentration of the colloids for ζ–potential measurements was kept at 2×10^9 particles mL^{-1} for all the samples and pHs of the colloidal suspensions were measured to be around 7.4. In our ζ-potential measurements, we used the zeta potentiometer to measure the free mobility and effective hydrodynamic sizes of NPs, which were then converted into ζ-potentials using simple theoretical formulas approximating the NP as a hard sphere homogenously coated with a charged thin layer.[3]

The electrochemical surface oxide stripping measurements were performed using a CHI 660E workstation (CH Instruments, Austin, Texas) at room temperature with a three-electrode system composed of a Pt wire as the auxiliary, a saturated calomel electrode (SCE) as the reference, and a glassy carbon electrode (GCE, 3 mm diameter) as the working electrode. The GCE was first polished with 0.3 mm alumina slurry, followed by washing with water and ethanol before use. 20 μL of colloidal suspensions of Au QSNPs or Au SRNPs with the same particle concentration of 1.0 x 10^{10} particles mL^{-1} were dropped and air-dried on the pretreated GCE at room temperature. 2 μL of Nafion solution (0.2 wt%) was then drop-dried to hold the NPs on the electrode surfaces. Therefore, there were nominally ~ 2.0 x 10^{8} particles on each GCE. Cyclic voltammetry (CV) measurements for oxide stripping were conducted in N_2-saturated 0.5 M H_2SO_4 solution at a potential sweep rate of 5 mV s^{-1}. The total charges associated with the Au oxide stripping were calculated based on the integrated areas of the striping peaks at ~ 0.94 V (vs. SCE). Assuming the specific charge associated with Au oxide stripping to be 450 μC cm^{-2},[4] the electrochemically active surface area (ECSA) of Au QSNPs was estimated to be 2.2 x 10^{4} nm^2 per particle, which was approximately ~43 % of the physical surface area of an ideal nanosphere with a diameter of 132 nm (5.5 x 10^{4} nm^2). The average ECSA of Au SRNPs was estimated to be 1.0 x 10^{5} nm^2 per particle, about 4.5 times of the ECSA of the Au QSNPs.

Surface-Enhanced Raman Scattering (SERS) Measurements:

The SERS measurements were performed using a Bayspec Nomadic confocal Raman microscope built on an Olympus BX51 reflected optical system with a 785 nm continuous

wave excitation laser. Excitation laser was focused on colloidal samples with a 10x objective [Numerical Aperture (NA) = 0.30, working distance (WD) = 11.0 mm, Olympus MPLFLN, excitation volume of ~100 fL].[5] The laser power for Raman excitation was 10.0 mW.

Thiol Ligand Adsorption Isotherms:

The equilibrium surface coverages of thiol ligands on Au SRNPs and QSNPs were characterized as a function of thiol ligand concentrations. Colloidal Au SRNPs or QSNPs suspended in water were incubated with various concentrations of 4-ATP or 4-MBN at room temperature for 24 h to reach the equilibria. The total volume of each incubated sample was 200 µL, and particle concentrations of the SRNPs and QSNPs were kept at 1.0 x 10^9 particles mL^{-1} and 4.5 x 10^9 particles mL^{-1}, respectively, such that the total apparent surface areas of SRNPs and QSNPs were nominally the same. The adsorption of 4-ATP or 4-MBN on the Au NPs was quantified by SERS. The integration time for each spectrum was 25 s and 100 s for SRNPs and QSNPs, respectively. The apparent surface coverages of 4-ATP on the Au NPs at various 4-ATP concentrations were quantified based on the SERS intensities of the 1080 cm^{-1} (C-S stretching mode) and 1590 cm^{-1} (aromatic C-C stretching mode) peaks normalized against those of the NPs with saturated 4-ATP monolayer coverages (NPs incubated with 100 µM 4-ATP for 24 h). The apparent surface coverages of 4-MBN at various 4-MBN concentrations were quantified based on the normalized peak intensities at 1080 cm^{-1} and 2226 cm^{-1} (C≡N stretching mode).

Thiol Ligand Adsorption Kinetics:

We used SERS to monitor the thiol ligand adsorption kinetics on the surfaces of Au SRNPs and QSNPs in real time at room temperature. The thiol ligand adsorption was initiated by introducing 4 μL of ethanolic solutions of 4-ATP or 4-MBN at certain concentrations into 200 μL of colloidal Au SRNPs (1.0×10^9 particles mL^{-1}) or Au QSNPs (4.5×10^{10} particles mL^{-1}). Immediately after the thiol ligands and the NPs were mixed, successive SERS spectra were collected in real time with various time intervals and spectral integration times of 5 s for SRNPs and 50 s for QSNPs, respectively, until reaching the maximum SERS intensities after sufficiently long incubation times. The apparent surface coverages of 4-ATP and 4-MBN were quantified as a function of incubation time based on the time-evolution of SERS intensities of the 1080 cm^{-1} mode for 4-ATP and the 2226 cm^{-1} mode for 4-MBN, respectively, normalized against those of the NPs with saturated equilibrium monolayer ligand coverages (NPs incubated with 100 μM of 4-ATP or 4-MBN for 24 h).

$NaBH_4$-Induced 4-ATP Desorption:

Au SRNPs and QSNPs with saturated surface coverages of 4-ATP (NPs incubated with 50 μM of 4-ATP for 24 h) were centrifuged and redispersed in water. 200 μL of 4-ATP-coated Au SRNPs (1.0×10^9 particles mL^{-1}) or Au QSNPs (4.5×10^9 particles mL^{-1}) were then mixed with 10 μL of $NaBH_4$ at various concentrations to initiate the 4-ATP desorption. The spectral integration times were 5 s for SRNPs and 50 s for QSNPs, respectively. The peak intensities at 1080 cm^{-1} were normalized against the initial peak intensities.

Thiol Ligand Exchange of 4-ATP with 4-MBN:

Au SRNPs and QSNPs with saturated surface coverages of 4-ATP (NPs incubated with 50 μM of 4-ATP for 24 h) were centrifuged and redispersed in water. 200 μL of 4-ATP-coated Au SRNPs (1.0×10^9 particles mL^{-1}) or Au QSNPs (4.5×10^9 particles mL^{-1}) were then mixed with various concentrations of 4-MBN to initiate the thiol ligand exchange. The total volume of each sample was kept at 210 μL. SERS spectra were collected with an excitation power of 10.0 mW. The time-evolution of the peak intensities at 2226 cm^{-1} was monitored to track the ligand exchange kinetics. The spectral integration times were 5 s for SRNPs and 50 seconds for QSNPs, respectively.

The ligand exchange measurements were also performed on Au SRNPs and QSNPs with unsaturated surface coverages of 4-ATP under the same experimental conditions. Au SRNPs with unsaturated 4-ATP coverage were fabricated by incubating the CTAC-coated Au SRNPs with 10.0 μM 4-ATP for 24 h. Au QSNPs with unsaturated 4-ATP coverage were fabricated by incubating the CTAC-coated Au QSNPs with 2.0 μM 4-ATP for 24 h.

Estimation of Enhancement Factors (EFs) of Raman Signals:

We estimated the enhancement factors (EFs) of Raman signals using the following equation:

$$EF = (I_{SERS} \times N_{normal}) / (I_{normal} \times N_{SERS}) \quad \text{(S1)},$$

where I_{SERS} is the intensity of a specific band in the SERS spectra of 4-ATP; I_{normal} is the intensity of the same band in the normal Raman spectra of 4-ATP under the same condition; N_{normal} is the number of probe molecules in the excitation volume for the normal Raman measurements; N_{SERS} is the number of adsorbed molecules on an individual particle.

We chose the Raman modes of 4-ATP at 1078 cm^{-1} for the EF calculations. N_{normal} was calculated by using the following expression:

$N_{normal} = (V \times D/M) \times N_A = 1.80 \times 10^{11}$ molecules (S2),

where V is the excitation volume (100 fL), D is the density of 4-ATP (1.17 g mL^{-1}), M is the molar mass of 4-ATP (125 g mol^{-1}) and $N_A = 6.02 \times 10^{23}$ mol^{-1} is the Avogadro constant.

To determine N_{SERS}, a monolayer of 4-ATP molecules with molecular footprint size of 0.39 nm^2 was assumed to be closely packed on the surface of each Au particle. The surface area of a QSNP was estimated as the surface area of a sphere that is 130 nm in diameter. The surface area of a SRNP was estimated as 4.5 times of that of a QSNP. We kept the concentrations of 4-ATP-coated QSNPs and SRNPs both at 1.0 X 10^9 particles mL^{-1} such that there were on average 0.1 particles in the laser focal volume.

The ensemble averaged EFs on the Au SRNPs and QSNPs were estimated to be 3.0×10^6 and 2.4×10^5, respectively, which were in very good agreement with our previous results obtained on surface-immobilized single nanoparticles.[1] In these calculations, we assumed that the binding footprint size of each 4-ATP on the nanoparticles was the same as that on a planar surface, which was previously measured to be 0.39 nm^2 per molecule. Considering the fact that the molecular packing density on highly curved surfaces should be lower than that on planar surfaces, the average enhancement factors on SRNPs might be underestimated.

Simplification of the Langmuir Kinetics of Ligand Adsorption to First-Order Rate Laws:

The polynomial expression of the varying-order rate equations for the ligand adsorption were derived by Liu and coworkers.[6] The ligand adsorption/desorption on nanoparticle surfaces can be considered as a reversible process described below:

$$L + S \underset{k_d}{\overset{k_a}{\rightleftharpoons}} S\text{-}L \qquad \text{(S3)},$$

in which L is the free ligand in the bulk solution, S refers to the ligand binding sites on the nanoparticle surfaces, and S-L is the ligand bound to the nanoparticle surfaces. k_a and k_d represent the adsorption and desorption rate constants, respectively. The surface coverage of the ligands at any time, θ_t, is defined as

$$\theta_t = \frac{q_t}{q_{\max}} = \frac{C_0 - C_t}{q_{\max} x} \qquad \text{(S4)},$$

in which q_t and q_{max} are the adsorption capacities of nanoparticles at any time and its maximum value, respectively. C_0 and C_t are the respective concentrations of ligands in solution at time zero and time t, while x represents the dosage of adsorbent. The overall rate equation for ligand adsorption can be further expressed as follows:

$$\frac{d\theta_t}{dt} = k_a C_t (1-\theta_t) - k_d \theta_t \qquad \text{(S5)}.$$

Equation S5 has been often referred to as the rate law for Langmuir adsorption kinetics, which has been widely applied to describe adsorption of ligands at solid surfaces. Inserting Equation S4 into Equation S5 yields

$$\frac{d\theta_t}{dt} = k_a q_{\max} x \theta_t^2 - (k_a C_0 + k_a q_{\max} x + k_d)\theta_t - k_a C_0 \qquad \text{(S6)}.$$

Equation S6 shows that the adsorption rate is a quadratic function of θ_t at given C_0 and x. When adsorption reaches equilibrium, $d\theta_t/dt$ becomes zero, and θ_t reaches its value at equilibrium, θ_{eq}. Solving Equation S6 under the equilibrium conditions gives

$$\theta_{eq}=\frac{K_{eq}(q_{\max}x+C_0)+1-\sqrt{\Delta}}{2K_{eq}q_{\max}x} \qquad \text{(S7)},$$

where $\Delta=K_{eq}^2(C_0-q_{\max}x)^2+2K_{eq}(C_0+q_{\max}x)+1$, and $K_{eq}=\frac{k_a}{k_d}$.

If we define that $k_1\equiv\sqrt{\Delta}\times k_d$ (S8), and $k_2\equiv k_{eq}q_{\max}xk_d$ (S9), then

$$\frac{d\theta_t}{dt}=k_1(\theta_{eq}-\theta_t)+k_2(\theta_{eq}-\theta_t)^2 \qquad \text{(S10)}.$$

Equation S10 shows that the overall adsorption rate, $d\theta_t/dt$, is the combination of the first-order term $k_1(\theta_{eq} - \theta_t)$ and the second-order term $k_2(\theta_e - \theta_t)^2$. The relative magnitude of k_1 over $k_2\times(\theta_{eq} - \theta_t)$, which is dependent upon C_0, governs the simplification of the overall kinetics to either the first- or the second-order rate laws.

By combining Equations S8, S9, and S10, we can obtain the follow equation:

$$\theta_{eq}-\frac{k_1}{k_2}=\frac{K_{eq}(q_{\max}x+C_0)+1-3\sqrt{\Delta}}{2K_{eq}q_{\max}x} \qquad \text{(S11)}.$$

When the ligand concentrations are far higher than that required for monolayer saturation of the particle surfaces, i.e. $C_0>>q_{\max}x$, $\Delta\approx(K_{eq}C_0+1)^2$. Therefore,

$$\theta_{eq}-\frac{k_1}{k_2}\approx\frac{K_{eq}C_0+1-3K_{eq}C_0-3}{2K_{eq}q_{\max}x}=-\frac{K_{eq}C_0+1}{K_{eq}q_{\max}x} \qquad \text{(S12)}.$$

If C_0 is sufficiently high, then $\theta_{eq}-\frac{k_1}{k_2}<<0<\theta_t$, based on which we can further get

$$k_1>>k_2(\theta_{eq}-\theta_t) \qquad \text{(S13)}.$$

Therefore, at sufficiently high ligand concentrations, the Langmuir kinetics of ligand adsorption can be simplified to a first-order rate law shown as follows:

$$\frac{d\theta_t}{dt} \approx k_1(\theta_{eq} - \theta_t) \qquad \text{(S14)}.$$

References for Experimental

1. Zhang, Q. F.; Large, N.; Nordlander, P.; Wang, H. J. Phys. Chem. Lett. 2014, 5, 370-374.

2. Zhang, Q. F.; Blom, D. A.; Wang, H. Chem. Mater. 2014, 26, 5131-5142.

3. Park, S.; Sinha, N.; Hamad-Schifferli, K. Langmuir 2010, 26, 13071-13075.

4. Trasatti, S.; Petrii, O. A. J. Electroanal. Chem. 1992, 327, 353-376.

5. Zhang, Q. F.; Zhou, Y.; Villarreal, E.; Lin, Y.; Zou, S.; Wang, H. Nano Lett. 2015, 15, 4161-4169.

6. Liu, Y.; Shen, L. Langmuir 2008, 24, 11625-11630.

7. Osawa, M.; Matsuda, N.; Yoshii, K.; Uchida, I. J. Phys. Chem. 1994, 98, 12702

8. Hu, X. G.; Wang, T.; Wang, L.; Dong, S. J. J. Phys. Chem. C 2007, 111, 6962-6969.

9. Huang, Y. F.; Wu, D. Y.; Zhu, H. P.; Zhao, L. B.; Liu, G. K.; Ren, B.; Tian, Z. Q. Phys. Chem. Chem. Phys. 2012, 14, 8485-8497.

10. Jing, H.; Zhang, Q. F.; Large, N.; Yu, C. M.; Blom, D. A.; Nordlander, P.; Wang, H. Nano Lett. 2014, 14, 3674-3682.

11. Takeyasu, N.; Kagawa, R.; Sakata, K.; Kaneta, T. J. Phys. Chem. C 2016, 120, 12163-12169.

12. Tay, L. L.; Hulse, J.; Kennedy, D.; Pezacki, J. P. J. Phys. Chem. C 2010, 114, 7356-7363.

13. Gkogkou, D.; Schreiber, B.; Shaykhutdinov, T.; Ly, H. K.; Kuhlmann, U.; Gernert, U.; Facsko, S.; Hildebrandt, P.; Esser, N.; Hinrichs, K.; Weidinger, I. M.; Oates. ACS Sensors 2016, 1, 318-323

14. Gao, X. P.; Davies, J. P.; Weaver, M. J. J. Phys. Chem. 1990, 94, 6858-6864.

15. Mrozek, M. F.; Wasileski, S. A.; Weaver, M. J. J. Am. Chem. Soc. 2001, 123, 12817-12825.

16. Perry, D. A.; Cordova, J. S.; Schiefer, E. M.; Chen, T. Y.; Razer, T. M.; Biris, A. S. J. Phys. Chem. C 2012, 116, 4584-4593.

1.3 Introduction

Almost all chemically synthesized colloidal inorganic nanoparticles, regardless of their sizes, shapes, and compositions, are coated with organic surface capping ligands, which play pivotal roles in guiding the nanocrystal growth during bottom-up colloidal syntheses.[1-8] The functionalization of nanoparticle surfaces with deliberately designed ligands, either through ligand-guided nanocrystal growth or post-synthetic ligand exchange, may introduce interesting modifications to the optical, electronic, and surface properties of the nanoparticles,[5] remarkably influencing a series of important interfacial processes, such as surface charge transfers,[7, 9, 10] catalytic molecular transformations,[11] targeted delivery in biological systems,[12-14] and programmed assembly of nanocrystals into suprastructures.[15-20] Rational optimization of nanoparticle surfaces for specific applications essentially relies on detailed mechanistic understanding of the dynamic interactions between the inorganic nanocrystal cores and the organic ligand shells.

It has long been known that a plethora of organothiol molecules spontaneously chemisorb onto macroscopic Au substrates exhibiting atomically flat surfaces through strong covalent Au-S interactions to form structurally ordered and thermodynamically stable self-assembled monolayers (SAMs).[21-24] The energetics and dynamics of the ligand-surface interactions, however, are drastically modified when nanoscale curvatures are introduced to the planar Au surfaces.[21] The effects of such nanoscale surface curvature become remarkably more pronounced when the thiolated ligands interact with ultrasmall, sub-5 nm Au nanoparticles whose surfaces are highly curved and dominated by undercoordinated surface atoms,[25-30] giving rise to a unique set of intriguing phenomena that are otherwise not observable on atomically flat Au surfaces, such as phase separation of subnanometer ligand domains,[31] altered pKa of surface ligands,[32] enhanced macromolecular crowding effect,[33] chemical patchiness-guided self-assembly,[16] and kinetic modulation of regioselective photoreactions.[34] To better understand the surface curvature effects, a series of in situ spectroscopic techniques, such as electron paramagnetic resonance,[35] nuclear magnetic resonance,[25] second harmonic generation,[36, 37] X-ray absorption spectroscopy,[26] and surface plasmon resonance spectroscopy,[38, 39] have been used in combination with calorimetry[40] to resolve the complex kinetic and thermodynamic profiles of the ligand-nanoparticle interactions. However, it still remains challenging to disentangle the intertwining thermodynamic, kinetic, and geometric factors that underpin the surface curvature-dependent ligand behaviors largely due to the surface structural complexity of chemically synthesized nanoparticles as well as the dynamic, multiscale, and heterogeneous nature of the ligand-surface and ligand-ligand interactions.

1.4 Results and Discussion

Here we scrutinize how the nanoscale surface curvature profoundly impacts the binding affinity and cooperativity as well as the adsorption/desorption/exchange kinetics of thiolated aromatic ligands on surface-textured Au nanoparticles using surface-enhanced Raman scattering (SERS) as an ultrasensitive plasmon-enhanced spectroscopic tool. SERS has unique time-resolving and molecular fingerprinting capabilities,[41, 42] allowing for the correlation of the interfacial ligand dynamics with detailed molecular structures in real time[43, 44] both at equilibrium and non-equilibrium conditions without separating the colloidal nanoparticles from their native, ligand-present environments. Previous studies on the interactions of organothiols with Au surfaces, however, have been focusing on either macroscopic planar Au substrates[21-24] or sub-5 nm Au nanoparticles,[25-30] neither of which possess the desired plasmonic properties exploitable for SERS. Here we are particularly interested in subwavelength Au colloids in a mesoscopic size regime (50-200 nm) because of their structural stability, plasmonic tunability, and tailorable surface textures. As shown in this work, subwavelength Au nanoparticles retain their colloidal stability under a wide range of ligand adsorption, desorption, and exchange conditions without forming nanoparticle aggregates. In addition, they exhibit intense plasmonic field enhancements optimizable for SERS-based quantification and characterization of surface ligands on colloidal nanoparticles, circumventing the irreproducibility issue caused by the interstitial "hot spots"[45-47] in nanoparticle aggregates. Furthermore, atomically flat facets and nanoscale surface roughness can be selectively created on individual nanoparticles while keeping the particles in the plasmonically active, subwavelength size regime.

We selectively synthesized subwavelength Au quasi-spherical nanoparticles (QSNPs) and surface roughened nanoparticles (SRNPs) with tunable overall particle sizes by kinetically maneuvering the seed-mediated nanocrystal growth following a protocol we previously developed.[48, 49] Slow nanocrystal growth resulted in the formation of thermodynamically stable, multifaceted Au QSNPs (Figure 1A), whereas Au SRNPs enclosed by highly curved surfaces (Figure 1B) represented the kinetically favored products under fast nanocrystal growth conditions.[48] In this work, the sizes of both QSNPs and SRNPs were tuned to be around 130 nm (Figure 1C) to ensure that the strikingly distinct interfacial ligand behaviors were intrinsically tied to the difference in surface curvatures rather than overall particle sizes.

As previously revealed by detailed electron microscopy characterizations,[49] the surfaces of SRNPs were enclosed by a mixture of undercoordinated and close-packed surface atoms on the highly curved and locally flat surface regions, respectively, whereas

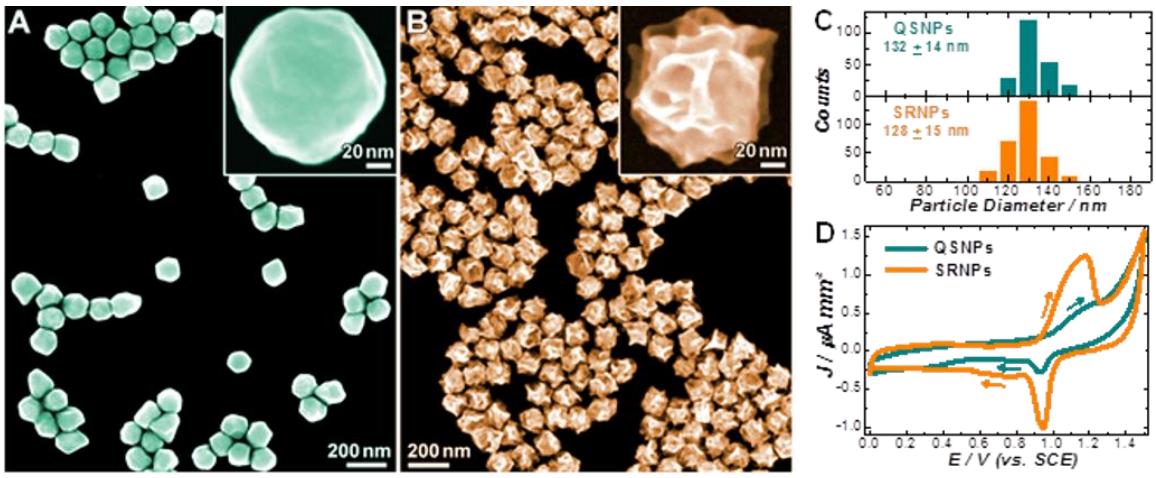

Figure 1. 1 Structures of Au QSNPs and SRNPs. SEM images of (A) Au QSNPs and (B) Au SRNPs. The insets show higher-magnification SEM images highlighting the nanoscale surface textures of individual particles. (C) Size distributions of Au QSNPs and SRNPs. The average particle sizes and standard deviations were obtained from more than 200 nanoparticles in SEM images. (D) CV curves of Au QSNPs and SRNPs on glassy carbon electrodes (GCEs) in 0.5 M H_2SO_4 electrolyte at a potential sweep rate of 5 mV s^{-1}. The arrows show the directions of the potential sweeps

the surfaces of QSNPs were dominated by {100} and {111} facets covered with close-packed surface atoms with a small fraction of undercoordinated surface atoms located at the particle edges, corners, and surface defects. A strong correlation existed between the characteristic surface oxidation potentials and the surface atomic coordination's, allowing us to use cyclic voltammetry (CV) to characterize the atomic-level surface structures of the Au QSNPs and SRNPs. During the anodic potential sweeps, Au QSNPs exhibited a major oxidation peak above 1.40 V vs. saturated calomel electrode (SCE), signifying the oxidation of the Au surface atoms on {100} and {111} facets,[50, 51] whereas the oxidation of the undercoordinated Au atoms on the highly curved surfaces of SRNPs occurred over a significantly lower potential range from 0.95 to 1.25 V (vs. SCE).[51, 52] During the cathodic potential sweeps, a sharp reduction peak emerged around 0.94 V (vs. SCE), which was an electrochemical signature of the stripping of the surface oxide layers.[51, 52] Comparison of the relative areas of the oxide stripping peaks revealed a 4.5-fold increase in the electrochemical surface area (ECSA) of each particle when switching from QSNPs to SRNPs.

The as-synthesized Au QSNPs and SRNPs were both capped with positively charged CTAC ligand bilayers, which could be completely displaced by organothiol ligands, such as 4-aminothiophenol (4-ATP). Upon complete surface ligand exchange of CTAC with 4-ATP, the ξ-potentials of the colloidal nanoparticles decreased by ~ 60 % while the hydrodynamic sizes remained essentially unchanged (Figures 1.2A-1.2C in Supporting Information). The introduction of nanoscale surface roughness to the subwavelength Au nanoparticles caused significant spectral red-shifts of the plasmon

resonance and further intensified local-field enhancements.[48] After ligand exchange, the plasmon resonances of both the QSNPs and SRNPs red-shifted by ~ 5 nm while the plasmon bandwidths and spectral line shapes remained essentially unchanged Figure 1.2D , verifying that both Au QSNPs and SRNPs well-maintained their colloidal stability, free of aggregation.

The temporal ξ-potential evolution of the colloidal nanoparticles dispersed in pure water indicated that the dissociation of 4-ATP from the particle surfaces was far slower than that of CTAC, exhibiting no detectable decrease in ξ-potentials over 30 days, due to

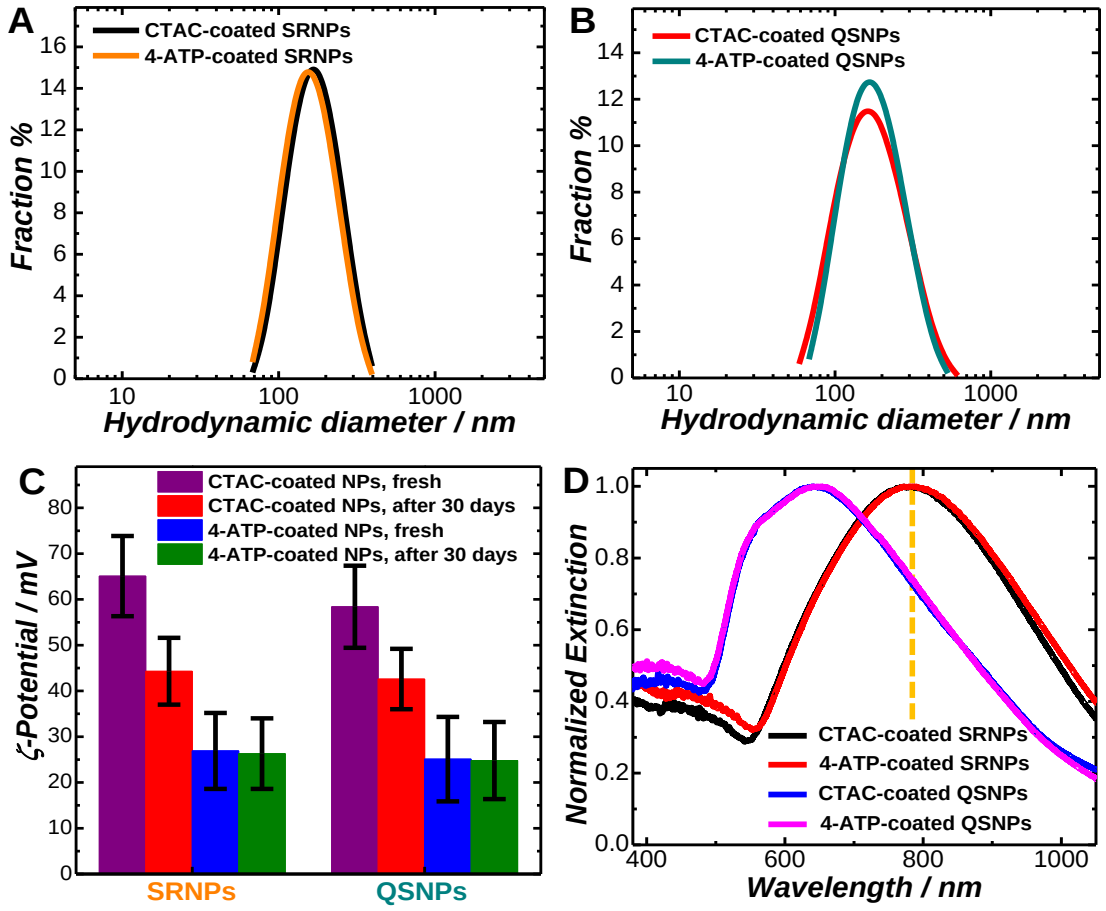

Figure 1. 2 Hydrodynamic diameters of (A) Au SRNPs and (B) Au QSNPs before 4-ATP adsorption and after incubation with 50 μM of 4-ATP for 24 h. (C) ζ-potentials of freshly prepared CTAC-coated and 4-ATP-coated NPs and the NPs after being store in water for 30 days at room temperature. (D) Extinction spectra of colloidal CTAC-coated and 4-ATP-coated Au SRNPs and Au QSNPs. The vertical dash line shows the wavelength (785 nm) of the excitation laser for SERS measurements.

the fact that the covalent Au-S interactions were remarkably stronger than the Au-CTAC interactions. We used SERS to quantify the surface coverage and characterize the structures of the chemisorbed 4-ATP ligands. We focused a near-infrared laser (785 nm) into an excitation volume of ~100 fL on the colloidal samples using a confocal Raman microscope such that each freely-diffusing nanoparticle was exposed to the excitation laser for a short time period limited by diffusion, effectively eliminating photothermal sample damage and plasmon-driven photoreactions (e.g. photocatalytic oxidative coupling of 4-ATP).[53]

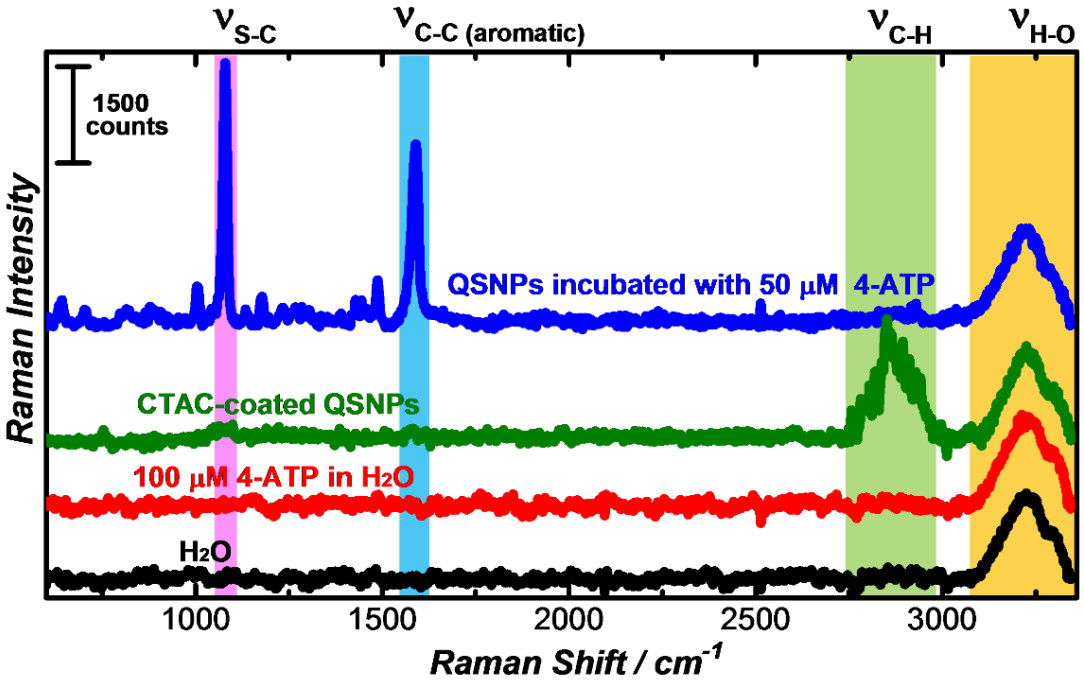

Figure 1. 3 Raman spectra of pure water, 100 µM of 4-ATP in water, and SERS spectra of freshly prepared CTAC-coated Au QSNPs and Au QSNPs incubated with 50 µM 4-ATP after 24 h. The concentrations of the colloidal QSNPs were kept at 4.5 x 10^9 particles mL^{-1}. The spectra were obtained at 785 nm excitation with a laser power of 10 mW and an integration time of 100 s. The SERS peaks at 1078 cm^{-1} and 1588 cm^{-1} were assigned to the C-S stretching mode and benzene ring stretching mode of surface-adsorbed 4-ATP, respectively. The two broad Raman band centered around 2870 cm^{-1} and 3230 cm^{-1} were assigned to the C-H stretching mode of surface-adsorbed CTAC and the O-H stretching mode of water, respectively. The spectra were off-set for clarity.

As shown in Figure 1.3, a broad SERS band corresponding to the C-H stretching mode of CTAC was observed around 2800 cm^{-1} on the CTAC-coated Au QSNPs, which completely

Table 1. 1 Assignments of the Major SERS peaks of 4-ATP

Raman Shift / cm^{-1}	Peak Assignments*
1015	$\alpha_{CCC} + \alpha_{CC}$ [7-11]
1078	$\nu_{C-S} + \nu_{CC}$ [7-11]
1173	$\beta_{C-H} + \nu_{CC}$ [10]
1480	$\nu_{C-N} + \beta_{C-H} + \nu_{CC}$ [7-9]
1588	ν_{CC} [7-11]

disappeared after the CTAC ligands were fully displaced with 4-ATP. When the Au QSNP surfaces were saturated with 4-ATP, the SERS signatures of 4-ATP were clearly resolved (see detailed peak assignments in Table 1.1 in Supporting Information), whereas no Raman signals of 4-ATP were detectable on 100 μM 4-ATP solution without Au nanoparticles.

The absence of the characteristic peak of S-H bond stretching at 2530 cm^{-1} strongly indicated that the SERS signals were from the 4-ATP ligands chemisorbed on nanoparticle surfaces with negligible interference from the unbound 4-ATP ligands remaining in the bulk solution. The Raman band corresponding to the O-H stretching mode of H_2O (3230 cm^{-1}) exhibited essentially fixed intensity and peak position for all the samples we measured, thereby serving as an internal reference for quantifying the relative SERS intensities of various Raman modes. At 785 nm excitation, 4-ATP-coated Au SRNPs exhibited SERS signals about 60 times stronger than those on the 4-ATP-coated Au QSNPs (Figure 1.4). The empirical average Raman enhancement factor was estimated to be on the order of 10^6 on SRNPs, about one order of magnitude higher than that on QSNPs, which

was in excellent agreement with previously reported Finite-Difference Time Domain calculations and the SERS data collected on surface-immobilized single nanoparticles.[48] Details of the enhancement factors estimation were presented in experimental section.

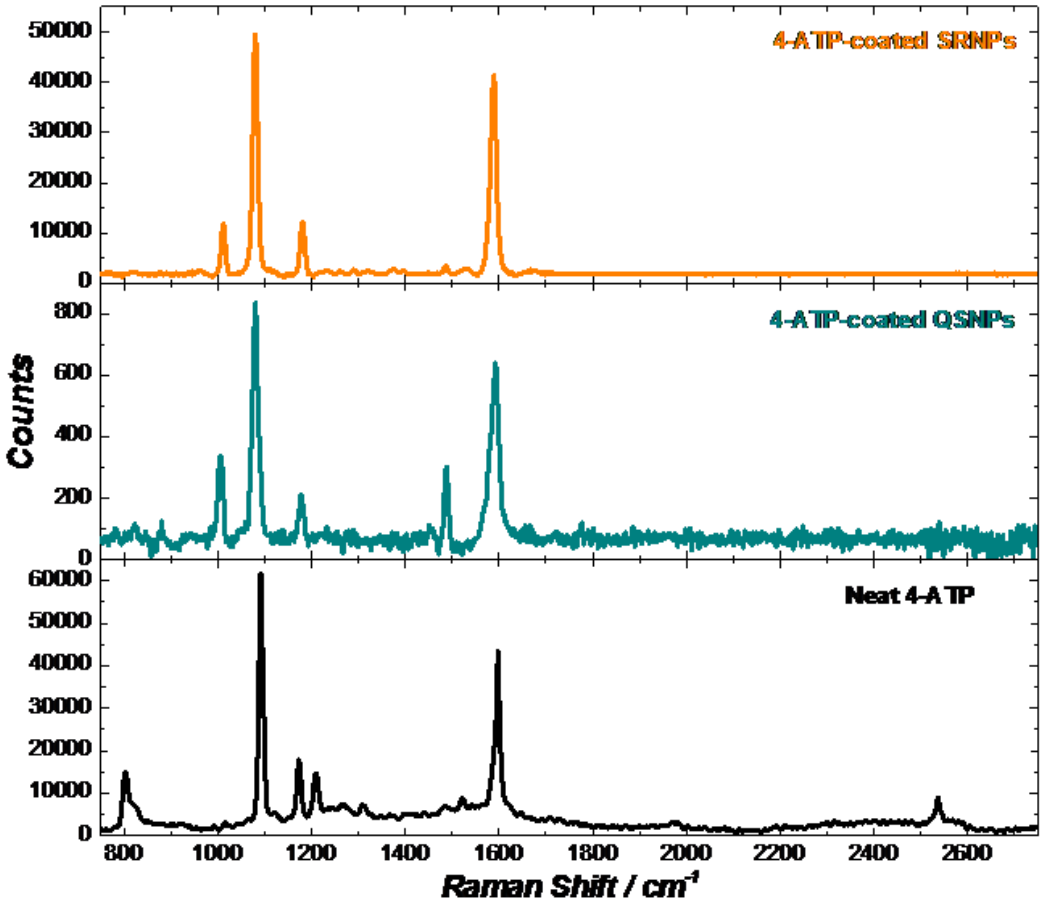

Figure 1. 4 SERS spectra of 4-ATP-coated Au SRNPs (top panel) and Au QSNPs (middle panel) and normal Raman spectrum of neat 4-ATP solid film (bottom panel). The spectra were obtained at 785 nm excitation with a laser power of 10 mW and an integration time of 100 s. The concentrations of SRNPs and QSNPs were both kept at 1.0 x 10^9 particles mL^{-1}.

We titrated the Au QSNPs and SRNPs with 4-ATP to displace the surface-bound CTAC (Figure 2A) and used SERS to quantify the apparent surface coverages of 4-ATP at equilibria, θ_{eq}. We incubated colloidal nanoparticles with various concentrations of 4-ATP for a sufficiently long time, i.e. 24 h, to ensure that the ligand adsorption/desorption

equilibrium was fully established at each titration point prior to the SERS measurements. As the 4-ATP concentration, $C_{4\text{-ATP}}$, progressively increased, the Raman peaks signifying the chemisorbed 4-ATP became increasingly more intense until reaching a plateau upon the saturation of the nanoparticle surfaces with 4-ATP (Figures 1.5B and 1.5C). The θ_{eq} at various $C_{4\text{-ATP}}$ were calculated by normalizing the intensities of the two major Raman peaks, the C-S stretching mode at 1078 cm^{-1} and the benzene ring stretching mode at 1588 cm^{-1}, against those corresponding to saturated 4-ATP surface coverages (obtained after incubation of QSNPs or SRNPs with 100 μM 4-ATP for 24 h). The ligand adsorption isotherms obtained from the 1078 cm^{-1} and 1588 cm^{-1} modes were shown in Figures 2D and 2E, respectively. We fitted the 4-ATP adsorption isotherms on Au QSNPs with the Hill equation shown below:

$$\theta_{eq} = \frac{K_1 C^{n_1}}{1 + K_1 C^{n_1}} \quad (1),$$

where K_1 was the equilibrium constant and n_1 was the Hill coefficient. The fitting results showed that 4-ATP strongly adsorbed to the faceted surfaces of QSNPs with micromolar-scale affinities in a noncooperative manner with Hill coefficients very close to 1, obeying the classical Langmuir adsorption model which involved the ligand binding to independent surface sites with a uniform binding affinity.

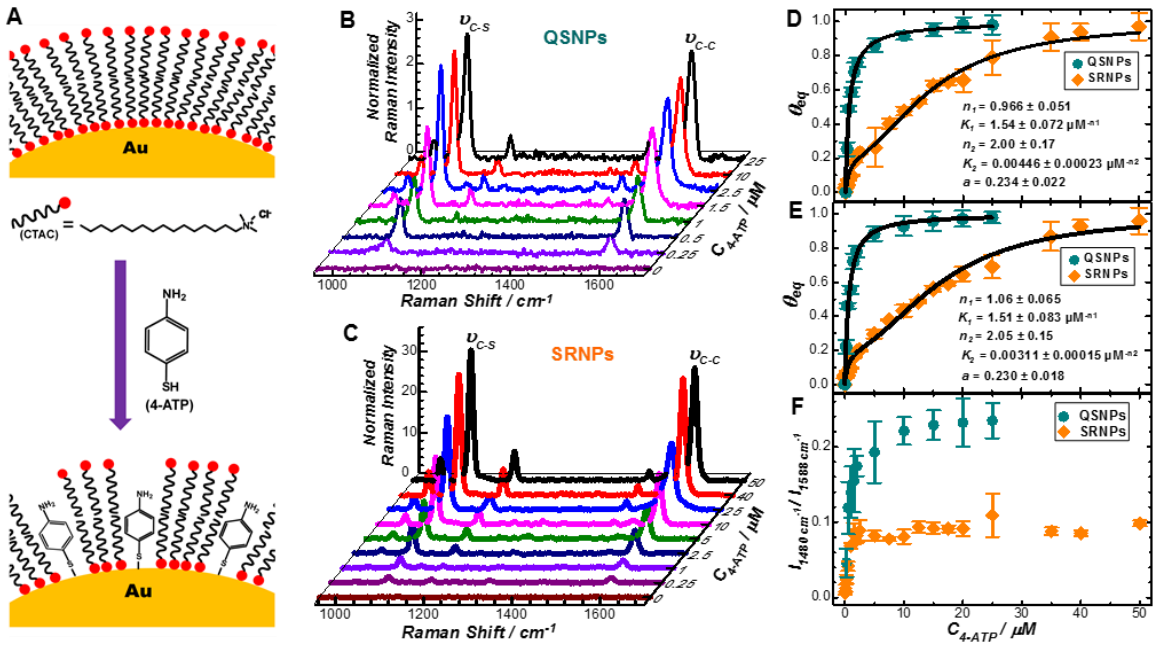

Figure 1. 5 Thermodynamics of 4-ATP adsorption on Au QSNPs and SRNPs. (A) Schematic illustration of ligand displacement of CTAC with 4-ATP. SERS spectra collected on (B) Au QSNPs and (C) Au SRNPs after the nanoparticles were incubated with various concentrations of 4-ATP for 24 h. The peak intensity at 3230 cm^{-1} (normal Raman peak of H_2O) was used as the internal reference for signal normalization. 4-ATP adsorption isotherms on Au QSNPs and SRNPs obtained from the (D) 1078 cm^{-1} and (E) 1588 cm^{-1} modes. The error bars represent the standard deviations obtained from 5 replicate samples. The solid black curves show the least squares curve fitting results. (F) Plots of $I_{1480cm^{-1}} / I_{1588cm^{-1}}$ vs. $C_{4\text{-ATP}}$ for Au QSNPs and SRNPs.

The 4-ATP binding isotherms on Au SRNPs, however, exhibited much more complicated profiles that cannot be interpreted by a simple Langmuir adsorption model. Because each SRNP was enclosed by both locally flat and curved surfaces, the contributions of two types of binding sites with remarkably different affinities and cooperativities must be considered using a two-component Hill equation:

$$\theta_{eq} = a \times \frac{K_1 C^{n_1}}{1 + K_1 C^{n_1}} + (1 - a) \times \frac{K_2 C^{n_2}}{1 + K_2 C^{n_2}} \quad (2),$$

where K_1 and n_1 were the equilibrium constant and Hill coefficient, respectively, for the ligand binding to the locally flat regions on SRNP surfaces. K_2 and n_2 were the equilibrium constant and Hill coefficient describing the binding of 4-ATP onto the highly curved regions on the SRNP surfaces. The fractional coefficient, a, refers to the fraction of ligands bound to flat surface regions. We fitted the binding isotherms of 4-ATP on SRNPs with Equation (2) to get a, K_2, and n_2, while adopting the same K_1 and n_1 values as those of QSNPs obtained from curve fitting using Equation (1). The binding affinity of 4-ATP to highly curved surfaces was approximately one order of magnitude lower than that to the locally flat Au surfaces (Figures 1.5D and 1.5E). The low-affinity ligand binding to the

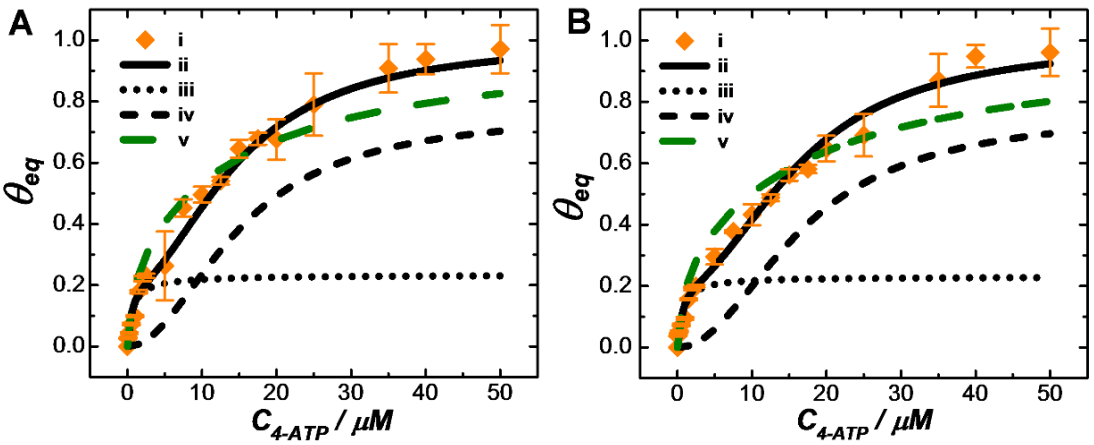

Figure 1. 6 4-ATP adsorption isotherms obtained on the basis of SERS intensities of (A) 1078 cm^{-1} and (B) 1588 cm^{-1} modes. Least squares curve fitting were conducted on the experimental results (i). Curves ii show the curve fitting results using Equation (2). The fitting results were further decomposed into a high binding affinity component (curves iii) and a low binding affinity component (curves iv), respectively. Curves v show the least squares fitting results assuming non-cooperative adsorption at the low affinity sites (assuming n_2 of 1). The R^2 values for curves v were 0.927 and 0.929 in panels A and B, respectively.

highly curved surface regions provided the major contribution (~ 77 %) to the overall binding isotherm of 4-ATP on SRNPs, whereas the low-affinity component was not

observed on QSNPs because the locally curved surfaces at the edges, corners, and defects only accounted for a negligibly small fraction of the surface areas of QSNPs. The adsorption of 4-ATP onto nanoscale curved surfaces was highly cooperative with Hill coefficients around 2 (Figures 1.5D, 1.5E, and Figure 1.6), while such cooperativity was not observed on atomically flat Au surfaces. Such surface curvature-dependent ligand

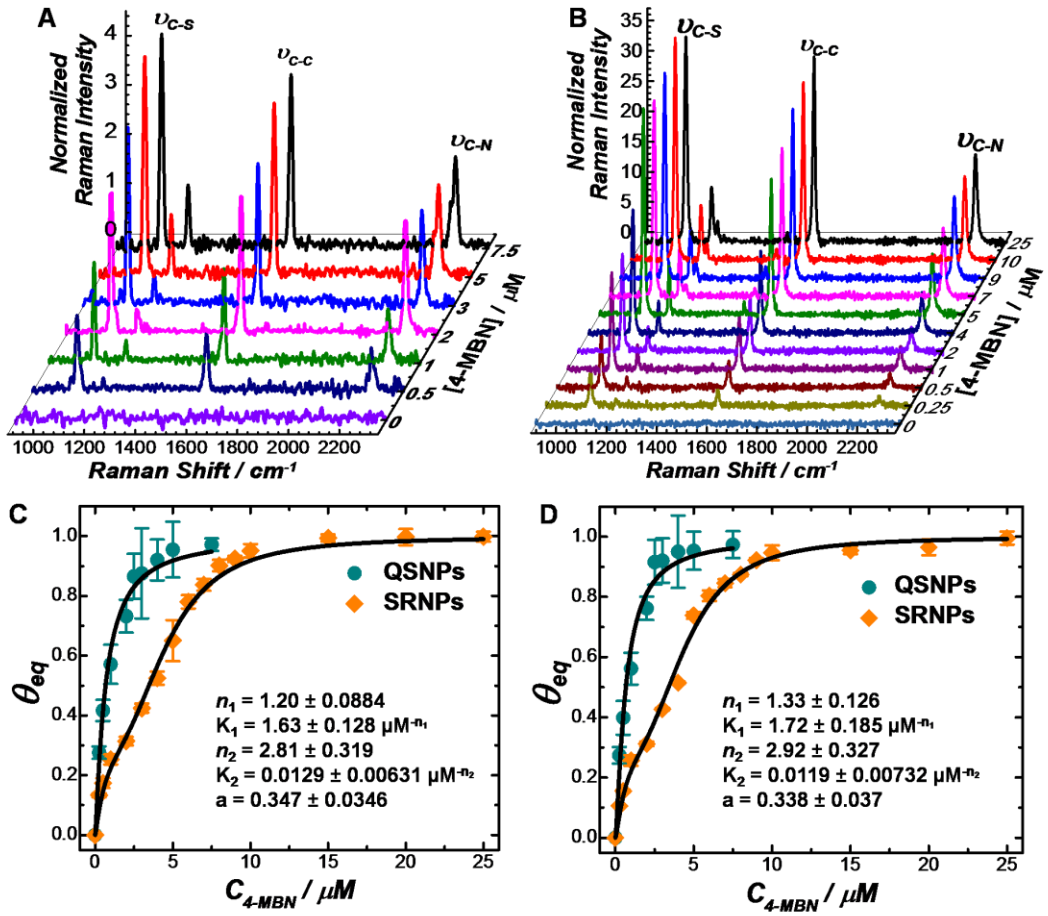

Figure 1. 7 SERS spectra collected on colloidal (A) Au QSNPs and (B) Au SRNPs after the NPs were incubated with various concentrations of 4-MBN for 24 h. The peak intensity at 3230 cm^{-1} (normal Raman peak corresponding to the O-H stretching mode of H_2O) was used as the internal reference for signal normalization. 4-MBN adsorption isotherms (plots of apparent surface-coverage of 4-MBN, $\theta_{4\text{-MBN}}$, vs. concentration of 4-MBN, $C_{4\text{-MBN}}$) on the surfaces of Au QSNPs and SRNPs obtained from the (C) 2226 cm^{-1} mode and (D) 1588 cm^{-1} mode in the SERS spectra. The error bars represent the standard deviations obtained from 5 replicate samples prepared under identical conditions. The solid black curves show the least squares curve fitting results. The R^2 values were all greater than 0.98.

adsorption behaviors were also observed on 4-mercaptobenzoicnitrile (4-MBN), a thiolated aromatic ligand exhibiting binding affinity and cooperativity similar to those of 4-ATP Figure 1.7). The SERS peak assignments of 4-NBM were listed in Table 1.2

Table 1. 2 Assignments of the Major SERS peaks of 4-MBN

Raman Shift / cm^{-1}	Peak Assignments*
1074	$\nu_{C-S} + \nu_{CC}$ [7-11]
1173	$\beta_{C-H} + \nu_{CC}$ [10]
1203	$\beta_{C-H} + \nu_{C-C\equiv N}$ [12, 14-16]
1582	ν_{CC} [7-11]
2226	$\nu_{C\equiv N}$ [13-16]

The SERS-based ligand titration assay allowed us to further correlate the structural ordering with the surface coverage of chemisorbed ligands. We found that the intensity of the SERS peak at 1480 cm^{-1}, which was assigned to a coupled $\nu_{C-N} + \beta_{C-H} + \nu_{(C-C)Ar}$ mode,[54] was sensitively dependent on the degree of structural ordering of chemisorbed 4-ATP. On Au QSNPS, the intensity ratios of the 1480 cm^{-1} to 1588 cm^{-1} peaks, $I_{1480cm^{-1}} / I_{1588cm^{-1}}$, progressively increased with $C_{4\text{-ATP}}$, reflecting the transition from randomly oriented molecules at low θ_{eq} to more ordered monolayer structures at higher θ_{eq} (Figure 1.5F). In contrast, on Au SRNPs, $I_{1480cm^{-1}} / I_{1588cm^{-1}}$ first increased with $C_{4\text{-ATP}}$ and reached a plateau upon saturation of the flat regions with 4-ATP. Further ligand adsorption to the highly curved regions at higher $C_{4\text{-ATP}}$ did not result in any further increase of $I_{1480cm^{-1}} / I_{1588cm^{-1}}$, strongly suggesting that 4-ATP on the nanoscale curved surfaces were significantly less ordered than those on the flat surfaces.

We further used SERS as an in situ spectroscopic tool to monitor the kinetics of thiolated ligand adsorption. Widely divergent results on the kinetics of the adsorption and assembly of organothiol ligands on Au surfaces have been reported in the literature,[55] and the time it takes to form a densely packed, pseudocrystalline ligand monolayer has been reported to vary over a diverse range of time scales from seconds[56] to minutes,[57] to hours,[58] and even up to several days.[39] The lack of consensus on the ligand adsorption kinetics is believed to stem from the structural diversity of the ligand molecules being studied and the heterogeneous distributions of ligand binding sites on the substrates with varying local surface curvatures. In the context of Langmuir adsorption kinetics, both first- and second-order rate laws have been commonly used to describe ligand adsorption kinetics, and the claims of which one is better than the other is quite often made based on a marginal difference in the correlation coefficients of curving fitting.[59] A more general form of the Langmuir kinetics can be expressed as a varying-order rate equation using the following polynomial expression:[59]

$$\frac{d\theta_t}{dt} = k_1(\theta_{eq} - \theta_t) + k_2(\theta_{eq} - \theta_t)^2 \qquad (3),$$

where θ_{eq} is the ligand coverage at equilibrium, θ_t is ligand coverage at reaction time, t, and k_1 and k_2 are the first- and second-order rate constants, respectively. The relative magnitude of k_1 over $k_2 \times (\theta_{eq}-\theta_t)$, which is dependent upon the initial concentration of ligands, governs the simplification of the overall kinetics to either the first- or second-order rate laws. Here we studied the ligand adsorption kinetics at a sufficiently high $C_{4\text{-ATP}}$ of 50 μM, far beyond that required for monolayer saturation of the particle surfaces. As shown by the theoretical derivations in Supporting Information, the ligand adsorption kinetics can be simplified to a first-order rate law in this high ligand concentration regime. The kinetics of 4-ATP

adsorption on Au QNSPs and SRNPs could be both well-fitted with a two-component first-order rate equation shown as follows:

$$\xi_{ad} = \frac{I_t}{I_{24h}} = f(1-e^{k_{slow}t}) + (1-f)(1-e^{k_{fast}t}) \quad (4),$$

where ξ_{ad} is the apparent progress of the ligand adsorption, which was quantified by normalizing the SERS intensities, I_t, against the values at equilibrium (24 h incubation), I_{24h}, of the 1078 cm^{-1} mode. k_{fast} and k_{slow} are the first-order rate constants of the fast and slow components, respectively. f is the fractional coefficient for the slow kinetic component.

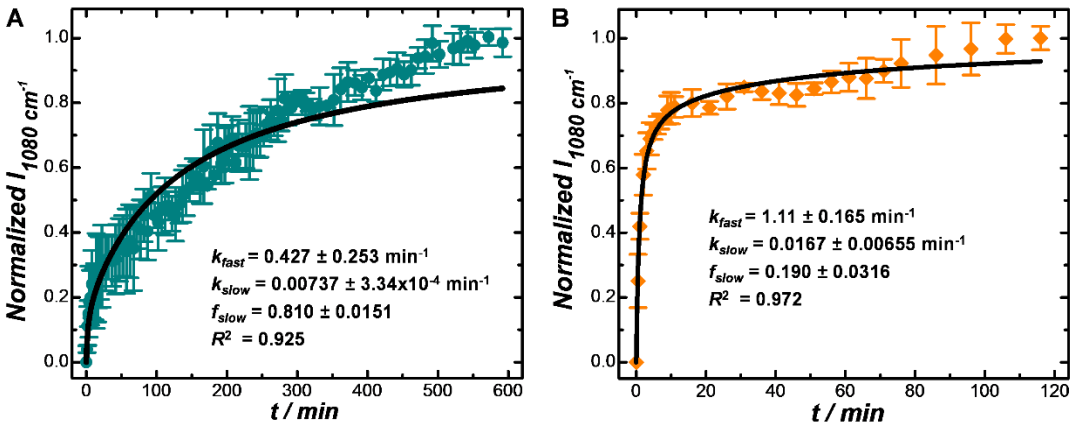

Figure 1. 8 Least squares curve fitting results using the second order Langmuir rate law (Equation (5)) for 4-ATP adsorption on (A) Au QSNPs and (B) Au SRNPs at 4-ATP concentration of 50 µM.

Significantly less satisfactory results (Figure 1-8) were obtained when fitting the kinetic data with a two-component second-order rate equation shown below:

$$\xi_{ad} = \frac{I_t}{I_{24h}} = f\frac{k_{slow}t}{1+k_{slow}t} + (1-f)\frac{k_{fast}t}{1+k_{fast}t} \quad (5).$$

The kinetics of 4-ATP adsorption on Au QSNPs was found to be dominated by the slow component with a f value around 0.8, whereas more than 70 % contribution to the

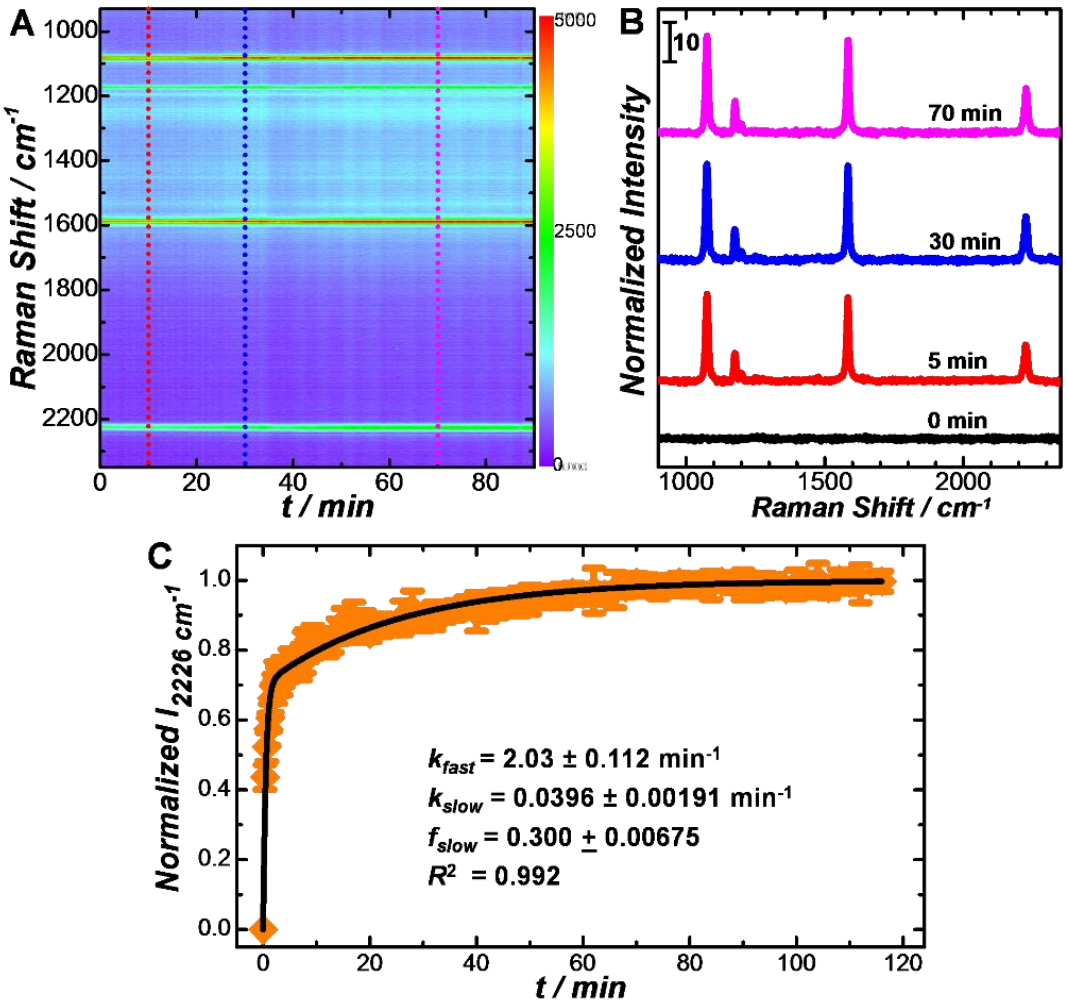

Figure 1. 9 Kinetics of 4-MBN adsorption on the surfaces of Au SRNPs. (A) Color-coded plots showing the time-resolved SERS spectra obtained on colloidal Au SRNPs incubated with 50 µM 4-MBN at room temperature. (B) Representative SERS spectra at incubation times of 0 min, 5 min, 30 min, and 70 min. The SERS intensities were normalized using the O-H stretching mode of water as an internal reference. (C) SERS intensities of the 2226 cm^{-1} mode ($\nu_{C\equiv N}$) plotted as a function of incubation time after exposure of Au SRNPs to 50 µM 4-MBN. The SERS intensities of the 2226 cm^{-1} mode were normalized against the values obtained after the adsorption-desorption equilibrium was reached (24 h incubation). The error bars represent the standard deviations obtained from 5 independent experimental runs. The solid black curves show the least squares curve fitting results using Equation (4). The curve fitting results and R^2 values were labeled in the figure.

overall kinetics of 4-ATP adsorption on SRNPs was provided by the fast component, strongly indicating that the adsorption of 4-ATP to Au nanoparticles occurred more rapidly

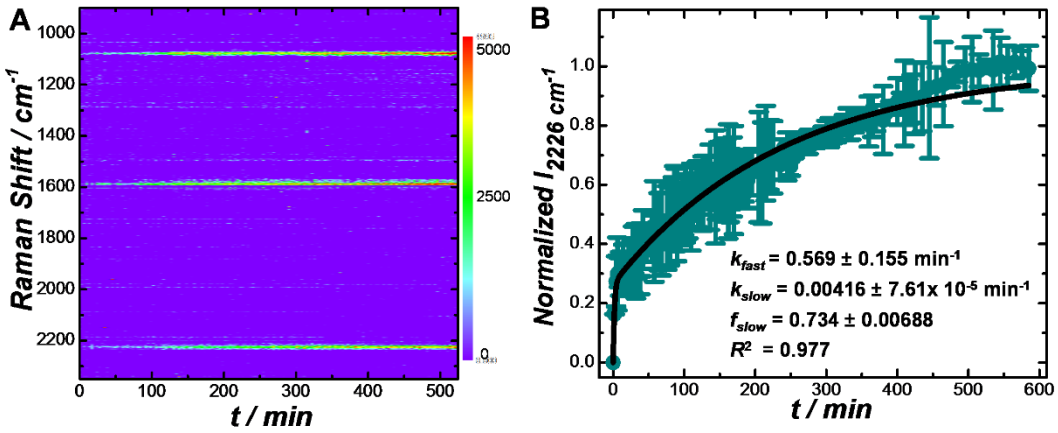

Figure 1. 10 Kinetics of 4-MBN adsorption on the surfaces of Au QSNPs. (A) Color-coded plots showing the time-resolved SERS spectra obtained on colloidal Au QSNPs incubated with 50 μM 4-MBN at room temperature. (B) SERS intensities of the 2226 cm^{-1} mode ($\nu_{C\equiv N}$) plotted as a function of incubation time after exposure of Au QSNPs to 50 μM 4-MBN. The SERS intensities of the 2226 cm^{-1} mode were normalized against the values obtained after the adsorption-desorption equilibrium was reached (24 h incubation). The error bars represent the standard deviations obtained from 5 independent experimental runs. The solid black curves show the least squares curve fitting results using Equation (4). The curve fitting results and R^2 values were labeled in the figure

on locally curved surfaces than on the atomically flat facets. Such surface curvature-dependent adsorption kinetic profiles were further confirmed when switching the oganothiol ligands from 4-ATP to 4-MBN (Figures 1-9 and 1-10).

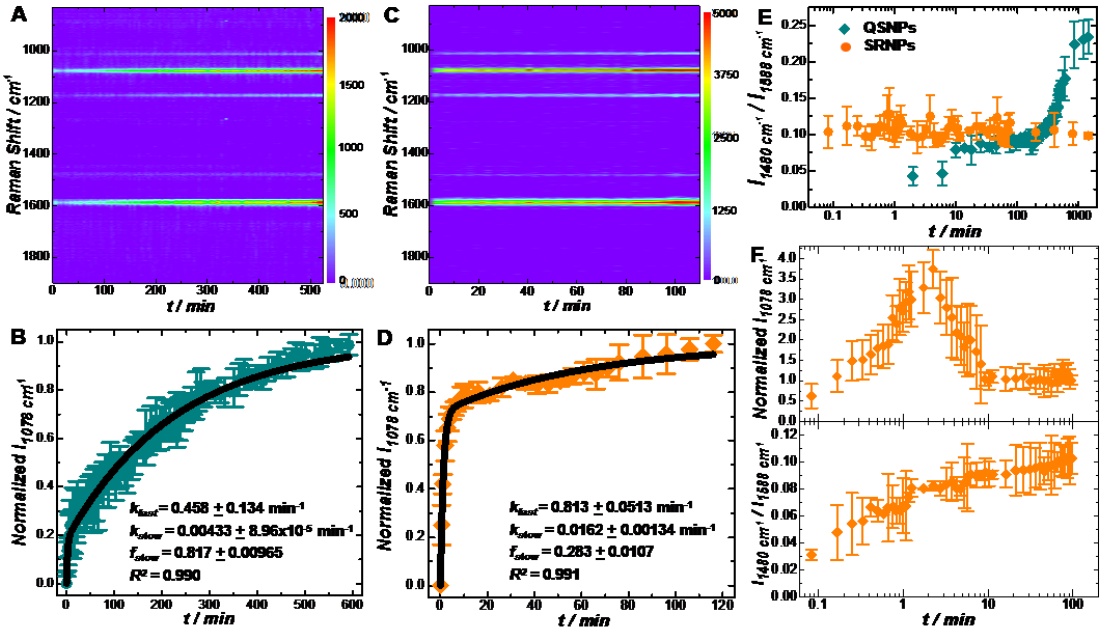

Figure 1. 11 Kinetics of 4-ATP adsorption on Au QSNPs and SRNPs. Time-resolved SERS spectra of colloidal (A) Au QSNPs and (C) Au SRNPs incubated with 50 μM 4-ATP at room temperature. Temporal evolution of SERS intensities of the 1078 cm^{-1} mode upon exposure of (B) Au QSNPs and (D) Au SRNPs to 50 μM 4-ATP. The SERS intensities of the 1078 cm^{-1} mode were normalized against the values obtained after the adsorption-desorption equilibrium was reached (24 h incubation). The solid black curves show the least squares curve fitting results. (E) Temporal evolution of $I_{1480\,cm^{-1}} / I_{1588\,cm^{-1}}$ during incubation of Au SRNPs and QSNPs with 50 μM 4-ATP. (F) Temporal evolution of the intensity of the 1078 cm^{-1} mode (upper panel) and $I_{1480\,cm^{-1}} / I_{1588\,cm^{-1}}$ (lower panel) upon exposure of Au SRNPs to 2.0 μM 4-ATP. The error bars represent the standard deviations obtained from 5 independent experimental runs.

We also kinetically monitored the structural ordering of the chemisorbed 4-ATP based on the temporal evolution of $I_{1480cm^{-1}} / I_{1588cm^{-1}}$ upon exposure of the nanoparticles to 50 μM 4-ATP (Figure 1-11 and Figure 1-12). Upon initiation of 4-ATP adsorption on Au QSNPs, $I_{1480cm^{-1}} / I_{1588cm^{-1}}$ remained around 0.08 until θ_{eq} reached ~ 85 % after 400 minutes,

indicating that the chemisorbed 4-ATP remained partially ordered in this sub-saturation coverage regime.

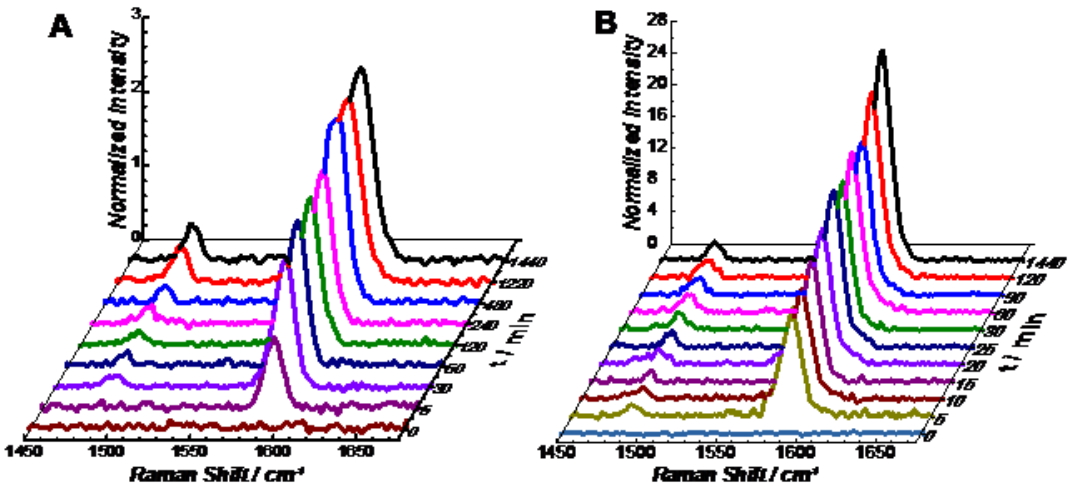

Figure 1. 12 Temporal evolution of the SERS spectra showing the intensity ratio of the 1480 cm^{-1} mode to the 1588 cm^{-1} mode upon exposure of (A) Au QSNPs and (B) Au SRNPs to 50 μM 4-ATP.

A sharp increase of $I_{1480cm^{-1}} / I_{1588cm^{-1}}$ was observed when θ_{eq} exceeded 85 % till reaching another plateau at $I_{1480cm^{-1}} / I_{1588cm^{-1}}$ of ~ 0.24, which signified the formation of the ordered pseudocrystalline ligand monolayer at saturated θ_{eq}. In contrast, the 4-ATP chemisorbed on the Au SRNPs, irrespective of θ_{eq}, exhibited $I_{1480cm^{-1}} / I_{1588cm^{-1}}$ values around an intermediate value of ~ 0.1 throughout the entire ligand adsorption process, suggesting that the chemisorbed 4-ATP on the highly curved surfaces of SRNPs remained much less ordered than those on the flat facets of QSNPs. We further studied the ligand adsorption kinetics on SRNPs at significantly lower $C_{4\text{-ATP}}$ where only partial surface coverages were

achieved at equilibrium. As shown in Figure 3F, the SERS intensity of the 1078 cm^{-1} mode rapidly increased to a maximum value within 3 minutes after exposure of the SRNPs to 2.0 μM 4-ATP, followed by a gradual decrease over a time scale of minutes before reaching the equilibrium. The rapidly increasing SERS signals at the initial stage came from the 4-ATP molecules chemisorbed on the highly curved surface regions of SRNPs, which then migrated to the flatter surface regions of SRNPs to form thermodynamically more stable ligand domains.

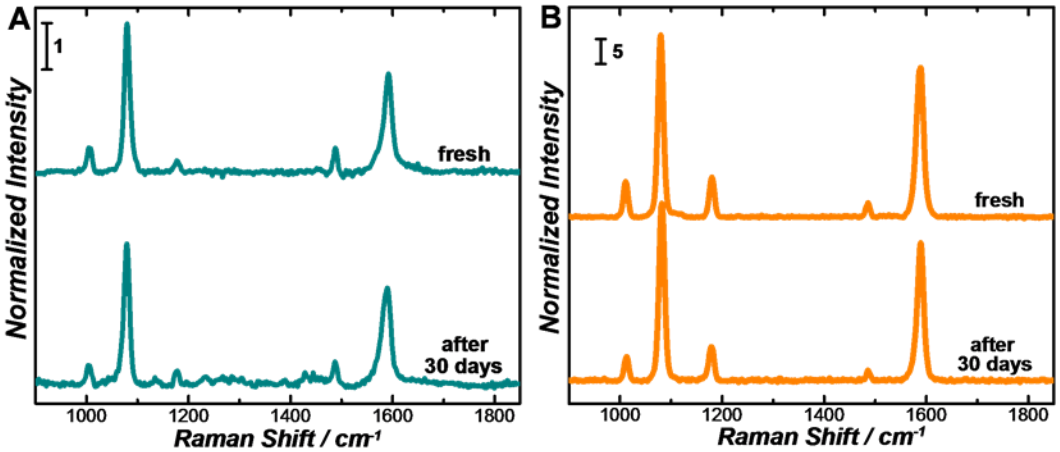

Figure 1. 13 (A) SERS spectra of freshly prepared 4-ATP-coated Au QSNPs (CTAC-coated Au QSNPs incubated with 50 μM 4-ATP for 24 h) and 4-ATP-coated Au QSNPs redispersed and stored in water at room temperature for 30 days. (B) SERS spectra of freshly prepared 4-ATP-coated Au SRNPs (CTAC-coated Au SRNPs incubated with 50 μM 4-ATP for 24 h) and 4-ATP-coated Au SRNPs redispersed and stored in water at room temperature for 30 days. The Raman intensities were normalized using the O-H stretching mode of water as an internal reference. The spectra were off-set for clarity.

Because the local plasmonic field enhancements at the highly curved surface regions are remarkably stronger than those on the flatter surface regions,[48] the SERS intensity gradually decreased as the 4-ATP ligands underwent the surface migration process. The $I_{1480cm^{-1}} / I_{1588cm^{-1}}$ values, however, kept increasing until reaching the

equilibrium, indicating a gradual transition from less ordered to more ordered ligand layer structures.

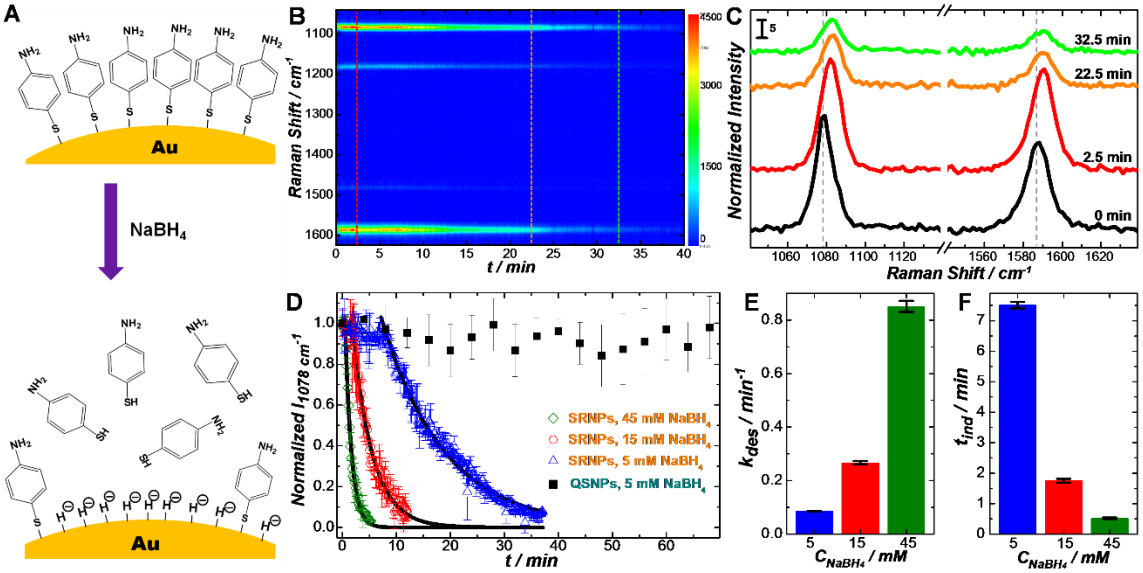

Figure 1. 14 $NaBH_4$-induced desorption of 4-ATP ligands. (A) Schematic illustration of $NaBH_4$-induced desorption of 4-ATP from Au nanoparticle surfaces. (B) Time-resolved SERS spectra of 4-ATP-coated SRNPs upon exposure to 5 mM $NaBH_4$ at room temperature. (C) Representative snapshot SERS spectra collected at 0 min, 2.5 min, 22.5 min, and 32.5 min. The Raman signals were normalized using the O-H stretching mode of H_2O as the internal reference. The spectra were off-set for clarity. (D) Temporal evolution of SERS intensities at 1078 cm^{-1} for 4-ATP-coated Au SRNPs and QSNPs exposed to various concentrations of $NaBH_4$. The SERS intensities were normalized against the initial peak intensities of the 1078 cm^{-1} mode before exposure of the nanoparticles to $NaBH_4$. The error bars represent the standard deviations obtained from 5 independent experimental runs. The solid black curves show the least squares curve fitting results. (E) k_{des} and (F) t_{ind} for the 4-ATP desorption from Au SRNPs at various $NaBH_4$ concentrations.

The desorption of chemisorbed 4-ATP ligands was found to be kinetically much slower than the ligand adsorption with almost no detectable decrease in the SERS intensities over a month when the colloidal 4-ATP-coacted QSNPs and SRNPs were stored in pure water (Figure 1-13). To further investigate the effects of surface curvature on the ligand desorption kinetics, we exposed the 4-ATP-coacted QSNPs and SRNPs to $NaBH_4$, which has shown unique capability to effectively remove organothiol adsorbates from Au

nanoparticle surfaces.[60] As schematically illustrated in Figure 1-14A, the $NaBH_4$-induced 4-ATP desorption from the Au nanoparticle surfaces is essentially driven by the formation of surface hydride, which exhibits a binding affinity significantly higher than those of organothiols to the Au surfaces.[60] The time-resolved SERS spectra collected in real time after exposing 4-ATP-coacted SRNPs to 5 mM $NaBH_4$ were shown in Figure 1-14B and several characteristic snapshot spectra at various ligand desorption stages were highlighted in Figure 1-14.

The mechanistic complexity of the $NaBH_4$-induced desorption of thiolated ligands was manifested by several noteworthy observations. (1) An induction time was observed at the initial stage before the thiolated ligand started to desorb from the surfaces of SRNPs most likely due to the presence of dissolved oxygen in water, which rapidly oxidized the surface hydride species derived from $NaBH_4$ and thereby suppressed the hydride-driven ligand desorption. An analogous induction time was previously observed during the metallic nanoparticle-catalyzed reduction of aromatic nitro compounds by borohydride, which was also driven by the active surface hydride species.[61] The origin of this induction time had long been under intense debate until recently Neretina and coworkers uncovered the underlying correlation between the dissolved oxygen and the induction time for the catalytic reduction reactions.[62] For $NaBH_4$-induced desorption of organothiol ligands, only when the dissolved oxygen was consumed to a critical depletion level can the hydride species reach a surface abundance sufficiently high for driving the ligand desorption. By increasing the $NaBH_4$ concentration, C_{NaBH_4}, the consumption of the dissolved oxygen became faster, resulting in shortening of the induction time (Figure 1-14D). (2) During the ligand desorption, the SERS peak intensities progressively decreased while all the

characteristic Raman modes of 4-ATP were well preserved, indicating that $NaBH_4$ induced the desorption of the ligands rather than reacting with the chemisorbed ligands to form other molecules. Interestingly, both the 1078 cm^{-1} mode and 1588 cm^{-1} mode upshifted by 2-3 cm^{-1} (Figure 1-14C) when hydride and 4-ATP coadsorbed on the SRNPs. The formation of surface hydride species involved interfacial transfer of electrons mediated by the metallic nanoparticles, causing an increase of the electron density at the nanoparticle surfaces, which could be precisely monitored based on the spectral shift of the plasmon resonances using single-particle scattering spectroscopy.[63] The electron enrichment at the metallic nanoparticle surfaces resulted in an increase of the electron densities in the chemisorbed 4-ATP, causing the spectral upshift of the SERS peaks of the adsorbates and in some cases even the emergence of transient, anomalous Raman features for some specific organothiol ligands.[60] (3) When $NaBH_4$ was in excess with respect to the 4-ATP chemisorbed on the particle surfaces, the desorption kinetics followed a pseudo-first-order rate law described by following equation:

$$\xi_{des} = \frac{I_t}{I_{t=0}} = e^{-k_{des}(t-t_{ind})} \qquad (6),$$

where ξ_{des} is the apparent progress of ligand desorption, which was quantified by normalizing the SERS intensities of the 1078 cm^{-1} mode, I_t, against the initial values, $I_{t=0}$. k_{des} is the pseudo-first-order rate constants and t_{ind} is the induction time. The k_{des} and t_{ind} values at various C_{NaBH_4} obtained from least squares curve fitting were shown in Figures 4E and 4F, respectively, which clearly showed that k_{des} increased while t_{ind} decreased as C_{NaBH_4} increased. While two kinetic components were clearly resolved for the ligand adsorption on SRNPs, the kinetics of $NaBH_4$-indcued ligand desorption from SRNPs could be fitted

adequately well with a single exponential component, strongly suggesting that the ligand desorption from the locally flat and curved surface regions of SRNPs was cooperative and

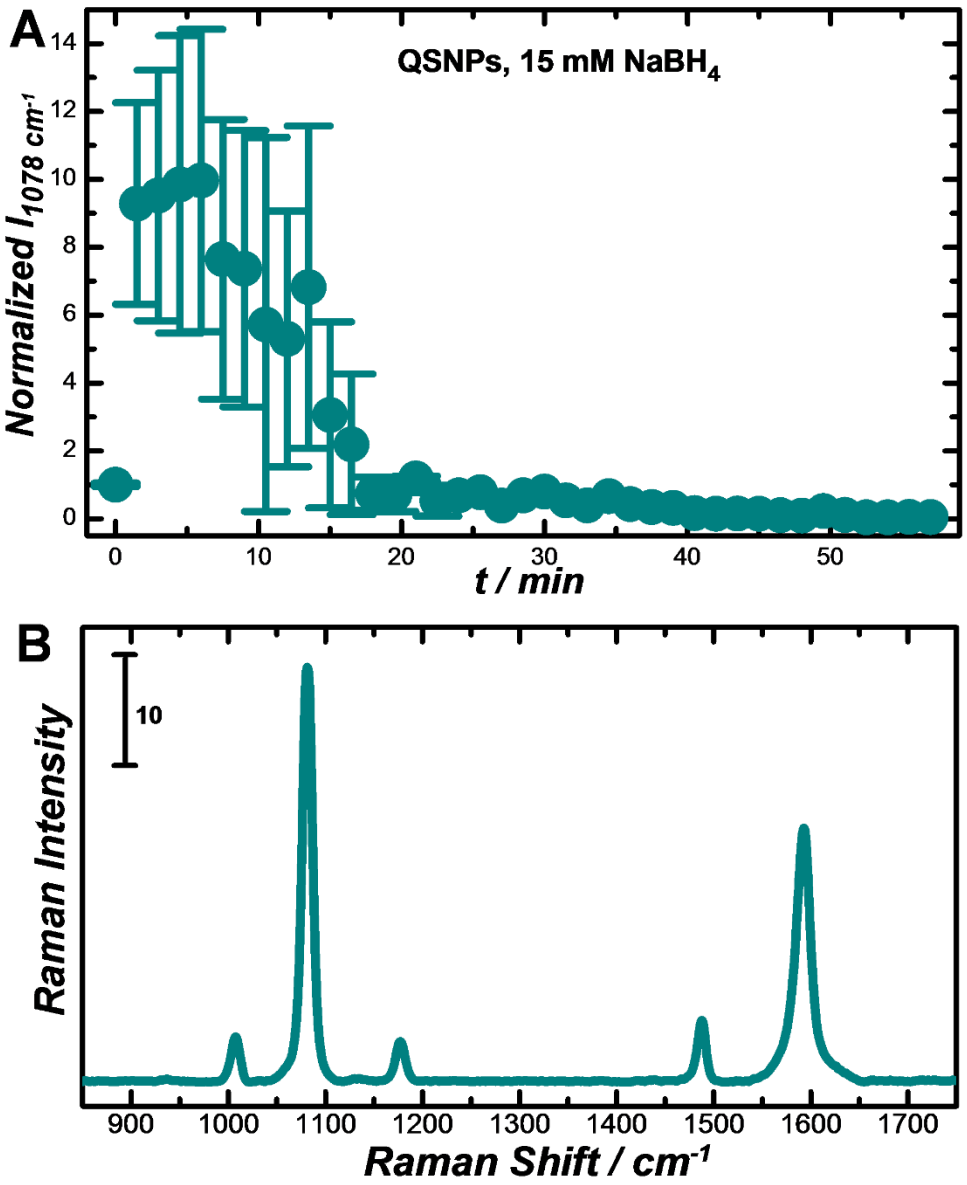

Figure 1. 15 (A) Time-evolution of the intensity of the 1078 cm^{-1} mode upon exposure of ATP-coated Au QSNPs to 15 mM NaBH4 at room temperature. The SERS intensities of the 1078 cm^{-1} mode were normalized against the initial value before mixing the ATP-coated Au QSNPs with $NaBH_4$. The error bars represent the standard deviations obtained from 5 independent experimental runs. (B) A representative SERS spectrum collected on aggregated Au QSNPs settled down at the bottom of the centrifuge tube after exposing the ATP-coated Au QSNPs to 15 mM $NaBH_4$ for 1 h

synergistic in nature and therefore became kinetically irresolvable under the current experimental conditions.

In striking contrast to the case of SRNPs, no apparent ligand desorption was observed upon exposure of 4-ATP-coated Au QSNPs to 5 mM $NaBH_4$ even over several hours (Figure 1-144D). Further increasing C_{NaBH_4} from 5 mM to 15 mM caused aggregation of the QSNPs. The SERS intensities tremendously increased immediately after mixing the 4-ATP-coated Au QSNPs with 15 mM $NaBH_4$ due to the formation of interstitial SERS hotspots in the interparticle junctions of aggregated nanoparticle clusters (Figure S11A in Supporting Information). As the aggregation further proceeded, larger scale aggregates started to precipitate out of the colloidal suspensions, resulting in decrease of the SERS intensities when the excitation laser was still focused in the solution. However, strong SERS signals of chemisorbed 4-ATP were detected when focusing the excitation laser on the precipitated nanoparticle aggregates (Figure 1-15), indicating that the 4-ATP ligands were still present on the particle surfaces. It remained challenging, however, to quantitatively study the kinetics of ligand desorption from QSNPs at this high C_{NaBH_4} due to the complication caused by nanoparticle aggregation.

The drastically different desorption behaviors of 4-ATP ligands observed on the QSNPs and SRNPs were rooted in the nanoscale surface curvature effects. On one hand, the 4-ATP ligands bound to the atomic flat surfaces are thermodynamically more stable and thereby more resistive against desorption than those on the highly curved surfaces. On the other hand, borohydride exhibited significantly stronger binding affinities to the undercoordinated surface atoms than to their close-packed counterparts exposed on the

{111}/{100} facets,[64] thereby propelling the formation of surface hydride species and thus the ligand desorption from the highly curved surfaces.

The surface curvature-dependent ligand adsorption and desorption behaviors further translated into the kinetic complexity of the exchange between thiolated ligands on Au nanoparticle surfaces. The exchange of thiolated ligands on Au surfaces is mechanistically complex and exhibits sophisticated overall kinetic profiles with widely divergent and even contradictory results existing in the literature.[65] On planar Au surfaces, the exchange of thiolated ligands has been observed to occur rapidly at some minority surface sites, hypothetically at the surface defects, terrace edges, and grain boundaries, even though the complete ligand exchange is accomplished over much longer time scales up to a few days.[28] Fast ligand exchange on the time scale of minutes has also been observed on sub-5 nm Au nanoparticles, conjecturally at the particle corners and edges, whereas the thiolated ligands on the facets of the nanoparticles undergo much slower exchange processes.[36] Such complex kinetic profiles implicate the coexistence of multiple pathways involved in the ligand exchange that are intimately tied to the local surface curvatures of the ligand-binding sites. Previous kinetic studies have shown that the thiolated ligands may undergo either associative (SN2-like) or dissociative (SN1-like) exchange processes, or even a combination of the two,[28, 35, 65, 66] depending on the molecular structures of the ligands, the surface structures of the Au nanoparticles, the solvents, the temperature, and the molar ratios between the incoming and outgoing ligands. Here we found that the ligand exchange of 4-ATP with 4-MBN on the Au nanoparticle surfaces (Figure 1-16A) was essentially a multistep process exhibiting multiple kinetic components far more complicated than a simple associative or dissociative exchange

process. We first achieved saturated surface coverage of 4-ATP on the SRNP surfaces by incubating the CTAC-coated SRNPs with 100 µM 4-ATP for 24 h, then isolated the 4-ATP-coated SRNPs from the unbound 4-ATP ligands through centrifugation and dispersion, and finally exposed the 4-ATP-coated SRNPs to various concentrations of 4-NBM to initiate the ligand exchange. Because the energy barrier for the 4-ATP desorption from the nanoparticle surfaces was relatively high and both 4-NBM and 4-ATP exhibited

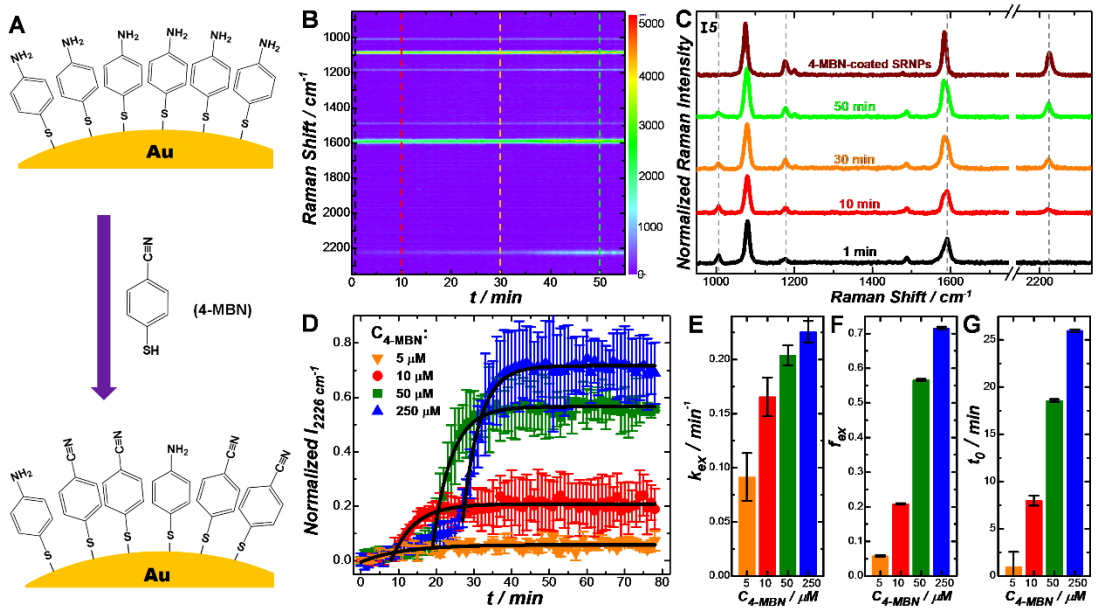

Figure 1. 16 Thiolated ligand exchange on highly curved nanoparticle surfaces. (A) Schematic illustration of ligand exchange of 4-ATP with 4-MBN on Au nanoparticle surfaces. (B) Time-resolved SERS spectra of 4-ATP-coated SRNPs (obtained through incubation of CTAC-coated SRNPs with 50 µM 4-ATP for 24 h) after exposure to 250 µM 4-MBN at room temperature. (C) Representative snapshot SERS spectra collected at 1 min, 10 min, 30 min, and 50 min. The SERS spectra of SRNPs fully covered with 4-MBN (obtained after incubating the CTAC-coated SRNPs with 100 µM 4-MBN for 24 h) was also shown for comparison. The Raman signals were normalized using the O-H stretching mode of H_2O as the internal reference. The spectra were off-set for clarity. (D) Temporal evolution of SERS intensities of the 2226 cm^{-1} mode upon exposure of 4-ATP-coated Au SRNPs to various concentrations of 4-MBN. The peak intensities were normalized against the intensity of the 2226 cm^{-1} peak of the SRNPs with saturated 4-MBN coverages. The error bars represent the standard deviations obtained from 5 independent experimental runs. The solid black curves show the least squares curve fitting results. (E) k_{ex}, (F) f_{ex}, and (G) t_0 at various $C_{4\text{-MBN}}$.

comparable molecular sizes and adsorption affinities to Au surfaces, the 4-NBM must be kept in great excess with respect to the 4-ATP chemisorbed on SRNP surfaces to kinetically boost the ligand exchange and thermodynamically shift the equilibrium toward the 4-NBM chemisorption.

We monitored the ligand exchange in real time using time-resolved SERS (Figures 1-16B and 1-16C). As the ligand exchange proceeded, the SERS intensity of the 2226 cm^{-1} mode, which was the characteristic Raman feature of the C≡N bond of 4-NBM,

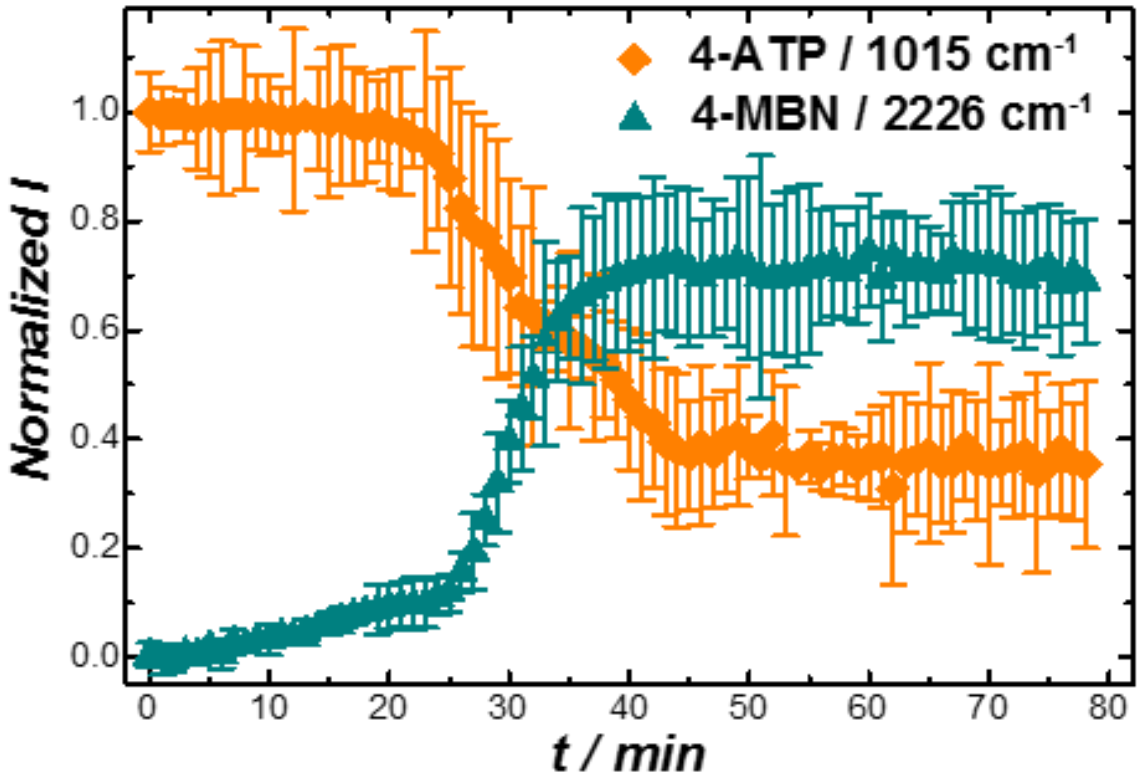

Figure 1. 17 Temporal evolution of SERS intensities of the 2226 cm^{-1} mode of 4-NBM and the 1015 cm^{-1} mode of 4-ATP upon exposure of 4-ATP-coated Au SRNPs to 250 μM 4-MBN. The intensities of the 2226 cm^{-1} peak were normalized against the intensity of the SRNPs with saturated 4-MBN coverages (obtained after incubating the CTAC-coated SRNPs with 100 μM 4-MBN for 24 h). The intensities of the 1015 cm^{-1} peak were normalized against the intensity of the SRNPs with saturated 4-ATP coverages (obtained after incubating the CTAC-coated SRNPs with 100 μM 4-ATP for 24 h). The error bars represent the standard deviations obtained from 5 independent experimental runs.

progressively increased, accompanied by weakening of the SERS peak at 1015 cm^{-1}, which was assigned to a coupled ring deformation mode of 4-ATP. The C-C ring stretching mode at 1588 cm^{-1} down-shifted by ~ 5 cm^{-1} when 4-ATP was displaced with 4-NBM, and such spectral down shifts could be interpreted as a consequence of decreased bond energies due to the substitution of an electron donating amino group with an electron withdrawing cyano group on the para-position of the thiolphenol derivatives.

We monitored the progress of the ligand exchange based on the temporal evolution of the SERS peak intensity at 2226 cm^{-1} (Figure 1-16E). Several intriguing phenomena were observed by time-resolved SERS during the ligand exchange. (1) We observed a pre-exchange time during which the SERS intensity of the 2226 cm^{-1} mode increased slowly following a zero-order kinetics until reaching a threshold value above which much faster ligand exchange occurred. As shown in Figure 1-17 in Supporting Information, during this pre-exchange time, the intensity of the 1015 cm^{-1} mode for 4-ATP remained almost unchanged, indicating the formation of an associative, pre-exchange complex comprising both 4-ATP and 4-NBM bound or partially bound to the same binding sites or in close proximity to the same binding sites. Only when the coverage of the associative, pre-exchange complex was built up to a certain threshold value could the rapid ligand exchange start to occur. Interestingly, such pre-exchange time was a unique feature for the exchange of thiolated ligands. When SRNPs with unsaturated 4-ATP coverages were exposed to excessive 4-NBM, no such pre-exchange time was observed as additional 4-NBM adsorbed onto nanoparticle surfaces (Figure 1-18). (2) Upon initiation of the ligand exchange, the peak intensity of the 2226 cm^{-1} mode increased much more rapidly than during the pre-exchange time until asymptotically attaining a non-unity value corresponding to the

fraction of ligand exchange at equilibrium, f_{ex}. The ligand exchange obeyed pseudo-first-order kinetics and the experimental results could be well-fitted using the following rate law:

$$\xi_{ex} = \frac{I_t}{I_{sat}} = f_{ex}(1 - e^{-k_{ex}(t-t_0)}) \quad (7),$$

where ξ_{ex} referred to the apparent progress of ligand exchange, which was equal to the SERS intensity of the 2226 cm^{-1} mode, I_t, normalized against that of the SRNPs with saturated 4-MBN coverages, I_{sat}. t_0 is the duration of pre-exchange time and k_{ex} is the pseudo-first-order rate constant of the ligand exchange. The k_{ex}, f_{ex}, and t_0 values obtained from least squares curve fitting at various 4-NBM concentrations, $C_{4\text{-NBM}}$, were shown in Figures 1-16E, 1-16F, and 1-16G, respectively. (3) Regardless of $C_{4\text{-NBM}}$, the ligand exchange was always initiated when the apparent coverage of the associative pre-exchange complex exceeded a threshold values around 16 % of f_{ex}. This was analogous to the $NaBH_4$-induced 4-ATP desorption, which required the accumulation of hydride to a certain threshold surface coverage prior to the occurrence of 4-ATP desorption. A linear relationship existed between t_0 and f_{ex} as shown in Figure 1-19, further verifying that the formation of the associative pre-exchange complex was a surface-controlled process obeying zero-order kinetics. (4) The ligand exchange never reached 100 % f_{ex} even at 4-NBM concentrations as high as 250 μM (f_{ex} of ~ 72 %). We hypothesized that only the 4-ATP chemisorbed on the highly curved surface regions of the SRNPs could be displaced with 4-NBM while the ligand exchange on the locally flat regions was kinetically so slow that it became not observable on the experimentally probed time-scales.

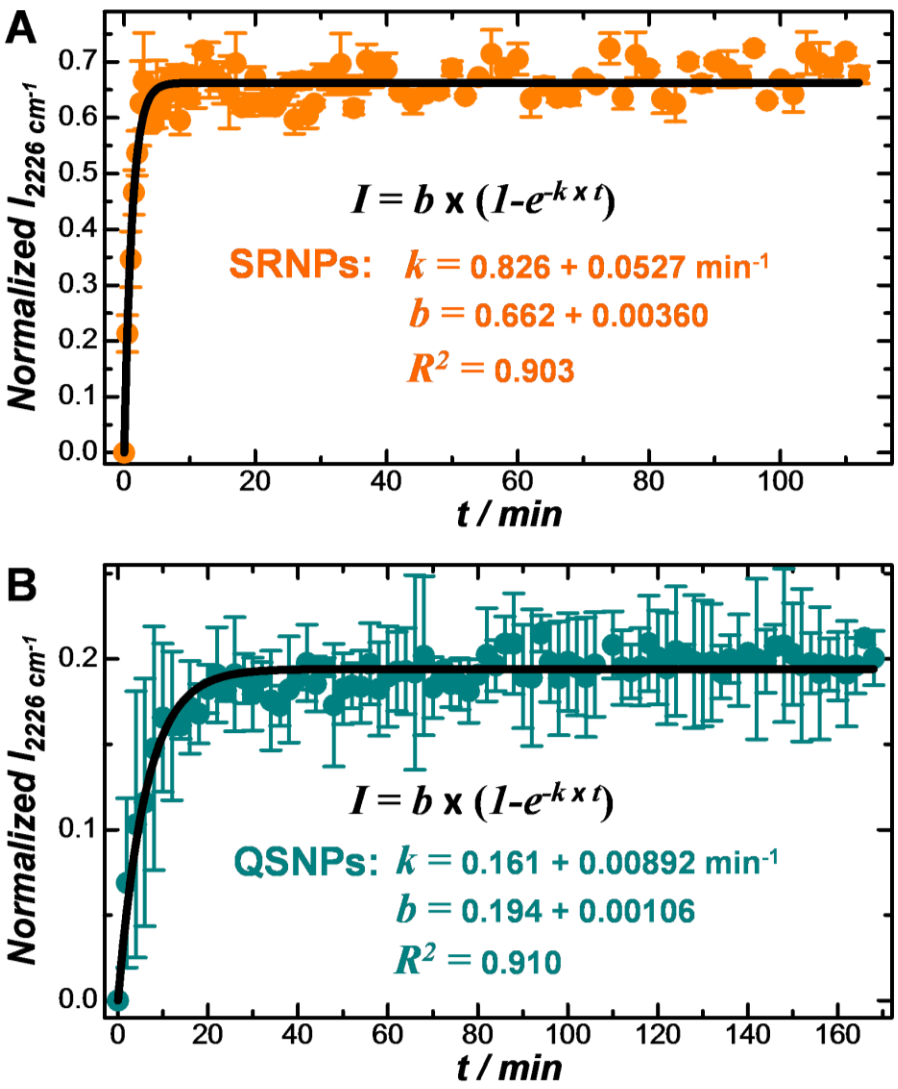

Figure 1. 18 SERS intensities of the 2226 cm^{-1} mode ($\nu_{C\equiv N}$) plotted as a function of incubation time after exposure of (A) Au SRNPs or (B) Au QSNPs with unsaturated 4-ATP coverage to 250 µM 4-MBN. The SERS intensities of the 2226 cm^{-1} mode were normalized against the values obtained of NPs with saturated 4-MBN coverages (incubation of CTAC-coated NPs with 50 µM 4-MBN for 24 h). The error bars represent the standard deviations of 3 experimental runs. Au QSNPs and Au SRNPs with unsaturated 4-ATP coverages were obtained through incubation of the NPs with 2 µM and 10 µM 4-ATP, respectively, for 24 h. The experimental results were fit with the rate law for first-order kinetics and the fitting results were shown as solid black curves.

This is because the 4-ATP ligands bound to the flat surfaces were thermodynamically more stable and thus exhibited higher energy barrier for the ligand exchange in comparison to their counterparts on the highly curved surfaces. When 4-ATP-coated Au QSNPs were exposed to 250 μM 4-NBM, the ligand exchange proceeded to an equilibrium with a f_{ex} around only 20 % (Figure 1-20), suggesting that only the 4-ATP ligands bound to the corners, edges, and surface defects of the QSNPs were exchangeable with 4-MBN.

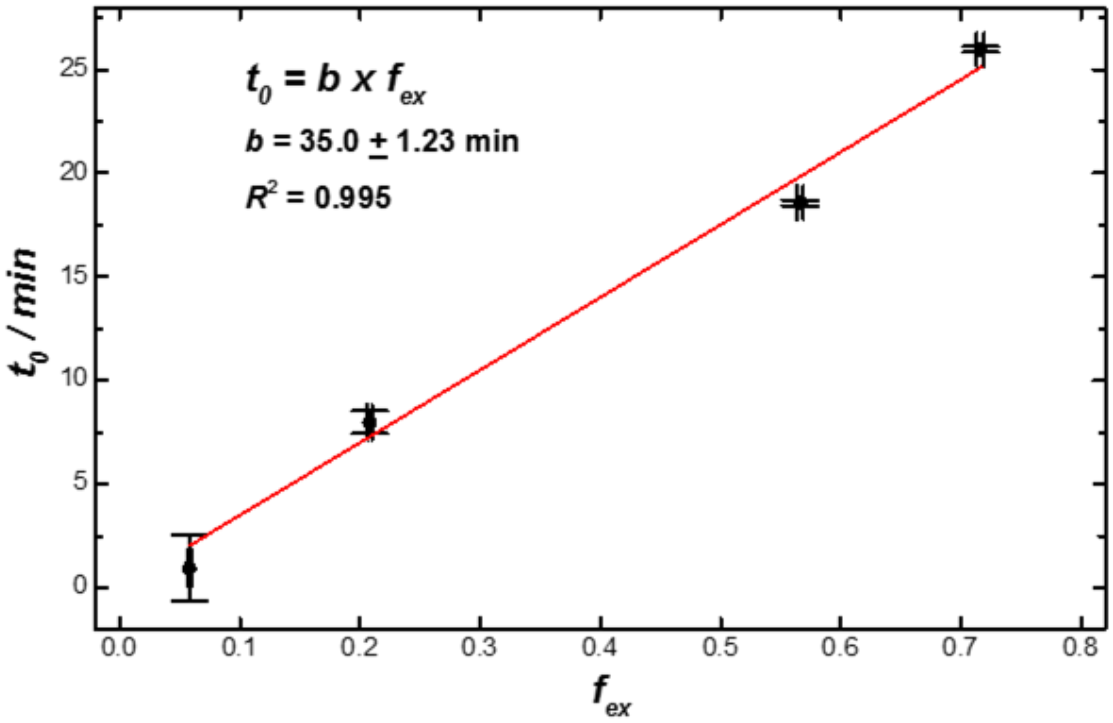

Figure 1. 19 Plots of pre-exchange time (t_0) vs. fraction of ligand exchange (f_{ex}) for the ligand exchange of 4-ATP with 4-MBN.

The quantitative insights gained from this work shed light on the complicated thermodynamic and kinetic landscapes underlying the surface curvature-dependent adsorption, desorption, and exchange behaviors of thiolated ligands on Au nanoparticle surfaces, providing an important knowledge framework that guides us to fine-tailor the

surface chemistry on nanoparticles for specific applications. The surface curvature-dependent interfacial ligand behaviors form the keystone for the site-selective

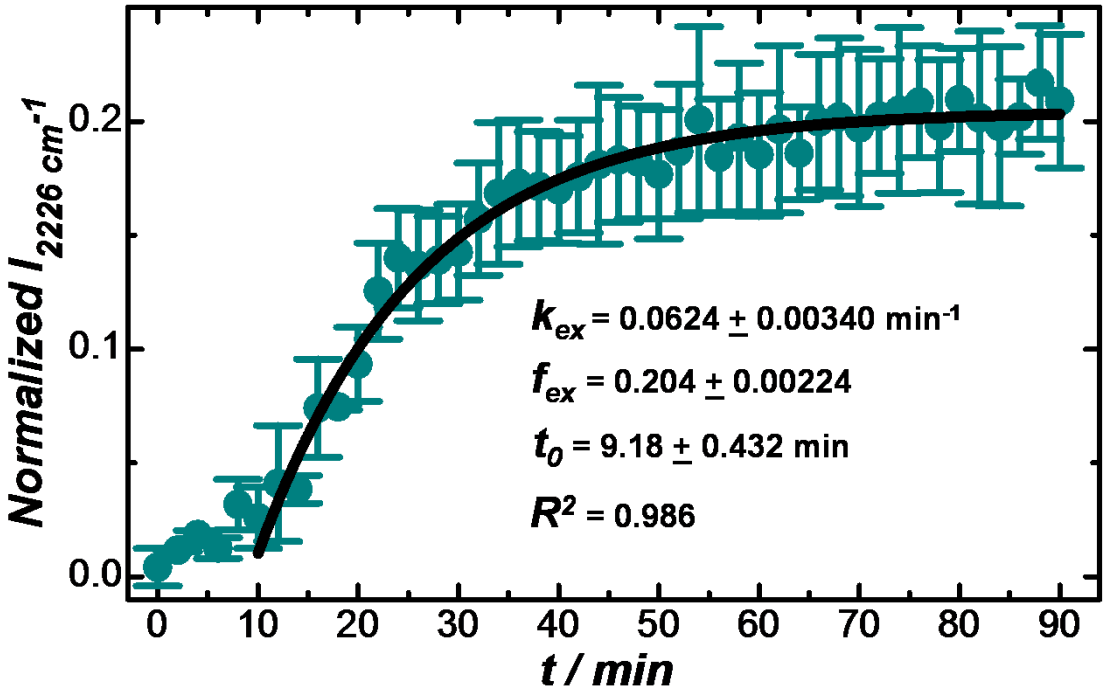

Figure 1. 20 SERS intensities of the 2226 cm^{-1} mode ($\nu_{C\equiv N}$) plotted as a function of incubation time after exposure of Au QSNPs with saturated 4-ATP coverage to 250 μM 4-MBN. The SERS intensities of the 2226 cm^{-1} mode were normalized against the values of the QSNPs fully covered with monolayer 4-MBN (obtained after incubation of CTAC-coated Au QSNPs with 50 μM 4-MBN for 24 h). The error bars represent the standard deviations of 3 experimental runs. The experimental results were fit with the rate law for first-order kinetics and the fitting results were shown as solid black curves.

functionalization of nanoparticle surfaces, allowing markedly different chemical reactions and supramolecular interactions to occur at distinct surface sites on the same nanoparticles. The incorporation of multiple surface functionalities, sometimes even dynamic molecular moieties, into individual multi-faced, Janus metallic nanoparticles, especially anisotropic

nanostructures with highly curved surface features, such as nanorods[6, 67] and nanoprisms,[68] represents a key step toward the construction of versatile nanocarriers for targeted drug delivery and multimodality bioimaging as well as the assembly of dynamically reconfigurable, active plasmonic metamaterials for sensing and photonic applications.

1.5 References

1. Yin, Y.; Alivisatos, A. P. Nature 2005, 437, 664-670.

2. Schliehe, C.; Juarez, B. H.; Pelletier, M.; Jander, S.; Greshnykh, D.; Nagel, M.; Meyer, A.; Foerster, S.; Kornowski, A.; Klinke, C.; Weller, H. Science 2010, 329, 550-553.

3. Liao, H. G.; Zherebetskyy, D.; Xin, H. L.; Czarnik, C.; Ercius, P.; Elmlund, H.; Pan, M.; Wang, L. W.; Zheng, H. M. Science 2014, 345, 916-919.

4. Zherebetskyy, D.; Scheele, M.; Zhang, Y. J.; Bronstein, N.; Thompson, C.; Britt, D.; Salmeron, M.; Alivisatos, P.; Wang, L. W. Science 2014, 344, 1380-1384.

5. Talapin, D. V.; Lee, J. S.; Kovalenko, M. V.; Shevchenko, E. V. Chem. Rev. 2010, 110, 389-458.

6. Murphy, C. J.; Thompson, L. B.; Alkilany, A. M.; Sisco, P. N.; Boulos, S. P.; Sivapalan, S. T.; Yang, J. A.; Chernak, D. J.; Huang, J. Y. J. Phys. Chem. Lett. 2010, 1, 2867-2875.

7. Carey, G. H.; Abdelhady, A. L.; Ning, Z. J.; Thon, S. M.; Bakr, O. M.; Sargent, E. H. Chem. Rev. 2015, 115, 12732-12763.

8. Desireddy, A.; Conn, B. E.; Guo, J. S.; Yoon, B.; Barnett, R. N.; Monahan, B. M.; Kirschbaum, K.; Griffith, W. P.; Whetten, R. L.; Landman, U.; Bigioni, T. P. Nature 2013, 501, 399-402.

9. Wu, Z. K.; Jin, R. C. Nano Lett. 2010, 10, 2568-2573.

10. Adams, D. M.; Brus, L.; Chidsey, C. E. D.; Creager, S.; Creutz, C.; Kagan, C. R.; Kamat, P. V.; Lieberman, M.; Lindsay, S.; Marcus, R. A.; Metzger, R. M.; Michel-Beyerle, M. E.; Miller, J. R.; Newton, M. D.; Rolison, D. R.; Sankey, O.; Schanze, K. S.; Yardley, J.; Zhu, X. Y. J. Phys. Chem. B 2003, 107, 6668-6697.

11. Lopez-Sanchez, J. A.; Dimitratos, N.; Hammond, C.; Brett, G. L.; Kesavan, L.; White, S.; Miedziak, P.; Tiruvalam, R.; Jenkins, R. L.; Carley, A. F.; Knight, D.; Kiely, C. J.; Hutchings, G. J. Nat. Chem. 2011, 3, 551-556.

12. Salem, A. K.; Searson, P. C.; Leong, K. W. Nat. Mater. 2003, 2, 668-671.

13. Gao, X. H.; Cui, Y. Y.; Levenson, R. M.; Chung, L. W. K.; Nie, S. M. Nat. Biotechnol. 2004, 22, 969-976.

14. Torchilin, V. P. Adv. Drug Deliv. Rev. 2006, 58, 1532-1555.

15. Boneschanscher, M. P.; Evers, W. H.; Geuchies, J. J.; Altantzis, T.; Goris, B.; Rabouw, F. T.; van Rossum, S. A. P.; van der Zant, H. S. J.; Siebbeles, L. D. A.; Van Tendeloo, G.; Swart, I.; Hilhorst, J.; Petukhov, A. V.; Bals, S.; Vanmaekelbergh, D. Science 2014, 344, 1377-1380.

16. Walker, D. A.; Leitsch, E. K.; Nap, R. J.; Szleifer, I.; Grzybowski, B. A. Nature Nanotech. 2013, 8, 676-681.

17. Nie, Z. H.; Fava, D.; Kumacheva, E.; Zou, S.; Walker, G. C.; Rubinstein, M. Nat. Mater. 2007, 6, 609-614.

18. Dong, A. G.; Chen, J.; Vora, P. M.; Kikkawa, J. M.; Murray, C. B. Nature 2010, 466, 474-477.

19. Lin, Y.; Skaff, H.; Emrick, T.; Dinsmore, A. D.; Russell, T. P. Science 2003, 299, 226-229.

20. Boal, A. K.; Ilhan, F.; DeRouchey, J. E.; Thurn-Albrecht, T.; Russell, T. P.; Rotello, V. M. Nature 2000, 404, 746-748.

21. Love, J. C.; Estroff, L. A.; Kriebel, J. K.; Nuzzo, R. G.; Whitesides, G. M. Chem. Rev. 2005, 105, 1103-1169.

22. Pensa, E.; Cortes, E.; Corthey, G.; Carro, P.; Vericat, C.; Fonticelli, M. H.; Benitez, G.; Rubert, A. A.; Salvarezza, R. C. Acc. Chem. Res. 2012, 45, 1183-1192.

23. Ulman, A. Chem. Rev. 1996, 96, 1533-1554.

24. Schlenoff, J. B.; Li, M.; Ly, H. J. Am. Chem. Soc. 1995, 117, 12528-12536.

25. Guo, R.; Song, Y.; Wang, G. L.; Murray, R. W. J. Am. Chem. Soc. 2005, 127, 2752-2757.

26. Cheng, H.; Yang, L. N.; Jiang, Y.; Huang, Y. Y.; Sun, Z. H.; Zhang, J.; Hu, T. D.; Pan, Z. Y.; Pan, G. Q.; Yao, T.; Bian, Q.; Wei, S. Q. Nanoscale 2013, 5, 11795-11800.

27. Luedtke, W. D.; Landman, U. J. Phys. Chem. B 1998, 102, 6566-6572.

28. Hostetler, M. J.; Templeton, A. C.; Murray, R. W. Langmuir 1999, 15, 3782-3789.

29. Templeton, A. C.; Wuelfing, M. P.; Murray, R. W. Acc. Chem. Res. 2000, 33, 27-36

30. Jadzinsky, P. D.; Calero, G.; Ackerson, C. J.; Bushnell, D. A.; Kornberg, R. D. Science 2007, 318, 430-433.

31. Jackson, A. M.; Myerson, J. W.; Stellacci, F. Nat. Mater. 2004, 3, 330-336.

32. Wang, D. W.; Nap, R. J.; Lagzi, I.; Kowalczyk, B.; Han, S. B.; Grzybowski, B. A.; Szleifer, I. J. Am. Chem. Soc. 2011, 133, 2192-2197.

33. Zaki, A.; Dave, N.; Liu, J. W. J. Am. Chem. Soc. 2012, 134, 35-38.

34. Zheng, Y. B.; Payton, J. L.; Song, T. B.; Pathem, B. K.; Zhao, Y. X.; Ma, H.; Yang, Y.; Jensen, L.; Jen, A. K. Y.; Weiss, P. S. Nano Lett. 2012, 12, 5362-5368.

35. Ionita, P.; Caragheorgheopol, A.; Gilbert, B. C.; Chechik, V. J. Am. Chem. Soc. 2002, 124, 9048-9049.

36. Dinkel, R.; Braunschweig, B.; Peukert, W. J. Phys. Chem. C 2016, 120, 1673-1682.

37. Dannenberger, O.; Buck, M.; Grunze, M. J. Phys. Chem. B 1999, 103, 2202-2213.

38. Georgiadis, R.; Peterlinz, K. P.; Peterson, A. W. J. Am. Chem. Soc. 2000, 122, 3166-3173.

39. Peterlinz, K. A.; Georgiadis, R. Langmuir 1996, 12, 4731-4740.

40. Ravi, V.; Binz, J. M.; Rioux, R. M. Nano Lett. 2013, 13, 4442-4448.

41. Campion, A.; Kambhampati, P. Chem. Soc. Rev. 1998, 27, 241-250.

42. Stiles, P. L.; Dieringer, J. A.; Shah, N. C.; Van Duyne, R. R. Annu. Rev. Anal. Chem. 2008, 1, 601-626.

43. Feng, Y. H.; Xing, S. X.; Xu, J.; Wang, H.; Lim, J. W.; Chen, H. Y. Dalton Trans. 2010, 39, 349-351.

44. DeVetter, B. M.; Mukherjee, P.; Murphy, C. J.; Bhargava, R. Nanoscale 2015, 7, 8766-8775.

45. Moskovits, M. J. Raman Spectrosc. 2005, 36, 485-496.

46. Halas, N. J.; Lal, S.; Chang, W. S.; Link, S.; Nordlander, P. Chem. Rev. 2011, 111, 3913-3961.

47. Xu, H. X.; Bjerneld, E. J.; Kall, M.; Borjesson, L. Phys. Rev. Lett. 1999, 83, 4357-4360.

48. Zhang, Q. F.; Large, N.; Nordlander, P.; Wang, H. J. Phys. Chem. Lett. 2014, 5, 370-374.

49. Zhang, Q. F.; Blom, D. A.; Wang, H. Chem. Mater. 2014, 26, 5131-5142.

50. Hamelin, A. J. Electroanal. Chem. 1996, 407, 1-11.

51. Zhang, J.; Langille, M. R.; Personick, M. L.; Zhang, K.; Li, S. Y.; Mirkin, C. A. J. Am. Chem. Soc. 2010, 132, 14012-14014.

52. Hamelin, A.; Martins, A. M. J. Electroanal. Chem. 1996, 407, 13-21.

53. Huang, Y. F.; Zhu, H. P.; Liu, G. K.; Wu, D. Y.; Ren, B.; Tian, Z. Q. J. Am. Chem. Soc. 2010, 132, 9244-9246.

54. Osawa, M.; Matsuda, N.; Yoshii, K.; Uchida, I. J. Phys. Chem. 1994, 98, 12702-12707.

55. Rouhana, L. L.; Moussallem, M. D.; Schlenoff, J. B. J. Am. Chem. Soc. 2011, 133, 16080-16091.

56. Schessler, H. M.; Karpovich, D. S.; Blanchard, G. J. J. Am. Chem. Soc. 1996, 118, 9645-9651.

57. Valkenier, H.; Huisman, E. H.; van Hal, P. A.; de Leeuw, D. M.; Chiechi, R. C.; Hummelen, J. C. J. Am. Chem. Soc. 2011, 133, 4930-4939.

58. Bain, C. D.; Troughton, E. B.; Tao, Y. T.; Evall, J.; Whitesides, G. M.; Nuzzo, R. G. J. Am. Chem. Soc. 1989, 111, 321-335.

59. Liu, Y.; Shen, L. Langmuir 2008, 24, 11625-11630.

60. Ansar, S. M.; Arneer, F. S.; Hu, W. F.; Zou, S. L.; Pittman, C. U.; Zhang, D. M. Nano Lett. 2013, 13, 1226-1229.

61. Herves, P.; Perez-Lorenzo, M.; Liz-Marzan, L. M.; Dzubiella, J.; Lu, Y.; Ballauff, M. Chem. Soc. Rev. 2012, 41, 5577-5587.

62. Menumerov, E.; Hughes, R. A.; Neretina, S. Nano Lett. 2016, 16, 7791-7797.

63. Eo, M.; Baek, J.; Song, H. D.; Lee, S.; Yi, J. Chem. Commun. 2013, 49, 5204-5206.

64. Zhang, Q. F.; Zhou, Y. D.; Villarreal, E.; Lin, Y.; Zou, S. L.; Wang, H. Nano Lett. 2015, 15, 4161-4169.

65. Caragheorgheopol, A.; Chechik, V. Phys. Chem. Chem. Phys. 2008, 10, 5029-5041.

66. Kassam, A.; Bremner, G.; Clark, B.; Ulibarri, G.; Lennox, R. B. J. Am. Chem. Soc. 2006, 128, 3476-3477.

67. Huang, X. H.; Neretina, S.; El-Sayed, M. A. Adv. Mater. 2009, 21, 4880-4910.

68. Jin, R. C.; Cao, Y. W.; Mirkin, C. A.; Kelly, K. L.; Schatz, G. C.; Zheng, J. G. Science 2001, 294, 1901-1903.

Chapter 2

Isocyanide Ligand dynamic interactions on highly curved gold nanoparticles: A comparative study using Plasmon enhanced spectroscopy.

2.1 Introduction

Surface functionalization of gold nanoparticles play a critical role in guiding nanocrystal growth, influencing the interfacial environment generating unique optical and physical properties [1-4]. The importance of understanding these underlying interfacial dynamics between ligand and nanoparticle have produced a great deal of work unraveling the roles of self-assembled monolayers (SAMs) like organothiol molecules on the surface of noble metal nanoparticle to thin films [5-8]. Although, extensive studies have been conducted investigating thiol ligand high affinity interaction with noble metal nanoparticles like gold, focusing on thermodynamic and in situ kinetic measurements of adsorption and exchange reactions [9-14], much less is known concerning the interfacial interaction of isocyanide ligands with gold. Several studies have explored the chemisorption of organoisocyanide molecules on metals, such as, Ag, Au, Cr, Co, Pt, Pd, and Ru [14-23]. Previous reports suggest that peak positioning is shifted based on binding and coordination of the N≡C-metal bond, with diisocyanide molecules revealing two distinct binding modes of 2121 and 2180 cm^{-1} for uncoordinated and coordinated, respectively [16]. These studies have reported a standing conformation of 1,4 phenylene diisocyanide, associated with a blue shift in SERS measurement of 2127 cm^{-1} for υ(N≡C) from that of normal Raman measurements for gold nanoparticles in the range of 20-60 nm, suggesting a donation from the carbon of the N≡C bond to the Au surface [24]. The vertical orientation of isocyanides like 1,4 phenylene diisocyanide are bound via the lone pair of electrons from the carbon on the N≡C, leaving the other N≡C pendant moiety free to interact with other substrates through the antibonding lone pairs on that side [24,25]. However, previous reports state that no SERS signal is detected until this pendant N≡C interacts with another Au

nanoparticle, creating dimers and interstitial hot spots, which gives more electromagnetic enhancement [25], while admitting that selection rules preclude the horizontal configuration on the gold surface. Here we present further investigation of isocyanide molecules, 4-nitrophenylisocyanide and 1,4 phenyl diisocyanide on Au surface roughened nanoparticle (SRNPs) with nanoscale surface texturing mimicking the high curvature of smaller nanoparticles. We also address the kinetics associated with adsorption and exchange to provide further mechanistic insight of multiple binding modes, terminal upright, bridging and flat [25], between gold and palladium surfaces on SRNPs.

2.2 Experimental Details

Chemicals and Materials:

Gold (III) chloride trihydrate ($HAuCl_4 \cdot 3H_2O$, ACS grade) was purchased from J.T. Baker. Sodium borohydride ($NaBH_4$, 99%), hydrochloric acid (HCl, 37%), and L-ascorbic acid (AA, 99.5%), Palladium (II)chloride (PdCl2, > 99.9%) were obtained from Sigma-Aldrich. Cetyltrimethylammonium chloride (CTAC, 96%), 4-Phenyldiisocyanide (C_7H_5NS, 4-PDIC, 97%) and 4- Nitrothiopenol (C6H5NO2S, 4-NTP, 80%) were obtained from Alfa Aesar. 4-Nitrophenylisocyanide (C7H4N2O2, 4-NPI, 98%) and cetyltrimethylammonium bromide (CTAB, > 98.0%) was obtained from TCI. All reagents were used as received without further purification. Ultrapure water (18.2 MΩ resistivity, Barnstead EasyPure II 7138) was used for all experiments.

Nanoparticle Synthesis:

Au surface roughened nanoparticles (SRNPs) and quasi-spherical nanoparticles (QSNPs) were synthesized using a kinetically controlled, seed-mediated nanocrystal

growth method, reported previously by our group. Colloidal Au seeds (~3 nm in diameter) were first prepared by reducing $HAuCl_4$ with $NaBH_4$ in the presence of CTAC. Briefly, 0.25 mL of $HAuCl_4$ (10 mM) was introduced into an aqueous solution of CTAC (10 mL, 100 mM) under magnetic stir. Then 0.30 mL of ice cold, freshly prepared $NaBH_4$ (10 mM) was quickly added to the solution containing both CTAC and $HAuCl_4$. The mixture solution was stirred for 1 min, then left undisturbed for 2 h, and finally diluted 1000-fold with 100 mM CTAC. The diluted seed colloids were used for the subsequent seed-mediated growth of Au SRNPs and QSNPs.

The growth solution for SRNPs was prepared by sequentially adding 0.50 mL of $HAuCl_4$ (10 mM) and 0.10 mL of AA (100 mM) into 10.0 mL of CTAC (100 mM) solution. To prepare Au SRNPs with average diameter of ~ 120 nm, 40 μL of the diluted Au seed solution was added into the growth solution. The reactants were gently mixed for 30 s and then left undisturbed at room temperature for 4 h. The as-obtained Au SRNPs were washed with water 3 times through centrifugation/redispersion cycles, and finally redispersed in water. The Au QSNPs were fabricated following a similar protocol for the Au SRNPs except for the addition of HCl. The growth solution was prepared by sequentially adding 0.50 mL of $HAuCl_4$ (10 mM), 0.20 mL of HCl (1.0 M), and 0.10 mL of AA (100 mM) into 10.00 mL of CTAC (100 mM) solution. After gently mixing the reactants for 30 s, the growth of Au QSNPs was initiated by adding 35 μL of the diluted Au seed solution, and then left undisturbed at room temperature for 4 h. The obtained Au QSNPs were washed with water 3 times and finally redispersed in water.

Preparation of Au-Pd core shell Nanocrystals

For palladium nanoparticles, Au surface roughened nanoparticles were synthesized with an heteroepitaxial growth of palladium on the surface generating the palladium shell without compromising the surface. This method was previously reported by Chun Hua Yan group. For the Au@Pd nanoparticles used in the following experiments, Au SRNP nanocrystals (1 mL, 5.0 x 10^9 particles mL^{-1}) of size ~130 nm in diameter were added to a growth solution containing cetyltrimethylammonium bromide (CTAB, 0.025 M, 4 mL), H_2PdCl_4 (0.01 M, 0.015 mL), and ascorbic acid (0.1 M, 0.008 mL). The resulting solution was gently inverted for 10 seconds to ensure thorough mixing, then left overnight undisturbed. Particles were centrifuged at 3000 rpm for 4 minutes and precipitate was then redispursed in 1 mL of water

Structural Characterizations of Nanoparticles:

The structures of the nanoparticles were characterized by scanning electron microscopy (SEM) using a Zeiss Ultraplus thermal field emission scanning electron microscope. The samples for SEM measurements were dispersed in water and drop-dried on silicon wafers. The optical extinction spectra of the NPs were measured on aqueous colloidal samples at room temperature using a Beckman Coulter Du 640 spectrophotometer.

ζ-potential measurements:

The hydrodynamic sizes and ζ–potentials of the colloidal NPs were measured at room temperature using ZETASIZER nanoseries (Nano-ZS, Malvern). The samples for ζ–potential measurements were all freshly prepared, centrifuged, and dispersed in water. The

concentration of the colloids for ζ–potential measurements was kept at 2 x 10^9 particles mL^{-1} for all the samples and pHs of the colloidal suspensions were measured to be around 7.4. Each sample was measured at various concentrations: 0, 0.5, 1.0, 2.5, 5.0, 10, 25, 50, 75, 100 μM of isocyanide ligands, 4-NPI, 4-PDIC and 4-NTP. In our ζ-potential measurements, we used the zeta potentiometer to measure the free mobility and effective hydrodynamic sizes of NPs, which were then converted into ζ-potentials using simple theoretical formulas approximating the NP as a hard sphere homogenously coated with a charged thin layer.[3]

In situ Isocyanide Ligand Adsorption:

We used SERS to monitor the thiol ligand adsorption kinetics on the surfaces of Au SRNPs and QSNPs in real time at room temperature. The isocyanide ligand adsorption was initiated by introducing 4 μL of ethanolic solutions of 4-NPI or 4-PDIC at certain concentrations into 200 μL of colloidal Au SRNPs (1.0 x 10^9 particles mL^{-1}) or Au QSNPs (4.5 x 10^{10} particles mL^{-1}). Immediately after the thiol ligands and the NPs were mixed, successive SERS spectra were collected in real time with various time intervals and spectral integration times of 2 s for SRNPs and 20 s for QSNPs, respectively, until after sufficiently long incubation times. The apparent surface coverages of 4-NPI and 4-PDIC were quantified as a function of incubation time based on the time-evolution of SERS intensities of the 1340 cm^{-1} for 4-NPI and 1595 cm^{-1} mode and 2177 cm^{-1} mode for both 4-NPI and 4-PDIC. However, there was no equilibrium reached for 4-NPI, which underwent a more complicated process.

Isocyanide Ligand Exchange of:

4-NPI with 4-NTP:

200 µL of Au SRNPs and 900 µL QSNPs with various surface coverages of 4-NPI (NPs incubated with at final concentrations of: 1, 5 and 50 µM of 4-NPI for 2 h) were centrifuged and supernatant was removed and redispersed in 195 µL water. 4-NPI-coated Au SRNPs (1.0×10^9 particles mL^{-1}) or Au QSNPs (4.5×10^9 particles mL^{-1}) were then mixed with final concentration of 50 µM of 4-NTP to initiate the thiol ligand exchange. The total volume of each sample was kept at 200 µL. SERS spectra were collected with an excitation power of 10.0 mW. The time-evolution of the peak intensities at 2177 cm^{-1} was monitored to track the ligand exchange kinetics. The spectral integration times were 2 s for SRNPs and 20 seconds for QSNPs, respectively. All measurements were replicated at least three times.

4-NTP with 4-NPI:

The ligand exchange measurements were carried out on Au SRNPs and QSNPs for saturated surface coverages of 4-NTP (50 µM final concentration) followed by the introduction of 4-NPI (50 µM final concentration) to initiate exchange under the same experimental conditions. SERs spectra was collected monitoring the evolution of 1080 cm^{-1} mode for 4-NTP and 2177 cm^{-1} for 4-NPI.

4-PDIC with 4-NTP

The ligand exchange measurements were also performed on Au SRNPs and QSNPs with various surface coverages of 4-PDIC under the same experimental conditions. Au SRNPs with unsaturated 4-PDIC coverage were fabricated by incubating the CTAC-coated Au SRNPs with final concentrations of: 1, 5 and 50 µM of 4-PDIC for 2 h) for 24 h. SERS

spectra was collected until no change was observed in the intensity of the 1080 and 1340 cm^{-1} mode associated with v(C-S) and $v(NO_2)$ respectively for 4-NTP and 2177 cm^{-1} mode for 4-PDIC. Measurements were conducted under the same experimental conditions as the previous exchange models.

DFT Calculations:

The exchange-correlation functional B3LYP was used for all the calculations. The basis set of light atoms was 6-31+G**, while for the heavy metal atoms, effective core potential was employed with the basis set def2-svp. The calculation was done by optimizing the geometry of the 4-metal-cluster substrate structures at first, constraints were applied to make sure tetrahedral structures were obtained. After substrate geometry optimization, the molecules were set at the different sites of the metal substrates and geometry of each complex structure was further optimized. The optimized geometries were used to calculate the Raman spectrum. The calculated Raman activities were converted to relative Raman intensities according to the equation below,

$$I_i = \frac{f(v_0 - v_i)^4 S_i}{v_i \left[1 - \exp\left(-\frac{hc\, v_i}{kT}\right)\right]}$$

Where v_0 is the exciting frequency in (cm^{-1}), v_i is the vibrational frequency of the ith normal mode, h, c, k are universal constants, and f is a suitably chosen common scaling factor for all peak intensities. The excitation frequency was set at to be 12738.85 cm^-1, which corresponds to 785nm incoming light. The scaling factor 1 was used for all the peak intensities, and the temperature was taken as 298.15 K. The relative Raman intensities were

further expanded with Lorentzian lineshape with 7 cm^-1 full width at half maximum. The binding energy was calculated by using the following equation:

$$\text{Binding Energy} = E_{(complex)} - E_{(molecule)} - E_{(metal\text{-}cluster)}$$

References:

1. P.L. Polavarapu, Ab Initio Vibrational Raman and Raman Optical Activity Spectra, J. Phys. Chem. 1990, 94, 8106-8 112 2. G. KERESZTURY, S. HOLLY, G. BESENYEI and J. VARGA, Vibrational spectra of monothiocarbamates-II.'" IR and Raman spectra, vibrational assignment, conformational analysis and ab initio calculations of S-rnethyl-N,N-dimethylthiocarbamate, Spectrochimlcn Acta, Vol.49A, No. 13/14, pp. 2007-2026, 1993

2.3 Results and discussion

Au SRNPs, were used for their tuneable plasmonic activity at a size of ~ 120 nm and their textured surface, which provide better enhancement than the more spherical particles, while also offering new insight due to the particles ability to mimic the high curvature of smaller nanoparticles. The Uv vis measurements reveal an extinction at 775 nm that is near resonant to the 785 nm laser used for excitation. For interfacial measurements on Pd nanoparticles, a thin conformal layer of palladium was epitaxially grown on the surface [26], both particles are shown in SEM images of figure 2.2A and C for Au and Au@Pd, respectively. The EDS measurements of the particles demonstrate the presence of Pd at ~20 % in the Au SRNP represented in figure 2.2D, while figure 2.2B shows no occurrence of Pd in normal Au SRNPs. Maximizing the plasmonic enhancement for the Au@Pd nanoparticle is extremely important for SERS quantification and

characterization of dynamics between ligand and nanoparticle. Extinctions were measured for various percentages of Pd, using a 20/80 % Pd/Au composition to ensure Pd fully developed conformal layer over the Au SRNPs while maintaining reasonable plasmonic features, figure 2.1.

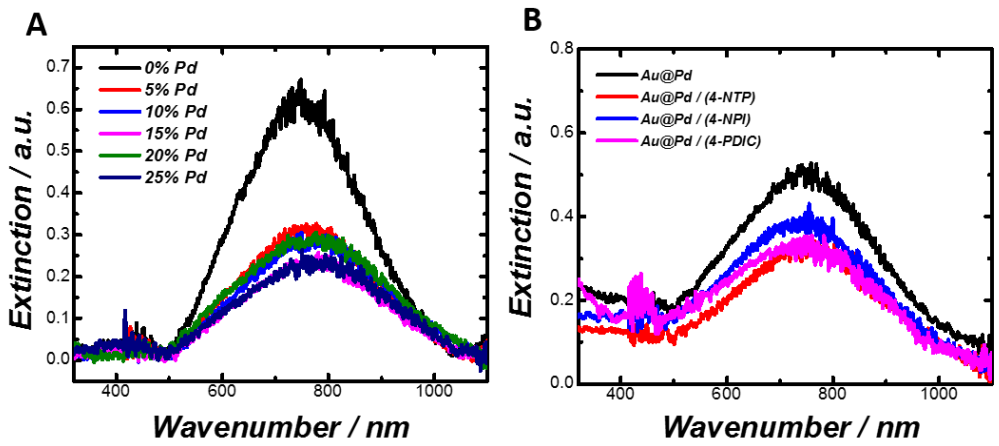

Figure 2. 2 UV Vis Extinction for A) Au SRNPs with outer shell compositions of 0, 5, 10, 15, 20, and 25 % Pd thickness of conformal layer. Extinction of Au@20% Pd conformal layer (B) with pNTP, NPI and PDIC capped ligands.

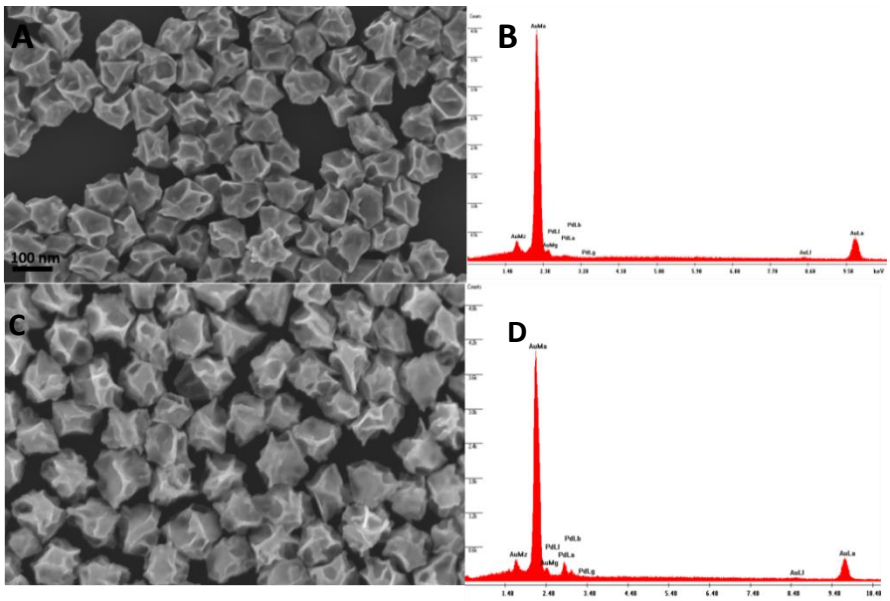

Figure 2. 1 SEM images A) AuSRNPs B) EDS measurements detailing composition for (A), C) Au@20%Pd SRNPs, D) EDS measurements for (C)

The Au SRNPs and Au@Pd core shell nanoparticles were exposed to various concentrations of isocyanide ligands, 4-NPI and 4-PDI with thiolated ligand, 4-nitrothiophenol (4-NTP) coated nanoparticles used for reference. Upon measuring the ζ-potential, there is a dramatic decrease and switch from positive to negative relative to the CTAC capped Au SRNP, figure 2.3 while for Au@Pd SRNPs there is no change from positive to negative, indicating a less negative surface contribution from the isocyanide molecule when attached to the palladium surfaces as the outer most layer [28], figure 2.4. Although there is a drastic change in the ζ-potential, the hydrodynamic diameter remains virtually unchanged throughout all concentrations for both isocyanide and thiolated ligands, indicating no aggregation from either nanoparticle.

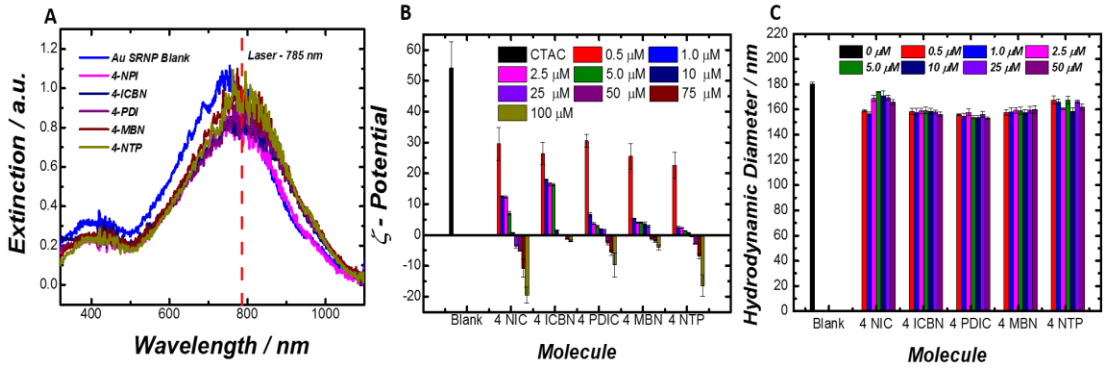

Figure 2. 3 UV Vis Extinction for A) Au SRNPs with outer shell compositions of 0, 5, 10, 15, 20, and 25 % Pd thickness of conformal layer. Extinction of Au@20% Pd conformal layer (B) with pNTP, NPI and PDIC cappe Representative extinction spectra (A) taken of Au SRNPs with various ligands: pNPI, ICBN, PDIC, pMBN and pNTP. Zeta potential measurements (B) taken one hour after adsorption process onto Au SRNPs for various concentration of ligands: 0.5, 1.0, 2.5, 5.0, 10, 25, 50, 75, 100 µM for each ligand: pNPI, ICBN, PDIC, pMBN and pNTP, with CTAC capped Au SRNP as reference. Hydrodynamic diameter measurements detailed in (C) for concentrations: 0.5, 1.0, 2.5, 5.0, 10, 25 and 50 µM for each ligand: pNPI, ICBN, PDIC, pMBN and pNTP, with CTAC capped Au SRNP used as reference for hydrodynamic diameter.

SERS spectra for 50 µM of 4-NPI and 4-NTP are plotted containing DFT calculations in comparison with normal Raman and SERS spectra, demonstrating the binding of isocyanide molecules in comparison to their thiolated counterparts, figure 2.5. We see that the adsorption of isocyanide molecules, like 4-NPI demonstrate a unique vibrational mode, 2177cm^{-1} corresponding to the υ(N≡C) stretch and 1350 cm^{-1} υ(NO_2), figure 2.5A, while 4-NTP, the thiol counterpart exhibits characteristic SERS vibrational mode 1080 cm^{-1} υ(C-S) and 1340 cm^{-1} υ(NO_2).

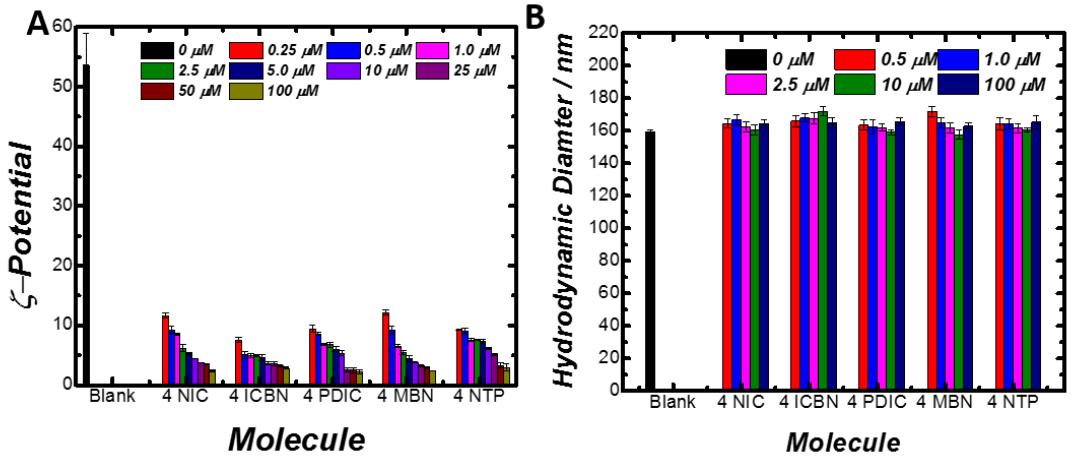

Figure 2. 4 Zeta potential measurements (B) taken 24 hours after adsorption process onto Au@20% Pd SRNPs for various concentration of ligands: 0.5, 1.0, 2.5, 5.0, 10, 25, 50, 75, 100 µM for each ligand: pNPI, ICBN, PDIC, pMBN and pNTP, with CTAC capped Au SRNP as reference. Hydrodynamic diameter measurements detailed in (C) for concentrations: 0.5, 1.0, 2.5, 5.0, 10, 25 and 50 µM for each ligand: pNPI, ICBN, PDIC, pMBN and pNTP, with CTAC capped Au@20% Pd SRNPs use as reference for hydrodynamic diameter. Error bars for all samples indicate standard deviation of 5 replicant measuments.

We see that the calculated modes for 4-NPI matches well to the experimental observations. The change in substrate shows a shift in the υ(N≡C) mode for 4-NPI on gold and palladium from that of neat 4-NPI. From the calculated spectra on Palladium, it shows evidence that the hollow position for the 4-NPI molecules is the preferred site for adsorption, figure 2.6, this is also supported by binding energy calculations, figure 2.7

showing a lower energy associated with more thermodynamically stable binding at the hollow sites on Pd surfaces. Figure 2.6 displays a small peak at 1991 cm^{-1} indicating a binding at the hollow position but also shows a band broadening at higher wavenumbers that correspond to binding at bridge sites. The normal Raman, SERS and DFT calculated spectra detail the υ(N≡C) mode at 2133, 2177 and 2180 cm^{-1} for Au surfaces respectively, highlighting the blue shift of 43 cm^{-1} for adsorption onto Au SRNPs, which has been attributed to electron donation from the isocyanide ligand to the gold from the anti-bonding

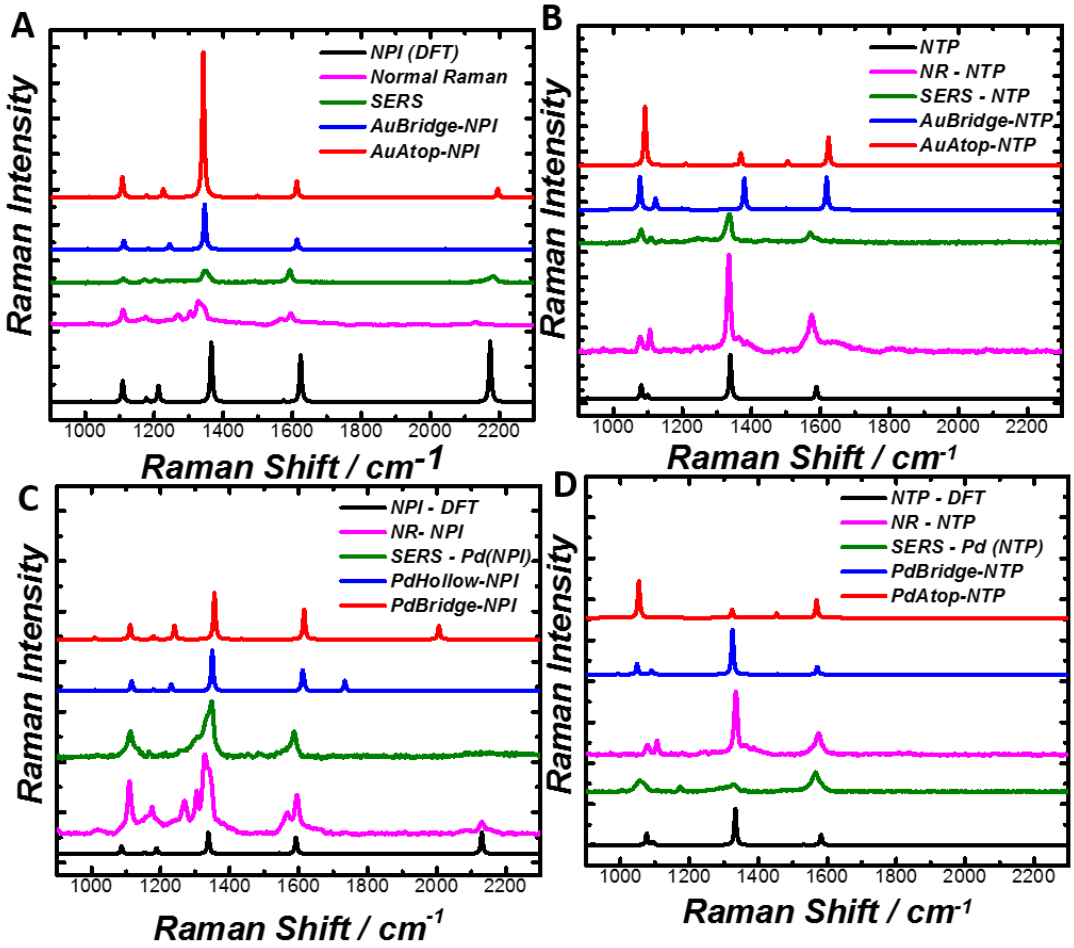

Figure 2. 5 Representative Raman spectra for A) NPI: i) DFT, ii) Normal Raman, iii) SERS, iv) Au Bridge – DFT, v) Au Atop – DFT. B) NTP: i) DFT, ii) Normal Raman, iii) SERS, iv) Au Bridge – DFT, v) Au Atop – DFT. C) NPI: : i) DFT, ii) Normal Raman, iii) SERS, iv) Pd Hollow – DFT, v) Pd Bridge – DFT. D) NTP: i) DFT, ii) Normal Raman, iii) SERS, iv) Pd Hollow – DFT, v) Pd Bridge – DFT.

characteristics of the lone pair on the carbon atom, increasing the Au-C bond strength. signifying the electron poor environment of the Au SRNP surface [29]. In contrast, when palladium is the substrate, the υ(N≡C) mode for the normal Raman, SERS and DFT are 2133, 1956 and 2005 cm^{-1}. Observably, there is an apparent downshift in the calculated vibrational mode υ(N≡C) associated with adsorption of 4-NPI on Au@Pd SRNPs, from 2133 to 1956 cm^{-1}. This downshift in vibrational mode associated with adsorption indicates that the configuration on the surface for isocyanide, 4-NPI, varies between both Au@Pd SRNP adsorbed 4-NPI and neat 4-NPI, with respect to binding interaction at the surface. However, this configuration associated with binding at the hollow site exhibits weak

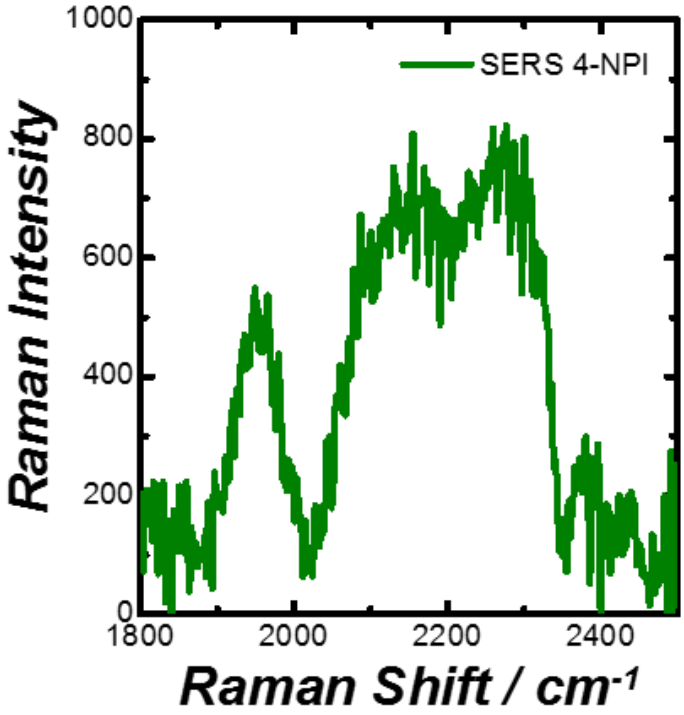

Figure 2. 6 Close up of Representative SERS spectra for 50 µM 4-NPI onto Au@Pd SRNPs, highlights lower intensity peaks at υ(N≡C)

intensity and is not highly visible in the SERS measurements and is present alongside a broad band beginning at 2151 cm^{-1}.

Additionally, the energy associated with the binding of both 4-NPI and 4-NTP at various sites on Au and Pd surfaces was calculated, revealing a preference for 4-NTP at the atop configuration for Au and slightly less favorable bridge conformation. Thiol ligand, 4-NTP as greater affinity to the Au surface over the isocyanide molecule, 4-NPI, which has a less favorable energy associated with the binding on gold surfaces, possibly creating less stable interactions at the Au-4-NPI interface as depicted in figure 2.7.

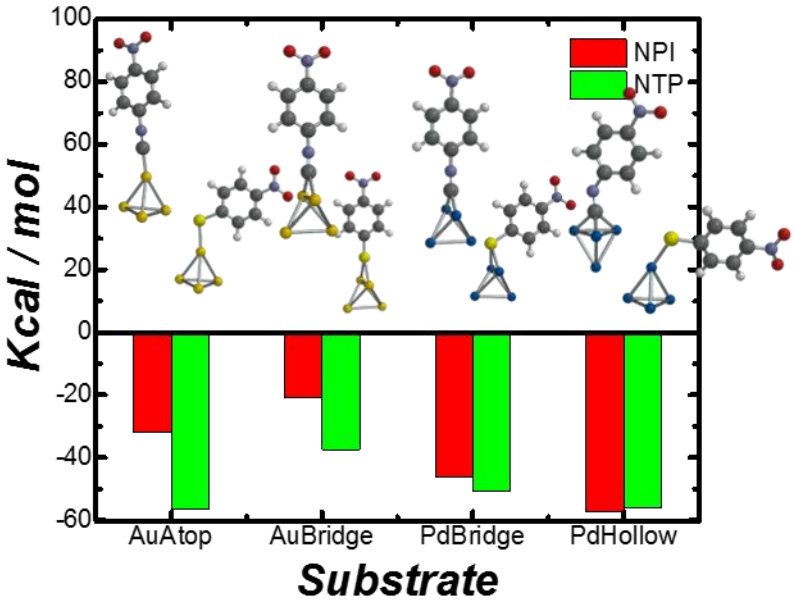

Figure 2. 7 Binding energy represented above for the various binding modes of NPI and NTP onto Au and Pd nanoparticles

However, when the substrate is changed to palladium (Pd) the isocyanide demonstrates a greater affinity to the Pd surface, by maintaining the more thermodynamically stable hollow coordination creating stronger bond interaction. Reports on Au electrodes suggest that surface potential of Au nanoparticles direct binding

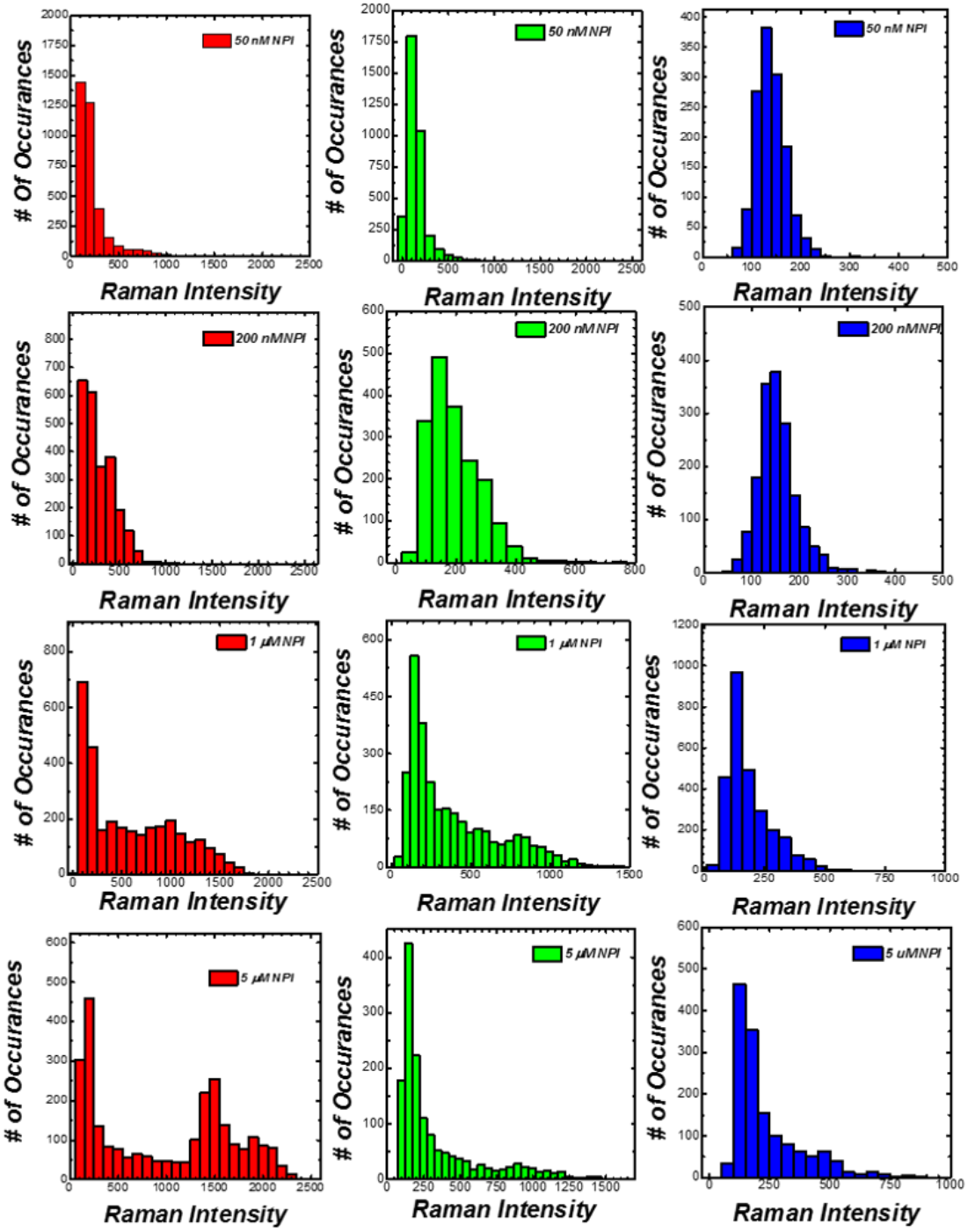

Figure 2. 8 Histogram plots of intensities associated with induction period for different adsorption concentrations of NPI tracking associated vibrational frequencies 1340 cm $^{-1}$ (NO_2), 1580 cm^{-1} (C-C), and 2177 cm^{-1} (C≡N) for A) 50 nM NPI from 5 different representative runs, B) 200 nM NPI from 6 different representative runs, C) 1 μM NPI from 10 different representative runs, D) 5 μM NPI from 7 different replicant runs

interactions, proposing upshifts of the υ(N≡C) is from contribution of σ-donation from the

isocyanide molecule possibly leading to increased N≡C bond strength, while downshifts correspond to greater effects from π-backdonation between the metal and isocyanide molecule [30], in this regard the downshift of 4-NPI onto Pd may be from increased π-back donation. The increased π-backdonation alludes to a less vertical orientation of the υ(N≡C) on the Au@Pd surface [29-31].

Adsorption / Fluctuation period

In order to gain further understanding of the link between surface adsorption for isocyanide molecules and the local environment of Au SRNPs, we observed in real time the SERS spectral evolution associated with the adsorption process. From figure 2.9, we see the initial adsorption process is very erratic in the beginning, with spectral features exhibiting random intensity trajectories. The color-coded plot illustrates the irregular adsorption of 5 µM 4-NPI. Over the first 10-minute period, the SERS spectra for 2177,

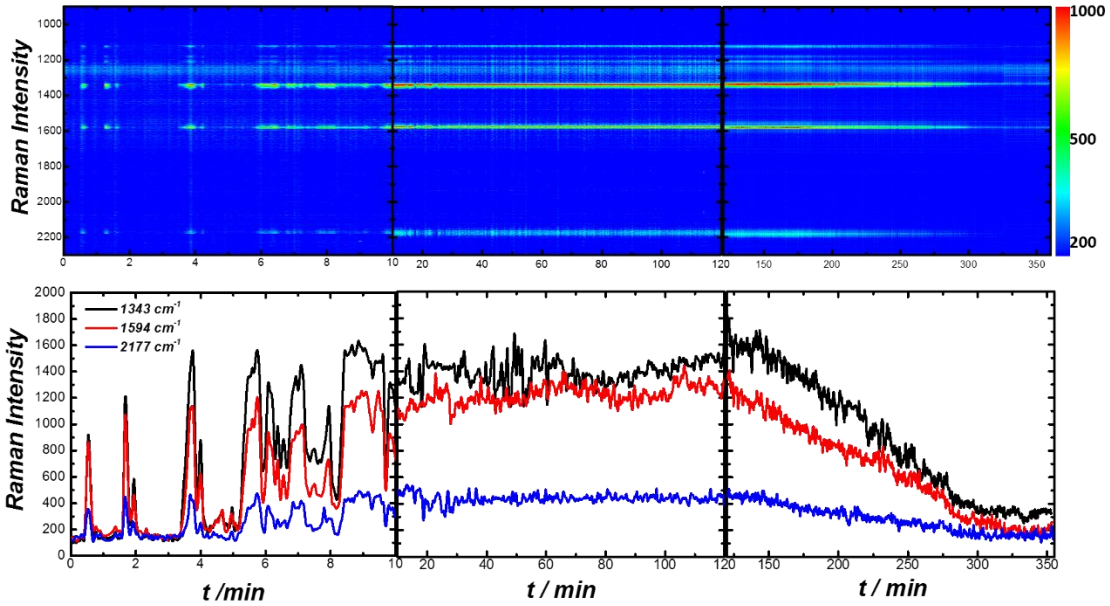

Figure 2. 9 Color coded plot depicting the A) Fluctuation B) adsorption and C) decay for 5 µM NPI interaction with Au SRNP. Below, time resolved Raman intensity trajectories (D-F) for the vibrational modes 1343 cm^{-1} (NO_2), 1594 cm^{-1} (C-C) and 2177 cm^{-1} (C≡N).

1595 and 1343 cm^{-1} associated with the adsorption of 4-NPI show periods of fluctuations for strong intensity followed by little to no intensity change until a certain point, signifying a more complex adsorption profile than expected. This was a common occurrence at lower concentrations of 200 nM, 1 and 5 µM 4-NPI, which is illustrated by histogram plots in figure 2.8, tracing the number of occurrences of the 1340 cm^{-1} υ (NO_2), 1580 cm^{-1} υ(C-C), and 2177 cm^{-1} υ(C≡N). This fluctuation resembles a much more random adsorption process. However, the introduction of higher concentration 4-NPI shows no fluctuations. The fluctuations are observed for 4-Phenyldiisocyanide (4-PDI), as well, revealing that the fluctuation is characteristic of this particular system, highly curved Au nanoparticles, adding another dimension to the adsorption process deviating from its thiolate counter parts, which at similar concentration show a no flickering during SERS measurements [12]. We believe this fluctuation period to be a consequence of molecular dynamics at the particle interface rather than a result from the diffusion of different particles. It may also be an indication of surface heterogeneity and not the particle to particle distinction.

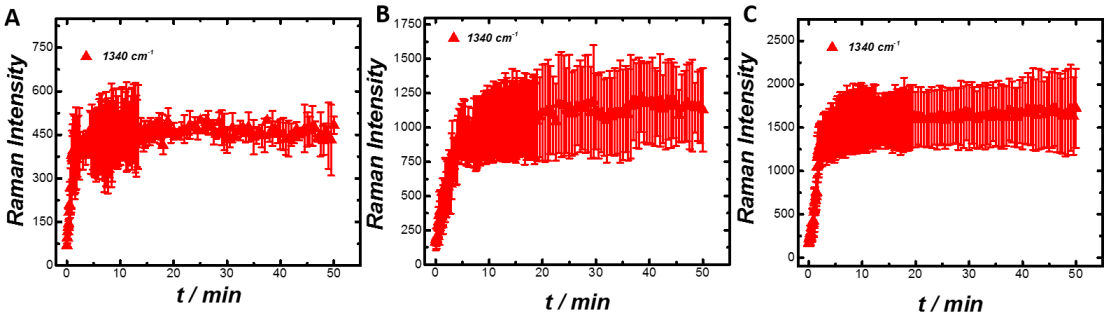

Figure 2. 10 Averaged SERS intensities for 1340 $cm^{-1}$for A) 200 nM, B) 1 µM, C) 5 µM

The initial fluctuation period is followed by a static period or a plateau in observed SERS intensity from the adsorption profile. Based upon SERS spectra, this period corresponds to a no further adsorption events occurring, revealing a short period of stability

on the highly curved and flatter regions. Although the adsorption events occur on different time scales due to the variation in fluctuation period, making quantification of the adsorption process much more complicated to resolve the contribution of the nanoparticle surface curvature. The averaged adsorption processes demonstrate considerable variation, generating large error bars, from replicant measurements, for concentrations: 200 nM, 1 and 5 µM. However, previous studies with thiol ligands indicate a substantially higher contribution to the characteristic adsorption kinetics from the local surface curvature on the surface of Au SRNPs that is different from locally flat regions. The large contribution from highly curved regions supports rapid adsorption with a smaller slower adsorption contribution from locally flat regions [12]. But for 4-NPI, the complex adsorption process makes it difficult to delineate effects of high curvature vs low curvature contribution. However, the profile illustrates a similar 2 component aspect, indicating that the 4-NPI, isocyanide molecules interact with the highly curved regions initially before adsorbing onto the surface at flatter more thermodynamically stable indices. This initial interaction is possibly the source of the fluctuation due to the variation in surface potential of the Au SRNP, containing many undercoordinated sites. One explanation is this interaction of 4-NPI and even the interaction of other isocyanide molecules is site selective first encounter the highly curved regions causing minor adsorption events but leading to significant intensity increase due to the local field enhancements at areas of high curvature before migrating to locally flat regions.

Desorption / Decay of 4-NPI

This stability is further disturbed as time progresses yielding a decrease in the Raman spectra, which is indicative of molecules leaving the surface in a desorption or

decay manner. The decay is observed for all concentrations of 4-NPI, with lower concentration, 1 and 5 µM exhibiting virtually total desorption from the surface and higher concentrations undergoing an incomplete desorption process that leaves residual 4-NPI molecules on the surface. At 50 µM of 4-NPI the desorption of the molecules ceases as is evident by the unchanging intensity for the vibrational modes 1340 cm $^{-1}$ (NO_2), 1580 cm^{-1} (C-C), and 2177 cm^{-1} (N≡C). The decay profile in this concentration regime underscores 3 regions of desorption: positive, negative and neutral curvature, with molecules persisting in areas with more neutral curvature. Neutral curvature offers greater stability, evident by the lack of desorption events occurring on Au quasispherical nanoparticles (QSNPs) for

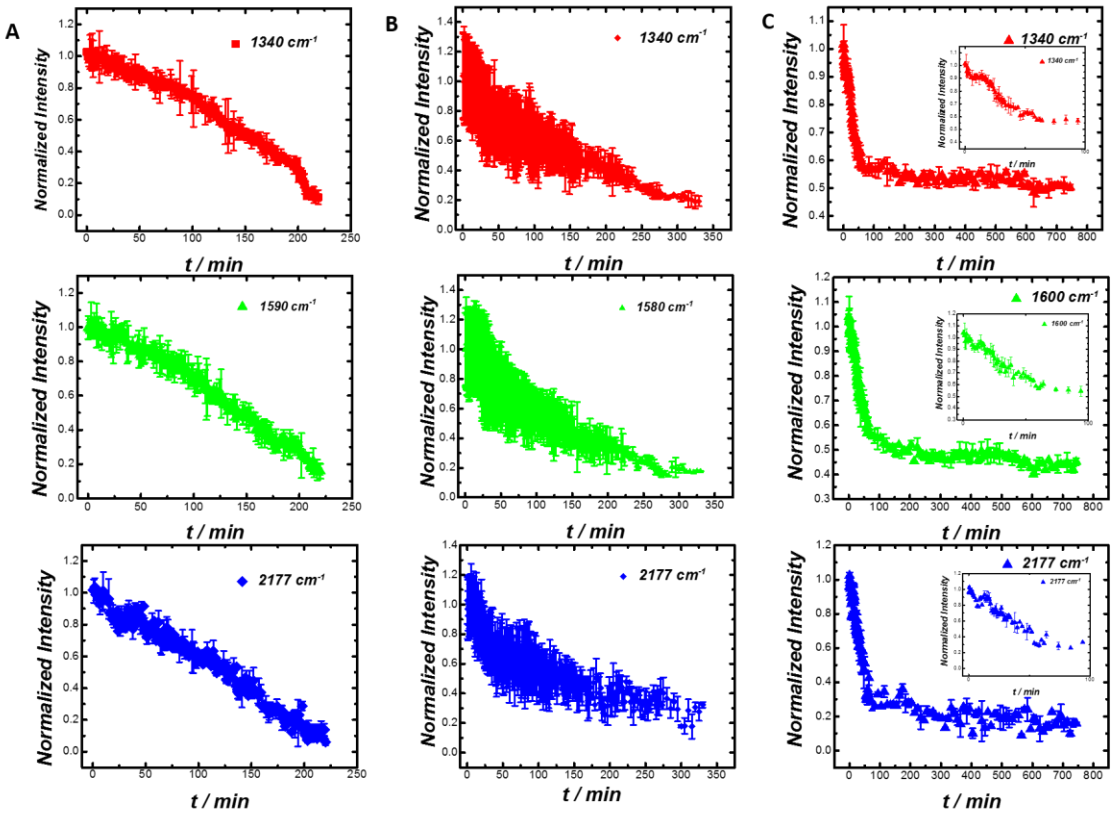

Figure 2. 11 Time resolved evolution of Raman intensity associated with the desorption of 1 µM NPI tracing the trajectory of 1340 cm $^{-1}$ (NO_2), 1580 cm^{-1} (C-C), and 2177 cm^{-1} (C≡N) for A)1 µM, B) 5 µM, C) 50 µM with error bars depicting the standard deviation from 5 replicant measurements.

concentrations of 10 µM, saturated coverage for Au QSNPs, after 24 hours no relative decrease in the SERS intensity was observed, as shown in figure 2.12. The overall decay profile at 1 and 5 µM appear different, with 1 µM possessing a more linear profile and 5 µM having more exponential decay but at the higher concentration 50 µM, the profile contains both a linear and exponential component. These two components highlight the effects of surface curvature, kinetic versus thermodynamic interactions between ligand and nanoparticle. Although

4-NPI Exchange with 4-NTP:

The spontaneous desorption of isocyanide molecule, 4-NPI, was surprising and further experimentation was limited to initiating exchange during the static period for thiolated ligand, 4-NTP. We monitored exchange events for the following concentrations: 1, 5 and 50 µM in real time, depicted in figure 2.13. The color-coded plots for 1 and 5 µM illustrate a majority exchange with 4-NTP. The Peaks associated with adsorption of 4-NTP, 1080 cm^{-1} υ(C-S) are visible instantly, signifying adsorption of 4-NTP in regions with little or no 4-NPI molecules, this is evident by the quick adsorption kinetics displayed by both 1and 5 µM. However, at these low concentrations, the exchange is also a very quick process, almost simultaneous with adsorption. But, increasing the concentration from 1 µM to 5 µM, there is the presence of some residual 4-NPI molecules on the surface, as illustrated by the trace evidence of the 2177 cm^{-1} peak associated with υ(C≡N) indicating a nominal amount of 4-NPI in regions of more thermodynamic stability. More convincing evidence is observed for 50 µM 4-NPI after introduction of 50 µM 4-NTP. Since the desorption of 4-NPI molecules from the Au SRNP surface is incomplete, the exchange yields better opportunity to observe the effects of ligand - ligand interaction with the

heterogenous surface structure of the Au SRNPs. Since there are no free binding sites, the initial adsorption is very limited, but the exchange kinetics are more significantly expressed and highlighted in the color-coded plots. 4-NTP mode 1080 cm^{-1} υ(C-S) intensity is more gradual as is the decrease in intensity for the vibrational mode of 4-NPI, 2177 cm^{-1} υ(N≡C), the gradual decrease in 2177 cm^{-1} follows a similar trajectory as well as time scale as the desorption of 50 µM 4-NPI making the possibility of desorption limited kinetic exchange

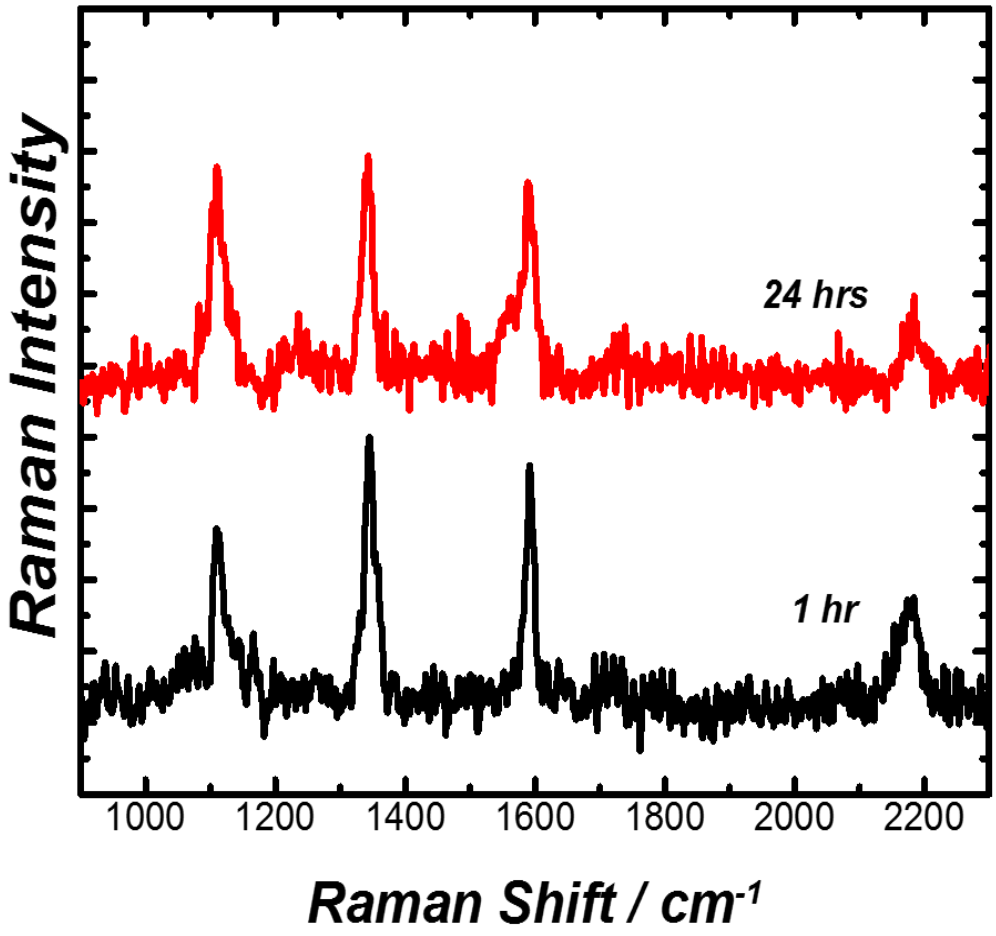

Figure 2. 12 SERS spectra for QSNP at 10 µM of 4-NPI at 1 hr and 24 hrs after adsorption

one possible explanation for the exchange dynamics. The lack of complete exchange and enduring presence of SERS signal from the 2177 cm^{-1} υ(N≡C) show that there are long lived 4-NPI molecules on the surface of Au SRNPs. One explanation is that these molecules are bound to the flatter regions on the nanoparticle surface, while the exchange of 4-NPI with 4-NTP occurs at the highly curved regions initially followed by a slower displacement of 4-NPI from regions and sites with greater preference for 4-NTP molecules, i.e. areas with neutral curvature or higher thermodynamic stability. The initial introduction of 4-NTP contributes to the instability of 4-NPI molecules jumpstarting the desorption allowing the exchange to proceed.

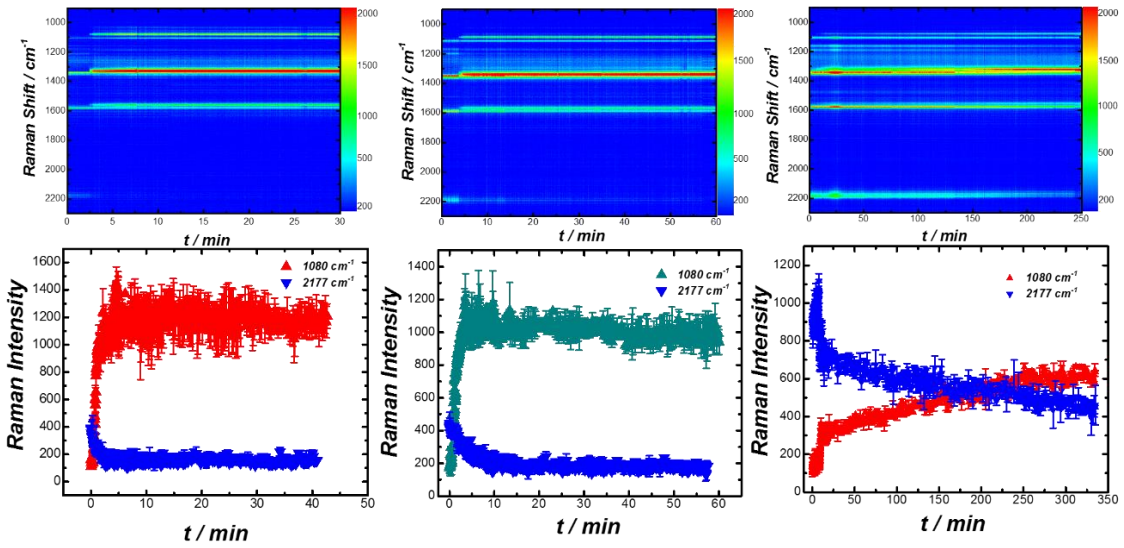

Figure 2. 13 Color coded plots representing the exchange of various concentrations of NPI adsorbed onto Au SRNP with 50 µM NTP. A) 1 µM, B) 5 µM and C) 50 µM NPI. Below representative trajectories for time resolved Raman intensities of 2177 cm^{-1} associated with (C≡N) vibrational mode and 1080 cm^{-1} (C-S) demonstrating the adsorption and exchange of NPI with NTP on the surface of the Au SRNPs for the following; D) 1 µM, E) 5 µM and F) 50 µM NPI. Error bars depict the standard deviation associated with 5 replicant runs.

PDIC Adsorption

Further investigation of 4-PDI, another isocyanide molecule, shows that the fluctuation is not unique to the 4-NPI molecule, however, as is illustrated by both the color-code plot and the time resolved SERS spectra monitoring the 1170 cm^{-1} υ(C-N), 1595 cm^{-1} υ(C-C) and 2177 cm^{-1} υ(C≡N), which are characteristic to the adsorption of 4-PDI to the Au SRNP surface. The presence of fluctuation for different isocyanide molecules and not for thiol molecules presents evidence of a lack stability between the 4-NPI and Au SRNP surface. The interfacial periodic disruption of 4-PDI adsorption, however, very possibly has different origins than the 4-NPI molecules, due to the overall final stability of the 4-PDI molecules on the Au SRNP surface, the 4-PDI molecule does not undergo the same desorption process as 4-NPI, in fact it is quite stable comparatively, like that of 4-NTP.

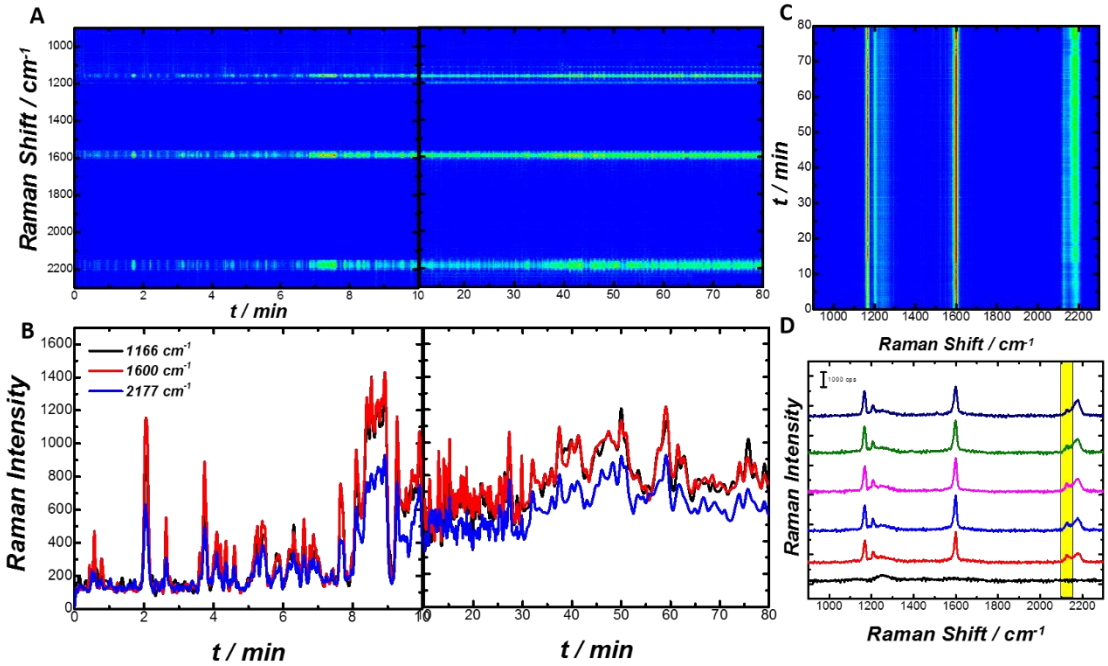

Figure 2. 14 Color coded plot for Adsorption of 5 µM PDIC including A) fluctuation followed by adsorption with time resolved Raman intensity trajectories for C) fluctuation and adsorption of PDIC onto Au SRNPs. Higher concentration, 50 µM PDIC adsorption represented by color coded plot (C), with SERS spectra associated with the time resolved adsorption depicted by (D).

More intriguing is the appearance of both 2133 and 2177 cm^{-1} peaks associated with υ(N≡C), two different binding modes on the surface of AU SRNPs. Calculated DFT spectra indicate atop conformation for N≡C at 2180 cm^{-1}, while free υ(N≡C) is up shifted to 2133, signifying the presence of bound and free 4-PDI on the surface of gold [31-34]. The SERS peak position at 2133 cm^{-1} and 2177 cm^{-1} during the initial binding phase of 4-PDI shows evidence that initial binding contains molecules of 4-PDI that are bound to the surface in an atop configuration with the free υ(N≡C) available to interact with the surrounding environment [16, 24, 25, 29, 31-34]. The intensity of the free υ(N≡C) conformation does not share the same intensity as the atop conformation as the adsorption process continues. One explanation for this is that the free N≡C slowly undergo an orientation change adopting another atop conformation as the other N≡C binds to the surface or due to site to site variation the 4-PDI molecules have greater interaction with other parts of the Au SRNP surface. Calculated 4-PDI interaction with gold surfaces provide evidence that the of a flat orientation for the 4-PDI molecules [32]. Although the two peaks, 2133 and 2177 cm^{-1} reveal a difference in conformation the surface, the peak overlap between the two is too great to accurate quantify the underlying details of associated with these binding modes, but there is enough quantitative evidence that the 4-PDI molecule experiences two different binding configurations at the surface.

Adsorption / Exchange of 4-NPI on Au@Pd

When contrasted to the Au@Pd core shell nanoparticles, the presence of 4-NPI on the surface is not only quite stable but the adsorption is almost quicker than our time resolving capabilities of the SERS measurements. In this instance we used Au@Pd core shell nanoparticles with 20% Pd composition, determined from EDS measurements, as

substrate as a control due to the more well understood nature between isocyanide molecules and palladium. We once again traced the trajectory of the adsorption for 50 µM 4-NPI

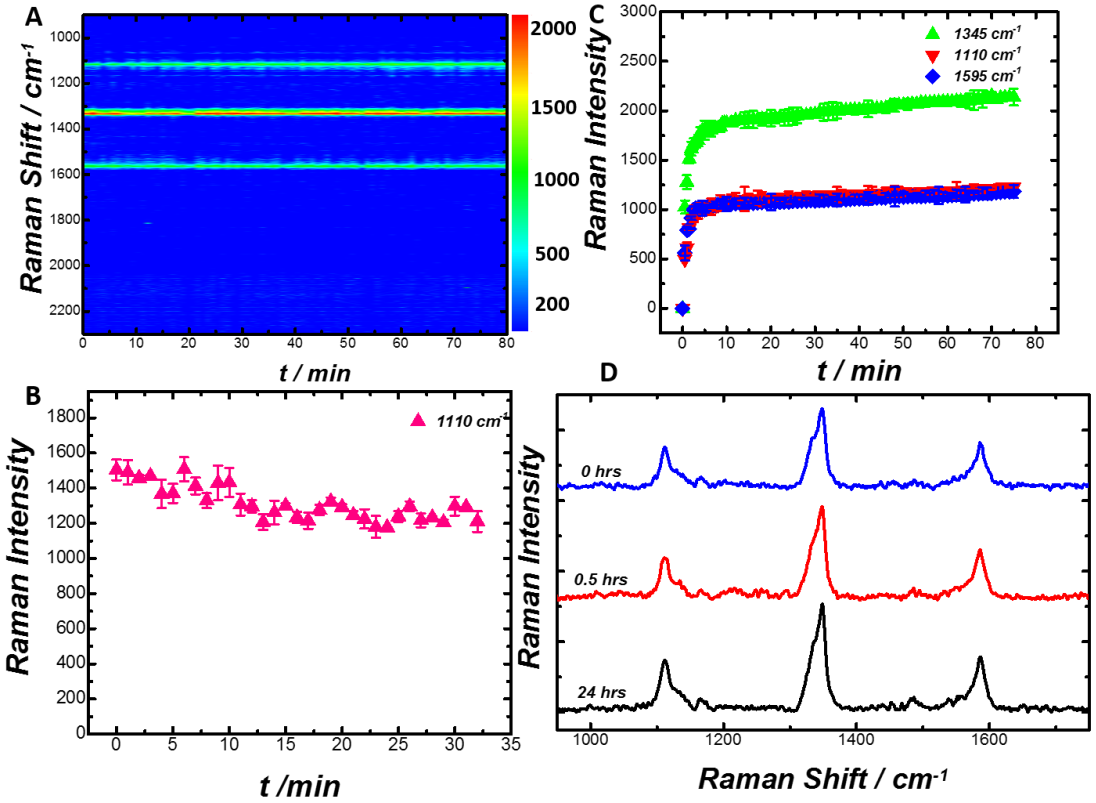

Figure 2. 15 Adsorption of 50 µM NPI represented by A) color coded plot with time resolved Raman intensity trajectories depicted in B) for the vibrational modes 1345 cm^{-1} (NO_2), 1110 cm^{-1} ad 1595 cm^{-1} (C-C), corresponding to adsorption of NPI onto Palladium surface, error bars are from standard deviation of 5 replicant runs. Exchange of 50 µM NPI with 50 µM NTP illustrated in C) color coded plot and D) representative SERS spectra for the exchange.

using the vibrational modes 1345 cm^{-1} υ(NO_2), 1110 cm^{-1} and 1595 cm^{-1} υ(C-C) to analyze the kinetics. Unfortunately, the peak associated with υ(N≡C) could not be resolved further limiting our investigation. The lack of peak evidence for the υ(N≡C) could reveal quite interesting orientation evidence regarding the interfacial interaction of the 4-NPI with the Au@Pd

SRNP from the electro-magnetic surface selections rules. For 4-NPI bound to palladium based on the computational models, the 4-NPI is adsorbed in the hollow regions of the Pd surface, possibly indicating coordination of the N≡C to three metal atoms on the surface, the shortened bond distance for the N≡C may change the orientation about the particle's surface, thereby impacting the selection rules for electromagnetic enhancement [25, 29, 36-39]. Experimental evidence demonstrates weak intensity and a great deal of band broadening

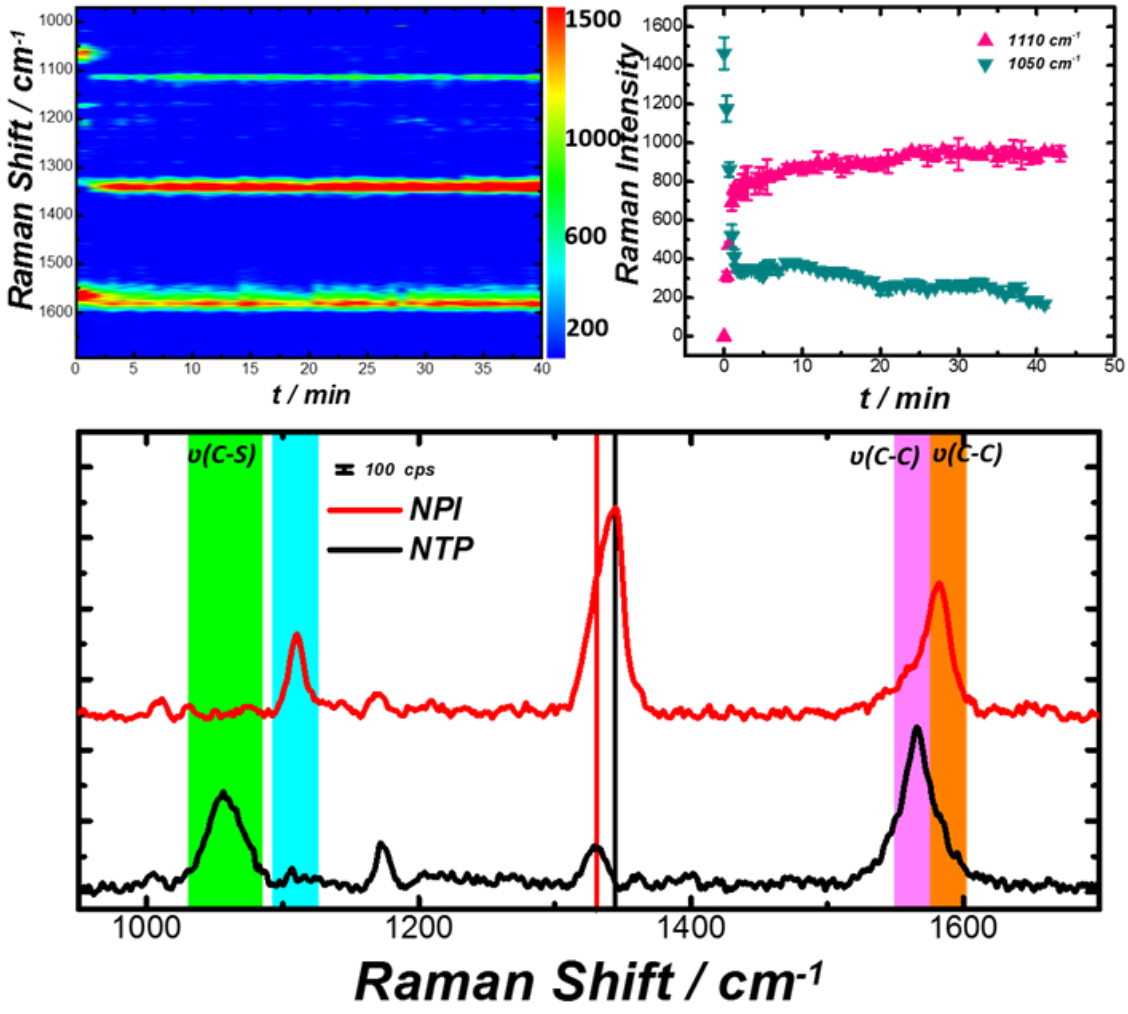

Figure 2. 16 Exchange illustrated for pNTP adsorbed onto Pd surface followed by introduction of NPI A) color coded plot B) time resolved Raman intensity trajectories for 1050 cm^{-1} (C-S) associated with pNTP and 1110 cm^{-1} associated with NPI, with error bars depicting the standard deviation of 5 replicant runs. After 24 hours, SERS spectra (C) depicting the final outcome of the exchange process between pNTP and NPI.

in the regions 1950, 2130and 2177 cm^{-1} for hollow, bridged and atop conformation respectively, this already weak intensity just may have been out of our ability to resolve properly.

This change in orientation may be enough to limit the SERS enhancement, especially when coupled with the already damped LSPR effect from the layer of Pd. The binding of 4-NPI is demonstrably more stable on the Pd surfaces than on Au. When the system of 4-NPI saturated Au@Pd SRNPs is incubated with thiol ligand, 4-NTP, the change in the spectral profile for 4-NPI changes nominally after 24 hrs, with little or no indication of adsorption or exchange of the 4-NPI with 4-NTP, as suggested by the total lack of 1080cm^{-1} υ(C-S) mode. On the contrary, when the Au@Pd SRNPs are saturated with 4-NTP and further exposed to the same concentration of isocyanide ligands, 50 µM of 4-NPI, the exchange is immediate. The rapid exchange is depicted in the color-coded plot in figure #, with the evolution of 1080 and 1110 cm^{-1} intensity trajectories shown in figure #B. Representative SERS spectra for initial and final exchange measurements are illustrated in figure #C, here the C-S vibrational mode from the bound 4-NTP is no longer visible, likely indicating the total exchange of 4-NTP from the Au@Pd SRNP surface. In comparison the stability of isocyanide molecules like 4-NPI is greater than on conventional Au SRNPs. This difference reveals information that the nature of the binding of the 4-NPI molecule to the surface dictates the interfacial surface chemistry in regard to adsorption, desorption and exchange.

2.4 Conclusion

The interaction of 4-NPI exhibits interesting adsorption phenomena, and poor stability for Au SRNPs. The fluctuation of both 4-NPI and 4-PDI suggest that the initial

adsorption phase is further complicated by overabundance of site to site variation and overall stability of the binding energies coupled with the varying surface potential. The binding of 4-NPI on Au SRNPs forms a vertical bond illustrated by the down shift of the υ(N≡C) mode from neat 4-NPI through the formation of atop configuration on single Au atoms. The large presence of undercoordinated Au atoms on the surface facilitate quick adsorption kinetics, while desorption kinetics are slow but still observable on a reasonable time scale. This structure makes it more susceptible to desorption and exchange by its thiol analog, 4-NTP, which is further verified by the stability of 4-NPI on the surface of smooth QSNPs. As for 4-PDI, we see the adsorption initiates in atop configuration with the free N≡C moiety interacting with Au SRNP surface in a manner that causes the 4-PDI to bind flatly to the surface. In comparison to binding onto palladium, we observe a shift in the binding mode further upshifting the υ(N≡C) mode from the 2130 cm^{-1} of neat 4-NPI to the 1950 cm^{-1} of binding at the hollow site. The binding to palladium shows more stabilized ligand outer shell, possibly due to the difference in electronic structure of palladium and the increased π-backdonation from metal to molecule. This investigation offers further insight to the interfacial dynamics of isocyanide molecules onto gold surfaces.

2.5 References

1. Talapin, D. V.; Lee, J. S.; Kovalenko, M. V.; Shevchenko, E. V. Chem. Rev. 2010, 110, 389– 458
2. Liao, H.G.; Zherebetskyy, D.; Xin, H. L.; Czarnik, C.; Ercius, P.; Elmlund, H.; Pan, M.; Wang, L.W.;Zheng, H. M. Science 2014

3. Murphy, C. J.; Thompson, L. B.; Alkilany, A. M.; Sisco, P. N.; Boulos, S. P.; Sivapalan, S. T.; Yang, J. A.;Chernak, D. J.; Huang, J. Y. J. Phys. Chem. Lett. 2010, 1, 2867– 2875
4. Villarreal, E.; Li, G. G.; Wang, H. Nanoscale 2018, 10, 18457.
5. Love, J. C.; Estroff, L. A.; Kriebel, J. K.; Nuzzo, R. G.; Whitesides, G. M. Chem. Rev. 2005, 105, 1103– 1169
6. Bain, C. D.; Troughton, E. B.; Tao, Y. T.; Evall, J.; Whitesides, G. M.; Nuzzo, R. G. J. Am. Chem. Soc. 1989,111, 321– 335
7. Dong, A. G.; Chen, J.; Vora, P. M.; Kikkawa, J. M.; Murray, C. B. Nature 2010, 466, 474– 477
8. Ulman, A. Chem. Rev. 1996, 96, 1533– 1554
9. Luedtke, W. D.; Landman, U. J. Phys. Chem. B 1998, 102, 6566– 6572
10. Guo, R.; Song, Y.; Wang, G. L.; Murray, R. W. J. Am. Chem. Soc. 2005, 127, 2752– 2757
11. Hostetler, M. J.; Templeton, A. C.; Murray, R. W. Langmuir 1999, 15, 3782– 3789
12. E. Villarreal, G. G. Li, Q. Zhang, X. Fu, and H. Wang, Nano Letters 2017, 17 (7), 4443–4452.
13. Schlenoff, J. B.; Li, M.; Ly, H. J. Am. Chem. Soc. 1995, 117, 12528– 12536
14. Cheng, H.; Yang, L. N.; Jiang, Y.; Huang, Y. Y.; Sun, Z. H.; Zhang, J.; Hu, T. D.; Pan, Z. Y.; Pan, G. Q.;Yao, T.; Bian, Q.; Wei, S. Q. Nanoscale 2013, 5, 11795– 11800
15. Hickman, J. J.; Laibinis, P. E.; Auerbach, D. I.; Zou, C.; Gardner, T. J.; Whitesides G. M.; Wrighton, M. S.Langmuir 1992, 8, 357

16. Robertson, M. J.; Angelici, R. J. Langmuir 1994, 10, 1488

17. Ontko, A. C.; Angelici, R. J. Langmuir 1998, 14, 1684

18. Lin, S.; McCarley, R. L. Langmuir 1999, 15, 151

19. Han, H. S.; Han, S. W.; Joo, S. W.; Kim, K. Langmuir 1999, 15, 6868

20. Huc, V.; Bourgoin, J.-P.; Bureau, C.; Valin, F.; Zalczer, G.; Palacin, S. J. Phys. Chem. B 1999, 103, 10489

21. Ansell, M. A.; Cogan, E. B.; Page, C. J. Langmuir 2000, 16, 1172

22. Henderson, J. I.; Feng, S.; Bein, T.; Kubiak, C. P. Langmuir 2000, 16, 6183.

23. Horswell, S. L.; O'Neil, I. A.; Schiffirin, D. J. J. Phys. Chem. B 2001, 105, 941

24. Shin, D.; Kim, K.; Shin, K. S. ChemPhysChem 2010, 11, 83– 86

25. Sung Jin Bae,†, Chung-ro Lee,⊥, Insung S. Choi,‡, Cheong-Soo Hwang,§, Myoung-seon Gong,⊥, Kwan Kim,∥ and, and Sang-Woo Joo*, The Journal of Physical Chemistry B 2002 106 (28), 7076-7080

26. Feng Wang, Chuanhao Li, Ling-Dong Sun, Haoshuai Wu, Tian Ming, Jianfang Wang, Jimmy C. Yu, and Chun-Hua Yan Journal of the American Chemical Society 2011 133 (4), 1106-1111

27. Kim, K.; Shin, D.; Kim, K. L.; Shin, K. S. Physical Chemistry Chemical Physics 2010, 12, 3747.

28. Kwan Kim, Ji Won Lee, Dongha Shin, Kyung Lock Kim, and Kuan Soo Shin,The Journal of Physical Chemistry C 2010 114 (21), 9917-9922

29. Robert J. Angelici and Mihaela Lazar Inorganic Chemistry 2008 47 (20), 9155-9165

30. Scott M. Gruenbaum,Matthew H. Henney,Sachin Kumar, and, and Shouzhong Zou The Journal of Physical Chemistry B 2006 110 (10), 4782-4792

31. Joo, S.-W.; Kim, Y.-S. Colloids and Surfaces A: Physicochemical and Engineering Aspects 2004, 234, 117.

32. Michael Garvey, John Kestell, Rasha Abuflaha, Dennis W. Bennett, Graeme Henkelman, and Wilfred T. Tysoe The Journal of Physical Chemistry C 2014 118 (36), 20899-20907

33. Allyn C. Ontko and and Robert J. Angelici Langmuir 1998 14 (11), 3071-3078

34. Scott M. Gruenbaum,Matthew H. Henney,Sachin Kumar, and, and Shouzhong Zou The Journal of Physical Chemistry B 2006 110 (10), 4782-4792

35. Creighton, J. A. Surface Science 1983, 124, 209.

36. Seong Ho Cho, Hyouk Soo Han, Du-Jeon Jang, Kwan Kim, and Myung Soo Kim The Journal of Physical Chemistry 1995 99 (26), 10594-10599

37. Nichols, H.; Hexter, R. M. The Journal of Chemical Physics 1981, 75, 3126.

38. Moskovits, M. Reviews of Modern Physics 1985, 57, 783.

Chapter 3
Grafting diazonium ligands to gold nanoparticle surfaces: Insights from plasmon enhanced spectroscopic measurements

3.1 Abstract

The interfacial dynamics of diazonium salts with nanoscale surface roughened Au-substrates represents a unique platform to study the adsorption, exchange and hydrogenation associated with adsorbed 4-diazoniumnitrobenzene tetrafluoroborate (4-DNB). Here plasmon enhanced Raman scattering was used as an ultrasensitive spectroscopic tool combining time-resolved and molecular fingerprinting capabilities to probe the interfacial dynamic interactions of diazonium salt adsorption onto surface roughened gold nanoparticles. The adsorption of diazonium salts onto textured Au-nanoparticles will facilitate the delineation of interfacial processes such as: binding affinity, stability and reactivity. In this way, the underlying mechanistic understanding of interaction between diazonium salts and the surface can be further elucidated at both equilibrium and non-equilibrium states, providing the framework for critical design principles towards robust and precise control over nanoparticle interfaces and surface chemistry.

3.2 Introduction

The surface composition of chemically synthesized inorganic nanoparticles plays a crucial role in guiding the nanocrystal boundaries dictating the surface chemistry and physical properties from specific geometries[1-3]. These functionalized surfaces derived from nanoparticle synthesis; either through direct ligand-guided nanocrystal growth or by post synthetic methods, impart a unique and dynamic ligand-nanoparticle interactive interfacial relationship modifying such properties as optical[4] and electronic properties triggering various interfacial processes of charge transfer[5], catalytic molecular transformations[6], 2-D and 3-D nanoscale assemblies[7-10], photoreactions[11-13], biosensing[14] and targeted drug

delivery[15-16]. Design principles for precise control over physical properties through ligand-nanoparticle dynamics and interfacial interactions depends on understanding the underlying, fundamental mechanisms associated with the interactive ligand-nanoparticle The interaction and dynamics between gold - thiol ligands, forming two dimensional monolayers onto 3-dimensional metallic nanoparticles have generated a tremendous amount of attention, being a focal point of nanoscience and thus a center for extensive research[17] as the most prevalent form of organic modification to metal surfaces, but more importantly, the understanding of interfacial and dynamic interactions of different ligand-nanoparticle interfaces must be elaborated for creating complete understanding towards design principles for optimization of ligand-nanoparticle structures.

The self-assembled monolayers (SAMs) of organothiols chemisorption has been the conventional and primary method of ligand modification to gold nanoparticles, and therefore the fundamental principles guiding the physical properties of these thiolated nanoparticles is the most studied[18-20]. However, recent reports and evidence suggest the grafting of diazonium ions, which has gained further interest as a means of surface functionalization through electrochemical grafting, originally to various carbon substrates including: glassy carbon electrodes[21-24], nanotubes[25], graphene[26], semi-conductor[27-29], industrial, coinage and noble metal surfaces[30], with gold gaining an increase of attention[31-33]. Spontaneous reduction of diazonium salts has presented another practical method of imparting a greater variety of ligands and properties to gold nanoparticles[34-37]. Previous reports emphasize this gold-aryl grafting is the consequence of a gold-carbon covalent interaction formed through a spontaneous mechanism after diazonium salts are reduced at the surface of a conductor generating a radical aryl that then bonds to the surface of the

substrate[38]. Although still under investigation and debate, the surface modification through diazonium grafting offers greater potential to probe and understand the nature of the Au-C bond that must lead to differing structural and electronic properties from the Au-S bond at the interface[39].

This investigation will provide new insight into such issues as thermodynamic stability, adsorption kinetics and catalytic reduction activity. Surface modification of Au nanoparticles through aryl grafting are intriguing for their bearing of wide range of functional groups[40] and due to the nature of what has been reported as multilayer structure [24, 29, 35, 37, 40-43], which is in stark contrast with the self-assembled monolayers capable of highly organized domains based on the energetics and interactions between adjacent thiol

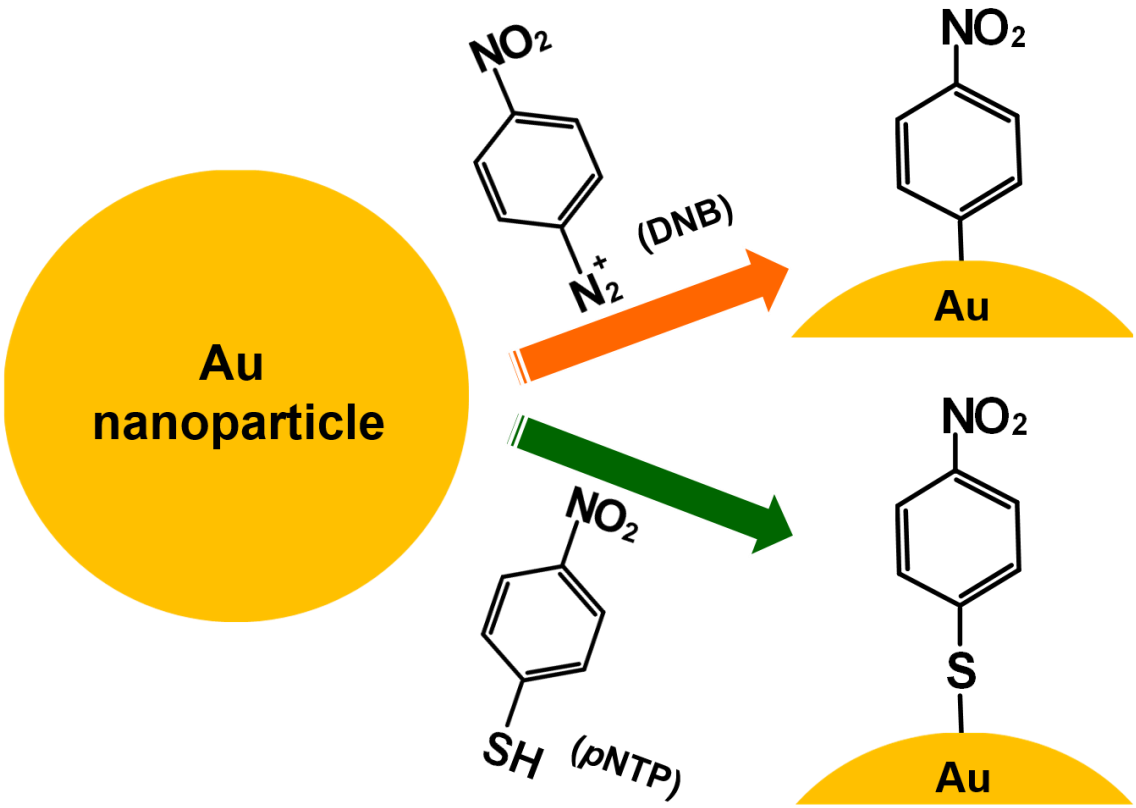

Schematic 3. 1 Cartoon representation of surface adsorption after Au nanoparticles are exposed to 4-DNB (top) and 4-NTP (bottom). Mechanism depicts the formation of Au-C bond in the case of 4-DNB adsorption and Au-S bond for adsorption of 4-NTP to the surface of gold.

ligands[38]. Also, reports have maintained that the covalent nature of the aryl grafting (Au-C) offers a strong bond interaction showing a high stability that in some cases is resistance to displacement or desorption[44, 45], and because of this interaction has been used for stabilizing of nanoparticles during synthesis and post-synthetic exchange[32]. These reports have found that the nature of this diazonium derived aryl film interaction with the substrate is very stable and not as susceptible to harsh conditions like their thiolated counter part[40]. Aryl grafting represents an alternative method of surface modification of metallic nanoparticles and a potential new avenue to understand the underlying interfacial nanoparticle-ligand interaction. The fundamental characteristics of the gold-diazonium bond offers a different pathway for mechanistic understanding than previously reported gold thiol interaction due to the nature of what has been reported as a gold-carbon (Au-C) covalent anchor to the substrate as depicted in schematic 3.1. The actual nature of spontaneous grafting of diazonium salts to gold surfaces has been greatly debated but previous reports demonstrated both theoretically and experimentally of this phenomenon onto gold substrates, such as, nanospheres and nanorods[40, 46].

3.3 Experimental:

Au Seed Synthesis:

Au seeds were prepared by the reduction of $HAuCl_4$ with $NaBH_4$ in a solution of (1-hexadecyl) trimethyl ammonium chloride (CTAC, Alfa Aeser 96%). To a solution of CTAC (10 mL, 0.1M), $HAuCl_4$ (0.25 mL, 10 mM) is added under stirring conditions. Ice cold, freshly prepared $NaBH_4$ (0.3 mL, 10 mM) is then added to the solution containing CTAC and $HAuCl_4$ and stirring is continued for 1 minute and then left undisturbed for 2 hours. Seed is diluted 1000-fold with CTAC (0.1 M) and diluted portion was used for seed mediate growth.

Au Surface Roughened Nanoparticles (SRNPs) Synthesis:

Au seeds were used in a seed mediated growth process to synthesize Au SRNPs. A growth solution containing CTAC (30 mL, 0.1 M) with sequential addition of $HAuCl_4$ (1.5 mL, 10 mM) followed by addition of ascorbic acid (AA, 0.6 mL, 0.1 M). The solution was then left undisturbed for 4 hrs. Particles settled to the bottom and supernatant was removed without disturbing the particles at the bottom. Particles were then resuspended in H_2O (6 mL, 18.2 MΩ resistivity, Barnstead EasyPure II 7138).

Au SRNPs Thermodynamic measurements:

4-DNB (4- Diazonium-Nitrobenzene tetrafluorborate)

For thermodynamic measurements of 4-DNB adsorption, Au SRNPs (100 µL, 0.625 nM) were aliquoted into Eppendorf tubes, washed and suspended in H_2O (200 µL, ultra 18.2 MΩ). Concentrated solutions of 4-DNB (4 µL) were diluted in 196 µL of H_2O to various final concentrations (0, 0.5, 1.0, 2.5, 5.0,10, 15, 25, 50, 100, 150, 200, 250, 300, 350, 400, 450, 500, 750, 1000 µM). The final 100 µL was then incubated for 96 hours for SERS measurements. SERS spectra were obtained on a Bayspec Nomadic confocal Raman microscope built on an Olympus BX51 reflected optical system with a 785 nm continuous wave excitation laser. Excitation laser was focused on solution with a 10X objective [Numerical Aperture (NA) = 0.30, working distance (WD) = 11.0 mm, Olympus MPLFLN]. Laser power was measured to be 10 mW at samples and integration time was 40 seconds. Normalization of thermodynamic data was obtained by dividing SERS intensity of all concentrations reported by the thermodynamic intensity for 100 µM (not reported).

4-NTP (4-Nitrothiophenol)

Thermodynamic measurements of 4-DNB adsorption onto Au SRNPs were performed in similar manner to the 4-DNB. Au SRNPs (100 µL, 0.625 nM) were aliquoted into Eppendorf tubes allowed to settle overnight and washed with H_2O (200 µL, ultrapure 18.2 MΩ) and suspended in 196 µL of ultrapure H_2O. A solution (4 µL) of various concentrations of 4-NTP was added to the 150 µL Au SRNPs to yield final concentrations (0, 0.5, 1.0, 1.5, 2.0, 2.5, 3.5, 5.0, 7.5, 10, 12.5, 15, 17.5, 20, 25, 35, 40, 45, 50, 60 µM). The final 100 µL solution was incubated for 24 and SERS spectra were obtained on the same Bayspec Nomadic confocal Raman microscope under same objective and 785 nm laser. Samples were illuminated with10 mW laser power for 10 seconds.

Monitoring Real Time Kinetics for 4-DNB and pNTP adsorption onto Au NPs:

Au SRNPs

4-DNB:

SERS monitoring of 4-DNB adsorption onto Au SRNPs was conducted by introducing 4 µL of 50 mM 4-DNB into 196 µL of Au SRNPs for a final concentration of 1000 µM 4-DNB. Immediately after introduction SERS spectra were obtained ever minute for the first 15 minutes followed by intervals of 2 minutes for 4 hours, 5 minutes for 3 hours and 10 minutes for 2 hours and 60 min for 29 hours, over the course of 36 hours. Full coverage adsorption was determined when the SERS intensity in kinetics measurements no longer increased and double confirmed with SERS spectra after 48, 72 and 96-hour incubation.

pNTP:

SERS monitoring of 4-NTP adsorption onto Au SRNPs was conducted in a similar manner by introducing 4 µL of 2.5 mM 4-NTP into 196 µL of Au SRNPs for a final concentration of 50 µM 4-NTP. Immediately after introduction SERS spectra were obtained after the first 30 seconds followed by intervals of 1 minute for 10 minutes, 5 minutes for 1 hour and 10 minutes for 1 hour. Full coverage adsorption was determined when the SERS intensity in kinetics measurements no longer increased and double confirmed with SERS spectra after 72-hour incubation

Time Resolved Ligand Exchange Measurements for 4-DNB Saturated Au SRNPs:

Au SRNPs

The ligand exchange interaction between 4-DNB coated Au SRNPs and introduction of free pMBN was monitored by SERS. Au SRNPs (200 µL, 1.25 nM) were washed 1X, suspended in ultrapure H_2O (196 µL, 18.2 MΩ) and then incubated in excess 4-DNB (4 µL, 50 mM) for 96 hours. Particles were then washed 1X and suspended in ultrapure H_2O (196 µL, 18.2 MΩ). Initial spectra were recorded and excess pMBN (4 µL, 5.0 mM) was introduced monitoring the increase in 2226 cm^{-1} corresponding to the υ(C≡N) vibrational stretch, exchange was completed when no increase in SERS intensity was observable. Measurement were recorded every 10 seconds for the first 3 minutes and then every 30 seconds for the following 2 minutes then every minute under 10 mW laser power and 10 second integration time. The ligand exchange experiment was conducted in triplicate to obtain error bars and standard deviation.

Thermodynamic Measurements of Ligand Exchange on Saturated 4-DNB Au NPs:

Au SRNPs

Adsorption of pMBN onto Au SRNPs saturated with 4-DNB was conducted by preparing fresh Au SRNPs (200 µL, 1.25 nM), washing 1X, suspending particles in ultraopure H_2O (196 µL, 18.2 MΩ) and then incubated for 96 hours in 4-DNB (4 µL, 50 mM). After incubation supernatant was removed after particles settled and suspended in ultrapure H_2O (196 µL, 18.2 MΩ) then exposed to various concentrations of pMBN (final concentrations: 0,10, 20, 25, 35, 50, 100, 150, 200 µM). SERS measurements were obtained with a laser power of 10 mW and at 10 second integration periods after a period of 24 and 48 hours to ensure thermodynamic equilibrium.

Monitoring Desorption Kinetics Measurements:

Au SRNPs / QSNPs

To monitor the desorption kinetics, 4-DNB (4 µL, 50 mM) was added to after Au SRNPs (200 µL, 1.25 nM) were washed 1X and suspended in ultrapure H_2O (196 µL, 18.2 MΩ) then incubated for 96 hours to ensure saturated coverage. After incubation supernatant was discarded and particles were suspended in ultrapure H_2O (190 µL, 18.2 MΩ). SERS spectra were obtained to confirm monolayer coverage before desorption reaction was initiated. After initial measurement, NH_3BH_3 (10 µL, 2 mM) was added and SERS spectra were obtained continuously every 10 seconds until SERs peak corresponding to 1340 cm^{-1} ($\upsilon(NO_2)$) was no longer visible. The procedure was repeated for Au SRNPs with increased NH_3BH_3 (10 µL, 200 mM) and with identical concentrations of NH_3BH_3 for Au SRNPs coated with 4-NTP.

Au QSNPs

For monitoring adsorption of 4-MBN on Au QSNPs (200 µL, 1.25 nM), particles were washed 1X, suspending particles in ultrapure H_2O (196 µL, 18 MΩ) and then exposed

to excess 4-MBN (4 µL, 2.5 mM). SERS measurements were obtained with a laser power of 10 mW and at 50 second integration periods with 2 minute intervals between measurements until no increase in SERS intensity was observed.

Au QSNPs

SERS monitoring of 4-ATP adsorption onto Au QSNPs was performed in a similar manner as with 4-ATP adsorption onto Au SRNPs. A sample of Au QSNPs (196 µL, 5.25 nM) was immediately monitored after introduction of 4 µL of 4-ATP (2.5 mM) at intervals of every 1 minute for 4 minutes, 2 minutes for 18 minutes, 5 minutes for 300 minutes and 10 minutes for 270 minutes. Completion of 4-ATP adsorption was determined by no increase in SERS intensity as well as obtaining confirmation of no SERS intensity increase after 24 hours from initial measurement.

Au QSNPs:

Ligand exchange measurements for Au QSNPs were conducted in similar fashion to that of Au SRNPs. Au QSNPs (200 µL, 5.25 nM) were washed 1X and dispersed in ultrapure H_2O (196 µL, 18.2 MΩ) then incubated for 24 hours in excess 4-DNB (4 µL, 2.5 mM). After incubation particles were washed 1X to remove unbound 4- ATP and dispersed again in ultrapure H_2O (196 µL, 18.2 MΩ). SERS spectra for 4-DNB covered molecules was initially recorded and then excess pMBN (4 µL, 5.0 mM). Thermodynamic measurements were taken under 10 mW laser power and with an integration time of 50 seconds, monitoring the 2226 cm^{-1} area for indication of 4-MBN binding.

Au QSNPs

For monitoring adsorption of 4-MBN on Au QSNPs that are partially saturated with 4-ATP, fresh Au QSNPs (200 µL, 1.25 nM) were washed 1X, suspending particles in ultrapure H_2O (196 µL, 18 MΩ) and then incubated for 24 hours in 4-ATP (4 µL, 125 µM). After incubation supernatant was removed after particles settled and suspended in ultrapure H_2O (196 µL, 18 MΩ) then exposed to excess 4-MBN (4 µL, 2.5 mM). SERS measurements were obtained with a laser power of 10 mW and at 50 second integration periods with 2-minute intervals between measurements until no increase in SERS intensity was observed.

Characterization:

The structures of the nanoparticles were characterized by SEM using a Zeiss Ultraplus thermal field emission scanning electron microscope. The samples for SEM measurements were dispersed in water and drop-dried on silicon wafers. The optical extinction spectra of the nanoparticles were measured on aqueous colloidal suspensions at room temperature, using a Beckman Coulter Du 640 spectrophotometer. ζ–potentials of colloidal NPs were measured at room temperature using ZETASIZER nanoseries (Nano-ZS, Malvern). The samples for ζ–potential measurements were all freshly prepared, centrifuged, and dispersed in ultrapure H_2O. The concentration of the colloids for ζ–potential measurements were kept at 1.25 nM for all the samples and pH of the colloidal suspensions was 7.4.

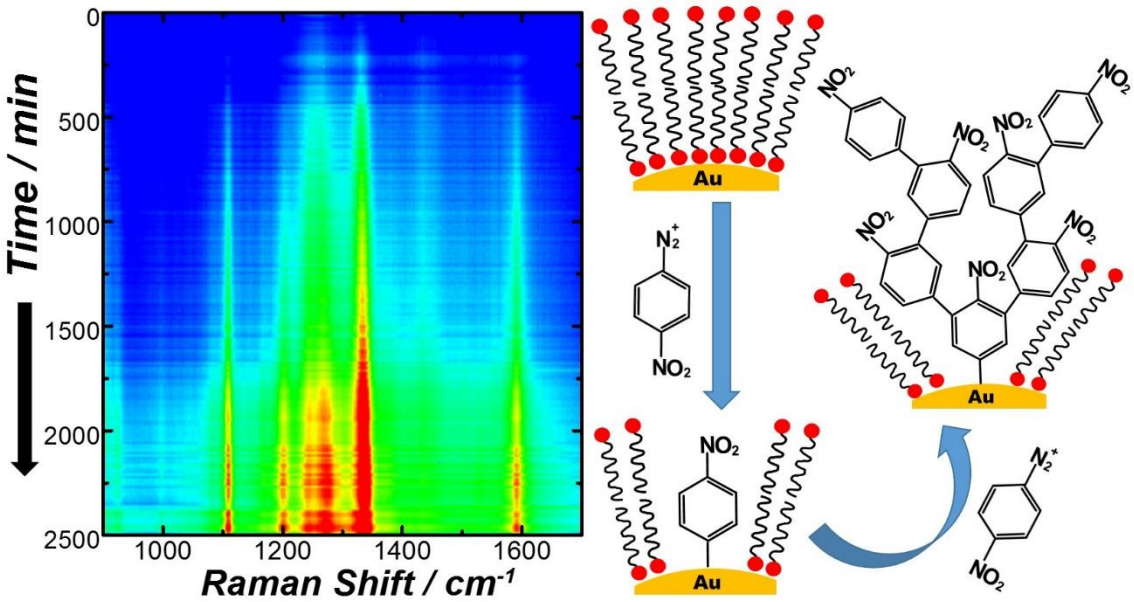

Schematic 3. 2 Left) - Color coded plot representing time evolution of 4-DNB adsorption onto highly curved Au SRNPs. (Right) – Schematic of illustration of Au – carbon bond after adsorption of diazonium and generation of multilayer complex as diazonium radicals interact with themselves creating branched structures on surface of gold.

3.4 Results and Discussion

Here we use SERS active highly curved, gold surface roughened nanoparticles (Au-SRNPS) capped with CTAC for both its plasmonic activity[47, 48], as well as, a platform to study the intrinsic role of aryl ligand grafting onto gold substrates. TEM images illustrate the highly curved nature of these nanoparticles, with an average size of 122 nm, figure 3-1. The experimental SERS spectra collected and shown in figure 3-2, provides the evidence associated with the Au-C bond[40] from grafting of 4-diazonium nitrobenzene (4-DNB), vibrational peak at 412 cm^{-1}, which is in line with previous SERS measurements reported by Mcdermott et. al, however the nature of the Au-C bond is still not fully understood.

Although, the grafting of diazonium onto gold nanoparticles is still relatively new, studies have shown evidence that the interaction of diazonium salts propagate multilayer formations, or thin polymer structures onto surfaces, as depicted from TEM images in figure 3-3A, which reveals a thin organic film covering the Au-SRNPs, while figure 3-3B shows no indication of multilayer formation from adsorption of 4-NTP, as thiolated molecules are particularly known for self-assembled monolayer (SAMs) formation onto gold surfaces[17, 49, 50]. Further investigation through hydrodynamic diameter measurements suggest an overall size increase, by almost 5X, of the Au-SRNPs after exposure to excess, 1 mM 4-DNB supporting the multilayer formation interpretation, while zeta potential measurements (inset figure 3-3C) show the negative potential increases for 4-DNB coated particles owing to the increased nitro groups present in the dendritic multilayer structure.

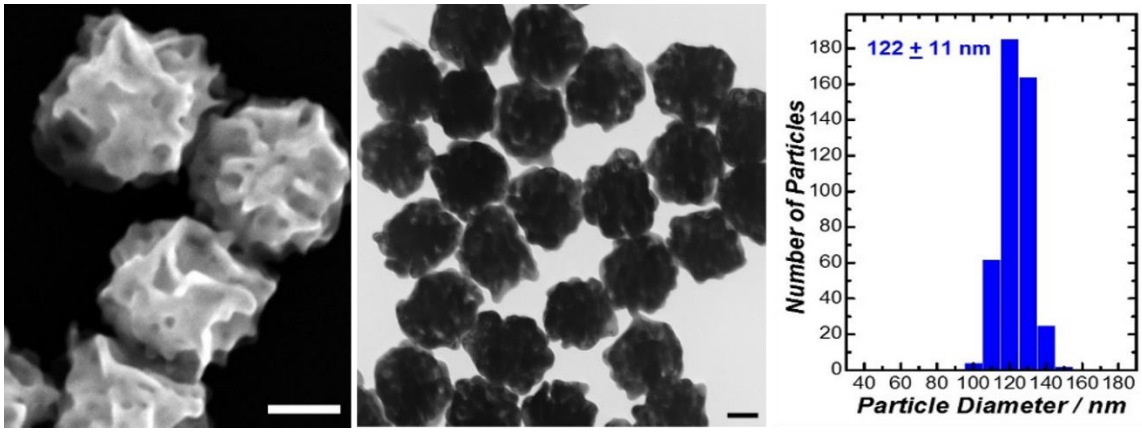

Figure 3. 1 SEM images (A) and TEM images (B) of Au SRNPs with histogram (C) illustrating average particle size distribution.

Moreover, UV Vis measurements illustrated in figure 3-3D show a shift in the extinction/plasmon after multilayer formation, with greater detail in plasmonic shift of 30 nm for 4-DNB coated Au-SRNPS detailed in figure 3-4A as the concentration of 4-DNB

increases from 1-800 µM, while the presence of peaks υ 1248 and 1278 cm^{-1} associated with multilayer formation[40], 3-4B of supporting information from SERS measurements, which is starkly different from the UV Vis data of monolayer formation of 4-NTP, which shows very little shift in plasmon with increasing concentration of 4-NTP. This plasmonic shift and the appearance of new SERS peaks is indicative of a change in the overall size by increased 4-DNB shell thickness.

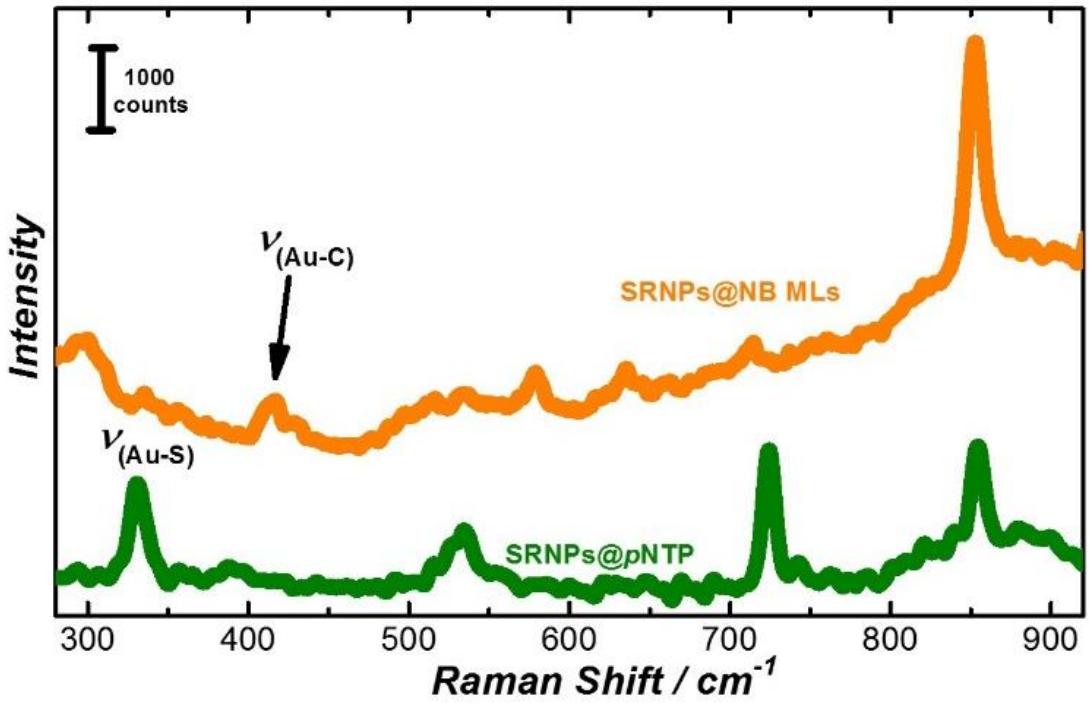

Figure 3. 2 Representative SERs spectra showing comparison between peaks associated with Au-C and Au-S bond from 4-DNB and pNTP respectively.

Comparison of thermodynamic equilibrium SERS measurements of CTAC, 4-NTP and 4-DNB coated Au-SRNPS, figure 3-3E shows 4-DNB multilayer shell structure, presenting evidence of the organic ligand shell from the appearance of peaks at 1210 cm^{-1}, 1248 cm^{-1} and 1278 cm^{-1}, which are not present in the SERS spectra of 4-NTP coated Au-SRNPs or CTAC coated Au-SRNPS. The presence of these new peaks is telling of a

difference in the surface structure, but more importantly, there is evidence of a dendritic like propagation forming mushroom or umbrella conformations with high concentrations of 4-DNB because of the presence of CTAC peaks still observable showing that not all CTAC is displaced from the Au surface like its thiol counterpart 4-NTP. The presence of broad peak at $\upsilon_{C\text{-}H}$ 2850 cm^{-1} is illustrated in figure 3-3F, indicating residual CTAC on Au-SRNPS coated with 4-DNB. Like other studies that observe residual ligands after exchange with diazonium salts[46], this information coupled with the multilayer propagation evidence suggest an adsorption that is not uniform over the entirety of the nanoparticle surface but propagation of multilayer structure through nucleation at specific sites. To better understand the adsorption of 4-DNB and this multilayer structure, concentration dependent

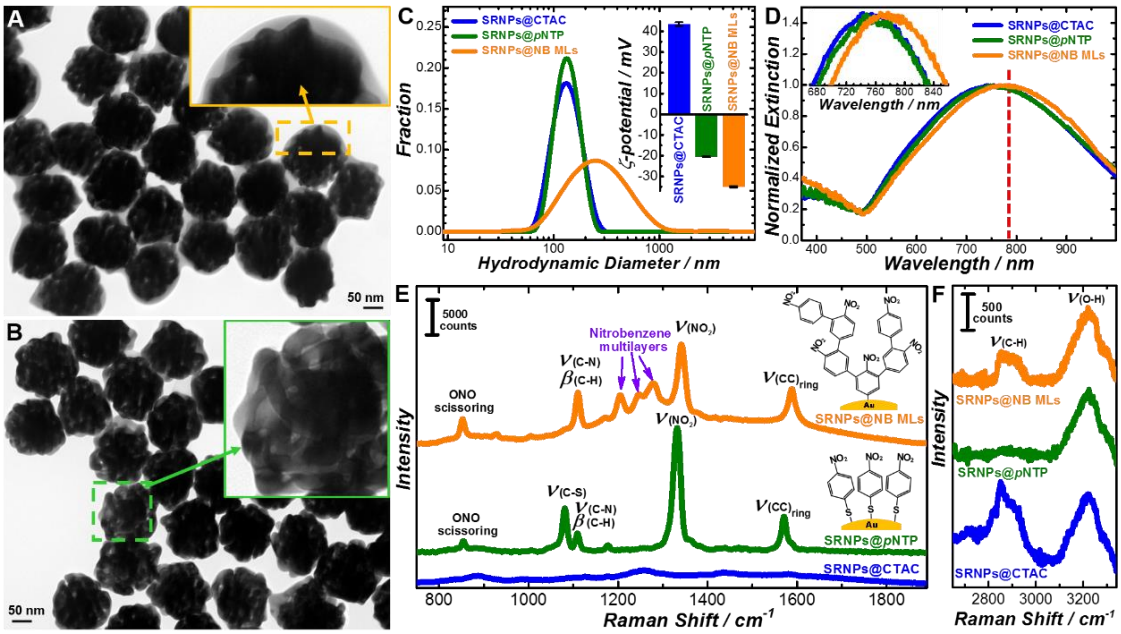

Figure 3. 3 TEM images depicting Au SRNPs after exposure to excess A) 4-DNB (1000 µM) and B) 4-NTP (100 µM). Hydrodynamic diameter depicted (C) and Extinction (D) for Au SRNPs coated with ligands: CTAC, 4-DNB and 4-NTP. Inset of (C) shows obtained ζ-potential measurements for the Au SRNPs coated with the 3 different ligands. Representative spectra are detailed in (E) for Au SRNPs coated with excess 4-DNB (1000 µM) , 4-NTP (100 µM) and CTAC (0.1 M) with (F) detailing close up of peaks corresponding to CTAC (C-H bond).

thermodynamic measurements were taken at 24, 48, and 96 hour intervals under 785 nm excitation laser, showing concentration threshold dependence for multilayer formation starting at about 25 µM, Figure 3-4B, and indicated by appearance of new peaks at frequencies υ 1210 and 1278 cm^{-1}, also denoted by the decrease in $\upsilon_{C\text{-}H}$ 2850 cm^{-1} associated with displaced CTAC by 4-DNB, which are depicted by representative spectrum in figures 3-5A and 3-5B, respectively. Due to the complexity of the binding interaction of 4-DNB with Au-SRNPs, curve fitting of desorption measurements for CTAC from the surface was performed to understand the characteristic adsorption model of the initial binding events, figure 3-5.

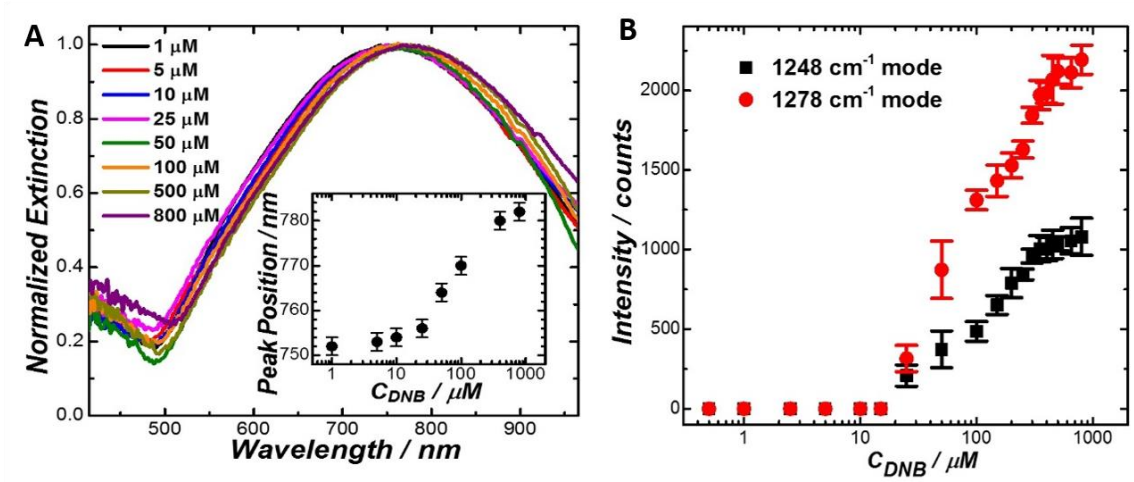

Figure 3. 4 Extinction spectra of Au SRNPs exposed to various concentrations of 4-DNB (A) with inset depicting plot of peak position shift as a function of 4-DNB concentration. Multilayer propagation is illustrated (B) by plotting peak intensity associated with υ_{ML} 1248 cm^{-1} and υ_{ML} 1278 cm^{-1} as a function of 4-DNB concentration.

Tracing the adsorption of 4-DNB was done indirectly, by monitoring the displacement of CTAC and plotting $1\text{-}\theta_{eq,\ CTAC}$, where $\theta_{eq,\ CTAC}$ represents the relative coverage of CTAC at equilibrium from as synthesized Au SRNPs. We see that the

adsorption of 4-DNB begins displacing CTAC immediately generating sites of nitrobenzene (NB) on the surface in a monolayer formation. Curve fitting of the disappearance of CTAC should follow conventional Langmuir model, where $\theta_{eq,\ NB\ monolayer}$ is calculated by subtracting the apparent coverage of CTAC ($\theta_{eq,\ CTAC}$) from apparent monolayer coverage, 1. The q_{max} is the maximum apparent coverage, K is the equilibrium constant and C_{DNB} is the concentration of DNB, detailed by the following equation:

$$\theta_{eq,NB\ monolayer} = 1 - \frac{I_{2850cm^{-1}}}{I_{0,2850cm^{-1}}} = 1 - \theta_{eq,CTAC} = q_{\max} \times \frac{K \times C_{DNB}}{1 + K \times C_{DNB}}$$

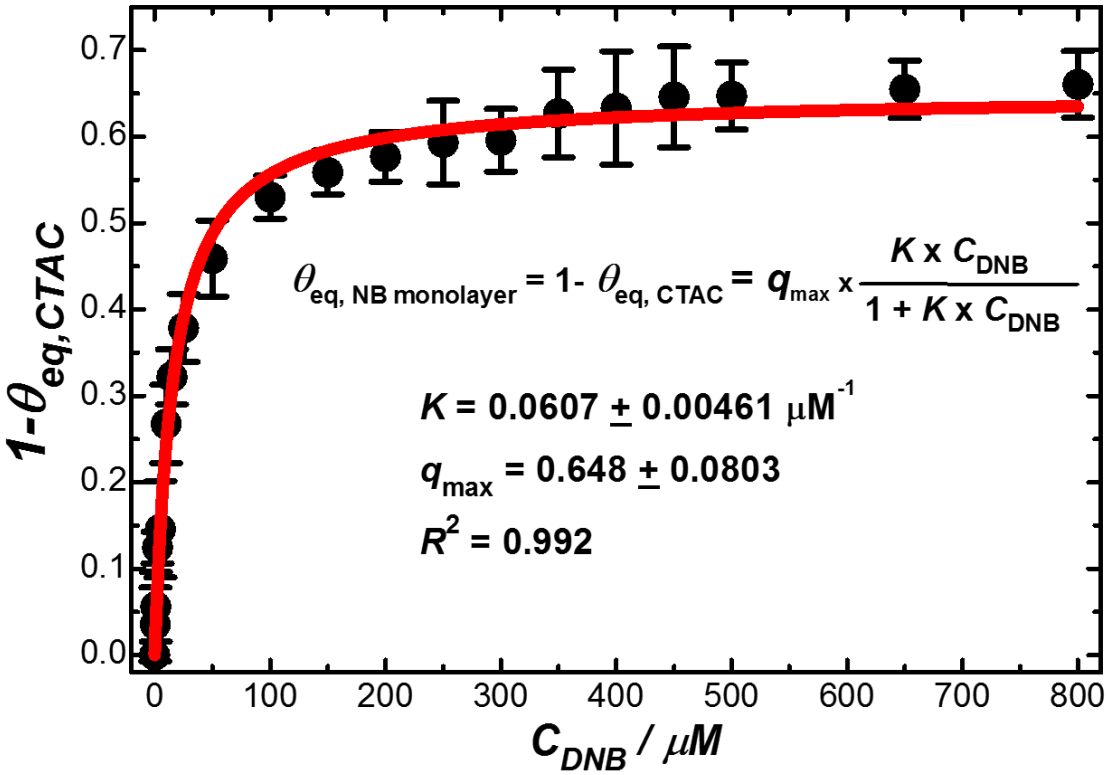

Figure 3. 5 Least squares fitting of 1-θ_{CTAC} , monolayer adsorption of 4-DNB onto Au SRNPs, where θ represents the intensity of the υ_{CTAC} 2850 cm^{-1} , normalized to the thermodynamic point, as a function of 4-DNB concentration.

However, the adsorption becomes more complicated and begins to deviate from conventional adsorption. When the surfaces of Au-SRNPS were fully coated with 4-DNB, thermodynamic measurements show the grafting of 4-DNB molecules onto the surface does not fully displace the adsorbed CTAC molecules and as the concentration of 4-DNB increases, adsorption of the 4-DNB onto the surface does not cause any significant decrease to the CTAC peak, but the SERS signal for υ_{NO2} 1340 cm^{-1} associated with 4-DNB

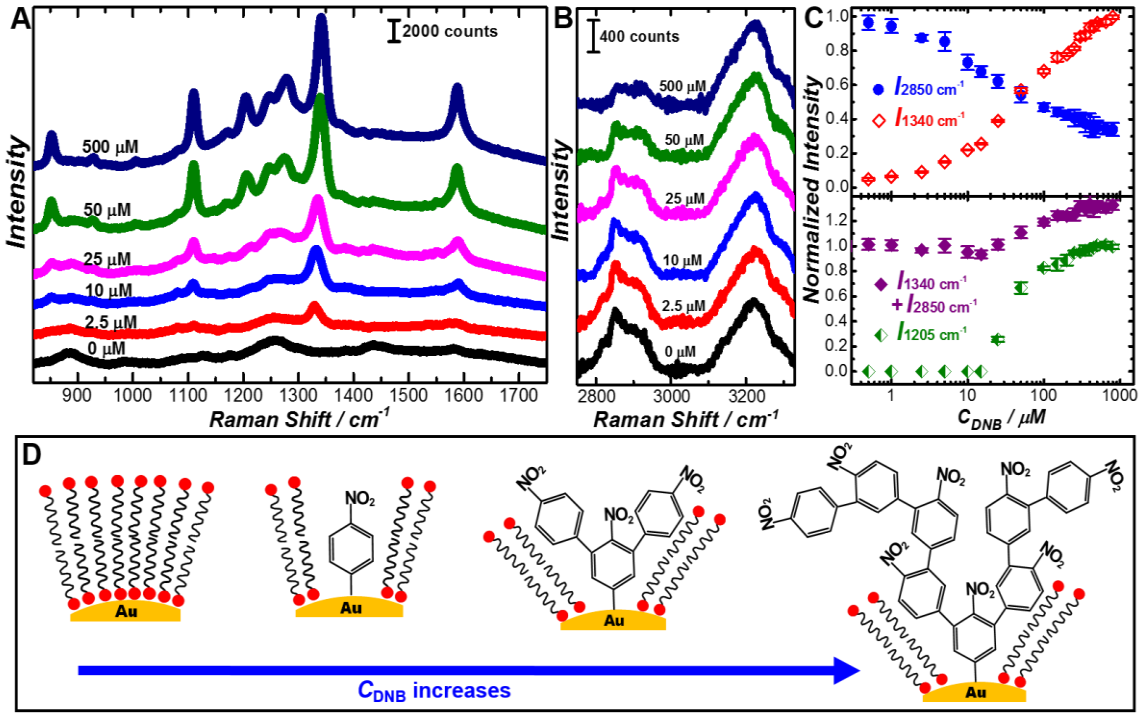

Figure 3. 6 Representative SERs spectra of (A) various concentrations (0, 2.5, 10, 25, 50, 500 µM) of 4-DNB and (B) close-up of peaks associated with CTAC (υ 2850 cm^{-1}) and H_2O (υ 3250 cm^{-1}). Plotted ratio of intensities (C) for CTAC (υ 2850 cm^{-1}) and NO_2 (υ 1340 cm^{-1}) as a function of concentration (TOP) and plotted ratio of sum for NO_2 (υ 1340 cm^{-1}) and CTAC (υ 2850 cm^{-1}) along with peak (υ 1205 cm^{-1}) corresponding to multilayer formation (BOTTOM), error bars associated with 3 replicate measurements. Schematic illustration (D) for multilayer propagation onto Au SRNPs surfaces as the concentration of 4-DNB increases.

adsorption continues to increase, suggesting no new adsorption on the surface of gold but the propagation of an increasingly larger structure made from 4-DNB molecules on the surface into dendritic mushroom like conformations. This is demonstrated in figure 3-6C by the presence of both molecules on the particle from the appearance of both peak intensities associated with υ_{NO2} 1340 cm^{-1} (4-DNB) and υ_{C-H} 2850 cm^{-1} (CTAC) with relative coverage exceeding what is generally expected with monolayer adsorption (Figure 3-6C, bottom panel), while monolayer coverage of 4-NTP is visualized in S5 of supporting information, with representative SE Rs spectra (A) detailed view of CTAC peak

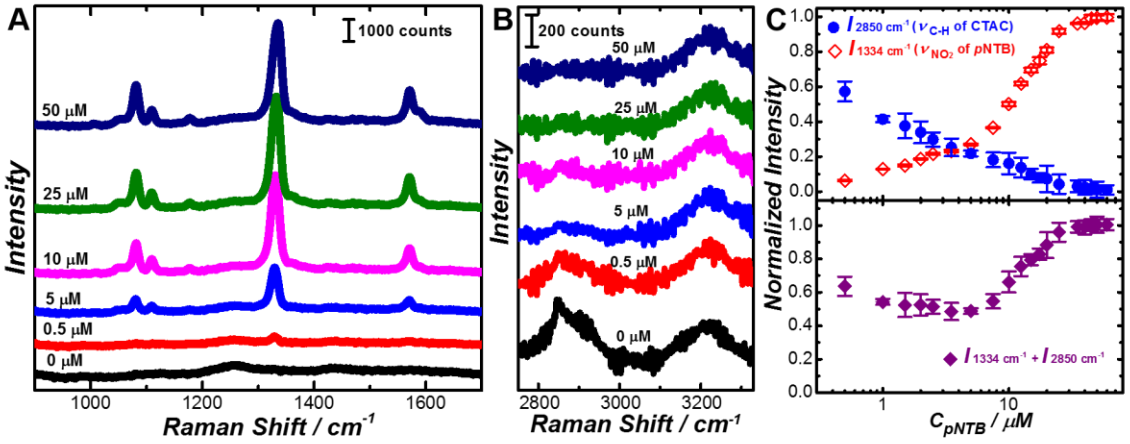

Figure 3. 7 SERs spectra collected after incubation of Au SRNPs with various concentrations of pNTP (A) with a close up (B) of the spectra detailing peak intensity associated with CTAC (υ 2850 cm^{-1}). C). Plotted ratios of intensity for CTAC (υ 2850 cm^{-1}) and NO_2 (υ 1334 cm^{-1}) as a function of concentration (TOP) and plotted sum of ratios for NO_2 (υ 1334 cm^{-1}) and CTAC (υ 2850 cm^{-1}) (Bottom).

disappearance (B) and combined peaks showing that as CTAC is displaced it is eventually replaced by 4-NTP (C). The slight decrease in the curve (Figure 3-7C) represents desorbed CTAC but a lag in 4-NTP adsorption due to kinetic effects, it takes high concentration to adsorb on highly curved regions because of kinetic stability of 4-NTP with those sites. There is clear evidence of only about 30% of CTAC remaining on the surface (top panel),

concentration dependent measurements in figure 3-6C (bottom panel) reveal a surface coverage that contains a shell consisting of both 4-DNB and CTAC capping molecules. The apparent desorption of CTAC, 65-70%, corresponds well with the density of highly curved regions associated with Au-SRNPs from curve fitting of binding Isotherms with a model thiol adsorption, figure 3-8, which is fitted with a 2-component adsorption equation:

$$\theta_{eq,pNTP} = \frac{I_{1340cm^{-1}}}{I_{sat,1340cm^{-1}}} = a \times \frac{K_1 \times C_{pNTP}^{n_1}}{1 + K_1 \times C_{pNTP}^{n_1}} + (1-a) \times \frac{K_2 \times C_{pNTP}}{1 + K_2 \times C_{pNTP}}$$

The binding isotherm is more complex than conventional Langmuir adsorption models, so two components are necessary and correspond to different binding sites based on the hill equation[48]. Because the Au-SRNPs is enclosed by both locally flat and highly curved regions, contribution to the binding of thiolated molecules from sites with markedly different affinities and cooperativity must be considered. The equation above represents a

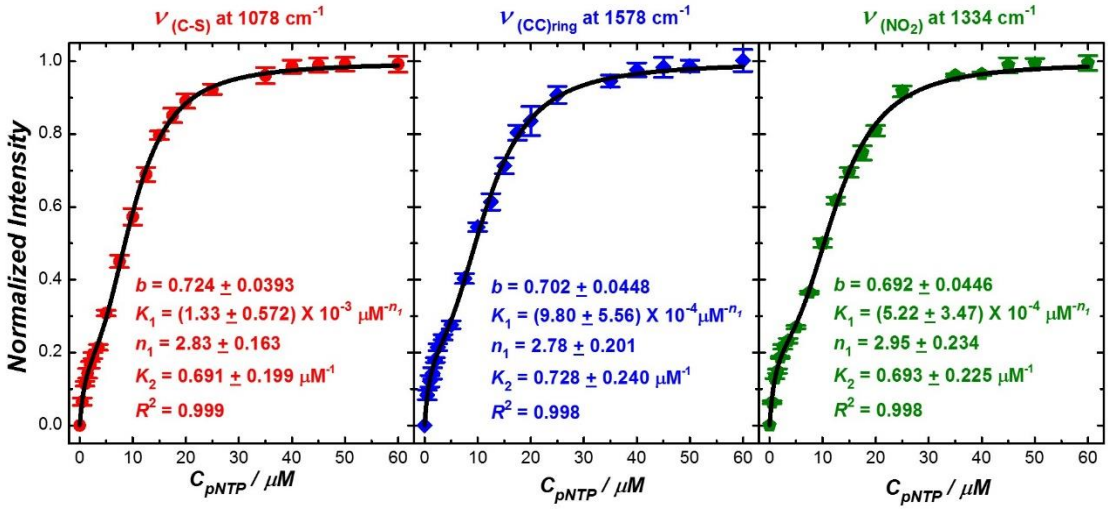

Figure 3. 8 Least square fitting for generated isotherms of pNTP adsorption onto Au SRNPs from tracking intensity of the following vibrational modes: $\upsilon_{C\text{-}S}$ 1078 cm^{-1} (Left), $\upsilon_{CC\text{-}ring}$ 1578 cm^{-1} (Middle), υ_{NO2} 1334 cm^{-1} (Right), normalized to thermodynamic intensity (100 μM – not shown).

2-component Hill equation with, a, refers to the fractional contribution of highly curved regions on the Au-SRNPs. Least squares fitting show approximately 70% of Au-SRNPs surface contain highly curved regions, figure 3-8. This interaction between 4-DNB adsorption onto the surface is illustrated in cartoon form (figure 3-6D) as the concentration of 4-DNB increases the amount of CTAC displaced decreases but does not fully disappear because 4-DNB begins to branch out after attachment to the highly curved regions of the nanoparticle generating a thicker organic ligand shell.

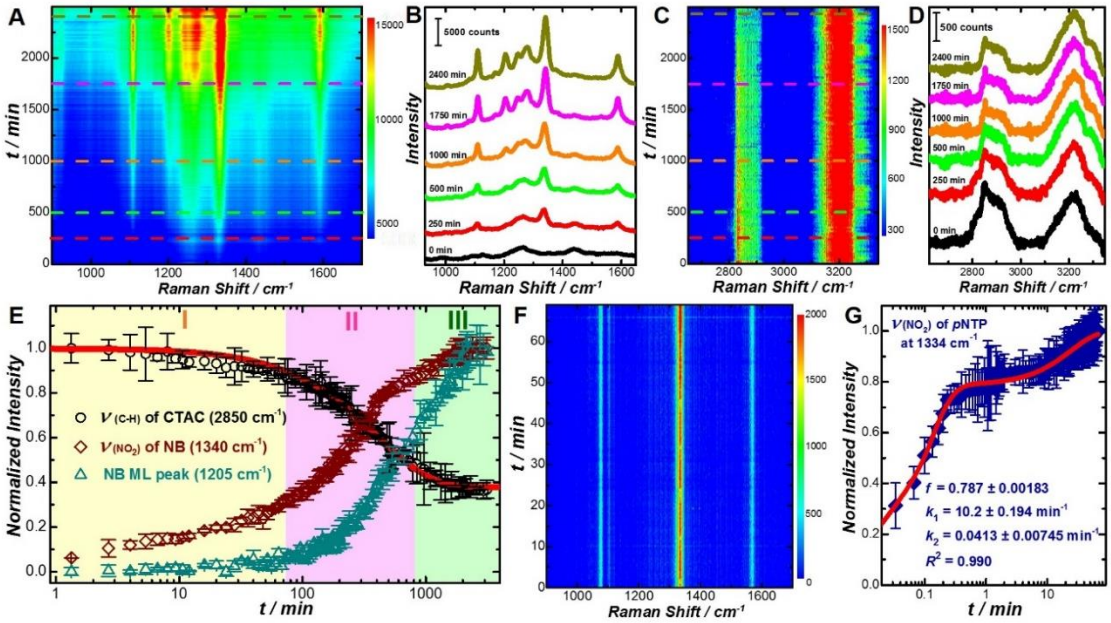

Figure 3. 9 Color coded plot of time resolved kinetics (A) and representative SERs spectra collected (B) of 4-DNB (1000 µM) adsorption onto Au SRNPs at various time periods throughout the reaction. Color coded plot (C) and representative SERs spectra (D) displaying intensity associated with CTAC (υ 2850 cm^{-1}) peak during adsorption of 4-DNB onto Au SRNPs surface. Plot represented (E) illustrates comparison of peaks intensities for CTAC (υ 2850 cm^{-1}), NO_2 (υ 1340 cm^{-1}) and NB ML (υ 1205 cm^{-1}) during reaction progress. Color coded plot (F) and graph (G) depict adsorption kinetics for pNTP (50 µM) tracing NO_2 peak (υ 1334 cm^{-1}).

Further in situ spectroscopic measurements of the kinetics associated with the grafting of 4-DNB to the surface of Au SRNPS using SERS gives additional insight to the

formation of organic shell structure of 4-DNB, while other kinetic studies using electrochemical quartz crystal microbalances have been previously investigated[36], but SERS offers the unique molecular fingerprinting capability, which allows us to monitor the local environment of the nanoparticle surface, through monitoring decrease of CTAC peak $\upsilon_{C\text{-}H}$ 2850 cm^{-1} and increase of peaks at 1205 cm^{-1} and 1285 cm^{-1} (Figures 3-9A-D). However, the kinetics associated with grafting becomes increasing complex, like thermodynamic measurements due to multilayer propagation, and resolving the interaction events between molecule-surface and molecule-molecules becomes extremely difficult. The observable kinetic data shows a slow desorption of CTAC molecules represented in region I followed by a faster desorption rate, which is detailed in region II and finally an additional lag in desorption depicted in region III (Figure 3-9E). Curve fitting details from displacement of weakly bound CTAC were analyzed using the following equation:

$$\xi_{des,CATC}(t) = \frac{I_{2850cm^{-1}}(t)}{I_{2850cm^{-1}}(t=0)} = b \times e^{-k_{des} \times t} + (1-b)$$

Correspondingly, the grafting of 4-DNB as pictured, follows an inverse relationship in region II, sharp increase in adsorption of 4-DNB while in regions I and III the adsorption experiences a significant lag, comparatively. However, the increase in signal from υ_{NO2} 1340 cm^{-1}, can be attributed to the formation of multilayer structure, as the increase of the υ_{NO2} 1340 cm^{-1} is accompanied by an increase in the υ1205 cm^{-1}, which is particularly indicative to multilayer formation of 4-DNB self-polymerization, which continues into region III and may be self-eliminating causing the polymerization to cease due to low accessibility to gold surface, which is necessary for the spontaneous reduction of diazonium salts[34-37]. Comparatively, the adsorption of 4-NTP (figure 3-9F), which is

illustrated by two exponentials signifying a kinetic binding preference to high index faceted sites first, followed by adsorption to low index faceted thermodynamically stable sites, demonstrates a stark difference in chemisorption of thiol molecule (4-NTP) versus grafting of diazonium (4-DNB). Surprisingly, grafting of 4-DNB is indiscriminate, unlike 4-NTP, there is no preference to binding on the surface of Au-nanoparticles. The binding of 4-NTP follows a two-exponential adsorption process identified through least squares curve fitting of υ_{NO2} 1340 cm^{-1} from SERS spectra (figure 3-9G and 3-10) from the following equation:

$$\xi_{ad,pNTP}(t) = \frac{I_{1340cm^{-1}}(t)}{I_{1340cm^{-1}}(t = 24h)} = f \times (1 - e^{k_1 \times t}) + (1 - f) \times (1 - e^{k_2 \times t})$$

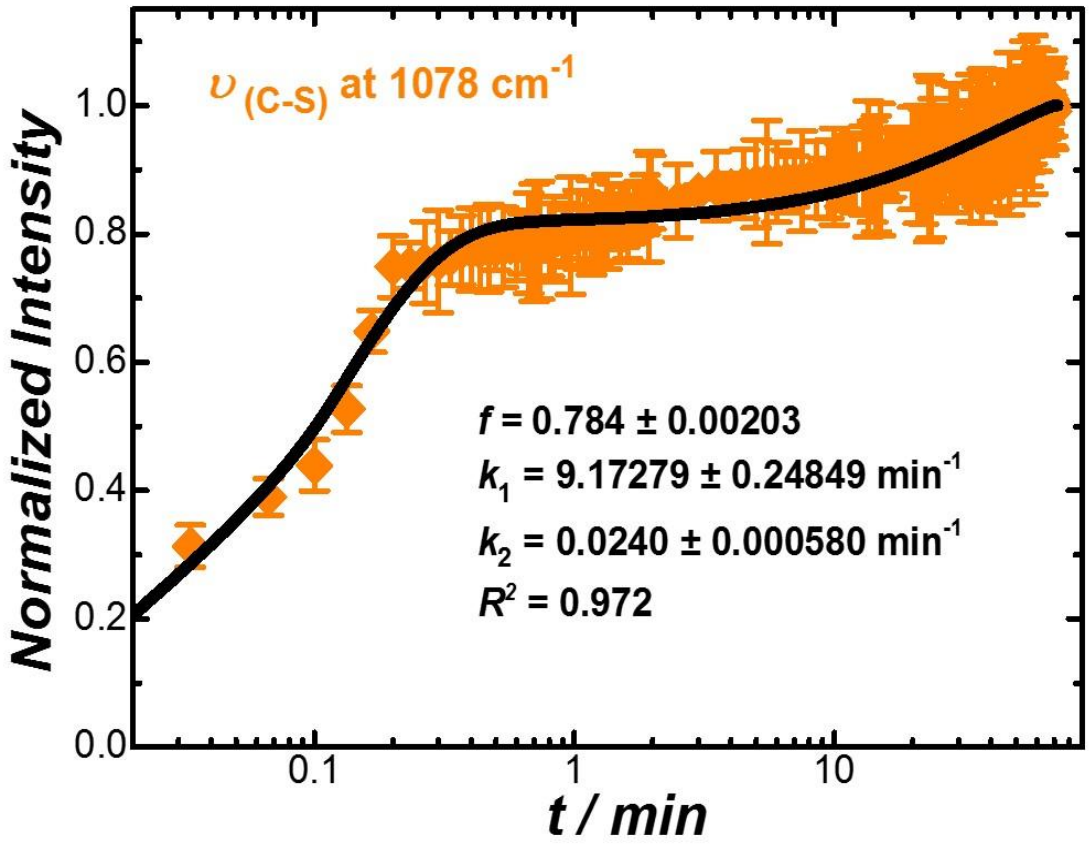

Figure 3. 10 Least squares fitting of pNTP (50 µM) adsorption kinetics onto Au SRNPs, normalized to thermodynamic point (after 24 hrs).

Previous reports show this kinetic favorability or preference of thiol ligands for the highly curved regions, demonstrated by a fast component, followed by a migration to more thermodynamically stable sites, demonstrated by a slow component, through least squares fitting of kinetic measurements[48], adsorption happens almost immediately onto highly curved region, where approximately 78% of the surface is dominated by highly curved regions from curve fitting of these kinetic models, figure 3-11. However, the overall adsorption characteristic of 4-DNB is too complex to quantitatively demonstrate, due to the duel interaction of 4-DNB with the gold surface and itself, unraveling the nature of

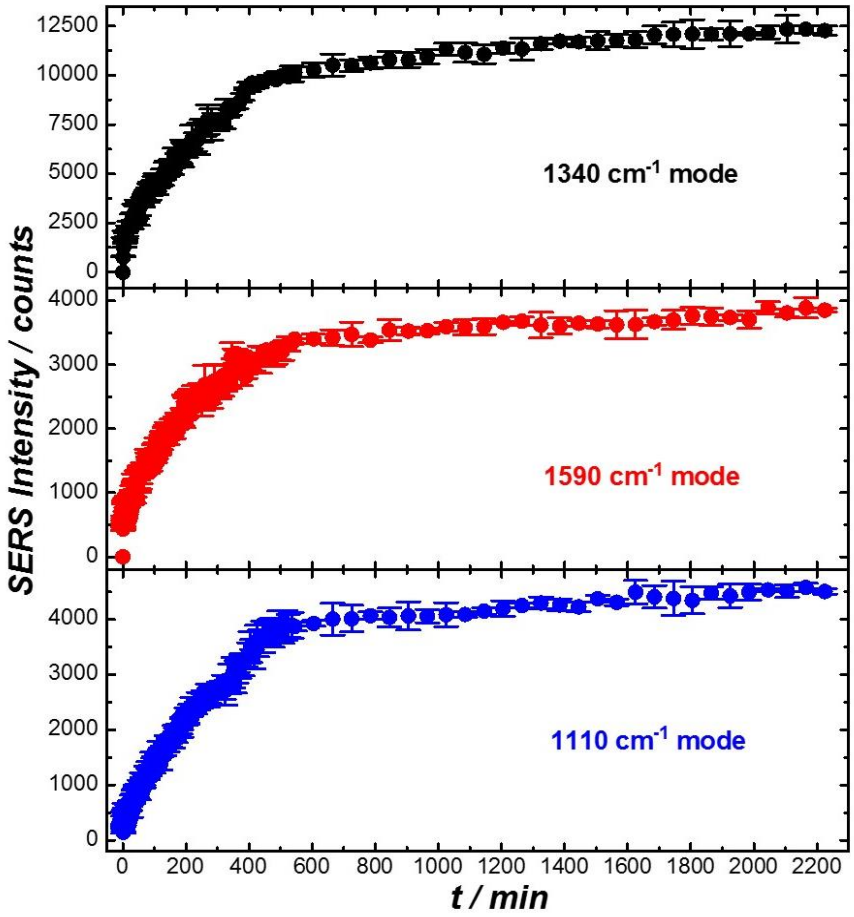

Figure 3. 11 Plotted 4-DNB adsorption kinetics onto Au SRNPs for corresponding modes: υ_{NO2} 1340 cm^{-1} , $\upsilon_{CC\text{-}ring}$ 1590 cm^{-1} , $\upsilon_{CC\text{-}ring}$ 1110 cm^{-1}

mechanistic understanding of this process is still a mystery and would need further investigation.

Surface functionalization through post synthetic means is crucial to optimizing the physical properties at the nanoparticle interface. Here, we explored the interfacial dynamics at thermodynamic equilibrium and in situ kinetics, associated with the exchange of surface grafted 4-DNB with para-mercaptobenzonitrile (p-MBN) to understand the interaction of grafted Au-C surface capping ligands when introduced to incoming thiolated ligand. From the SERS spectra associated with thermodynamic equilibrium measurements of Au-SRNPs coated with pMBN and Au-SRNPS coated with 4-DNB after exchange with pMBN (figure 3-12A and 3-13) reveals that the grafted 4-DNB is not completely displaced from the surface, but more interesting, the peaks υ1205 cm^{-1} associated with the multilayer formation disappear, as the peak for $\upsilon_{C\equiv N}$ 2226 cm^{-1}, from pMBN, increases (figure 3-12B) , signifying a disruption to the multilayer formation by the presence of incoming ligand, however, the υ_{NO2} 1340 cm^{-1} decreases but does not completely disappear indicating the residual presence of 4-DNB (~30%) on the surface (figure 3-12C), suggesting only displacements at highly curved regions, while locally flat regions retain 4-DNB molecules. Further spectral evidence suggests that pMBN binds to the surface, with adsorption firstly at sites with residual CTAC, followed by a possible displacement of 4-DNB from more kinetically favorable sites, the highly curved regions of the nanoparticle, which is apparent from the almost immediate adsorption of pMBN onto the surface of Au-SRNPs presented in the SERS spectra (figure 3-12D-F). The adsorption of pMBN follows a single exponential, signified in the equation below, due to the replacing CTAC on the surface,

however, the pMBN does not replace the 4-DNB from the low index thermodynamically favorable areas due to the process being kinetically slow.

$$\xi_{ad,pMBN}(t) = \frac{I_{2226cm^{-1}}(t)}{I_{2226cm^{-1}}(t=24h)} = \alpha_{pMBN,ad} \times (1 - e^{-k_{pMBN,ad} \times t})$$

The introduction of pMBN reveals the unstable nature of the multilayer formation, disrupting the outer organic shell to a point where a signal is no longer observable from the presence of multilayer structure leaving a suspected layer of isolated islands formation of 4-DNB and exposing larger areas of the gold surface (figure 3-12F) once covered by 4-

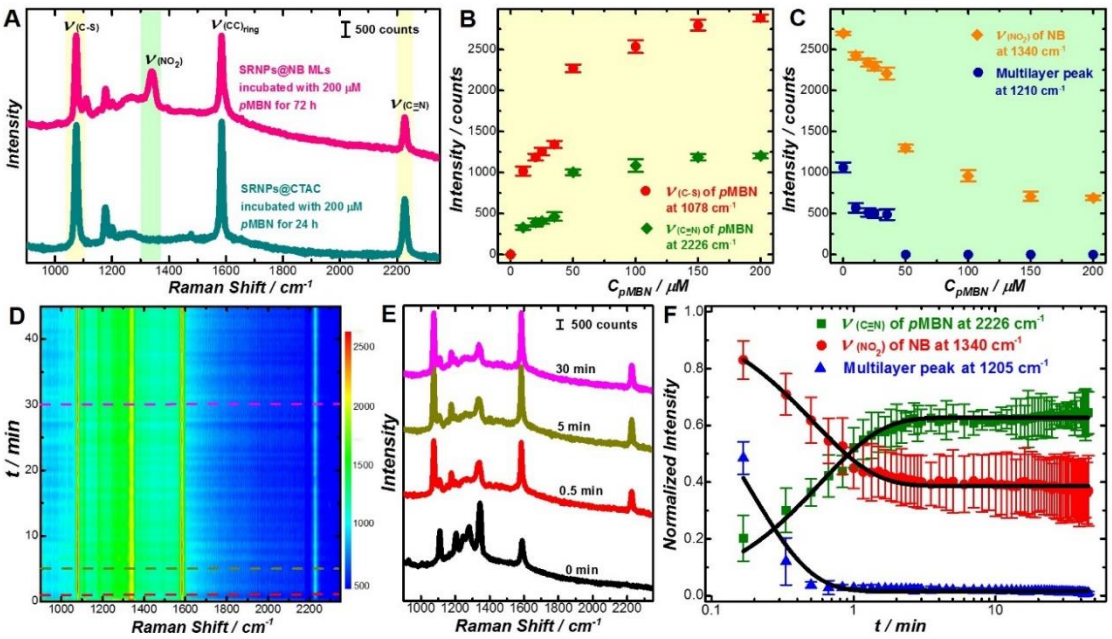

Figure 3. 12 Representative SERs spectra (A) of Au SRNPs incubated with excess (200 μM) pMBN for 24 hrs (Bottom) and 4-DNB coated AuSRNPs exposed to excess pMBN (200 μM) for 72 hrs (TOP). Plots of pMBN adsorption illustrating peak intensities associated with (B) $\upsilon_{C\text{-}S}$ 1078 cm^{-1} , $\upsilon_{C\equiv N}$ 2226 cm^{-1} and (C) υ_{NO2} 1340 cm^{-1} and υ_{ML} 1210 cm^{-1} as a function of pMBN concentration. Color coded plot (D) and representative SERs spectra (E) detailing adsorption kinetics for pMBN onto Au SRNPs previously coated with 4-DNB at selective time intervals during reaction. F) Plot demonstrating peaks associated with adsorption kinetics of pMBN onto 4-DNB coated Au SRNPs; , $\upsilon_{C\equiv N}$ 2226 cm^{-1} , υ_{NO2} 1078 cm^{-1} and υ_{ML} 1210 cm^{-1} normalized to thermodynamic points for pMBN and 4-DNB.

DNB multilayer overgrowth. The desorption or displacement of 4-DNB follows single exponential decay and was fitted using the following equation:

$$\xi_{des,NB}(t) = \frac{I_{1340cm^{-1}\,or\,1270cm^{-1}}(t)}{I_{1340cm^{-1}\,or\,1270cm^{-1}}(t=0)} = \alpha_{NB,des} \times e^{-k_{NB,des} \times t} + (1-\alpha_{NB,des})$$

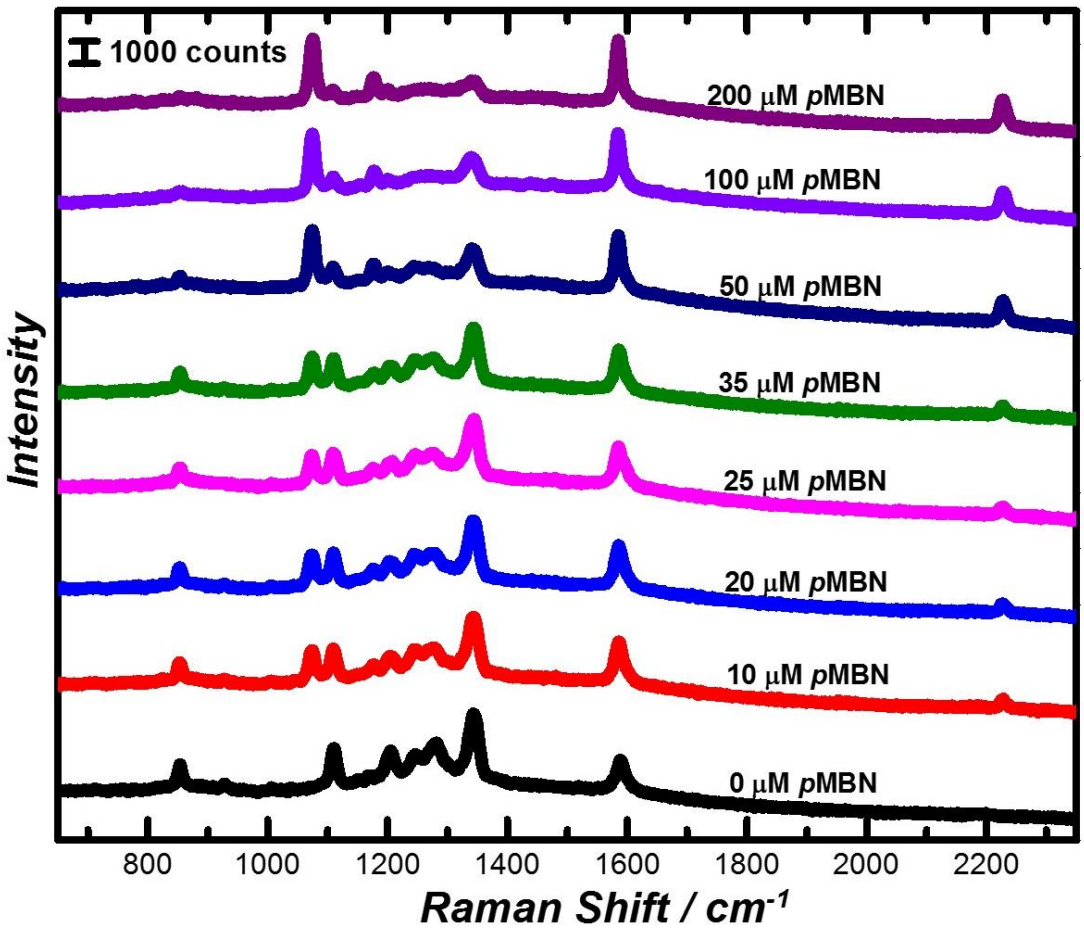

Figure 3. 13 Representative SERs spectra 4-DNB coated of Au SRNPs exposed to various concentrations (0, 10, 20, 25, 35, 50, 100, 200 μM) of pMBN.

We see from SERS measurements on Au-QSNPs that the displacement of aryl grafted molecules on the surface is not kinetically favorable, when 4-MBN molecules are introduced to the Au-QSNPs, there is spectral evidence of adsorption, by the appearance of $\upsilon_{C\equiv N}$ 2226 cm^{-1} and $\upsilon_{C\text{-}S}$ 1073 cm^{-1} suggesting displacement and exchange at the corner

and edge sites of the nanoparticle, while leaving 4-DNB molecules at low index sites. This displacement occurs on the high index facets, similar to the exchange on Au-SRNPs, which

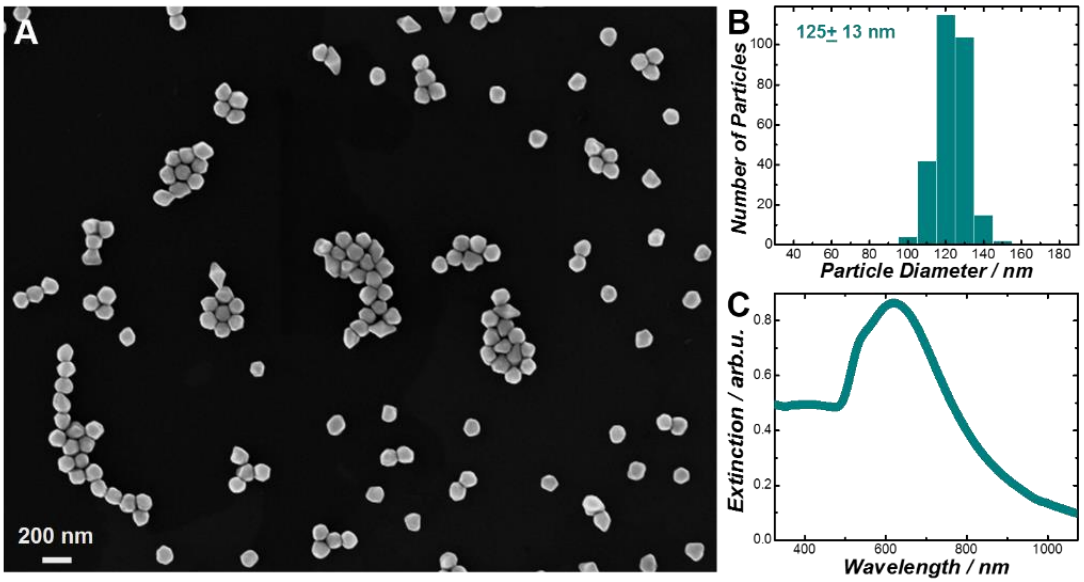

Figure 3. 14 SEM image of Au QSNPs (A), particle diameter distribution illustrated in (B) and extinction spectra of Au QSNPs (C).

occurs at the high index low affinity binding sites, leaving residual 4-DNB at low index high affinity binding sites evident from the binding isotherm of 4-NTP onto Au-SRNPs. Consequently, the displacement of the aryl molecules is kinetically a very slow process, which is interpreted as being more stable and tightly bound to the lower index facets, figure 3-15, as previously reported.

This interaction represents a unique platform to gain further quantitative insight to the nature of catalytic activity associated with ligand adsorption onto Au nanoparticles containing numerous highly curved regions. Here we used the catalytic hydrogenation of nitro functional group on surface bound 4-DNB as a model reaction to study the intrinsic

relationship and reactivity of the covalently bound diazonium ligands, we also evaluated the catalytic hydrogenation of immobilized 4-NTP molecules on the surface of Au-SRNPs to further enhance understanding of how the intrinsic interfacial interaction of self-assembled monolayers (SAMS) from 4-NTP and the multilayered configuration of 4-DNB surface adsorption onto these highly curved regions of Au-SRNPS. SERS spectra were collected for colloidal solutions of both 4-DNB multilayered and 4-NTP SAMs at excitation of 785 nm. Catalytic hydrogenation reactions were initiated by introduction of 2mM and 200 mM of ammonia borane (AB) to solutions containing.

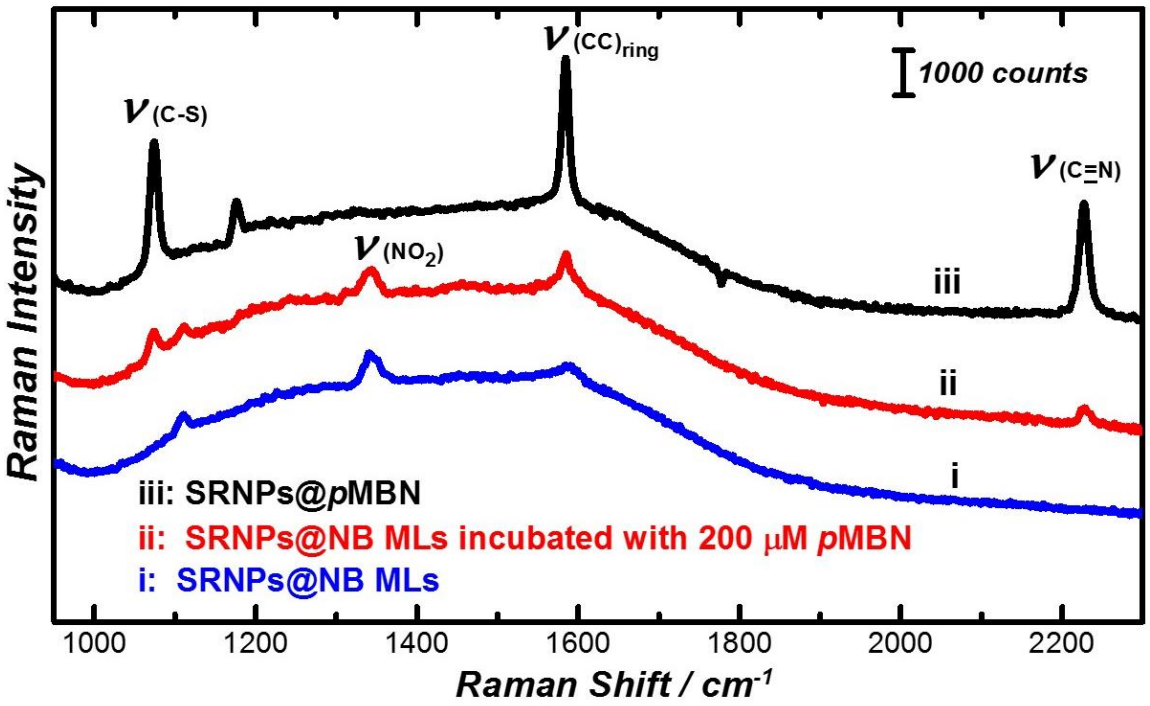

Figure 3. 15 Representative SERs spectra for Au QSNPs incubated with: i) excess 4-DNB, ii) coated with 4-DNB, then exposed to excess pMBN, iii) excess pMBN

The cartoon pictured in figure 3-16A, shows there are two mechanistic pathways suggested by SERS evidence of intermediates during the catalytic hydrogenation of the nitro group on both 4-DNB and 4-NTP, unimolecular, which is the selected by the 4-DNB molecule, while the pNTP molecule favors a bimolecular pathway (figure 3.16E). Interestingly, the presence of an intermediate species is observed in the SERS spectra detailed as a color-coded plot and representative SERS spectra (figure 3.16B-C). Comparatively, the color-coded plot and representative SERS spectra for hydrogenation of pNTP depict the intermediate associated with the bimolecular pathway. We see from desorption measurements provided (Figure 3.17 A) the rate constants associated with

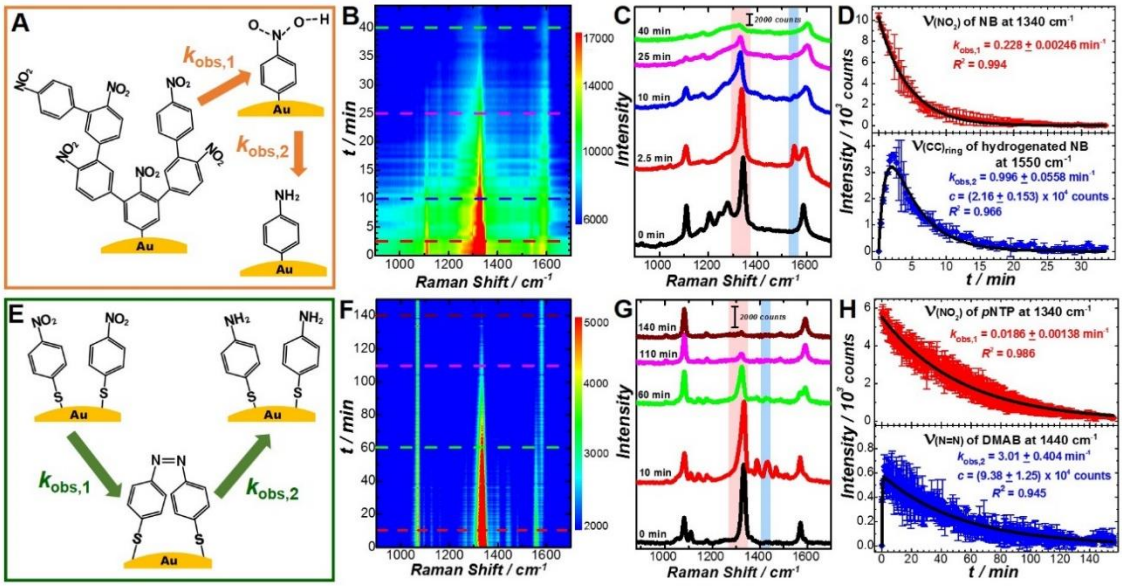

Figure 3. 16 Schematic cartoon (A), color coded intensity map (B), and representative spectra (C) of hydrogenation reaction for 4-DNB after exposure to various concentrations of ammonia borane (AB). Least squares fitting (D) of hydrogenation kinetics from peaks υ_{NO2} 1340 cm^{-1} and intermediate, υ_{CC} 1550 cm^{-1} . Schematic cartoon (E), color coded plot (F) and representative SERs spectra (G) of hydrogenation reaction of pNTP after exposure to various concentrations of ammonia borane (AB). Least squares fitting (H) of hydrogenation reaction kinetics of pNTP from peaks υ_{NO2} 1340 cm^{-1} and intermediate, $\upsilon_{N=N}$ 1440 cm^{-1} . All error bars depicted represent values from 3 replicate measurements.

pseudo-first order kinetics, $k_{obs,1}$ for reactants, from least squares fitting of the $I_R(t)$ trajectories by using rate equation:

$$I_R(t) = I_{R,t=0} \times e^{-k_{obs,1} \times t}$$

shows the hydrogenation reaction proceeds much faster, with a higher rate constant, because of the direct hydrogenation, unimolecular pathway of 4-DNB. While the rate constants for the second step were obtained, $k_{obs,\ 2}$, for intermediates were determined through least squares fitting of $I_I(t)$ trajectories displayed in figure 3-16D and 3-16H using the following rate equation:

$$I_I(t) = \frac{k_{obs,1} \times C}{k_{obs,2} - k_{obs,1}} \times (e^{-k_{obs,1} \times t} - e^{-k_{obs,2} \times t})$$

The unimolecular pathway consists of direct hydrogenation, υ_{CC} 1550 cm^{-1}, of the NO_2 moiety in the para position to the grafted carbon on the surface, while the bimolecular pathway requires two adjacent pNTP molecules to form the dimercaptoazobenzene (DMAB) molecule ($\upsilon_{N=N}$ 1440 cm^{-1}), followed by a reduction of the molecule to form two

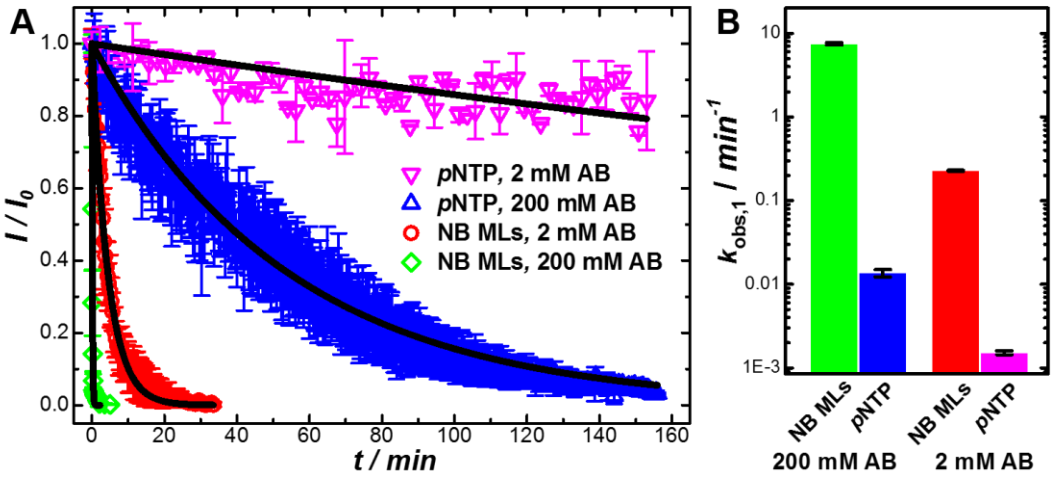

Figure 3. 17 least squares fitting of hydrogenation reaction kinetics (A) and plot of observed rate constants (B) for Au SRNPs coated with pNTP and 4-DNB exposed to various concentrations of ammonia borane.

hydrogenated species, 4-aminothiophenol (4-ATP). As shown in figure 3-16D, $k_{obs,1}$ is much less than $k_{obs,2}$ indicating the rate limiting step for hydrogenation of 4-DNB is a hydrogenated nitro species with υ_{CC} 1550 cm^{-1}. Because SERS measurements were taken in solution phase of colloidal samples, particles spend little time under laser illumination and measurements are ensembled averaged, the effect of plasmon driven photoreduction of 4-NTP were avoided, as well as, any photothermal contribution to the reaction kinetics. The nature of the 4-DNB adsorption allows for greater penetration of ammonia borane (AB) to the surface of the Au-SRNPs, which could contribute to the much larger rate constants for the 4-DNB hydrogenation reaction than that of 4-NTP hydrogenation, figure 317. Even at concentrations of 2 mM AB, the hydrogenation of 4-DNB proceeds at a faster rate than for the hydrogenation of pNTP, which shows little to no hydrogenation. Only at high concentrations of 200 mM does the hydrogenation reaction proceed but at a slow more resolvable rate.

3.5 Conclusion:

The nature of ligand surface dynamics is critical to nanoparticle stability and function. Thermodynamic measurements of 4-DNB organic ligand shell formation reveal a multilayered structure propagated concurrently with monolayer formation creating mushroom or umbrella like dendritic structures on the surface of gold nanoparticles dominated with regions of high curvature. These structures have areas of no 4-DNB adsorption but contain other ligands, which can be easily displaced by thiol ligands creating separate ligand domains or boundaries. However, the beginning adsorption stage appears follow Langmuir binding model but eventually deviates due to multilayer propagation

through nucleation at specific sites of 4-DNB. Kinetics associated with adsorption reveal a slow growth mechanism of multilayer structure initiated through reduction of diazonium salt at the gold surface. Furthermore, catalytic hydrogenation reaction shows a preference for unimolecular path of reducing nitro group from 4-DNB detailing that covalently grafted ligands have differing energetic pathways than that of thiols and may be worth exploiting towards more robust nanostructured interfaces. This study sheds new and interesting insight to the underlying fundamental interaction of ligands and nanoparticle surfaces telling of a more complex dynamic relationship between ligand-nanoparticle interface. Providing this information is the groundwork for generating design principles for custom nanoparticle interfaces guiding precision surface chemistry towards better tunability of nanocrystal growth and post-exchange functionalization of nanoparticles.

3.6 References:

1. Tao, A. R.; Habas, S.; Yang, P. D., Shape control of colloidal metal nanocrystals. Small 2008, 4 (3), 310-325.
2. Chen, X.; Jensen, L., Understanding the shape effect on the plasmonic response of small ligand coated nanoparticles. Journal of Optics 2016, 18 (7).
3. Peng, S.; McMahon, J. M.; Schatz, G. C.; Gray, S. K.; Sun, Y. G., Reversing the size-dependence of surface plasmon resonances. Proceedings of the National Academy of Sciences of the United States of America 2010, 107 (33), 14530-14534.

4. Jain, P. K.; Huang, X.; El-Sayed, I. H.; El-Sayad, M. A., Review of some interesting surface plasmon resonance-enhanced properties of noble metal nanoparticles and their applications to biosystems. Plasmonics 2007, 2 (3), 107-118
5. Adams, D. M.; Brus, L.; Chidsey, C. E. D.; Creager, S.; Creutz, C.; Kagan, C. R.; Kamat, P. V.; Lieberman, M.; Lindsay, S.; Marcus, R. A.; Metzger, R. M.; Michel-Beyerle, M. E.; Miller, J. R.; Newton, M. D.; Rolison, D. R.; Sankey, O.; Schanze, K. S.; Yardley, J.; Zhu, X. Y., Charge transfer on the nanoscale: Current status. Journal of Physical Chemistry B 2003, 107 (28), 6668-6697.
6. Lopez-Sanchez, J. A.; Dimitratos, N.; Hammond, C.; Brett, G. L.; Kesavan, L.; White, S.; Miedziak, P.; Tiruvalam, R.; Jenkins, R. L.; Carley, A. F.; Knight, D.; Kiely, C. J.; Hutchings, G. J., Facile removal of stabilizer-ligands from supported gold nanoparticles. Nature Chemistry 2011, 3 (7), 551-556.
7. Warner, M. G.; Hutchison, J. E., Linear assemblies of nanoparticles electrostatically organized on DNA scaffolds. Nature Materials 2003, 2 (4), 272-277.
8. Lin, Y.; Skaff, H.; Emrick, T.; Dinsmore, A. D.; Russell, T. P., Nanoparticle assembly and transport at liquid-liquid interfaces. Science 2003, 299 (5604), 226-229.
9. Cheng, W. L.; Campolongo, M. J.; Cha, J. J.; Tan, S. J.; Umbach, C. C.; Muller, D. A.; Luo, D., Free-standing nanoparticle superlattice sheets controlled by DNA. Nature Materials 2009, 8 (6), 519-525.
10. Zhao, Y.; Thorkelsson, K.; Mastroianni, A. J.; Schilling, T.; Luther, J. M.; Rancatore, B. J.; Matsunaga, K.; Jinnai, H.; Wu, Y.; Poulsen, D.; Frechet, J. M. J.;

Alivisatos, A. P.; Xu, T., Small-molecule-directed nanoparticle assembly towards stimuli-responsive nanocomposites. Nature Materials 2009, 8 (12), 979-985.

11. Zheng, Y. B.; Payton, J. L.; Song, T. B.; Pathem, B. K.; Zhao, Y. X.; Ma, H.; Yang, Y.; Jensen, L.; Jen, A. K. Y.; Weiss, P. S., Surface-Enhanced Raman Spectroscopy To Probe Photoreaction Pathways and Kinetics of Isolated Reactants on Surfaces: Flat versus Curved Substrates. Nano Letters 2012, 12 (10), 5362-5368.
12. Huang, Y. F.; Zhu, H. P.; Liu, G. K.; Wu, D. Y.; Ren, B.; Tian, Z. Q. J. Am. Chem. Soc. 2010, 132, 9244.
13. Kim, M.; Hohman, J. N.; Cao, Y.; Houk, K. N.; Ma, H.; Jen, A. K. Y.; Weiss, P. S., Creating Favorable Geometries for Directing Organic Photoreactions in Alkanethiolate Monolayers. Science 2011, 331 (6022), 1312-1315.
14. Haes, A. J.; Van Duyne, R. P., A nanoscale optical biosensor: Sensitivity and selectivity of an approach based on the localized surface plasmon resonance spectroscopy of triangular silver nanoparticles. Journal of the American Chemical Society 2002, 124 (35), 10596-10604.
15. Choi, C. H. J.; Alabi, C. A.; Webster, P.; Davis, M. E., Mechanism of active targeting in solid tumors with transferrin-containing gold nanoparticles. Proceedings of the National Academy of Sciences of the United States of America 2010, 107 (3), 1235-1240.
16. Dreaden, E. C.; Alkilany, A. M.; Huang, X.; Murphy, C. J.; El-Sayed, M. A., The golden age: gold nanoparticles for biomedicine. Chemical Society Reviews 2012, 41 (7), 2740-2779.

17. Love, J. C.; Estroff, L. A.; Kriebel, J. K.; Nuzzo, R. G.; Whitesides, G. M., Self-assembled monolayers of thiolates on metals as a form of nanotechnology. Chemical Reviews 2005, 105 (4), 1103-1169.
18. Sardar, R.; Funston, A. M.; Mulvaney, P.; Murray, R. W., Gold Nanoparticles: Past, Present, and Future. Langmuir 2009, 25 (24), 13840-13851
19. Luedtke, W. D.; Landman, U. J. Phys. Chem. B 1998, 102, 6566−6572.
20. Ulman, A. Chem. Rev. 1996, 96, 1533−1554
21. Allongue, P.; Delamar, M.; Desbat, B.; Fagebaume, O.; Hitmi, R.; Pinson, J.; Saveant, J. M., Covalent modification of carbon surfaces by aryl radicals generated from the electrochemical reduction of diazonium salts. Journal of the American Chemical Society 1997, 119 (1), 201-207.
22. Delamar, M.; Hitmi, R.; Pinson, J.; Saveant, J. M., COVALENT MODIFICATION OF CARBON SURFACES BY GRAFTING OF FUNCTIONALIZED ARYL RADICALS PRODUCED FROM ELECTROCHEMICAL REDUCTION OF DIAZONIUM SALTS. Journal of the American Chemical Society 1992, 114 (14), 5883-5884.
23. Kariuki, J. K.; McDermott, M. T., Nucleation and growth of functionalized aryl films on graphite electrodes. Langmuir 1999, 15 (19), 6534-6540
24. Kariuki, J. K.; McDermott, M. T., Formation of multilayers on glassy carbon electrodes via the reduction of diazonium salts. Langmuir 2001, 17 (19), 5947-5951
25. Bahr, J. L.; Yang, J. P.; Kosynkin, D. V.; Bronikowski, M. J.; Smalley, R. E.; Tour, J. M., Functionalization of carbon nanotubes by electrochemical reduction of aryl

diazonium salts: A bucky paper electrode. Journal of the American Chemical Society 2001, 123 (27), 6536-6542.

26. Qiu, Z. P.; Yu, J.; Yan, P.; Wang, Z. J.; Wan, Q. J.; Yang, N. J., Electrochemical Grafting of Graphene Nano Platelets with Aryl Diazonium Salts. Acs Applied Materials & Interfaces 2016, 8 (42), 28291-28298.
27. Stewart, M. P.; Maya, F.; Kosynkin, D. V.; Dirk, S. M.; Stapleton, J. J.; McGuiness, C. L.; Allara, D. L.; Tour, J. M., Direct covalent grafting of conjugated molecules onto Si, GaAs, and Pd surfaces from aryidiazonium salts. Journal of the American Chemical Society 2004, 126 (1), 370-378.
28. Pinson, J.; Podvorica, F., Attachment of organic layers to conductive or semiconductive surfaces by reduction of diazonium salts. Chemical Society Reviews 2005, 34 (5), 429-439
29. Collins, G.; Fleming, P.; O'Dwyer, C.; Morris, M. A.; Holmes, J. D., Organic Functionalization of Germanium Nanowires using Arenediazonium Salts. Chemistry of Materials 2011, 23 (7), 1883-1891.
30. Bernard, M. C.; Chausse, A.; Cabet-Deliry, E.; Chehimi, M. M.; Pinson, J.; Podvorica, F.; Vautrin-Ul, C., Organic layers bonded to industrial, coinage, and noble metals through electrochemical reduction of aryldiazonium salts. Chemistry of Materials 2003, 15 (18), 3450-3462.
31. Laforgue, A.; Addou, T.; Belanger, D., Characterization of the deposition of organic molecules at the surface of gold by the electrochemical reduction of aryldiazonium cations. Langmuir 2005, 21 (15), 6855-6865

32. Mirkhalaf, F.; Paprotny, J.; Schiffrin, D. J., Synthesis of metal nanoparticles stabilized by metal-carbon bonds. Journal of the American Chemical Society 2006, 128 (23), 7400-7401

33. Chevalier, C. L.; Landis, E. C., Electrochemical Attachment of Diazonium-Generated Films on Nanoporous Gold. Langmuir 2015, 31 (31), 8633-8641

34. Mesnage, A.; Lefevre, X.; Jegou, P.; Deniau, G.; Palacin, S., Spontaneous Grafting of Diazonium Salts: Chemical Mechanism on Metallic Surfaces. Langmuir 2012, 28 (32), 11776-

35. Adenier, A.; Cabet-Deliry, E.; Chausse, A.; Griveau, S.; Mercier, F.; Pinson, J.; Vautrin-Ul, C., Grafting of nitrophenyl groups on carbon and metallic surfaces without electrochemical induction. Chemistry of Materials 2005, 17 (3), 491-501

36. Jayasundara, D. R.; Cullen, R. J.; Soldi, L.; Colavita, P. E., In Situ Studies of the Adsorption Kinetics of 4-Nitrobenzenediazonium Salt on Gold. Langmuir 2011, 27 (21), 13029-13036

37. Berisha, A.; Combellas, C.; Kanoufi, F.; Decorse, P.; Oturan, N.; Medard, J.; Seydou, M.; Maurel, F.; Pinson, J., Some Theoretical and Experimental Insights on the Mechanistic Routes Leading to the Spontaneous Grafting of Gold Surfaces by Diazonium Salts. Langmuir 2017, 33 (35), 8730-8738.

38. Shewchuk, D. M.; McDermott, M. T., Comparison of Diazonium Salt Derived and Thiol Derived Nitrobenzene Layers on Gold. Langmuir 2009, 25 (8), 4556-4563

39. de la Llave, E.; Ricci, A.; Calvo, E. J.; Scherlis, D. A., Binding between Carbon and the Au(111) Surface and What Makes It Different from the S-Au(111) Bond. Journal of Physical Chemistry C 2008, 112 (45), 17611-17617

40. Laurentius, L.; Stoyanov, S. R.; Gusarov, S.; Kovalenko, A.; Du, R. B.; Lopinski, G. P.; McDermott, M. T., Diazonium-Derived Aryl Films on Gold Nanoparticles: Evidence for a Carbon-Gold Covalent Bond. Acs Nano 2011, 5 (5), 4219-4227.
41. Menanteau, T.; Levillain, E.; Breton, T., Electrografting via Diazonium Chemistry: From Multilayer to Monolayer Using Radical Scavenger. Chemistry of Materials 2013, 25 (14), 2905-2909.
42. Menanteau, T.; Dias, M.; Levillain, E.; Downard, A. J.; Breton, T., Electrografting via Diazonium Chemistry: The Key Role of the Aryl Substituent in the Layer Growth Mechanism. Journal of Physical Chemistry C 2016, 120 (8), 4423-4429
43. Combellas, C.; Kanoufi, F.; Pinson, J.; Podvorica, F. I., Sterically hindered diazonium salts for the grafting of a monolayer on metals. Journal of the American Chemical Society 2008, 130 (27), 8576-8580
44. Paulik, M. G.; Brooksby, P. A.; Abell, A. D.; Downard, A. J., Grafting aryl diazonium cations to polycrystalline gold: Insights into film structure using gold oxide reduction, redox probe electrochemistry, and contact angle behavior. Journal of Physical Chemistry C 2007, 111 (21), 7808-7815
45. Guo, L. M.; Ma, L. P.; Zhang, Y. L.; Cheng, X.; Xu, Y.; Wang, J.; Wang, E. K.; Peng, Z. Q., Spectroscopic Identification of the Au-C Bond Formation upon Electroreduction of an Aryl Diazonium Salt on Gold. Langmuir 2016, 32 (44), 11514-11519
46. Ahmad, R.; Boubekeur-Lecaque, L.; Nguyen, M.; Lau-Truong, S.; Lamouri, A.; Decorse, P.; Galtayries, A.; Pinson, J.; Felidj, N.; Mangeney, C., Tailoring the Surface Chemistry of Gold Nanorods through Au-C/Ag-C Covalent Bonds Using

Aryl Diazonium Salts. Journal of Physical Chemistry C 2014, 118 (33), 19098-19105

47. Zhang, Q. F.; Large, N.; Nordlander, P.; Wang, H., Porous Au Nanoparticles with Tunable Plasmon Resonances and Intense Field Enhancements for Single-Particle SERS. Journal of Physical Chemistry Letters 2014, 5 (2), 370-374.
48. Villarreal, E.; Li, G. F. G.; Zhang, Q. F.; Fu, X. Q.; Wang, H., Nanoscale Surface Curvature Effects on Ligand-Nanoparticle Interactions: A Plasmon-Enhanced Spectroscopic Study of Thiolated Ligand Adsorption, Desorption, and Exchange on Gold Nanoparticles. Nano Letters 2017, 17 (7), 4443-4452
49. Nielsen, J. U.; Esplandiu, M. J.; Kolb, D. M., 4-nitrothiophenol SAM on Au(111) investigated by in situ STM, electrochemistry, and XPS. Langmuir 2001, 17 (11), 3454-3459.
50. Cecchet, F.; Lis, D.; Guthmuller, J.; Champagne, B.; Fonder, G.; Mekhalif, Z.; Caudano, Y.; Mani, A. A.; Thiry, P. A.; Peremans, A., Theoretical Calculations and Experimental Measurements of the Vibrational Response of p-NTP SAMs: An Orientational Analysis. Journal of Physical Chemistry C 2010, 114 (9), 4106-4113.

Chapter 4
Unconventional Azo-Coupling Reactions on Gold Nanoparticle Surfaces

4.1. Introduction

The ability to modify surfaces with specific molecules via self-assembly are critical to further understanding for rational optimization of materials through precise surface functionalization. The surface functionalization has profound impact, influencing the optical, catalytic and electronic properties for applications in biosensing [1], photoreactions [2, 3], plasmonics [4] and molecular electronics [5]. Covalent modification of surfaces through electrochemical grafting has been a method used for attaching aryl films to functionalize silicon, glass and carbon-based substrates [6-10]. More recently the functionalization of aryl films onto gold surfaces have been of great interest. Reports have suggested that diazonium salts are electrochemically or spontaneously reduced at the surface of conductors to generate aryl films [10-20]. The newly derived aryl films are believed to form extended networks, oligomers and even polymer like formations on the surface [17, 20-23], through a process that is still widely debated. Here we investigate the stability of this extended network formed by the spontaneous reduction of 4-diazoniumnitrobenzene tetrafluoroborate (4-DNB) on Au surface roughened nanoparticles in solution phase, observing the interactions between the covalently adsorbed multilayers (ML) with foreign ligands and chemisorbed monolayers in the form of 4-aminothiophenol (4-ATP) with 4-DNB.

4.2 Experimental

Chemicals and Materials:

Gold(III) chloride trihydrate (HAuCl4·3H2O, ACS grade) was purchased from J.T. Baker. Sodium borohydride (NaBH4, 99%), hydrochloric acid (HCl, 37%), and L-ascorbic acid

(AA, 99.5%) were obtained from Sigma-Aldrich. Cetyltrimethylammonium chloride (CTAC, 96%), Diazonium-Nitrobenzene tetrafluorborate (C6H4N3O2 · BF4, 4-DNB, 97%), 4-nitrothiophenol (C6H5NO2S, pNTP, 80%), and 4-Aminothiophenol (C6H7NS, 4-ATP, 97%) were obtained from Alfa Aesar. All reagents were used as received without further purification. Ultrapure water (18.2 MΩresistivity, Barnstead EasyPure II 7138) was used for all experiments.

Nanoparticle Synthesis:

Au-surface roughened nanoparticles (SRNPs) and quasispherical nanoparticles (QSNPs) were synthesized from Au seeds by a kinetically controlled seed mediated growth process, previously reported by Wang research group. Colloidal Au seeds of 3 nm in diameter, were synthesized initially by the reduction of $HAuCl_4$ with $NaBH_4$ in a solution of (1-hexadecyl) trimethyl ammonium chloride. Firstly, $HAuCl_4$ (0.25 mL, 10 mM) is added to the solution of CTAC (10 mL, 0.1M) under constant stirring conditions. Followed by, freshly prepared ice cold $NaBH_4$ (0.3 mL, 10 mM) is then injected into a solution containing CTAC (10 mL, 0.1M) and $HAuCl_4$ (0.250 mL, 0.010 M) under constant stirring for 1 minute and then left undisturbed for 2 hours. Seed is diluted 1000-fold with CTAC (0.1 M) and diluted portion was used for seed mediate growth.

The growth solution for Au SRNPs was prepared by sequentially adding 1.50 mL of $HAuCl_4$ (10 mM) and 0.60 mL of AA (100 mM) into 10.0 mL of CTAC (100 mM) solution. To prepare Au SRNPs with average diameter of ~ 120 nm, 120 μL of the diluted Au seed solution was added into the growth solution. The reactants were gently mixed for 30 s and then left undisturbed at room temperature for 4 h. The as-obtained Au SRNPs

were washed with water 3 times through centrifugation/redispersion cycles, and finally redispersed in water, (6 mL, 18.2 MΩ resistivity, Barnstead EasyPure II 7138).

The Au QSNPs were fabricated following a similar protocol for the Au SRNPs except for the addition of HCl. For relative size of ~120 nm, the growth solution was prepared by sequentially adding 1.50 mL of $HAuCl_4$ (10 mM), 0.60 mL of HCl (1.0 M), and 0.30 mL of AA (100 mM) into 10.00 mL of CTAC (100 mM) solution. After gently mixing the reactants for 30 s, the growth of Au QSNPs was initiated by adding 105 μL of the diluted Au seed solution, and then left undisturbed at room temperature for 4 h. The obtained Au QSNPs were washed with water 3 times and finally redispersed in water

Surface Enhanced Raman Scattering (SERS) Measurements:

All SERS measurements were performed using a Bayspec Nomadic confocal Raman microscope built on an Olympus BX51 reflected optical system with a 785-nm continuous wave excitation laser. Excitation laser was focused on colloidal samples with a 10x objective [Numerical Aperture (NA) = 0.30, working distance (WD) = 11.0 mm, Olympus MPLFLN, excitation volume of 100 fL].5 The laser power for Raman excitation was 10.0 mW.

Equilibrium Exchange Measurements:

4-DNB (4- Diazonium-Nitrobenzene tetrafluorborate) / pATP (4- Aminothiophenol) Isotherm:

Exchange measurements of pATP onto Au SRNPs saturated with 4-DNB was conducted by preparing fresh Au SRNPs (200 μL, 1.25 nM), washing 1X, suspending particles in ultraopure H_2O (150 μL, 18.2 MΩ) and then incubated for 96 hours in 4-DNB

(50 µL, 4 mM). After incubation, supernatant was removed after particles settled and suspended in ultrapure H_2O (196 µL, 18.2 MΩ) then exposed to various concentrations of pATP (final concentrations: 0, 1, 5, 10, 20, 25, 50, 100, 250, 500, 1000 µM). SERS spectra were obtained on a Bayspec Nomadic confocal Raman microscope built on an Olympus BX51 reflected optical system with a 785 nm continuous wave excitation laser. Excitation laser was focused on solution with a 10X objective [Numerical Aperture (NA) = 0.30, working distance (WD) = 11.0 mm, Olympus MPLFLN]. SERS measurements were obtained with a laser power of 10 mW and at 20 second integration time to monitor vibrational modes: : 4-DNB – 1210 cm^{-1} (Multilayer, ML), 4-ATP – 1080 cm^{-1} υ(C-S), 1480 cm^{-1} ν(C-N) + β(C-H) + ν(CC); and 1390, 1440 cm^{-1} ν(N=N) + ν(CC) + β(C-H) corresponding to the vibrational modes associated with 4-DNB, pATP and dimerization.

4-DNB (4- Diazoniumnitrobenzene tetrafluorborate) / pNTP (4- Nitrothiophenol) Isotherm:

Exchange measurements of pNTP onto Au SRNPs saturated with 4-DNB was conducted by preparing fresh Au SRNPs (200 µL, 1.25 nM), washing 1X, suspending particles in ultraopure H_2O (150 µL, 18.2 MΩ) and then incubated for 96 hours in 4-DNB (50 µL, 4 mM). After incubation, supernatant was removed after particles settled and suspended in ultrapure H_2O (196 µL, 18.2 MΩ) then exposed to various concentrations of pATP (final concentrations: 0, 0.5, 1, 2.5, 5, 10, 20, 25, 50, 100, 150, 250, 50, 1000µM). SERS spectra obtained were used to monitor the change in vibrational modes: 4-DNB – 1210 cm^{-1} (Multilayer, ML), pNTP – 1080 cm^{-1} υ(C-S); and 1390, 1440 cm^{-1} ν(N=N) + ν(CC) + β(C-H) corresponding to the vibrational modes associated with 4-DNB, pNTP and

dimerization. SERS measurements were obtained with a laser power of 10 mW and at 20 second integration time.

4-ATP / 4-DNB Isotherm:

Exchange measurements of 4-DNB onto Au SRNPs saturated with 4-ATP was conducted by preparing fresh Au SRNPs (200 µL, 1.25 nM), washing 1X, suspending particles in ultraopure H_2O (150 µL, 18.2 MΩ) and then incubated for 24 hours in 4-ATP (50 µL, 0.4 mM). After incubation, supernatant was removed after particles settled and suspended in ultrapure H_2O (196 µL, 18.2 MΩ) then exposed to various concentrations of 4-DNB (final concentrations:0, 25, 50, 100, 250, 500 µM). SERS spectra obtained were used to monitor the change in vibrational modes: 4-ATP – 1080 cm^{-1} υ(C-S), 1480 cm^{-1} ν(C-N) + β(C-H) + ν(CC); 4-DNB – 1210 cm^{-1} (Multilayer, ML) and 1390, 1440 cm^{-1} ν(N=N) + ν(CC) + β(C-H) corresponding to the vibrational modes associated with, pATP, 4-DNB and dimerization. SERS measurements were obtained with a laser power of 10 mW and at 20 second integration time

4 ATP limited coverage Dimer reaction with DNB

Exchange measurements of 4-DNB onto Au SRNPs coated with various concentrations of 4-ATP was conducted by preparing fresh Au SRNPs (200 µL, 1.25 nM), washing 1X, suspending particles in ultrapure H_2O (150 µL, 18.2 MΩ) and then incubated for 24 hours in various concentrations of 4-ATP (0, 0.5, 1.5, 2.5, 5, 10, 15, 20 µM)). After incubation, supernatant was removed after particles settled and suspended in ultrapure H_2O (150 µL, 18.2 MΩ) then exposed to various concentrations of 4-DNB (50 µL, 4.0 mM). SERS spectra obtained were used to monitor the change in vibrational modes: 4-ATP –

1080 cm^{-1} υ(C-S), 1480 cm^{-1} ν(C-N) + β(C-H) + ν(CC); 4-DNB – 1210 cm^{-1} (Multilayer, ML) and 1390, 1440 cm^{-1} ν(N=N) + ν(CC) + β(C-H) . SERS measurements were obtained with a laser power of 10 mW and at 20 second integration time

Time Resolved Ligand Exchange Measurements – Au SRNPs

4-DNB + 4-ATP

The ligand exchange interaction between 4-DNB coated Au SRNPs and introduction of free 4-ATP was monitored by SERS. Au SRNPs (200 µL, 1.25 nM) were washed 1X, suspended in ultrapure H_2O (196 µL, 18.2 MΩ) and then incubated in excess 4-DNB (4 µL, 50 mM) for 96 hours. Particles were then washed 1X and suspended in ultrapure H_2O (196 µL, 18.2 MΩ). Initial spectra were recorded and excess pATP (4 µL, 5.0 mM) was introduced monitoring 4-DNB – 1210 cm^{-1} (Multilayer, ML), 4-ATP – 1080 cm^{-1} υ(C-S), 1480 cm^{-1} ν(C-N) + β(C-H) + ν(CC); and 1390, 1440 cm^{-1} ν(N=N) + ν(CC) + β(C-H) corresponding to the vibrational modes associated with 4-DNB, pATP and dimerization. Measurement were recorded every 20 seconds for the first 5 minutes and then every 30 seconds for the following 5 minutes then every minute under 10 mW laser power and 10 second integration time. The ligand exchange experiment was conducted in triplicate to obtain error bars and standard deviation.

4-DNB + pNTP

The ligand exchange interaction between 4-DNB coated Au SRNPs and of free pNTP was monitored by SERS and carried out in a similar method as the previous exchange with 4-ATP. Au SRNPs (200 µL, 1.25 nM) were washed 1X, suspended in ultrapure H_2O (196 µL, 18.2 MΩ) and then incubated in excess 4-DNB (4 µL, 50 mM) for

96 hours. Particles were then washed 1X and suspended in ultrapure H_2O (196 µL, 18.2 MΩ). Initial spectra were recorded and excess pNTP (4 µL, 5.0 mM) was introduced monitoring the 4-DNB – 1210 cm^{-1} (Multilayer, ML), pNTP – 1080 cm^{-1} υ(C-S); and 1390, 1440 cm^{-1} ν(N=N) + ν(CC) + β(C-H) corresponding to the vibrational modes associated with 4-DNB, pNTP and dimerization. Measurements were completed when no increase in SERS intensity was observable. Measurement were recorded every 10 seconds for the first 3 minutes and then every 30 seconds for the following 2 minutes then every minute under 10 mW laser power and 10 second integration time. The ligand exchange experiment was conducted in triplicate to obtain error bars and standard deviation.

4-ATP +4-DNB

The ligand exchange interaction between 4-ATP coated Au SRNPs and introduction of free pATP was monitored by SERS. Au SRNPs (200 µL, 1.25 nM) were washed 1X, suspended in ultrapure H_2O (196 µL, 18.2 MΩ) and then incubated in excess 4-DNB (4 µL, 5.0 mM) for 24 hours. Particles were then washed 1X and suspended in ultrapure H_2O (196 µL, 18.2 MΩ). Initial spectra were recorded and excess 4-DNB (4 µL, 5.0 mM) was introduced 4-DNB – 1210 cm^{-1} (Multilayer, ML), 4-ATP – 1080 cm^{-1} υ(C-S), 1480 cm^{-1} ν(C-N) + β(C-H) + ν(CC); and 1390, 1440 cm^{-1} ν(N=N) + ν(CC) + β(C-H) corresponding to the vibrational modes associated with 4-DNB, pATP and dimerization. Measurement were recorded every 20 seconds for the first 5 minutes and then every 30 seconds for the following 5 minutes then every minute under 10 mW laser power and 10 second integration time. The ligand exchange experiment was conducted in triplicate to obtain error bars and standard deviation

Chemical Reaction of 4-DNB and 4-ATP:

4-DNB and 4-ATP were mixed in a cuvette at molar ratios of 0, 0.1, 0.25, 0.5, 1, 2, 2.5, 5, 10, 25, 50 of DNB / ATP and reaction was monitored with Uv Vis spectrometer at 418 nm. Representative reaction of molar ratio 10 was then monitored in real time with Uv-vis to track kinetics of chemical reaction without the presence of Au SRNPs.

SERS measurements for chemical reaction were then taken after chemical reaction was complete by incubating the reacted molecules (4-DNB + 4-ATP, 200 µL of molar ratio 10) with Au SRNPs (1.25 nM) overnight and then taking measurements with laser power of 10 mW at an integration time of 20 seconds. The procedure was then repeated with 4-DNB and pNTP at the same molar ratios of: 0, 0.1, 0.25, 0.5, 1, 2, 5, 10, 25, 50. All measurements were done in triplicate to obtain standard deviation and error bars.

DFT Calculations:

The exchange-correlation functional B3LYP was used for all the calculations. The basis set of light atoms was 6-31+G**, while for the heavy metal atoms, effective core potential was employed with the basis set def2-svp. The calculation was done by optimizing the geometry of the 4-metal-cluster substrate structures at first, constraints were applied to make sure tetrahedral structures were obtained. After substrate geometry optimization, the molecules were set at the different sites of the metal substrates and geometry of each complex structure was further optimized. The optimized geometries were used to calculate the Raman spectrum. The calculated Raman activities were converted to relative Raman intensities according to the equation below,

$$I_i = \frac{f(v_0 - v_i)^4 S_i}{v_i \left[1 - \exp\left(-\frac{hc\, v_i}{kT}\right)\right]}$$

Where v_0 is the exciting frequency in (cm^{-1}), v_i is the vibrational frequency of the ith normal mode, h, c, k are universal constants, and f is a suitably chosen common scaling factor for all peak intensities. The excitation frequency was set at to be 12738.85 cm^-1, which corresponds to 785nm incoming light. The scaling factor 1 was used for all the peak intensities, and the temperature was taken as 298.15 K. The relative Raman intensities were further expanded with Lorentzian lineshape with 7 cm^-1 full width at half maximum. The binding energy was calculated by using the following equation:

$$\text{Binding Energy} = E_{(complex)} - E_{(molecule)} - E_{(metal\text{-}cluster)}$$

Characterization:

The structures of the nanoparticles were characterized by SEM using a Zeiss Ultraplus thermal field emission scanning electron microscope. The samples for SEM measurements were dispersed in water and drop-dried on silicon wafers. The optical extinction spectra of the nanoparticles were measured on aqueous colloidal suspensions at room temperature, using a Beckman Coulter Du 640 spectrophotometer.

4.3 Results and Discussion:

When attempting to conduct exchange reactions on 4-DNB saturated Au SRNPs with various concentrations of 4-ATP, something interesting occurred during the SERS measurements. The 4-DNB molecules were anchored to the surface and Au SRNPs were separated from their incubation solution and then introduced to various concentration of 4-ATP: 0, 1, 5, 10, 20, 25, 50, 100, 250, 500, 1000 µM, as in previous exchange measurement. Figure 4.1A shows the unintended consequences of the exchange measurements, SERS spectra are shown highlighting the reactants, 4-DNB, 4-ATP and the products 4-

mercaptoazobenzene (4-MAB) and diazoaminothiobenzne (DATB) (proposed product of 4-ATP saturated Au SRNPs with various concentrations of 4-DNB, which will be addressed later. Figure 4.1B contains representative SERS spectra, a detailed view, of peaks associated with proposed molecule on surface). Au SRNP particles were incubated with excess, 1000 µM, 4-DNB to ensure an extended network of aryl ligands was formed, based on previous investigations from our group. The 4-DNB saturated Au SRNPs were prepared for exchange, with thermodynamic measurements taken 24 hours later. Thermodynamic measurements conducted for this process yield the presence of 4-ATP peak 1080 cm^{-1} υ(C-S), signifying chemisorption related binding to the Au SRNP surface, figure 4.1 C. Further increasing of 4-ATP concentration to 50 µM, causes a sharp increase in SERS intensity of the 1080 cm^{-1} mode, which is correlated to new peak formation at in 1390 and 1440 cm^{-1} υ(N≡N) associated with azo formation [24, 25], as depicted in figure 4.1 D and E. Previous reports have confirmed the presence of a multilayer structure defined by

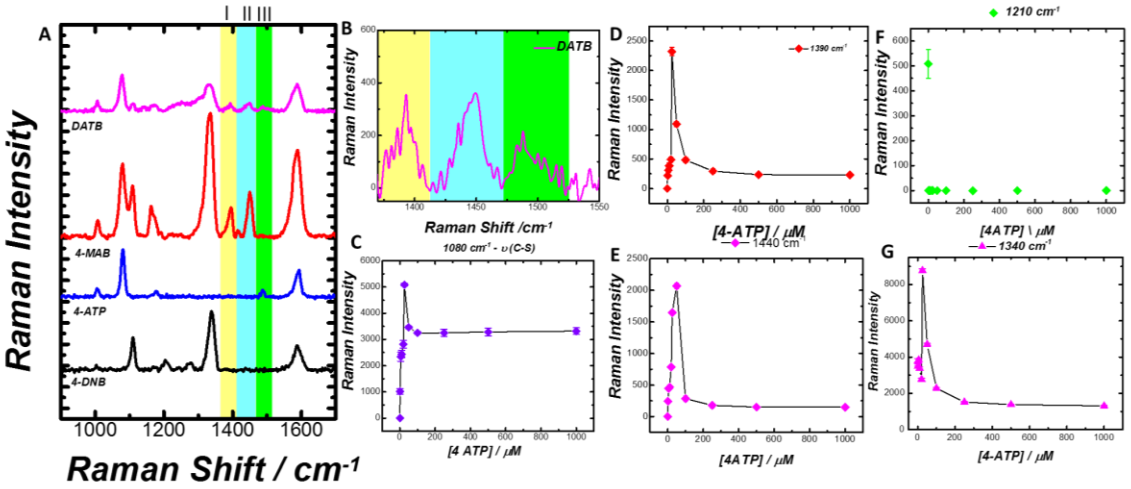

Figure 4. 1 Representative SERS spectra depicted in A) 50 uM 4-DNB, 50 uM 4-ATP and products: 4-MAB, 4-DATB. Up close view of peaks associated with product of 4-ATP and 4-DNB (B), highlighted to emphasize difference from Azo molecule peaks. Part C-G repesenting thermodynamic points for the diazonium coupling with various concentrations of 4-ATP: 0, 1, 5, 10, 20, 25, 50, 100, 250, 500, 1000 µM. Peaks analyzed associated with the reactant 4-DNB (1210, 1340 cm^{-1}), 4-ATP (1080 cm^{-1}) and product, 4-MAB (1390 cm^{-1} and 1440 cm^{-1})

intensities from 1210 cm^{-1}mode [17, 20-23], but when introduced to the lowest concentration of 4-ATP, 1 µM, the multilayer is greatly disturbed with no SERS intensity observed after the introduction of 4-ATP, figure 4.1 F. The $\upsilon(NO_2)$ peak from 4-DNB also demonstrates a correlated increase with the formation of the $\upsilon(N{\equiv}N)$ peaks, 1390 and 1440 cm^{-1}, which is shown in figure 4.1 G, signifying a change in the local environment on the Au SRNP

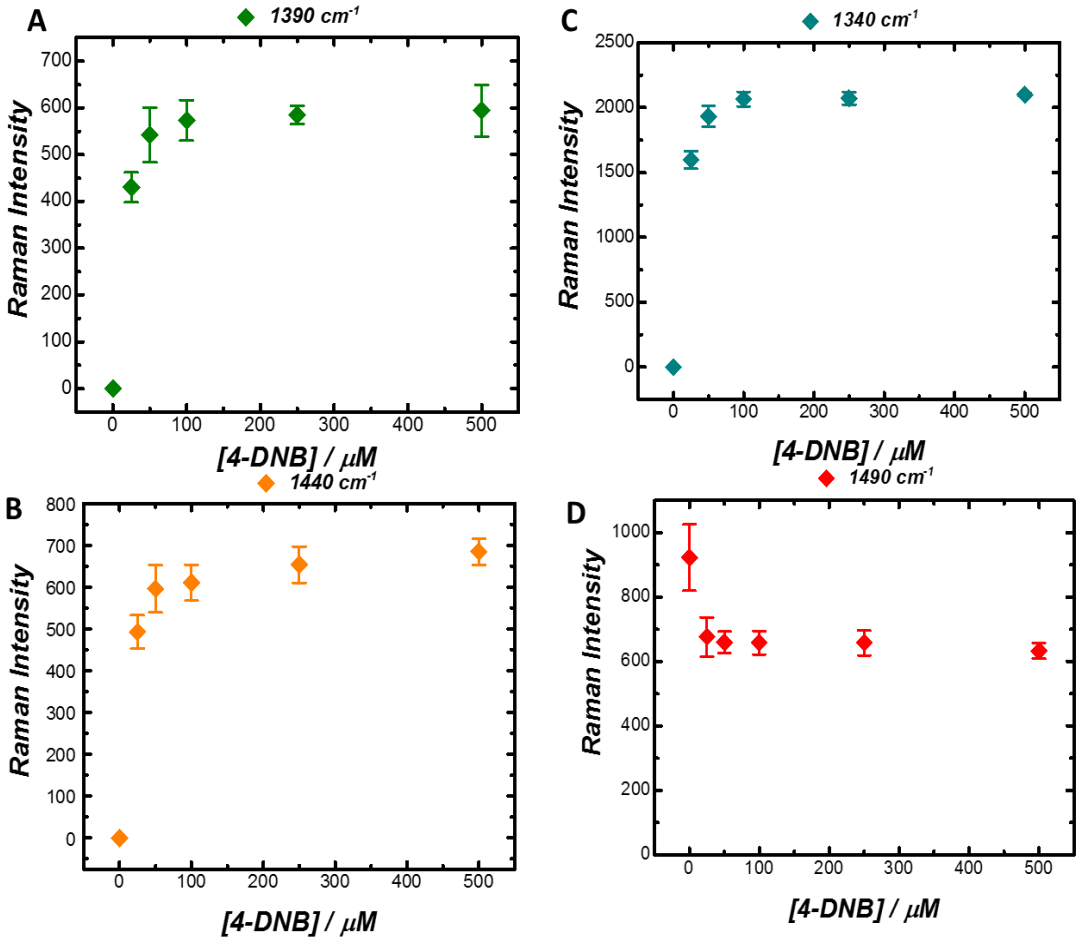

Figure 4. 2 Thermodynamic measurements for 50 uM 4-ATP saturated Au SRNPs after introduction of various concentration of 4-DNB; 0, 25, 50, 100, 250 and 500 uM. Measurements trace evolution of SERS intensity for the following peaks associated with the diazoaminthioenzene (DATB), 4-ATP and 4-DNB, A) DATB - 1390 cm-1, B) DATB - 1440 cm-1, C) 4-DNB - 1340 cm-1, D) DATB / 4-ATP - 1490 cm-1.

surface, possibly a consequence of combined SERS intensity from both 4-DNB and 4-MAB [24]. Although molecules like 4-diazoniumnitrobenzene tetrafluoroborate, are reactive

on their own in water, yielding azo molecules when introduced to other substituted aromatic molecules [26]. These diazonium molecules are anchored to the surface and to other 4-DNB molecules, reducing the free diazonium in solution to near zero until the disruption of the so-called ML, which is illustrated by the disappearance of 1210 cm^{-1} peaks.

When the Au SRNPs saturated with 4-ATP and introduced to various concentrations of 4-DNB: 0, 25, 50, 100, 250, 500 µM, we do not observe the same phenomena. The thermodynamic measurements, figure 4.2, suggest that there is a concentration regime where the newly adsorbed 4-ATP molecules and 4-DNB molecules on the surface are coupled together, indicated by the huge increase in SERS intensity at ~50 µM 4-ATP. Previously we research by our group suggest that the 4-DNB creates a network of umbrella like structures that allow for the adsorption of other molecules, like 4-ATP. Furthermore, these two molecules must be present on the surface for the coupling to proceed and they

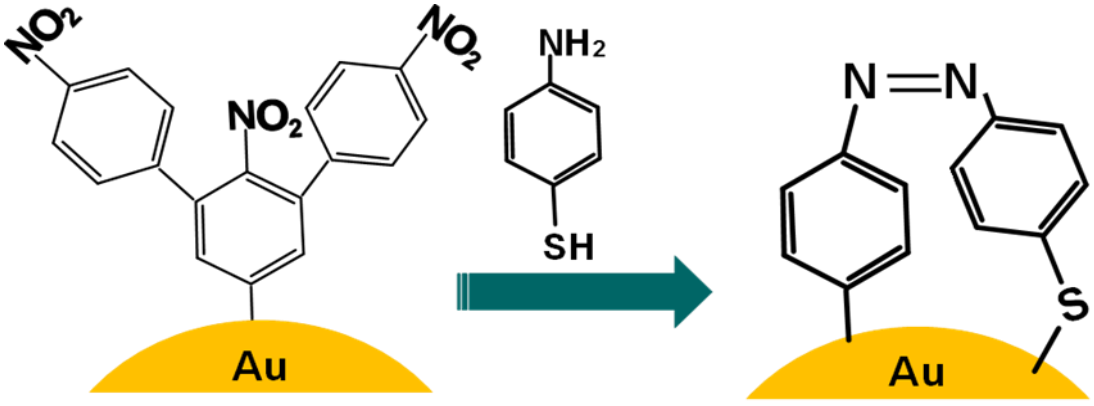

Schematic 4. 1 Depiction of interaction of extended multilayer (ML) network with incoming 4-ATP molecule on Au surface.

must be in a proximity to each other enough to form the new product on the surface as portrayed in schematic 4-1. As the concentration of 4-ATP increases, there is a pronounced

decrease in the SERS intensity for all vibrational modes involved except the υ(C-S) mode at 1080 cm^{-1}, possibly due to increased packing of 4-ATP on the surface preventing 4-DNB from accessing 4-ATP molecules to react.

When reversing the exchange i.e. incubating the Au SRNPS with 50 µM 4-ATP, to ensure the nanoparticle surface is saturated, and then exposing them to various concentrations of 4-DNB; 0, 25, 50, 100, 250 and 500 µM, the spectral profile for these measurements does not yield the same results, figure 4.1 B. The presence of both 1390and 1440 cm^{-1} modes are still present but the intensity is altered, as well as, maintaining the spectral features of the original 4-ATP molecules and incorporating the $\upsilon(NO_2)$ from the 4-DNB. We found that the SERS peak intensity at 1480 cm^{-1}, which was assigned to a coupled υC−N + βC−H + υ(C−C)Ar mode [27] for 4-ATP, is present during the entire reaction, from the introduction of the 4-DNB to 4-ATP. This peak coupled with the azo υ(N≡N), 1390 and 1440 cm^{-1} may signify the structural integrity of the 4-ATP molecule with additional features. We previously showed that this 1480 cm^{-1} peak is associated with the orientation of the 4-ATP molecule, i.e. it increases with greater packing density or when the molecules are in a more vertical position [27]. We propose that the new structure is a combination of 4-ATP and 4-DNB, which has been referred to as diazoaminobenzene molecule anchored by the Au-S bond yielding a diazoaminothiobenzene (DATB) molecule on the surface, depicted in schematic 1. Although, this reaction has been reported to occur by converting adsorbed 4-ATP to diazonium ion with $NaNO_2$ / HCl, followed by introduction of more 4-ATP on gold electrodes [28], our method is initiated only in H_2O. We suggest that due to the steric hindrances and type of packing of the 4-ATP to the surface of the Au SRNPs, the production of the diazoaminothiobenzene is formed from the N_2^+

portion of the diazonium reacting to the NH_2 moiety of the adsorbed 4-ATP. When the molecules are not in the presence of Au SRNPs, the reaction proceeds in a different manner, by interaction of the diazonium meta the sulfur atom, portrayed in schematic 4.2.

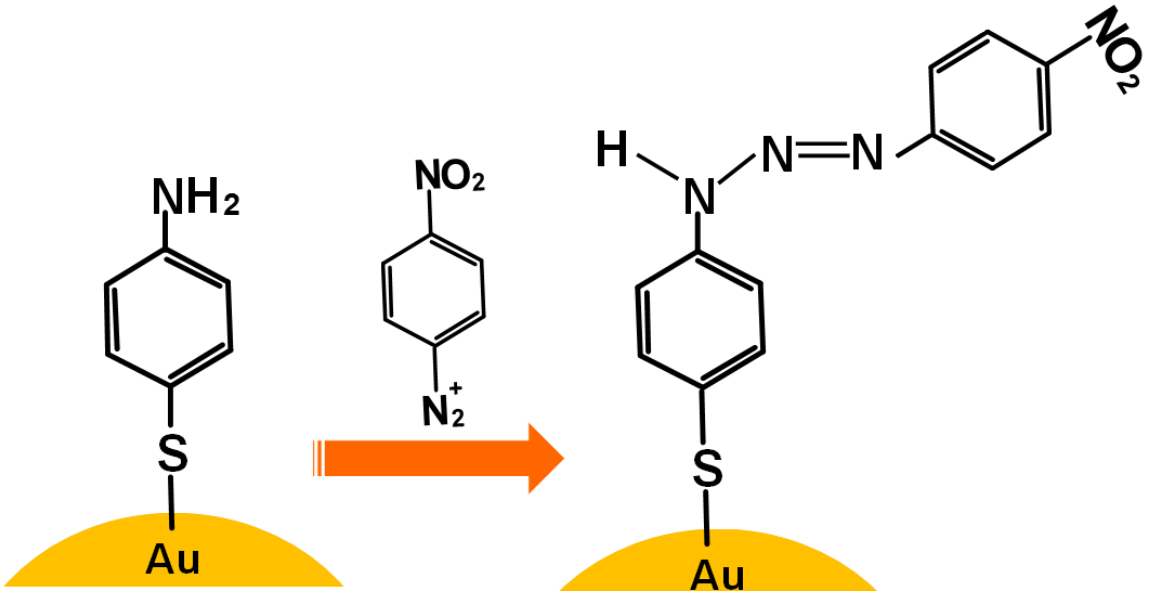

Schematic 4. 2 Possible reaction between saturated 4-ATP adsorbed Au SRNPs with incoming 25, 50, 100, 250, 500 uM 4-DNB

When the 4-ATP molecule is bound to the Au SRNPs, the introduction of 4-DNB molecules have very few binding sites to choose from, apart from the surface of the Au SRNP or the position meta to the Au-S bond. We further investigate, in situ, the kinetics of the diazoaminothiobenzene reactions by monitoring in real time the evolution of specific peak intensities, 1080, 1440, 1210, 1390, and 1110 cm^{-1} modes. Figure 4.3 A illustrates the adsorption of 4-ATP in the gaps between and underneath the umbrella conformations of the 4-DNB. From the kinetics profiles, we interpret that the initial adsorption of 4-ATP on the surface occurs at regions in between 4-DNB molecules. The intensity of 1080 cm^{-1} peak, represented in figure 4.3A, experiences a rapid increase in the beginning while the

1210 cm^{-1} peak, associated with ML formation, figure 4-3C, has an immediate decrease to near zero intensity. The introduction of 4-ATP absolutely disrupts the multilayer structure but the intensity for 1440 and 1390 cm^{-1} of υ(N≡N) has a more gradual growth, figure 4.3B and D, with the reaction terminating well after the 4-ATP reaches its relative saturation of free sites on the Au SRNPs.

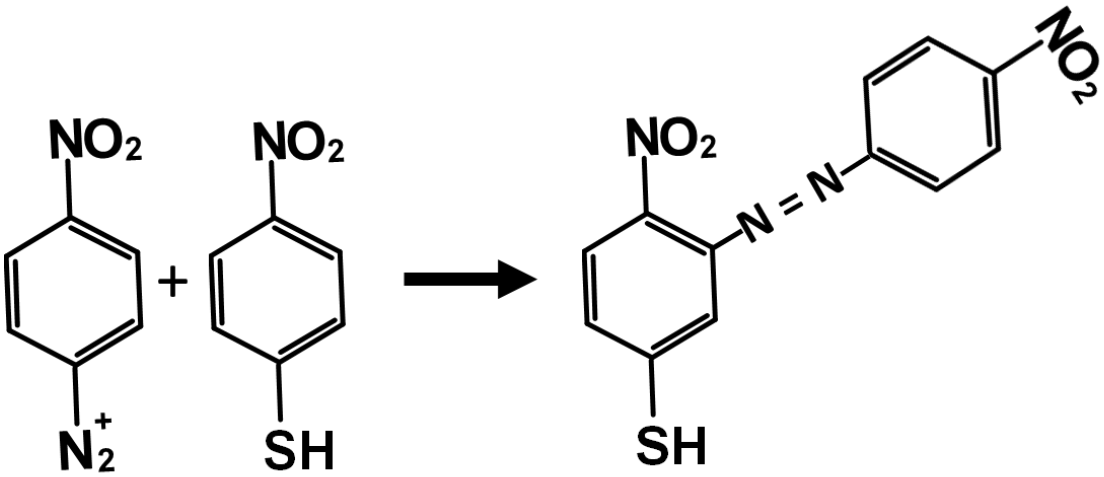

Schematic 4. 3 Original pathway for reaction of-ATP and-DNB

The 4-DNB has a characteristic peak of 1110 cm^{-1} signifying υ(C-N) + β(C-H)[17], which is not affected by the incoming 4-ATP ligand, figure 4.3E, leading to the assumption that the 4-DNB covalently bonded to the surface remain structurally sound. The total adsorption and reaction process is depicted in color coded plot, figure 4.3F, highlighting the spectral features of 4-MAB formation. Azo coupling without the presence of Au SRNPs was investigate with uv vis measurements, figure 4.4, and then by SERS, figure 4.6, to verify that this is a chemical reaction rather than photochemical reaction. Reaction was

allowed to proceed in dark for 24 hrs, then incubated with 1.0 x 10^9 particles mL^{-1}, the same concentration used throughout the experiment for consistency.

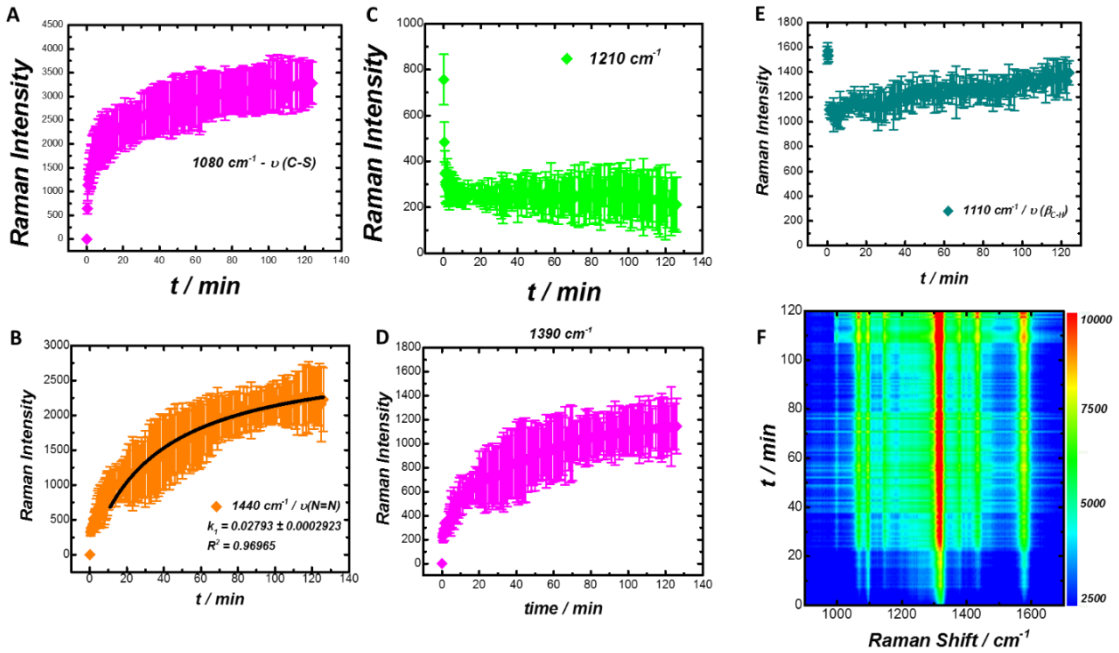

Figure 4. 3 Kinetic measurements for azo reaction of 4-DNB saturated Au SRNPs with 50 µM 4-ATP. Kinetic measurements for adsorption of 4-ATP, evolution of A) 1080 cm^{-1} υ(C-S) mode for 4-ATP. B) 1440 cm^{-1}, AZO coupling υ(N≡N), least squares curve fitting. C) Evolution of 1210 cm^{-1} multilayer (ML) peak associate with extended network of diazonium molecules on Au SRNPs, D) 1390 cm^{-1} υ(N≡N) mode for azo formation, D) 1110 cm^{-1}, 4-DNB υ(C-C) adsorbed on the Au SRNPs surface and F) color code plot illustrating the entire kinetic process depicting evolution of 4-DNB to mercaptoazobenzene (MAB) molecule. All kinetic measurements were done in triplicate with error bars representing the standard deviation.

When 4-DNB and 4-ATP are mixed in solution at various ratios, the product yields a similar SERS spectrum to the surface reaction of NB and 4-ATP. But in solution the 4-DNB's azo (N_3^+) freely associates with the 4-ATP molecules, this is not the same situation when both molecules are bound to the Au SRNPs. The azo radical is no longer present, having reacted long before the introduction of 4-ATP. We hypothesize that the interaction

with both NB bound molecules and 4-ATP bound molecules alter the electronic structure, changing the surface chemistry of the molecules initiating the reaction on the surface.

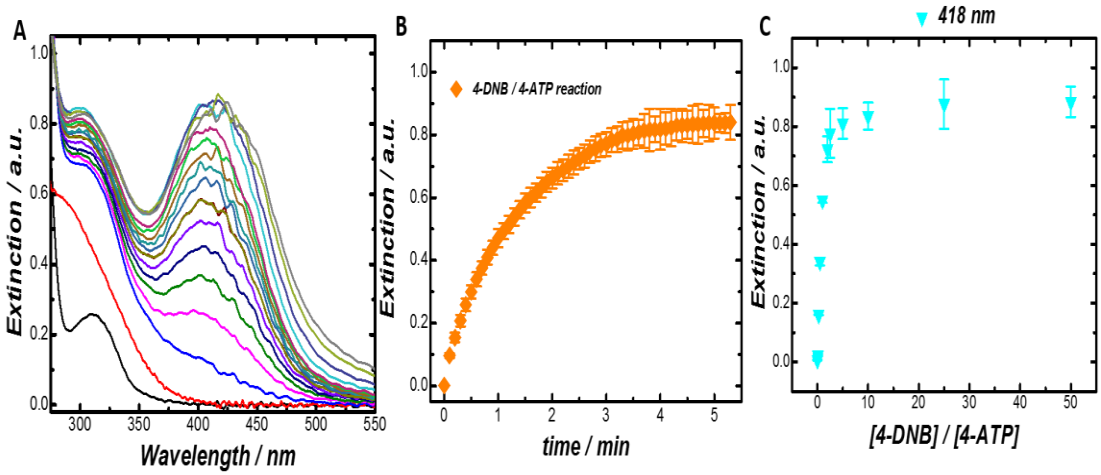

Figure 4. 4 Uv vis measurement for 4-DNB reacting with 4-ATP, in the absence of Au SRNPs with A) time resolved uv vis measurements, B) temporal evolution of 418 nm peak associated with azo formation, C) thermodynamic points for ratio of 4-DNB : 4-ATP

Monitoring the reverse reaction, 4-ATP saturated Au SRNPs exposed to various concentrations of 4-DNB: 25, 50, 100, 250, 500 µM, we observe a distinctly different kinetic profile regarding the reaction kinetics. In this case, we can monitor the temporal evolution of the 1340cm^{-1} $\upsilon(NO_2)$ mode, figure 4-4A, and 1440 cm^{-1} mode $\upsilon(N\equiv N)$ depicted in figure 4.5B. From these profiles we were able to obtain k-values through least squares fitting for both nitro and azo vibrational modes. The temporal evolution curves were fitted with two exponentials corresponding with two components k_{fast} and k_{slow} revealing pseudo-first order kinetic relationship of the DATB reaction. However, we could not properly determine the kinetics associated with the first reaction that generated the 4-

MAB molecules due to the complexity of multilayers present at the initiation of the reaction.

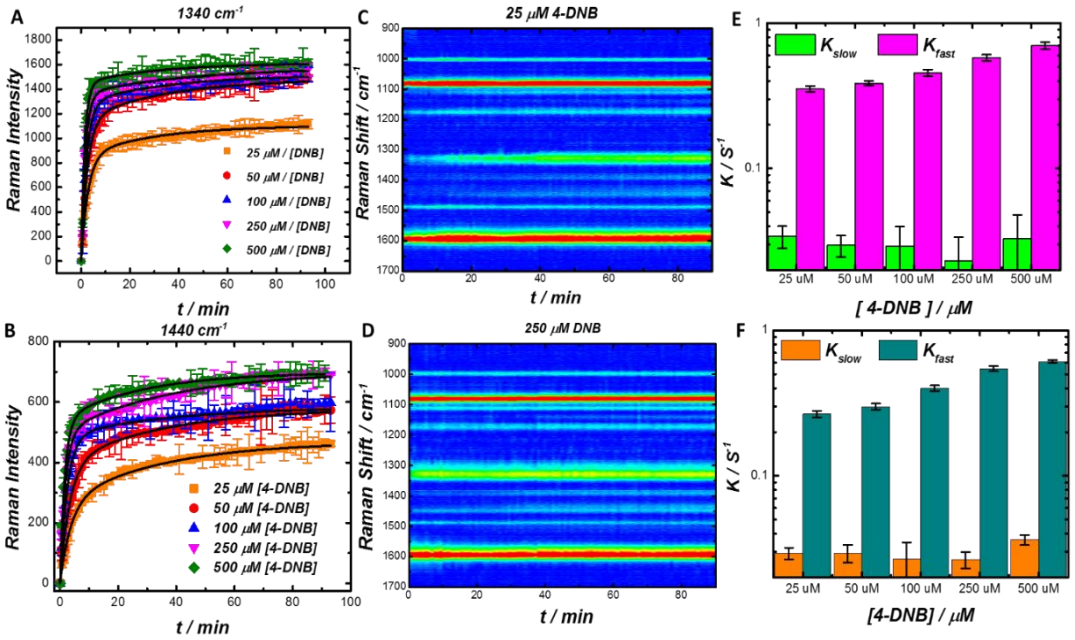

Figure 4. 5 Temporal evolution of SERS intensities of the A) 1340 cm^{-1}, B) 1440 cm^{-1}, mode upon exposure of 4-ATP-coated Au SRNPs to various concentrations of 4-DNB. Time-resolved SERS spectra of 4-ATP-coated SRNPs (obtained through incubation of CTAC-coated SRNPs with 50 µM 4-ATP for 24 h) after exposure to C) 25 µM and D) 250 µM 4-DNB at room temperature. The error bars represent the standard deviations obtained from five independent experimental runs. The solid black curves show the leastsquares curve fitting results. (E) k – vales for 1340 cm^{-1} (F) k – values for 1440 cm^{-1} at various [Concentration] 4-DNB

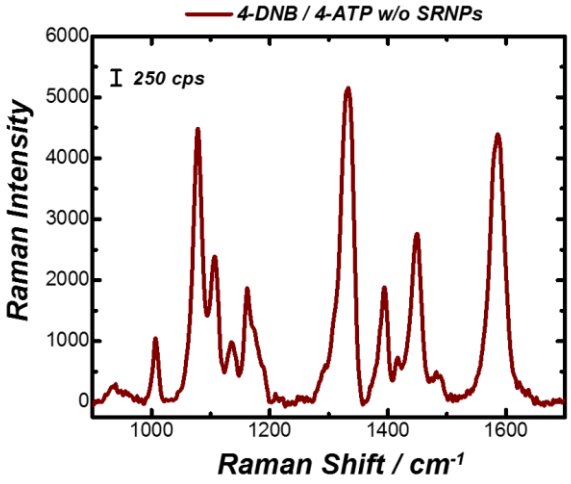

Figure 4. 6 SERS spectra for azo reaction (4-DNB + 4-ATP) in the absence of Au SRNPs.

4.4 Conclusion

The formation of new molecules 4-MAB on the surface of Au SRNPs presents a new opportunity for custom surface functionalization. This reaction does not proceed in the conventional manner due to the bound aryl ligands and no diazonium ions present in solution. We offer detailed evidence of the destruction of the multilayer coinciding with the formation of 4-MAB. The kinetics associated with this reaction are more complex and not easily interpretable because of the multilayer structure. The reaction on Au SRNPs offers another pathway for azo coupling with different kinetics than when the reaction proceeds without Au SRNPs. As for the reverse reaction, the formation of DATB on the surface of Au SRNPs is believed to be a process that proceeds with pseudo-first order kinetics, revealing that the rate constants for the reaction increase with increasing concentration of 4-DNB, however, the product formation reaches a maximum between 50 – 100 µM of 4-DNB, any more does not generate more DATB.

4.5 References

1. Haes, A. J.; Van Duyne, R. P., A nanoscale optical biosensor: Sensitivity and selectivity of an approach based on the localized surface plasmon resonance spectroscopy of triangular silver nanoparticles. Journal of the American Chemical Society 2002, 124 (35), 10596-10604
2. Kim, M.; Hohman, J. N.; Cao, Y.; Houk, K. N.; Ma, H.; Jen, A. K. Y.; Weiss, P. S., Creating Favorable Geometries for Directing Organic Photoreactions in Alkanethiolate Monolayers. Science 2011, 331 (6022), 1312-1315.

3. Zheng, Y. B.; Payton, J. L.; Song, T. B.; Pathem, B. K.; Zhao, Y. X.; Ma, H.; Yang, Y.; Jensen, L.; Jen, A. K. Y.; Weiss, P. S., Surface-Enhanced Raman Spectroscopy To Probe Photoreaction Pathways and Kinetics of Isolated Reactants on Surfaces: Flat versus Curved Substrates. Nano Letters 2012, 12 (10), 5362-5368
4. Chen, X.; Jensen, L., Understanding the shape effect on the plasmonic response of small ligand coated nanoparticles. Journal of Optics 2016, 18 (7).
5. Adams, D. M.; Brus, L.; Chidsey, C. E. D.; Creager, S.; Creutz, C.; Kagan, C. R.; Kamat, P. V.; Lieberman, M.; Lindsay, S.; Marcus, R. A.; Metzger, R. M.; Michel-Beyerle, M. E.; Miller, J. R.; Newton, M. D.; Rolison, D. R.; Sankey, O.; Schanze, K. S.; Yardley, J.; Zhu, X. Y., Charge transfer on the nanoscale: Current status. Journal of Physical Chemistry B 2003, 107 (28), 6668-6697
6. Buriak, J. M. Organometallic Chemistry on Silicon andGermanium Surfaces. Chem. Rev. 2002, 102, 1271–1308.
7. Ulman, A. Formation and Structure of Self-Assembled Monolayers. Chem. Rev. 1996, 96, 1533–1554.
8. Pinson, J.; Podvorica, F., Attachment of organic layers to conductive or semiconductive surfaces by reduction of diazonium salts. Chemical Society Reviews 2005, 34 (5), 429-439
9. Laforgue, A.; Addou, T.; Belanger, D., Characterization of the deposition of organic molecules at the surface of gold by the electrochemical reduction of aryldiazonium cations. Langmuir 2005, 21 (15), 6855-6865
10. Shewchuk, D. M.; McDermott, M. T., Comparison of Diazonium Salt Derived and Thiol Derived Nitrobenzene Layers on Gold. Langmuir 2009, 25 (8), 4556-4563

11. Bernard, M. C.; Chausse, A.; Cabet-Deliry, E.; Chehimi, M. M.; Pinson, J.; Podvorica, F.; Vautrin-Ul, C., Organic layers bonded to industrial, coinage, and noble metals through electrochemical reduction of aryldiazonium salts. Chemistry of Materials 2003, 15 (18), 3450-3462.
12. Laforgue, A.; Addou, T.; Belanger, D., Characterization of the deposition of organic molecules at the surface of gold by the electrochemical reduction of aryldiazonium cations. Langmuir 2005, 21 (15), 6855-6865
13. Chevalier, C. L.; Landis, E. C., Electrochemical Attachment of Diazonium-Generated Films on Nanoporous Gold. Langmuir 2015, 31 (31), 8633-8641
14. Jayasundara, D. R.; Cullen, R. J.; Soldi, L.; Colavita, P. E., In Situ Studies of the Adsorption Kinetics of 4-Nitrobenzenediazonium Salt on Gold. Langmuir 2011, 27 (21), 13029-13036
15. Berisha, A.; Combellas, C.; Kanoufi, F.; Decorse, P.; Oturan, N.; Medard, J.; Seydou, M.; Maurel, F.; Pinson, J., Some Theoretical and Experimental Insights on the Mechanistic Routes Leading to the Spontaneous Grafting of Gold Surfaces by Diazonium Salts. Langmuir 2017, 33 (35), 8730-8738.
16. Shewchuk, D. M.; McDermott, M. T., Comparison of Diazonium Salt Derived and Thiol Derived Nitrobenzene Layers on Gold. Langmuir 2009, 25 (8), 4556-4563
17. Laurentius, L.; Stoyanov, S. R.; Gusarov, S.; Kovalenko, A.; Du, R. B.; Lopinski, G. P.; McDermott, M. T., Diazonium-Derived Aryl Films on Gold Nanoparticles: Evidence for a Carbon-Gold Covalent Bond. Acs Nano 2011, 5 (5), 4219-4227.
18. Paulik, M. G.; Brooksby, P. A.; Abell, A. D.; Downard, A. J., Grafting aryl diazonium cations to polycrystalline gold: Insights into film structure using gold oxide reduction,

redox probe electrochemistry, and contact angle behavior. Journal of Physical Chemistry C 2007, 111 (21), 7808-7815

19. Guo, L. M.; Ma, L. P.; Zhang, Y. L.; Cheng, X.; Xu, Y.; Wang, J.; Wang, E. K.; Peng, Z. Q., Spectroscopic Identification of the Au-C Bond Formation upon Electroreduction of an Aryl Diazonium Salt on Gold. Langmuir 2016, 32 (44), 11514-11519
20. Ahmad, R.; Boubekeur-Lecaque, L.; Nguyen, M.; Lau-Truong, S.; Lamouri, A.; Decorse, P.; Galtayries, A.; Pinson, J.; Felidj, N.; Mangeney, C., Tailoring the Surface Chemistry of Gold Nanorods through Au-C/Ag-C Covalent Bonds Using Aryl Diazonium Salts. Journal of Physical Chemistry C 2014, 118 (33), 19098-19105
21. Menanteau, T.; Dias, M.; Levillain, E.; Downard, A. J.; Breton, T., Electrografting via Diazonium Chemistry: The Key Role of the Aryl Substituent in the Layer Growth Mechanism. Journal of Physical Chemistry C 2016, 120 (8), 4423-4429
22. Combellas, C.; Kanoufi, F.; Pinson, J.; Podvorica, F. I., Sterically hindered diazonium salts for the grafting of a monolayer on metals. Journal of the American Chemical Society 2008, 130 (27), 8576-8580
23. Kariuki, J. K.; McDermott, M. T., Formation of multilayers on glassy carbon electrodes via the reduction of diazonium salts. Langmuir 2001, 17 (19), 5947-5951
24. Yi-Fan Huang, Hong-Ping Zhu, Guo-Kun Liu, De-Yin Wu, Bin Ren, and Zhong-Qun Tian Journal of the American Chemical Society 2010 132 (27), 9244-9246
25. Sai Duan, Yue-Jie Ai, Wei Hu, and Yi Luo The Journal of Physical Chemistry C 2014 118 (13), 6893-6902
26. Patai, Saul, The chemistry of diazonium and diazo groups, Chichester [England] ; New York : J. Wiley, 1978

27. Esteban Villarreal, Guangfang Grace Li, Qingfeng Zhang, Xiaoqi Fu, and Hui WangNano Letters 2017 17 (7), 4443-4452

28. Li, F.; Feng, Y.; Dong, P.; Tang, B. Biosensors and Bioelectronics 2010, 25, 2084.

Chapter 5
Carving the Growing Nanocrystals: Coupling Seed-Mediated Growth with Oxidative Etching

5.1 Introduction

This work presents multiple experimental evidences coherently showing that the versatile structural evolution of Au nanocrystals during seed-mediated growth under the guidance of foreign metal ions and halide-containing surfactants is essentially dictated by the dynamic interplay between oxidative etching and nanocrystal growth. Coupling nanocrystal growth with oxidative etching under kinetically controlled conditions enables in situ surface carving of the growing nanocrystals, through which the surface topography of shape-controlled nanocrystals can be deliberately tailored on the nanometer length-scale.

Precise geometry control of nanocrystals through deliberately designed colloidal syntheses forms the keystone for the fine-tuning and rational optimization of the plasmonic and catalytic properties of metallic nanoparticles for widespread applications in nanophotonics,[1] molecular sensing,[2] catalysis,[3] and biomedicine.[4] Fundamentally intriguing and methodologically invaluable to the colloidal nanoscience communities has been the seed-mediated growth of metallic nanocrystals exhibiting thermodynamically unexpected anisotropic geometries.[5-23] The remarkable level of precision and versatility of geometry control realized through seed-mediated growth has been best manifested by the controlled transformations of preformed isotropic Au nanocrystal seeds into an entire family of geometrically distinct anisotropic Au nanostructures, such as nanorods,[5-8] nanoprisms,[9, 10] nanobipyramids,[11] and high-index faceting nanopolyhedra,[12-16] under kinetically controlled conditions synergistically guided by foreign metal ions, most commonly Ag^{+}, and halide-containing surfactants, typically cetyltrimethylammonium bromide (CTAB) and cetyltrimethylammonium chloride (CTAC).

Although the seed-mediated synthetic protocols developed for various anisotropic nanocrystal geometries appear fairly similar at first glance, variation of any of the synthetic parameters, even to a slight degree, may drastically modify the shapes of the resulting nanocrystals.[13, 17, 18, 23] Such subtlety and versatility of the syntheses are intrinsically tied to the mechanistic complexity of the seed-mediated nanocrystal growth processes. The mechanisms underlying the anisotropic structural evolution of Au nanoparticles have so far been discussed mainly in the context of shape-controlled nanocrystal growth dictated not only by the crystallographic habit of the parental seeds but also more profoundly by the structure-directing additives that regioselectively and dynamically passivate the surfaces of the evolving nanocrystals.[5-23] Several critical aspects regarding the detailed shape-evolving mechanisms, such as the driving force for symmetry-breaking, the structural dynamics at the evolving particle/solution interfaces, and the exact roles of Ag^+ foreign cations and the halide counter ions of the surfactants, however, have long been intensively debated and still remain ambiguous.[6, 17, 18, 24-28] According to the shape-defining rules proposed by Mirkin and coworkers,[17] the seed-mediated shape evolution of multifaceted Au nanocrystals is essentially dictated by the underpotential deposition (UPD) of Ag adatoms on Au nanocrystal surfaces, which selectively stabilizes certain types of crystallographic facets. The halide anions, on the other hand, regulate the Au deposition kinetics by forming complexes with ionic gold species and further modulate the coverage and stability of the Ag UPD adlayer through surface capping. Previous experimental observations and computational results suggest that a strong synergy exists between the Ag UPD layer and the surface-capping halide anions.[6, 17, 18, 25] While the above-mentioned shape-defining rules seem broadly applicable when interpreting ample examples in the

literature, our observations reported here strongly indicate that the growth of Au nanocrystals is entangled with oxidative etching under the Ag^{+}- and CTAC-coguided seed-mediated growth conditions, and thus is mechanistically even more complicated than people typically thought. To fully decipher the complex mechanisms underpinning the intriguing structural evolution of nanocrystals during seed-mediated growth, oxidative etching must be added as a pivotal missing piece to the puzzle.

5.2 Experimental Details

Chemicals and Materials

All reagents were used as received without further purification. Gold(III) chloride trihydrate (HAuCl4·3H2O, ACS grade) was purchased from J.T. Baker. Sodium borohydride (NaBH4, 99%), hydrochloric acid (HCl, 37%), and L-ascorbic acid (AA, 99.5%) were obtained from Sigma-Aldrich. Cetyltrimethylammonium chloride (CTAC, 96%) and silver nitrate (AgNO3, 99.9995% metal basis) were obtained from Alfa Aesar. Ultrapure water (18.2 MΩ resistivity, Barnstead EasyPure II 7138) was used for all experiments.

Synthesis of Au Seeds

Colloidal Au seeds (~ 4 nm in diameter) were synthesized by reducing HAuCl4 with NaBH4 in the presence of CTAC following a previously reported protocol.1-3 Briefly, 0.25 mL of HAuCl4 (10 mM) was introduced into an aqueous solution of CTAC (10 mL, 100 mM) under magnetic stir. Then 0.30 mL of ice cold, freshly prepared NaBH4 (10 mM) was quickly added to the solution containing both CTAC and HAuCl4. The mixture solution was stirred for 1 min, then left undisturbed for 2 h at room temperature under

ambient air, and finally diluted 1000-fold with 100 mM CTAC. The diluted seed colloids were used for the subsequent seed-mediated growth of various nanostructures.

Seed-Mediated Nanocrystal Growth

The shape-controlled nanocrystal growth was initiated by introducing 40 μL of the diluted Au seeds into an aqueous growth solution containing HAuCl4, AA, HCl, AgNO3, and CTAC. The total volume of the growth solution was 10 mL and the concentrations of CTAC and HAuCl4 were kept at 100 mM and 500 μM, respectively. The concentrations of HCl, AA, and AgNO3 were systematically varied to tune the rate of the nanocrystal growth relative to that of oxidative etching, based on which the shapes and surface topography of the resulting nanocrystals were fine-tailored. Upon the addition of seeds, the reactants were gently mixed for 30 s and then left undisturbed at room temperature for various reaction times. To control the concentration of oxygen dissolved in the growth solutions, the reaction mixtures were kept under ambient air or purged with N2 or O2 prior to (for 1 h) and throughout the reaction processes. The as-obtained nanoparticles were washed with water 3 times through centrifugation/redispersion cycles, and finally redispersed in water.

Structural Characterizations

The structures of the nanoparticles were characterized by scanning electron microscopy (SEM) using a Zeiss Ultraplus thermal field emission scanning electron microscope. The samples for SEM measurements were dispersed in water and drop-dried on silicon wafers. An energy dispersive spectroscopy (EDS) elemental analysis unit attached to the microscope was used to map the spatial distribution of Au and Ag elements in each nanoparticle. The bulk Ag:Au atomic ratios of various samples were quantified

based on the relative areas of the Ag Lα and Au Lα peaks in the spectra. The Au seeds were imaged by transmission electron microscopy (TEM) using a Hitachi HT7800 transmission electron microscope, which was operated at an accelerating voltage of 120 kV. XPS measurements were carried out using a Krato AXIS Ultra DLD XPS system equipped with a monochromatic Al Kα source. The samples for XPS measurements were all freshly prepared and dried in vacuum before being loaded into the XPS chambers. The surface Ag:Au atomic ratios of various samples were quantified based on the relative areas of the Ag 3d and Au 4f peaks in the spectra. The sample penetration depth of the XPS measurements under the current experimental conditions was calibrated to be ~ 1 nm,4 roughly corresponding to 5 atomic layers from the outer surface of the nanoparticles. Therefore, the formation of a saturated monolayer coverage of Ag UPD adatoms on the Au nanoparticles would ideally result in an Ag/Au atomic ratio of ~ 0.25. The standard deviations of the Ag:Au atomic ratios quantified by EDS and XPS were S3 obtained from 3 samples synthesized under identical conditions and shown as the error bars in Figure 1H, Figure S7, and Figure S11. The optical extinction spectra of the nanoparticles were measured on aqueous colloidal suspensions at room temperature using a Beckman Coulter Du 640 spectrophotometer. The total amounts of gold and silver remaining in the supernatant at various reaction times were quantified using a Finnigan ELEMENT XR double focusing magnetic sector field inductively coupled plasma-mass spectrometer (SF-ICP-MS) after separating the nanocrystals from the growth solutions.

Additional Discussion of the Temporal Evolution of Optical Extinction Spectra

The surface-roughened quasi-spherical nanoparticles (SRQSNPs), surface-textured concave nanocubes (STCNCs), and excavated cuboctahedral nanoparticles (ECONPs) all

exhibited plasmonic characteristics sensitively dependent upon their sizes, shapes, and surface topography. Therefore, the structural evolution of the nanocrystals could be monitored in situ using optical extinction spectroscopy without separating the nanocrystals from their growth solutions. The plasmon resonance band of the Au-Ag alloy SRQSNPs progressively red-shifted and broadened as the particle size increased (Figure S8A), in line with previous observations on the surface-roughened Au nanoparticles.5 When the SRQSNPs became larger than ~ 150 nm, a spectral feature corresponding to the quadrupole resonance emerged around 650 nm in addition to the dipole resonance due to phase retardation effects.6-9 For the STCNCs, the surface indentation led to spectral redshift of the plasmon resonance, while the nanoscale surface texturing caused significant broadening of the peaks (Figure S8B). During the growth of ECONPs, the plasmon resonance peak first underwent a red-shifting and broadening process due to surface indentation and texturing, and then blue-shifted upon corner truncation at the later stages of the reactions (Figure S8C). Besides the plasmon resonance peaks in the visible and near-infrared, the spectral feature in the wavelength range below 400 nm arose from the interband electronic transitions of Au. Because the intensity of extinction due to interband transitions was qualitatively proportional to the Au mass in the nanocrystals, the rate of the mass increase of growing nanocrystals could be straightforwardly tracked by monitoring the temporal evolution of the optical extinction at 350 nm (Figure S8D), which showed that the nanocrystal growth rates decreased with increase of HCl concentration.

5.3 Results and Discussion

We employed CTAC-capped Au colloids (~ 4 nm in diameter, see Figure S1 in Electronic Supplementary Information†) as the seeds to guide the shape evolution of Au nanocrystals at room temperature under ambient air in aqueous growth solutions containing $HAuCl_4$ as the ionic gold precursor, CTAC as a surface-capping surfactant, ascorbic acid (AA) as a mild reducing agent, $AgNO_3$ as the source of Ag^+ foreign ions, and HCl as a pH regulator. In the absence of seeds, $AuCl_4^-$ was first reduced by AA to form $AuCl_2^-$, which was further reduced to metallic Au upon the addition of seeds to the growth solution.[6, 13, 18] The rate of the seed-mediated Au reduction was pH dependent, increasing with the pH of the growth solution.[6, 17, 18, 28] On the other hand, the O_2 dissolved in the growth solution was capable of mildly oxidizing the Au atoms on the surfaces of the growing nanocrystals to form $AuCl_2^-$ with the aid of Cl^- as the complexing agent through the following reaction:[29]

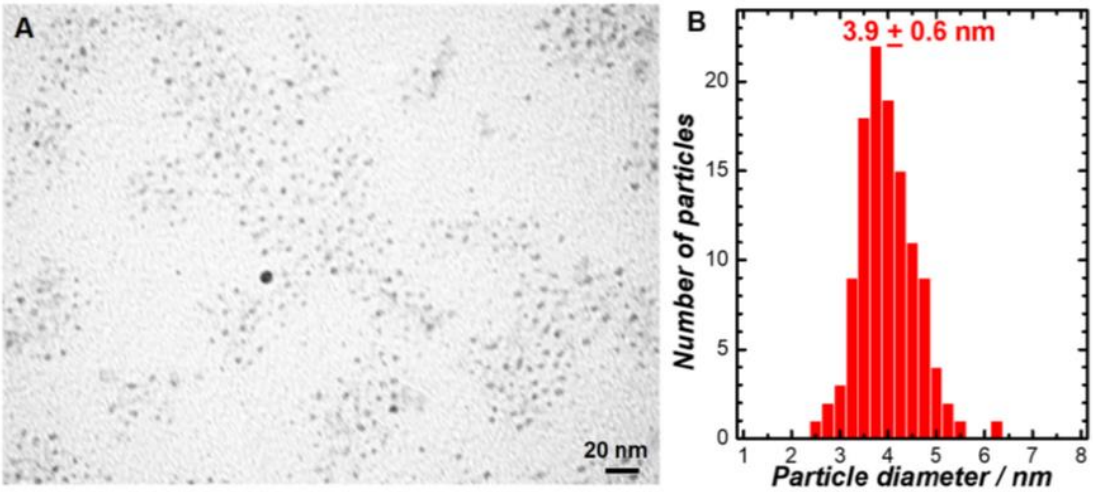

Figure 5. 1 (A) TEM image and (B) size distribution of colloidal Au seeds

This etching process could be kinetically boosted by simply decreasing the pH of

$$4Au + O_2 + 8Cl^- + 4H^+ \rightarrow 4AuCl_2^- + 2H_2O$$

the growth solution without introducing any additional strong oxidants. As demonstrated by Wang, Stucky, and coworkers,[29] preformed single-crystalline Au nanorods underwent a shortening process driven by selective etching along their longitudinal axis in the presence of dissolved O_2 and CTAC or CTAB in an acidic environment. Xia and coworkers [30-32] also employed halide anions and O_2 in polyol solvents as mild etchant pairs to carve the surfaces of metallic nanocrystals in a site-selective manner. Here, we used HCl as a unique synthetic knob to tune the relative rates of oxidative etching vs. nanocrystal growth, through which we were able to fine-tailor the surface topography of nanocrystals adopting several primary geometries, such as quasi-spheres, cubes, and cuboctahedra, by controllably carving the surfaces of the growing nanocrystals in situ.

Increase of HCl concentration, C_{HCl}, in the growth solution sped up the oxidative etching while simultaneously slowing down the nanocrystal growth. We systematically varied the C_{HCl} in the range of 0-25 mM while fixing the concentrations of $HAuCl_4$, $AgNO_3$, CTAC, and AA at 500 μM, 50 μM, 100 mM, and 1.2 mM, respectively. After the reactions proceeded for 16 h, we kinetically trapped the resulting nanostructures by separating them from their native growth solutions through centrifugation followed by redispersion in water. As revealed by the scanning electron microscopy (SEM) images in Figure 1A-1G, alteration of C_{HCl} markedly modified the shapes and surface topography of the resulting nanocrystals. At C_{HCl} below 3 mM, the isotropic seeds evolved into surface-roughened quasi-spherical nanoparticles (SRQSNPs, Figure 1A-1B) as a consequence of mild etching of fast-growing nanocrystals. In the intermediate C_{HCl} regime (5-15 mM), the etching effects became more pronounced, resulting in surface-textured concave nanocubes

(STCNCs, Figure 1C-1E), which were derived from nanocubes through selective corrosion of the {100} side facets coupled with preferential Au deposition on the edges. When C_{HCl} was further increased to above 15 mM, oxidative etching became even faster while nanocrystal growth was further slowed down, leading to the formation of excavated cuboctahedral nanoparticles (ECONPs, Figure 1F-1G), a geometry derived from a nano-cuboctahedron by creating indentation on the {100} facets while retaining the {111} facets at the truncated corners.

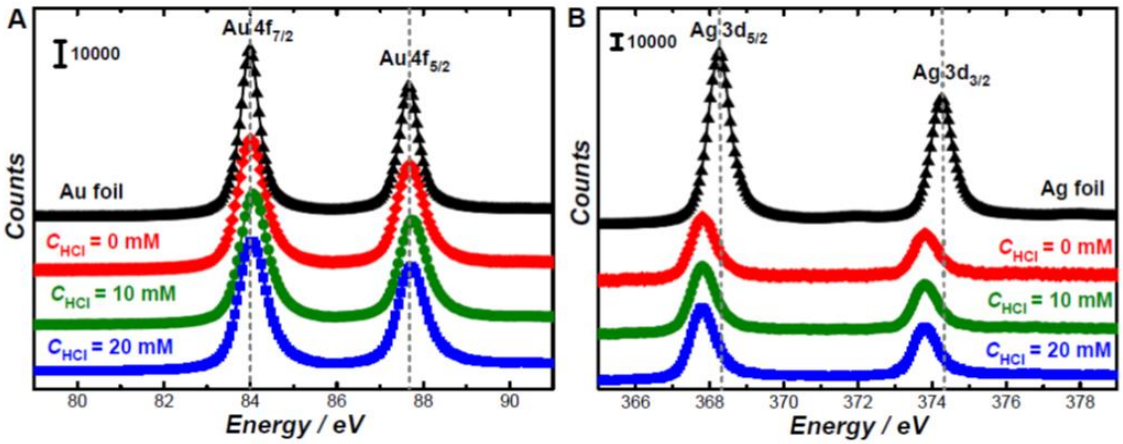

Figure 5. 2 XPS spectra of (A) Au 4f and (B) Ag 3d regions of nanoparticles synthesized after 16 h in 100 mM CTAC, 50 μM AgNO3, 500 μM HAuCl4, and 1.2 mM AA in the presence of 0, 10, and 20 mM HCl. The spectra of a bulk Au foil and Ag foil were also shown for comparison. The spectra were offset for clarity

We used X-ray photoelectron spectroscopy (XPS) and energy dispersive spectroscopy (EDS) to characterize the surface and bulk compositions of the nanoparticles, respectively. In comparison to the XPS features of bulk Ag and Au foils, the Ag 3d peaks of the nanoparticle samples significantly downshifted by ~ 0.4 eV, while the Au 4f peaks slightly upshifted by less than ~ 0.05 eV (Figure S2†), indicating the atomic intermix of Ag with Au either on the surfaces or in the sub-surface regions of the nanocrystals.[13, 28]

While Ag signals were clearly resolvable by XPS on all samples, Ag became almost undetectable by EDS on the samples synthesized at C_{HCl} above 5 mM (Figure S3†). In Figure 1H, we compared the surface and bulk Ag/Au atomic ratios quantified by XPS and EDS, respectively, for the nanoparticle samples obtained at various C_{HCl}.

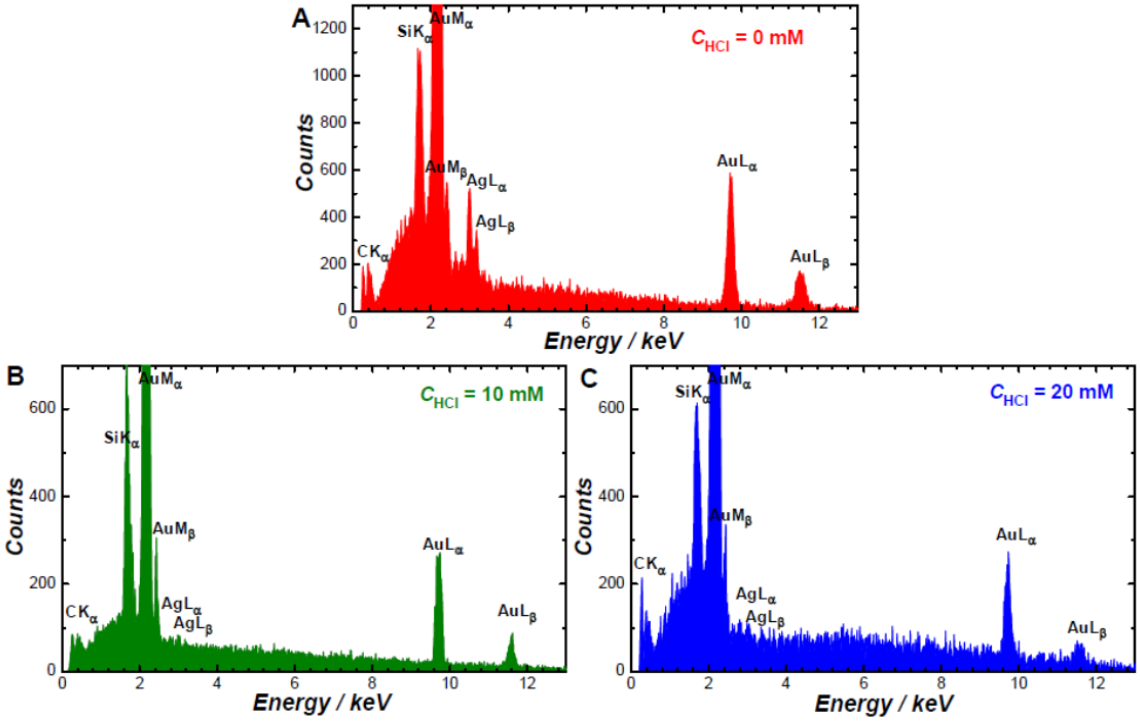

Figure 5. 3 EDS spectra of nanoparticles synthesized after 16 h in 100 mM CTAC, 50 µM AgNO3, 500 µM HAuCl4, 1.2 mM AA, and (A) 0, (B) 10, and (C) 20 mM HCl. The Si signals were from the Si substrates.

At C_{HCl} below 5 mM, EDS and XPS gave nominally the same Ag/Au atomic ratios (in the range of ~0.08-0.15), indicating that the SRQSNPs were essentially composed of Au-Ag alloys rather than phase-segregated core-shell heterostructures. Such alloy structure was further confirmed by EDS elemental mapping (Figure S4†). For the nanoparticles synthesized at C_{HCl} above 5 mM, the EDS signals of Ag became vanishingly weak while the surface Ag/Au atomic ratios quantified by XPS remained in the range of 0.15-0.22,

strongly indicating that Ag existed as a UPD atomic adlayer on the nanocrystal surfaces. The structural transition from Au-Ag alloy nanocrystals to Ag adatom-capped Au nanocrystals as C_{HCl} increased could be well interpreted as a consequence of pathway switch from Au-Ag codeposition to Ag UPD-mediated Au deposition. Detailed mechanisms underpinning this pathway switch were recently elucidated by our group using shape-controlled nanorod overgrowth as a prototypical system.[28]

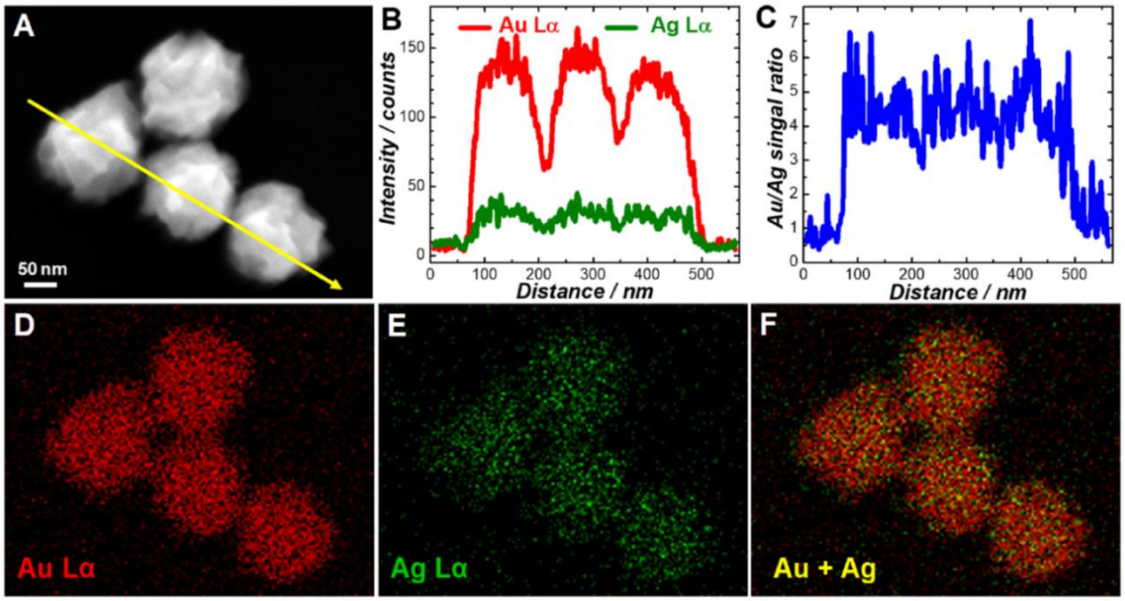

Figure 5. 4 (A) SEM image of Au-Ag alloy surface-textured quasi-spherical nanoparticles synthesized after 16 h in a growth solution containing 100 mM CTAC, 50 μM AgNO3, 500 μM HAuCl4, and 1.2 mM AA. (B) Line-profiles of EDS intensities of Au Lα and Ag Lα, and (C) line-profile of Au/Ag signal ratios across the yellow line in panel A. EDS elemental maps of (D) Au, (E) Ag, and (F) overlay of Au + Ag.

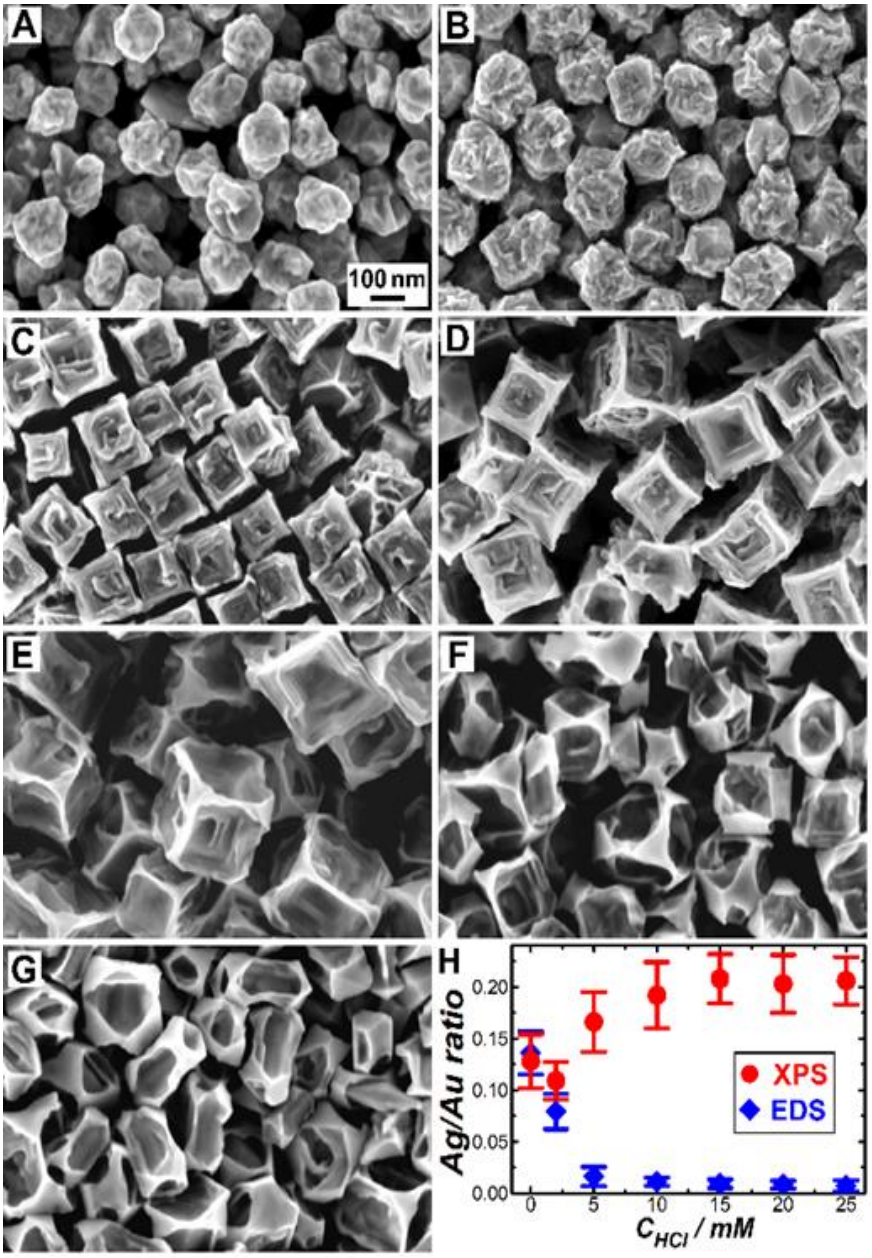

Figure 5. 5 SEM images of nanoparticles synthesized after 16 h in growth solutions containing 100 mM CTAC, 50 μM $AgNO_3$, 500 μM $HAuCl_4$, and 1.2 mM AA at various C_{HCl}: (A) 0, (B) 2, (C) 5, (D) 10, (E) 15, (F) 20, (G) 25 mM. All SEM images share the same scale bar in panel A. (H) Ag/Au atomic ratios quantified by XPS (red circles) and EDS (blue rhombi) for nanoparticles synthesized at various C_{HCl}. The error bars represent the standard deviations obtained from 3 samples synthesized under identical conditions

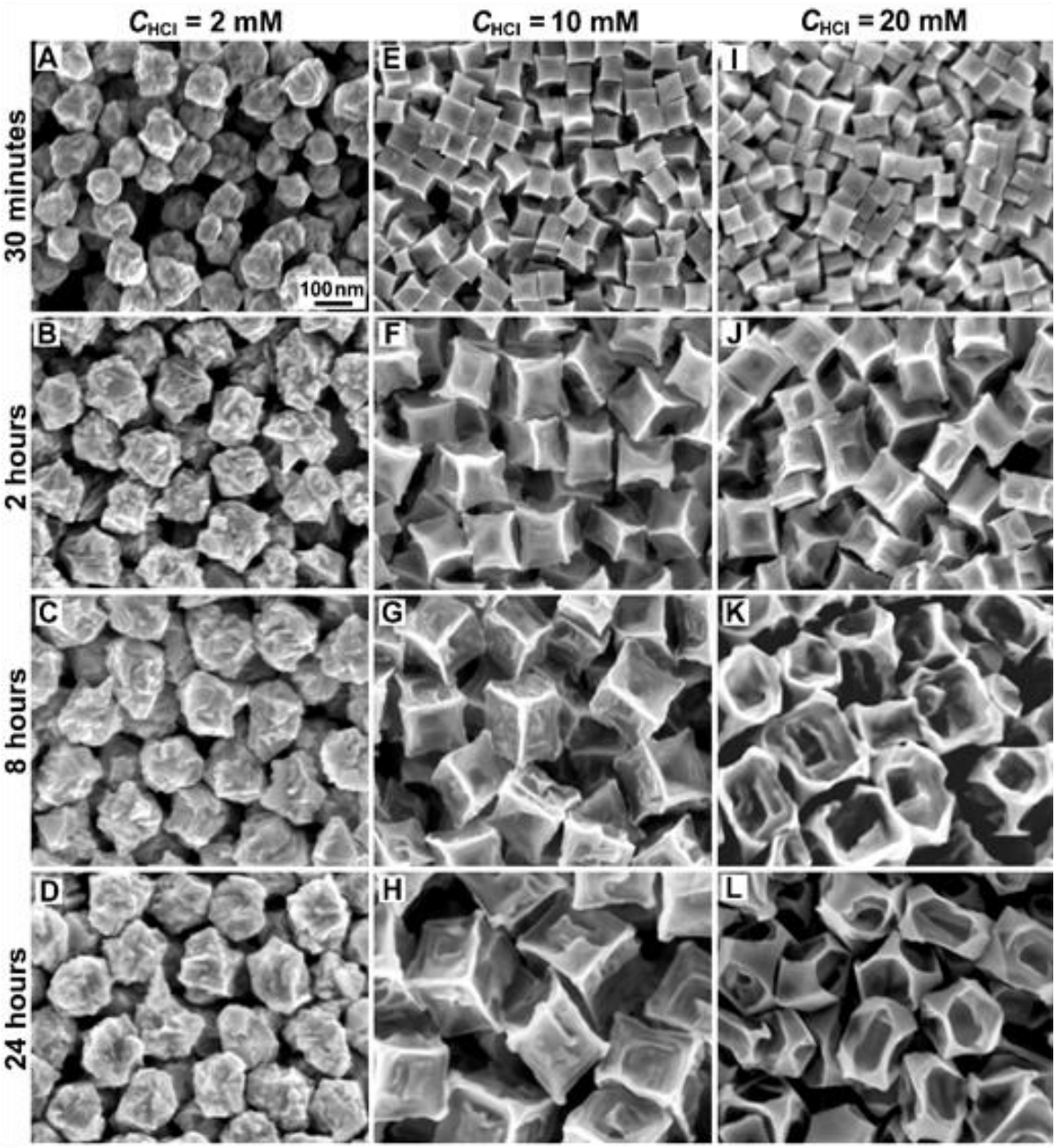

Figure 5. 6 SEM images of nanoparticles synthesized in growth solutions containing 50 µM $AgNO_3$, 500 µM $HAuCl_4$, 100 mM CTAC, and 1.2 mM AA at different C_{HCl} after various reaction times: (A) 2 mM HCl, 0.5 h; (B) 2 mM HCl, 2 h; (C) 2 mM HCl, 8 h; (D) 2 mM HCl, 24 h; (E) 10 mM HCl, 0.5 h; (F) 10 mM HCl, 2 h; (G) 10 mM HCl, 8 h; (H) 10 mM HCl, 24 h; (I) 20 mM HCl, 0.5 h; (J) 20 mM HCl, 2 h; (K) 20 mM HCl, 8 h; (L) 20 mM HCl, 24 h. All SEM images share the same scale bar in panel A.

Under this condition, fast etching of the slowly-growing nanocrystals led to not only the indentation of the side facets but also preferential oxidation of the undercoordinated surface atoms at the corners of the cube-shaped nanocrystals (Figure 2I-2L). Therefore, well-defined, thermodynamically favored {111} facets gradually developed at the truncated corners when the nanocrystal growth became much slower than etching at the late stages of the reactions.

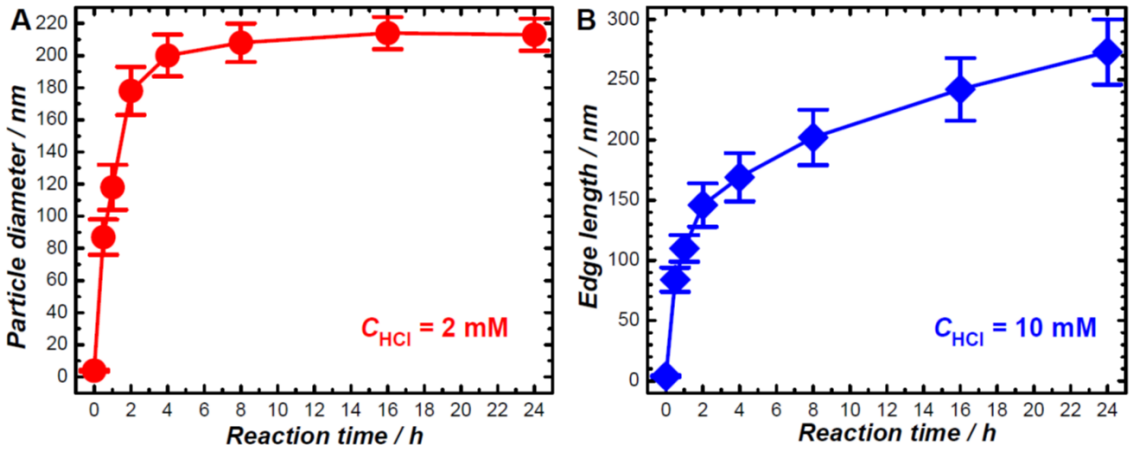

Figure 5. 7 Temporal evolution of particle sizes during the seed-mediated nanocrystal growth in growth solutions containing 100 mM CTAC, 50 μM AgNO3, 500 μM HAuCl4, 1.2 mM AA, and (A) 2 and (B) 10 mM HCl. The average particle sizes and standard deviations were obtained from 100 particles in the SEM images for each sample. The Au seeds were 3.9 + 0.6 nm in diameter.

We tracked the temporal evolution of the nanocrystal compositions ex situ using XPS and EDS (Figure S6†). The Ag/Au stoichiometric ratios of the alloy SRQSNPs remained essentially unchanged during seed-mediated growth, suggesting that Au and Ag were deposited at a constant relative rate. When the nanocrystal shape evolution was dominated by Ag-UPD, the Ag adatom coverage on the nanoparticle surfaces (quantified

by XPS) increased over time till reaching equilibria, while the Ag signals remained almost undetectable by EDS throughout the entire processes.

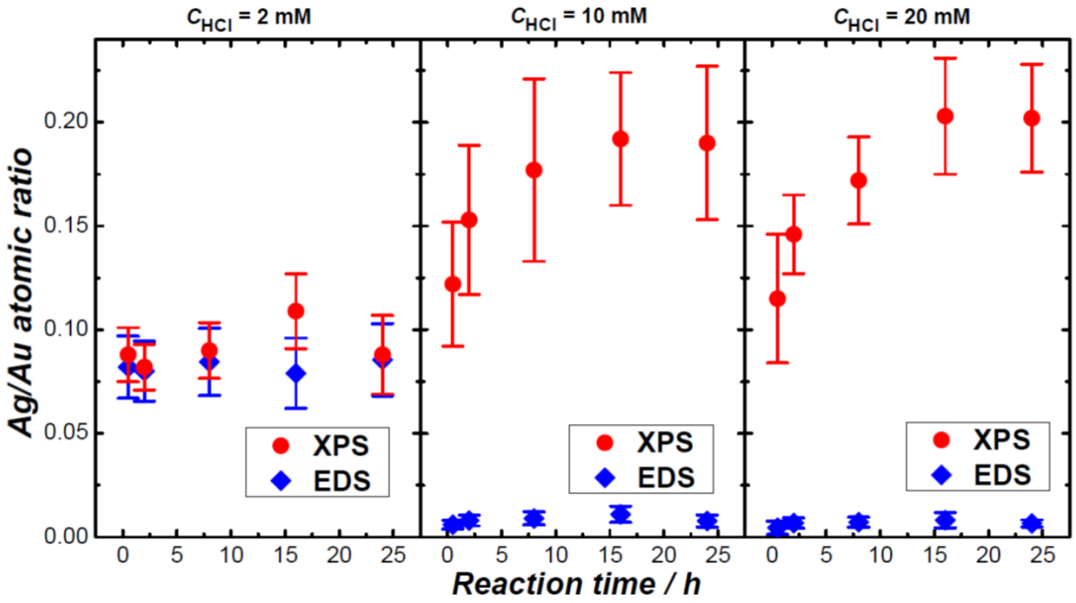

Figure 5. 8 Temporal evolution of surface Ag/Au atomic ratio (quantified by XPS) and bulk Ag/Au atomic ratio (quantified by EDS) during seed-mediated nanocrystal growth in growth solutions containing 100 mM CTAC, 50 μM AgNO3, 500 μM HAuCl4, 1.2 mM AA, and (left panel) 2, (middle panel) 10, and (right panel) 20 mM HCl. The error bars represent the standard deviations obtained from 3 samples synthesized under identical conditions.

We also used inductively coupled plasma mass spectrometry (ICP-MS) to quantify the total amounts of gold and silver remaining in the supernatant at various reaction times after separating the nanocrystals from the growth solutions (Figure S7†). At C_{HCl} of 2 mM, the total amounts of both gold and silver in the growth solutions progressively decreased until reaching the deposition/etching equilibrium as a consequence of seed-mediated Au-Ag co-deposition. When Ag UPD-mediated Au deposition occurred at C_{HCl} of 10 and 20 mM, the gold precursors were gradually consumed while the total amount of silver species in the growth solutions remained almost unchanged.

The structural evolution of the nanocrystals was further monitored in situ using optical extinction spectroscopy without separating the nanocrystals from their growth solutions. As shown in Figure S8†, increase of particle sizes, development of surface concavity, and introduction of surface textures all led to spectral redshift and broadening of the plasmon resonance peaks, whereas the plasmon resonances blue-shifted upon corner truncation. The temporal evolution of the extinction spectroscopic features was discussed

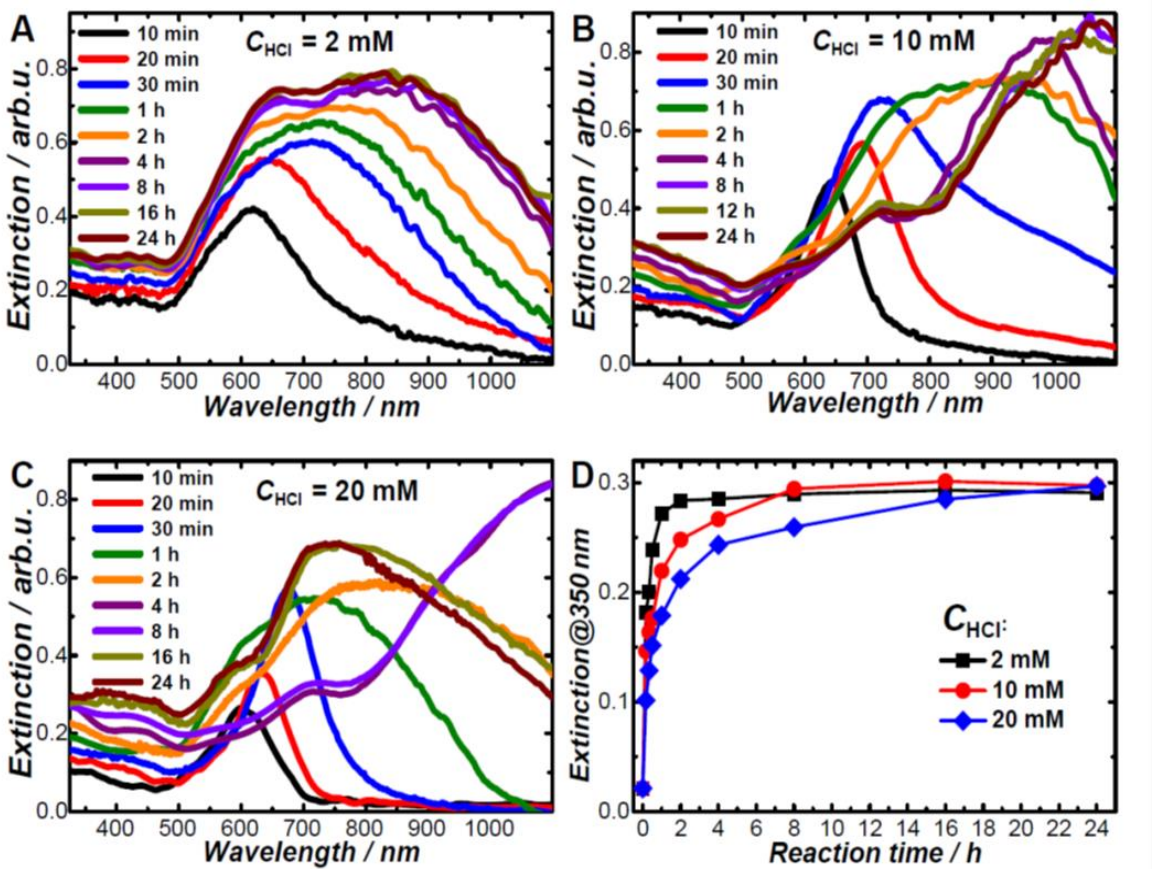

Figure 5. 9 Temporal evolution of optical extinction spectra during nanocrystal growth in 100 mM CTAC, 50 µM AgNO3, 500 µM HAuCl4, 1.2 mM AA, and (A) 2 mM, (B) 10 mM, and (C) 20 mM HCl. (D) Temporal evolution of optical extinction at 350 nm.

in greater detail in figure 5.10.

Increasing AA concentration, C_{AA}, while keeping the other synthetic parameters unchanged allowed us to accelerate the nanocrystal growth without modifying the etching

rate. At C_{HCl} of 2 mM, the surface roughness of the nanocrystals could be tailored by varying the relative growth and etching rates, achieving the highest degree of surface texturing within a C_{AA} window of 1-2 mM (Figure 5.11A-5.11C†).

At C_{HCl} of 20 mM, structural transitions from ECONPs to STCNCs and eventually to SRQSNPs were observed as C_{AA} progressively increased from 1 to 5 mM (Figure S9D-S9F†) due to acceleration of nanocrystal growth. The oxidative etching could also be kinetically modulated without changing the nanocrystal growth rate by simply varying the concentration of O_2 dissolved in the growth solution. Saturating the growth solution with O_2 resulted in loss of nanoscale surface textures and decrease of particle sizes (Figure S10A-S10C†) due to enhanced oxidative etching.

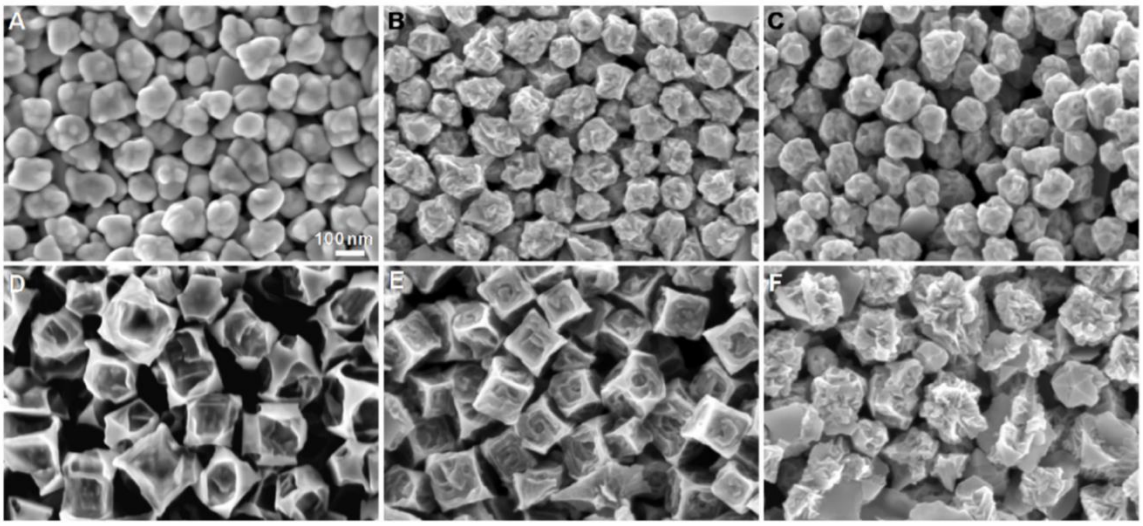

Figure 5. 11 Effects of AA. SEM images of nanoparticles synthesized after 16 h in growth solutions containing 100 mM CTAC, 50 μM AgNO3, 500 μM HAuCl4, and various concentrations of AA and HCl: (A) 0.5 mM AA, 2 mM HCl; (B) 1 mM AA, 2 mM HCl; (C) 5 mM AA, 2 mM HCl; (D) 1 mM AA, 20 mL HCl; (E) 2.5 mM AA, 20 mL; (F) 5 mM AA, 20 mM HCl. All SEM images share the same scale bar in panel A.

When the growth solution was purged with N_2 to eliminate the dissolved O_2, the oxidative etching was effectively suppressed, and the surface-roughened quasi-spherical

morphology was preserved over a broad C_{HCl} range even up to 20 mM (Figure S10D-S10F†). Interestingly, both the surface and bulk Ag/Au atomic ratios of the nanocrystals

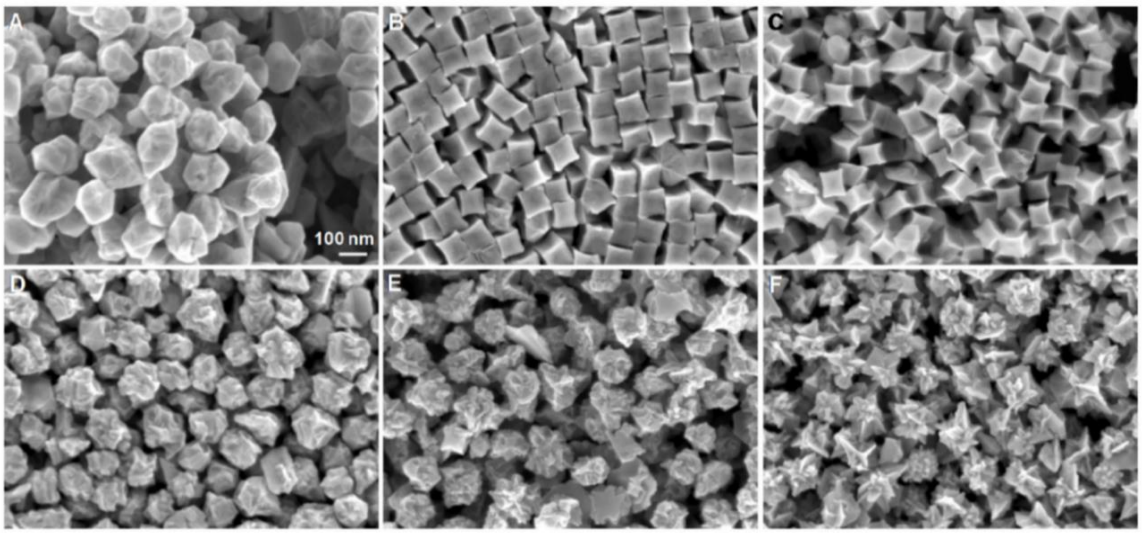

Figure 5. 12 Effects of dissolved oxygen. SEM images of nanoparticles synthesized after 16 h in oxygen-purged growth solutions containing 100 mM CTAC, 50 μM AgNO3, 500 μM HAuCl4, 1.2 mM AA, and (A) 2, (B) 10, and (C) 20 mM HCl. SEM images of nanoparticles synthesis after 16 h in deoxygenated (purged with N2) growth solutions containing 100 mM CTAC, 50 μM AgNO3, 500 μM HAuCl4, 1.2 mM AA, and (D) 2, (E) 10, and (F) 20 mM HCl. All SEM images share the same scale bar in panel A

appeared almost independent of the concentration of O_2 dissolved in the growth solution (Figure 5.12), indicating that the nanocrystal compositions were essentially determined by the relative Ag and Au deposition rates rather than the relative rates of etching vs. growth. While the effects of Ag^+ foreign ions on the seed-mediated growth of Au nanocrystals of various shapes have been well-documented in the literature,[6, 17, 18, 24-28] we found that the Ag^+ foreign ions also played crucial roles in guiding the regioselective etching of nanocrystal surfaces. At C_{HCl} of 20 mM, the degree of corner truncation increased while the surface concavity decreased as the $AgNO_3$ concentration, C_{Ag}, progressively increased in the range of 20-60 μM (Figure 5.14A-C). Increase of C_{Ag} resulted in higher coverage of

Ag UPD adatoms on the side facets of a cube-shaped nanoparticle, effectively slowing down the surface indentation process.

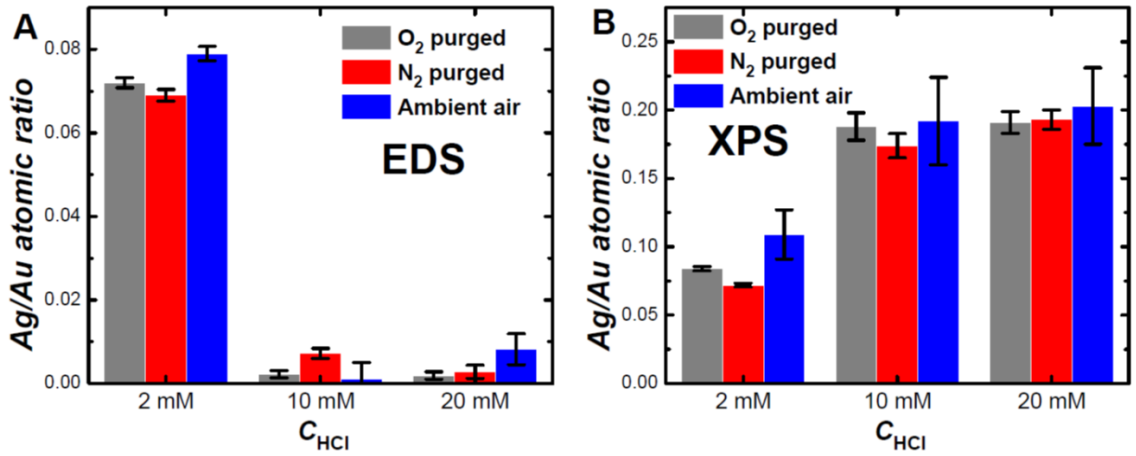

Figure 5. 13 (A) Bulk Ag/Au atomic ratio quantified by EDS and (B) surface Ag/Au atomic ratio quantified by XPS for nanoparticle samples synthesized after 16 h in growth solutions containing 100 mM CTAC, 50 μM AgNO3, 500 μM HAuCl4, 1.2 mM AA, and 2, 10, and 20 mM HCl. The growth solutions were either exposed to ambient air or purged with O2 or N2. The error bars represent the standard deviations obtained from 3 samples synthesized under identical conditions.

However, the undercoordinated surface atoms located around the corners of a cube-shaped nanocrystal still remained prone to etching. Preferential etching of the corners with respect to the side facets, coupled with preferential Au deposition on the edges led to the formation of ECONPs. When C_{HCl} decreased to 10 mM, the surfaces of the STCNCs became less concave and increasingly smoother while the sharp corners were still preserved as the surface coverage of Ag adatoms increased (Figure 3D-F), primarily due to slower etching of the corners and side facets. Removal of $AgNO_3$ from the growth solution resulted in faster oxidative etching, drastically modifying the structure-transforming process.

Under the Ag-free conditions, the Au seeds evolved into SRQSNPs at low C_{HCl}. As C_{HCl} increased, the feature sizes of surface textures increased, and well-defined crystallographic facets started to develop on the nanocrystal surfaces, resulting in blue-shift of the plasmon resonance in the extinction spectra (Figure 5.15). We further compared

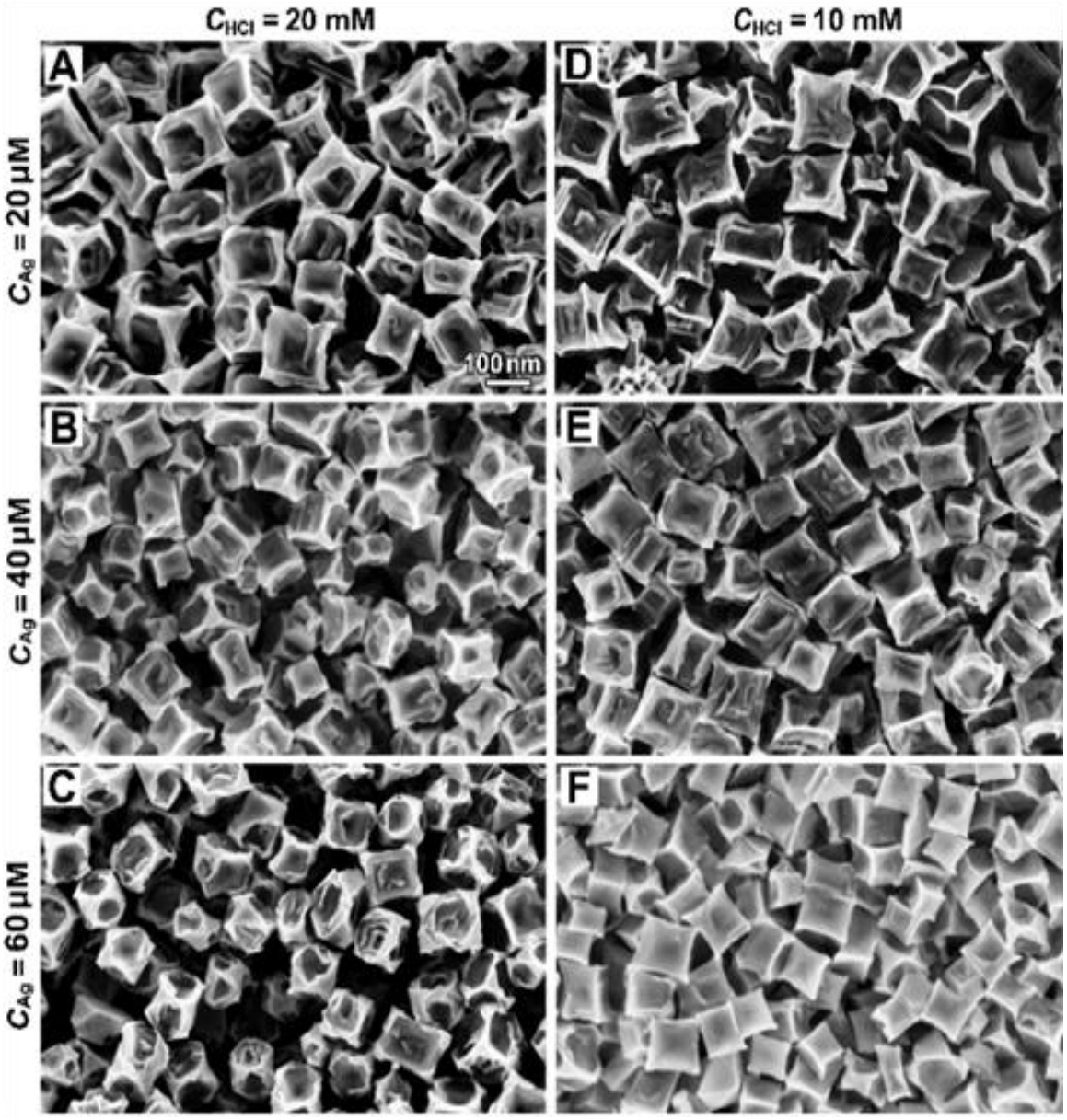

Figure 5. 14 SEM images of nanoparticles synthesized after 16 h in growth solutions containing 100 mM CTAC, 500 µM $HAuCl_4$, 1.2 mM AA, and various concentrations of HCl and $AgNO_3$: (A) 20 mM HCl, 20 µM $AgNO_3$; (B) 20 mM HCl, 40 µM $AgNO_3$; (C) 20 mM HCl, 60 µM $AgNO_3$; (D) 10 mM HCl, 20 µM $AgNO_3$; (E) 10 mM HCl, 40 µM $AgNO_3$; (F) 10 mM HCl, 60 µM $AgNO_3$. All SEM images share the same scale bar in panel A.

the post-synthetic etching of preformed Au concave nanocubes and Au-Ag alloy SRQSNPs in etching solutions containing 100 mM CTAC and 10 mM HCl, either with or without 50 μM $AgNO_3$. Apparently, the etching proceeded significantly faster in the Ag-free environment, resulting in more drastic decrease of the

particles sizes (Figure 5.16).

The Au SRQSNPs synthesized in the absence of Ag^+ foreign ions appeared even more vulnerable to oxidative etching than the Au-Ag alloy SRQSNPs, completely losing their surface textures after exposure to an etching solution containing 100 mM CTAC and 10 mM HCl under ambient air for 16 h (Figure 5.17). Therefore, the nanoscale surface textures were essentially a unique structural feature resulting from in situ mild surface etching of nanocrystals growing at appropriate rates.

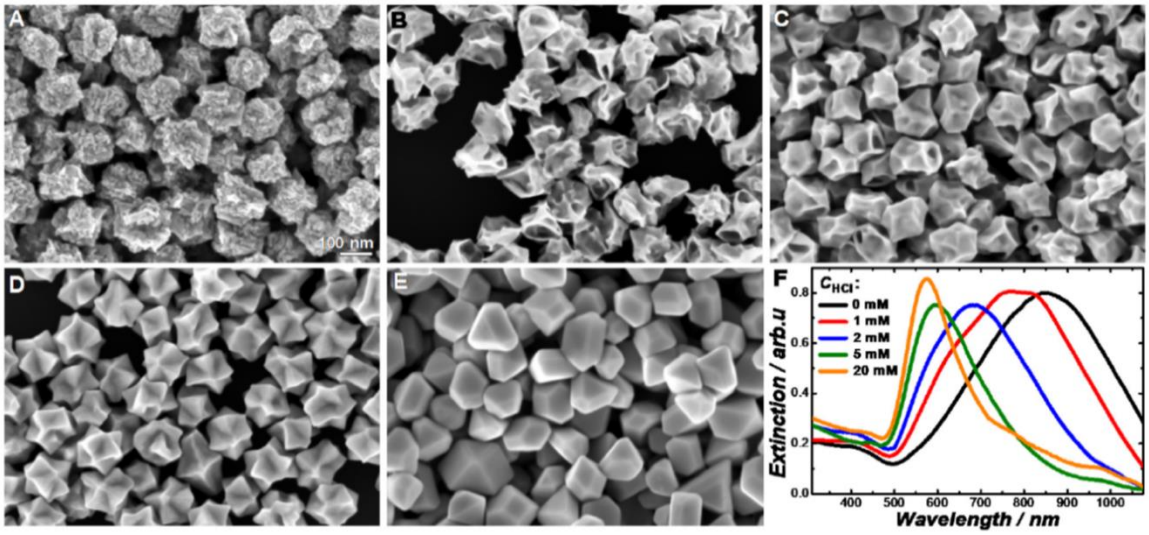

Figure 5. 15 Etching and growth of Au nanoparticles in the absence of AgNO3. Au nanoparticles synthesized after 16 h in growth solutions containing 100 mM CTAC, 500 μM HAuCl4, 1.2 mM AA, and (A) 0, (B) 1, (C) 2, (D) 5, and (E) 20 mM HCl. All SEM images share the same scale bar in panel A. (F) Optical extinction spectra of colloidal Au nanoparticles synthesized after 16 h in growth solutions containing 100 mM CTAC, 500 μM HAuCl4, 1.2 mM AA, and various concentrations of HCl as labeled in the figure.

In summary, multiple observations coherently indicate that oxidative etching interplays with nanocrystal growth under kinetically controlled conditions to guide the versatile structural evolution of Au nanocrystals during seed-mediated growth. This work provides important implications that may help us more comprehensively understand the seed-mediated growth of complex nanostructures when revisiting previously reported examples in the literature. Seed-mediated growth of various anisotropic nanostructures, such as nanorods and nanoprisms, may all involve site-selective etching of the growing nanocrystals, especially at the early stages when the symmetry of the isotropic seeds gets broken.[6, 9, 10, 26, 27] Another interesting example is the overgrowth of concave nanocube seeds into hollow Au nano-octahedra in a growth solution containing AA and HCl at a significantly higher $AgNO_3/HAuCl_4$ ratio of 1:1.[33] While the formation of the hollow octahedral nanoparticles was previously interpreted as the consequence of Ag UPD-stabilized {111} facet growth at the corners of the concave nanocube seeds, it is highly

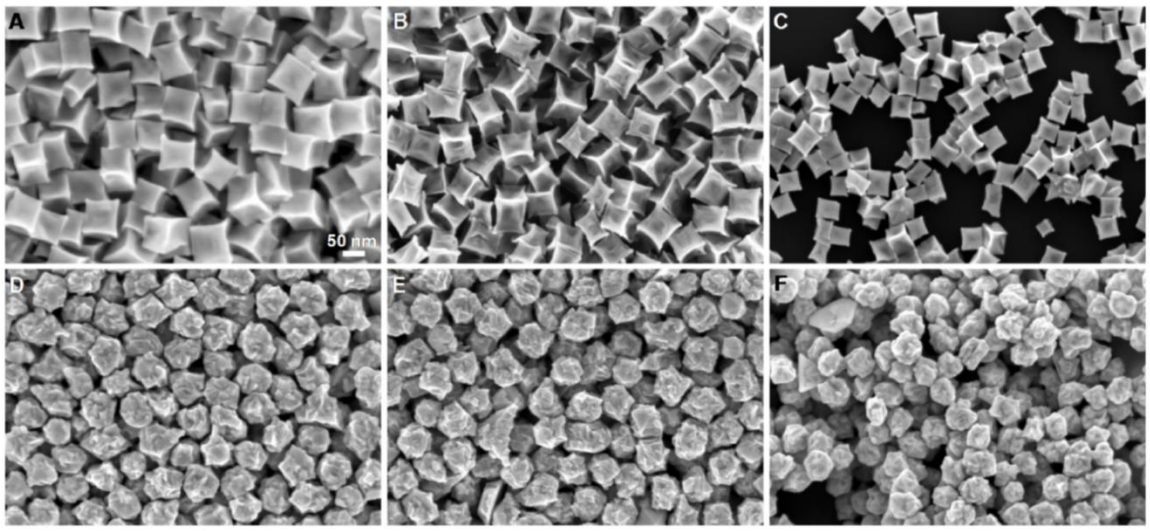

Figure 5. 16 Etching and growth of Au nanoparticles in the absence of AgNO3. Au nanoparticles synthesized after 16 h in growth solutions containing 100 mM CTAC, 500 μM HAuCl4, 1.2 mM AA, and (A) 0, (B) 1, (C) 2, (D) 5, and (E) 20 mM HCl. All SEM images share the same scale bar in panel A. (F) Optical extinction spectra of colloidal Au nanoparticles synthesized after 16 h in growth solutions containing 100 mM CTAC, 500 μM HAuCl4, 1.2 mM AA, and various concentrations of HCl as labeled in the figure.

likely that oxidative etching is also responsible for the growth of the intraparticle cavities. Here we have demonstrated that the nanoscale surface topography of shape-controlled nanocrystals can be fine-tailored through deliberate kinetic control of oxidative etching with respect to nanocrystal growth. Introduction of nanoscale surface textures to sub-wavelength metallic nanoparticles greatly expands the plasmonic tuning range and enhances the local electric fields exploitable for plasmon-enhanced spectroscopies.[34] In addition, surface-textured metallic nanoparticles may serve as an ideal model system for us to study how nanoscale surface texturing affects the light scattering properties of roughened nanostructures naturally existing in environmental and biological systems,[35] such as atmospheric dust particles and subcellular organelles. Furthermore, the surface-textured nanocrystals are enclosed by highly abundant undercoordinated surface atoms,

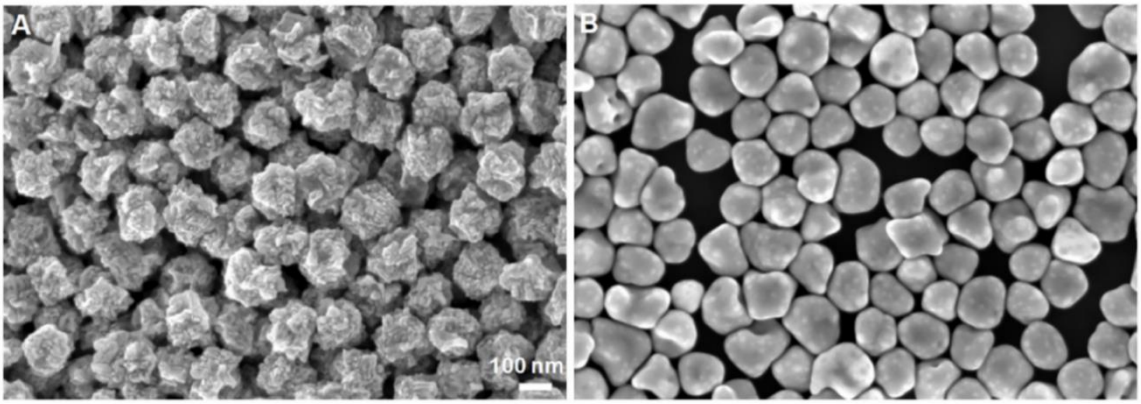

Figure 5. 17 (A) SEM image of nanoparticles synthesized after 1 h in a growth solution containing 100 mM CTAC, 500 μM HAuCl4, 50 μM AgNO3, 1.2 mM AA, and 10 mM HCl. SEM images of the nanoparticles shown in panel A after post-synthetic etching for 16 h in etching solutions containing 100 mM CTAC and 10 mM HCl (B) in the presence of 50 μM AgNO3 and (C) in the absence of AgNO3. (D) SEM image of nanoparticles synthesized after 1 h in a growth solution containing 100 mM CTAC, 500 μM HAuCl4, 50 μM AgNO3, 1.2 mM AA, and 2 mM HCl. SEM images of the nanoparticles shown in panel D after post-synthetic etching for 16 h in etching solutions containing 100 mM CTAC and 10 mM HCl (E) in the presence of 50 μM AgNO3 and (F) in the absence of AgNO3. All SEM images share the same scale bar in panel A. In all these experiments, the preformed nanoparticles were first separated from their growth solution through centrifugation, then washed with water through redispersion and centrifugation, and finally redispersed in the etching solutions.

which may serve as the active sites for heterogeneous catalysis.[36] Combination of desired plasmonic and catalytic properties on the same metallic nanocrystals further enables us to monitor intriguing catalytic molecular transformations in real time using plasmon-enhanced Raman scattering as a time-resolving and molecular finger-printing spectroscopic tool.[37-39] As exemplified by this work and several previous publications,[30, 40-42] judiciously coupling nanocrystal growth with oxidative etching, galvanic replacement, or other redox processes enables controlled synthesis of structurally sophisticated nanocrystals exhibiting exotic geometries and fine-tailored surface topography, greatly enhancing our capabilities to further fine-optimize the optical and catalytic properties of nanoparticles for specific applications.

5.4 References

1. A. Moreau, C. Ciraci, J. J. Mock, R. T. Hill, Q. Wang, B. J. Wiley, A. Chilkoti and D. R. Smith, Nature, 2012, 492, 86-89.

2. J. N. Anker, W. P. Hall, O. Lyandres, N. C. Shah, J. Zhao and R. P. Van Duyne, Nat. Mater., 2008, 7, 442-453.

3. C. Chen, Y. J. Kang, Z. Y. Huo, Z. W. Zhu, W. Y. Huang, H. L. L. Xin, J. D. Snyder, D. G. Li, J. A. Herron, M. Mavrikakis, M. F. Chi, K. L. More, Y. D. Li, N. M. Markovic, G. A. Somorjai, P. D. Yang and V. R. Stamenkovic, Science, 2014, 343, 1339-1343.

4. P. K. Jain, X. H. Huang, I. H. El-Sayed and M. A. El-Sayed, Acc. Chem. Res., 2008, 41, 1578-1586.

5. B. Nikoobakht and M. A. El-Sayed, Chem. Mater., 2003, 15, 1957-1962.

6. S. E. Lohse and C. J. Murphy, Chem. Mater., 2013, 25, 1250-1261.

7. J. Perez-Juste, I. Pastoriza-Santos, L. M. Liz-Marzan and P. Mulvaney, Coord. Chem. Rev., 2005, 249, 1870-1901.

8. L. Scarabelli, A. Sanchez-Iglesias, J. Perez-Juste and L. M. Liz-Marzan, J. Phys. Chem. Lett., 2015, 6, 4270-4279.

9. J. E. Millstone, S. J. Hurst, G. S. Metraux, J. I. Cutler and C. A. Mirkin, Small, 2009, 5, 646-664.

10. L. Scarabelli, M. Coronado-Puchau, J. J. Giner-Casares, J. Langer and L. M. Liz-Marzan, ACS Nano, 2014, 8, 5833-5842.

11. M. Z. Liu and P. Guyot-Sionnest, J. Phys. Chem. B, 2005, 109, 22192-22200.

12. J. A. Zhang, M. R. Langille, M. L. Personick, K. Zhang, S. Y. Li and C. A. Mirkin, J. Am. Chem. Soc., 2010, 132, 14012-14014.

13. M. L. Personick, M. R. Langille, J. Zhang and C. A. Mirkin, Nano Lett., 2011, 11, 3394-3398.

14. Q. Zhang, N. Large and H. Wang, ACS Appl. Mater. Interfaces, 2014, 6, 17255-17267.

15. T. Ming, W. Feng, Q. Tang, F. Wang, L. D. Sun, J. F. Wang and C. H. Yan, J. Am. Chem. Soc., 2009, 131, 16350-16351.

16. T. T. Tran and X. M. Lu, J. Phys. Chem. C, 2011, 115, 3638-3645.

17. M. R. Langille, M. L. Personick, J. Zhang and C. A. Mirkin, J. Am. Chem. Soc., 2012, 134, 14542-14554.

18. S. E. Lohse, N. D. Burrows, L. Scarabelli, L. M. Liz-Marzan and C. J. Murphy, Chem. Mater., 2014, 26, 34-43.

19. Y. N. Xia, X. H. Xia and H. C. Peng, J. Am. Chem. Soc., 2015, 137, 7947-7966.

20. C. J. DeSantis, A. A. Peverly, D. G. Peters and S. E. Skrabalak, Nano Lett., 2011, 11, 2164-2168.

21. R. G. Weiner, M. R. Kunz and S. E. Skrabalak, Acc. Chem. Res., 2015, 48, 2688-2695.

22. W. X. Niu, W. Q. Zhang, S. Firdoz and X. M. Lu, J. Am. Chem. Soc., 2014, 136, 3010-3012.

23. T. K. Sau and C. J. Murphy, J. Am. Chem. Soc., 2004, 126, 8648-8649.

24. J. A. Edgar, A. M. McDonagh and M. B. Cortie, ACS Nano, 2012, 6, 1116-1125.

25. N. Almora-Barrios, G. Novell-Leruth, P. Whiting, L. M. Liz-Marzan and N. Lopez, Nano Lett., 2014, 14, 871-875.

26. M. J. Walsh, S. J. Barrow, W. M. Tong, A. M. Funston and J. Etheridge, ACS Nano, 2015, 9, 715-724.

27. M. J. Walsh, W. M. Tong, H. Katz-Boon, P. Mulvaney, J. Etheridge and A. M. Funston, Acc. Chem. Res., 2017, 50, 2925-2935.

28. Q. Zhang, H. Jing, G. G. Li, Y. Lin, D. A. Blom and H. Wang, Chem. Mater., 2016, 28, 2728-2741.

29. C. K. Tsung, X. S. Kou, Q. H. Shi, J. P. Zhang, M. H. Yeung, J. F. Wang and G. D. Stucky, J. Am. Chem. Soc., 2006, 128, 5352-5353.

30. Y. Q. Zheng, J. Zeng, A. Ruditskiy, M. C. Liu and Y. N. Xia, Chem. Mater., 2014, 26, 22-33.

31. M. C. Liu, Y. Q. Zheng, L. Zhang, L. J. Guo and Y. N. Xia, J. Am. Chem. Soc., 2013, 135, 11752-11755.

32. A. Ruditsicy, M. Vara, H. Huang and Y. N. Xia, Chem. Mater., 2017, 29, 5394-5400.

33. M. R. Langille, M. L. Personick, J. Zhang and C. A. Mirkin, J. Am. Chem. Soc., 2011, 133, 10414-10417.

34. Q. F. Zhang, N. Large, P. Nordlander and H. Wang, J. Phys. Chem. Lett., 2014, 5, 370-374.

35. H. Wang, K. Fu, R. A. Drezek and N. J. Halas, Appl. Phys. B-Lasers Opt., 2006, 84, 191-195.

36. Q. F. Zhang, D. A. Blom and H. Wang, Chem. Mater., 2014, 26, 5131-5142.

37. Q. F. Zhang, L. L. Han, H. Jing, D. A. Blom, Y. Lin, H. L. L. Xing and H. Wang, ACS Nano, 2016, 10, 2960-2974.

38. Q. F. Zhang, Y. D. Zhou, E. Villarreal, Y. Lin, S. L. Zou and H. Wang, Nano Lett., 2015, 15, 4161-4169.

39. J. W. Zhang, S. A. Winget, Y. R. Wu, D. Su, X. J. Sun, Z. X. Xie and D. Qin, ACS Nano, 2016, 10, 2607-2616.

40. Z. N. Wang, H. Wang, Z. R. Zhang, G. Yang, T. O. He, Y. D. Yin and M. S. Jin, ACS Nano, 2017, 11, 163-170.

41. L. Polavarapu, D. Zanaga, T. Altantzis, S. Rodal-Cedeira, I. Pastoriza-Santos, J. Perez-Juste, S. Bals and L. M. Liz-Marzan, J. Am. Chem. Soc., 2016, 138, 11453-11456.

42. L. Chen, F. Ji, Y. Xu, L. He, Y. F. Mi, F. Bao, B. Q. Sun, X. H. Zhang and Q. Zhang, Nano Lett., 2014, 14, 7201-7206.